DISSERTATION

ELUCIDATING TRANSLATION CONTROL OF ARGONAUTE IN LIVE CELLS BY DEVELOPING A TETHERABLE BIOSENSOR WITH SINGLE-MRNA RESOLUTION

Submitted by

Charlotte A. Cialek

Department of Biochemistry and Molecular Biology

In partial fulfillment of the requirements

For the Degree of Doctor of Philosophy

Colorado State University

Fort Collins, Colorado

Summer 2021

Doctoral Committee:

Advisor: Timothy Stasevich
Co-advisor: Taiowa Montgomery

Fred Hoerndli
Erin Nishimura
Eric Ross

ABSTRACT

ELUCIDATING TRANSLATION CONTROL OF ARGONAUTE IN LIVE CELLS BY DEVELOPING A TETHERABLE BIOSENSOR WITH SINGLE-MRNA RESOLUTION

Translation is an essential step for all living beings. It stands as the final hurdle of converting our genetic code into functional protein products. A culmination of specific factors heavily regulates what, when, and how much of a given peptide product is translated (**Chapter 1**). Though many technological advancements have expanded our understanding of translational control, they have often opened many new questions due to the high complexity of this process. Recently, a technique called Nascent Chain Tracking (NCT) was able to image translation with single molecule resolution in living cells (**Chapter 2**). NCT-based technologies have overcome some of the limitations of conventional in vivo and in vitro approaches to study translation. Though these NCT-based technologies accomplished detection of heterogeneity of translation dynamics, they were not capable of studying how specific factors mediate translational control.

The process of translation can be controlled by small RNA silencing pathways that restrict or completely block protein production. Of these, microRNAs (miRNAs) direct translational repression and mRNA decay by guiding the enzyme Argonaute and its associated proteins to partially complementary sequences on target mRNAs (**Chapter 1**). The dynamics of miRNA-mediated gene silencing, and in particular the role of Argonaute on translation, remain difficult to interpret due to pathway's

complexity, long (minutes-to-hours) timescale, and conflicting results from different studies.

To address these problems, we developed technology to directly visualize and quantify the impact of human Argonaute2 (Ago2) on translation and subcellular localization of individual reporter mRNAs in living cells (**Chapter 3**). Translation and Tethering (TnT) is a tethering-based single molecule reporter that simultaneously monitors translation and Ago2-tethering status in live human cells. Since this technique is microscopy-based, its readout includes valuable subcellular localization and intensity information over timeframes ranging from seconds to hours, which describe when, where, and how much translation and tethering is occurring per single-mRNA. Finally, to simplify using this multi-construct, multi-probe system, we adapted a cell loading technique, called bead loading, to introduce TnT plasmids and proteins simultaneously into adherent cells (**Chapter 4**).

Our TnT system reflects endogenous miRNA-mediated gene silencing when we compared it to natural miRNA-target site recruitment. Using the TnT system, we find that Ago2 association leads to progressive repression of translation at individual mRNA. The timescale of silencing was similar to that of translation, consistent with a role for Ago2 in blocking translation initiation and subsequent runoff of the ribosomes already engaged in translation elongation. At early timepoints, we observed occasional brief bursts of translational activity at Ago2-tethered mRNAs undergoing silencing, suggesting that translational repression may initially be reversible. At late timepoints, Ago2-tethered mRNA were redirected into P-bodies where they remained translationally silenced for 10+ hours, which was the duration of the experiment.

These results provide a framework for exploring miRNA-mediated gene regulation in live cells at the single molecule level (**Chapter 5**). Furthermore, due to the adaptability of the TnT system, it will likely have wide-ranging application in studying RNA-protein interactions more generally.

ACKNOWLEDGEMENTS

I would like to thank my co-mentors, Tim Stasevich and Tai Montgomery, who forged the collaboration that made this project possible. Throughout my experience in graduate school, they provided mentorship on how to think scientifically and creatively and extract understanding from experiments. I am fortunate to have had the opportunity to learn and grow as a rigorous, meticulous scientist from them. I also sincerely thank my doctoral committee members, Fred Hoerndli, Erin Nishimura and Eric Ross, for their attention to my project over the years and all of their inspiring ideas and contributions.

In addition, the research presented here would not have been possible without scientific contributions from Tatsuya Morisaki, Ning Zhao, Gabriel Galindo, Amanda Koch, and Matthew Saxton. I thank each of these researchers for their time and effort, and for being wonderful to work with. Additionally, significant contributions in experimental design and assay development came from O'Neil Wiggan, Chris Allen, Nick Flint, and Drew Tonsager. O'Neil, especially, was an invaluable scientific mentor who offered endless advice and encouragement. I would like to specifically recognize Tatsuya Morisaki, Kristen Brown, Tim Stasevich, and the GAUSSI program for teaching me how to code, a skillset that was instrumental in the research here presented.

I owe an enormous debt of gratitude to my labmates O'Neil Wiggan, Ning Zhao, Linda Forero, Phil Fox, Tatsuya Morisaki, Amanda Koch, Adam Koch, Gabriel Galindo, Matthew Saxton, Kristen Brown, Joshua Svendsen, Kailee Reed, Tarah Vijayasarathy, and Brooke Montgomery. Exchanging ideas with these folks helped solve problems, push my research forward, and explore new ideas.

I am immensely grateful to all the members of the Biochemistry and Molecular Biology department, especially my fellow graduate students, for creating such a collaborative, convivial, supportive environment. Specifically, I recognize and thank my cohort of Amanda Koch, Dylan Parker, Robert Wimbish, Colleen Watkins, and Matthew Marzo for their incredible support and friendship, from helping me pass my first-year oral exam to numerous conversations about our science over beers and around campfires. Also, my sincere gratitude goes to Travis Sanders for his patience, encouragement, and endless support as he helped me get through the final stretch of my PhD.

I would like to recognize the several scientific mentors who made an important impact on me throughout these years, including Jean Peccoud, Mark Zabel, Heather Matthews, Carol Wilusz, James Bamburg, Santiago DiPietro, and Tingting Yao. I would also like to give recognition to the several mentors who guided my path towards graduate school, including Greg and Katrina Clines, Spencer Anthony-Cahill, Robert Winn, Alec Lindsay, John Reebers, David Wood, and Michael Joy.

Finally, and most importantly, I would like to thank my family, Mom, Dad, Tyler, Audrey, and Wesley, and my lifelong friend Julia Apsey, for their unrelenting support and encouragement. I am so fortunate to have such an amazing, loving family, and none of this would have been possible without them.

TABLE OF CONTENTS

CHAPTER 1:
Background

This section discusses (1) the importance and variety of gene expression regulation and translation control mechanisms and (2) how Argonaute/microRNA work together to silence an mRNA.[1]

1.1. Gene expression regulation

Every cell is a tiny vessel filled with the machinery necessary to carry out the molecular-scale reactions which constitute life. This machinery, which is largely composed of proteins, maintains cell survival by allowing the cell to react to changes in its intra- or extracellular environment. Each component works autonomously to carry out tiny, specific reactions based on “decisions”, such as binding efficiency, concentration or probability. For these many molecular “decisions” to work together, an immense level of complexity is necessary for this extremely delicate balance to result in controlled, sustained survival.

As one can imagine, control over a cell’s complicated protein machinery is essential for keeping cellular processes running smoothly. The three general methods that cells use to achieve control over their protein composition and activity is by (i) removing unnecessary proteins through targeted decay pathways, (ii) modifying proteins to up- or down-regulate their activity, and (iii) making new proteins through gene expression. Simply put, a balance of protein synthesis and degradation produce a cell’s proteome,

[1]This chapter is composed of previously unpublished writing, including some ideas inspired by Cialek et al. (2021).

and the activity of this proteome varies based on modifications. This balance is achieved by synthesizing proteins through gene expression. Strictly regulating which genes are expressed is how an organism can be composed of a diverse variety of cell types, each containing different proteomes that all come from the same, single genomic set of DNA instructions.

1.1.1 Gene expression is regulated at the transcription and translation levels

Gene expression consists of multiple steps, each controlled by respective regulation mechanisms. These steps include transcription, the process of decoding a DNA gene into an mRNA transcript, and translation, the process of using the transcript template to produce functional protein machinery. Though these processes happen concurrently and are colocalized in archaea and bacteria, eukaryotic cells have higher complexity leading to additional regulation of gene expression. Most notably, eukaryotic transcription happens in the nucleus, and transcripts are thought to be licensed and exported before being translated. Initiating transcription requires a combination of highly regulated factors (general and specific transcription factors) and newly synthesized mRNA are modified (splicing, capping, poly-A tailing) and exported before being able to begin to be translated into protein (Gonatopulos-Pournatzis & Cowling 2014, Hershey et al. 2019, Stewart 2019). Throughout the rest of this piece of writing, I will focus exclusively on eukaryotic gene expression.

The extent to which a gene can be expressed as a protein is first controlled at the level of transcription, where cell machinery decides whether to transcribe a mRNA from its DNA gene and how many copies of mRNA to produce. Next, cytoplasmic machinery

decides how much protein to translate from each mRNA before mRNA decay and when to decay the mRNA (Buccitelli & Selbach 2020). A strong positive correlation between mRNA and protein levels demonstrates that gene expression (a combination of transcription and translation) is the dominant determinant of cellular protein levels, far outweighing effects of protein degradation (Schwanhäusser et al., 2011; Reviewed in Buccitelli & Selbach 2020).

Translation is the intricate, meticulous process of using a mRNA sequence to generate a polypeptide sequence, thus creating a protein. This is performed by a ribosome, a large conglomeration of ribosomal RNAs and proteins forming a two-subunit machine capable of accomplishing this task (Reviewed in Hershey et al. 2019; Gebauer & Hentze, 2004). Ribosomes initiate translation only after several heavily regulated steps. First, before translation can begin, several initiation factors must accumulate at the 5' end of the mRNA and form an initiation complex. The initiation complex, composed of the cap binding factor eIF4E, the helicase eIF4A, and the scaffold eIF4G, recruits the 43S ribosomal subunit, composed of the 40S subunit plus a methionine-loaded initiator tRNA, which can scan along the mRNA sequence in the 5' to 3' direction until it recognizes and halts at a start codon. At this point, a 60S ribosomal subunit is recruited and binds to the 43S ribosomal subunit, forming an 80S ribosomal subunit, which can then begin translation. The ribosome proceeds to translate along the mRNA, progressively decoding each mRNA codon and incorporating its respective amino acid into the growing polypeptide chain. When a stop codon is reached, the polypeptide chain and the two ribosomal subunits (40S and 60S) are released (Reviewed in Hershey et al. 2019; Gebauer & Hentze, 2004).

In mammalian cell culture, gene expression, as a whole, is controlled at the levels of transcription (predicted to explain ~35% of the variability of protein levels) and translation (predicted to explain ~55% of the variability of protein levels; Schwanhäusser et al., 2011). Transcription, as the first step in gene expression, can be considered as more of an “on” or “off” switch for protein expression. For example, some genes are only expressed, turned “on”, in a specific cell type, during a phase of the cell cycle, or upon a specific molecular signal, and are otherwise silenced, turned “off”. Translation, on the other hand, rapidly and immediately impacts the protein composition in cells since it is the last step of protein synthesis, thus explaining a large portion of variability between mRNA and protein levels. For example, translation at upstream open reading frames (uORFs) is normally silenced but becomes upregulated as soon as minutes cell stress (Wang et al. 2016). By controlling transcription and translation, cells tune translation in many ways, as discussed in the next section, by a general set of mechanisms referred to as translation control.

1.1.2 Translation control

After an mRNA is created through transcription, the level of its protein production can be controlled by either (i) translation regulation or (ii) mRNA decay (Schwanhäusser et al., 2011; reviewed in Buccitelli & Selbach 2020). Translation regulation is controlling how many ribosomes translate protein from a mRNA. Control of this step can come from slowing elongation to produce proteins more slowly and/or create ribosomal traffic jams, slowing ribosomes initiating translation, or completely reducing or shutting off translation initiation (Buccitelli & Selbach 2020). Decaying an mRNA also achieves down regulation of translation by physically destroying the template needed for

translation. Unlike translation regulation, which can be tuned and toggled, mRNA decay is irreversible: translation of the peptide encoded by the mRNA would require the cell to regenerate new copies of mRNA by cycling back to transcription (Buccitelli & Selbach 2020, Hershey et al., 2019).

Many levels of translation regulation exist for cells to maintain homeostatic levels of proteins or modify their proteome based on signals or stimuli (Hershey et al., 2019). Each step of translation -- (i) initiation, (ii) elongation and (iii) termination -- is governed by an accompanying set of regulatory factors. Many translation control mechanisms target initiation since this step dictates if translation of an mRNA should occur. Further, initiation is thought to be the rate limiting since it takes longer for a ribosome to initiate (~30 seconds to initiate a ribosome) than subsequent elongation reactions (~0.2 seconds to translate a codon; (Ingolia et al., 2016; Morisaki et al., 2016; Yan et al., 2016; Palmiter 1975). Moreover, translation initiation is a relatively easy step to target, since it can be halted by disrupting one or more of the several non-covalent bonds between the requisite factors. However, a growing body of evidence also shows that important translation control functions can and do also occur during ribosome elongation (Richter & Coller, 2015).

Translation is regulated on two levels: global (which is sequence-agnostic) and gene-specific (which is sequence-specific). A global method for regulating translation is essential as it can help a cell rapidly change its overall level of protein synthesis. For example, when a cell is under stress, it can rapidly shut down global cell translation by phosphorylating the translation initiation factor eIF2α (Pakos-Zebrucka et al., 2016). This is thought to reduce the energy consumption required for translation and allow for

translation machinery to focus on a subset of important genes that are resistant to stress-induced translation control (Buchan & Parker, 2009; Mateju, Eichenberger, Voigt, et al., 2020). Another example is FragileX Mental Retardation Protein (FMRP), which controls protein synthesis in the brain. FMRP is thought to associate with the open reading frame (ORF) of ~1000 different mRNAs in a sequence-agnostic manner to slow or stall ribosome elongation by either steric obstruction (Darnell et al., 2011), phase separation (Tsang et al., 2019), or perhaps a combination of the two. In contrast, controlling translation can be achieved when a factor targets a specific mRNA, e.g. by sequence recognition. This allows for selection of which transcripts to up- or down-regulate based on identifying and targeting a specific sequence. For example, this strategy is used during stress to select which ORFs should be licenced for translation. Upon mTOR activation, the La-Related Protein 1 (LARP1) targets and binds to a regulatory sequence called 5′ terminal oligopyrimidine (5’ TOP), which promotes translation at 5’TOP-harboring mRNA (Hinnebusch et al., 2016). The many peptides encoded in 5’TOP mRNA are thought to have important functions for surviving during stress conditions (Buchan & Parker, 2009).

A large, diverse consortium of factors execute translation control, many of which are RNA binding proteins (RBPs). There are ~1,500 predicted human RNA binding proteins (constituting 7.5% of our proteome), many of which target mRNAs to control expression levels, and they range in sequence specificity from sequence-specific to sequence-agnostic (Gerstberger et al., 2014).

1.2 Translation control by the microRNA Induced Silencing Complex

Though a multitude of fascinating translation control factors exist, in this body of work we specifically studied the factor Argonaute (Ago), the effector protein of the microRNA (miRNA) silencing pathway. An Ago protein and a miRNA bind to form the miRNA Induced Silencing Complex (miRISC), which can downregulate, or silence, gene expression (**Figure 1.1**). miRISC-mediated gene silencing is especially interesting due to its prevalence: there are about 2,000 predicted types of miRNA in the human genome, which are estimated to target about 12,500 genes (~60% of the human genome; Friedman et al., 2009; Kozomara & Griffiths-Jones, 2014; Willyard, 2018). Since miRNA target sites are conserved, it is predicted that the same miRNA may target up to 400 different mRNA (Friedman et al., 2009). The miRNA silencing pathway is essential in metazoan development; though Ago-knokout (and therefore miRNA-deficient) cells can survive in culture conditions, Ago-knockout mouse embryos will not survive gestation (Lykke-Andersen et al., 2008). Further, dysregulation of specific miRNA results in a multitude of diseases, including cancer (Ardekani & Naeini, 2010; Peng & Croce, 2016). Moreover, miRNAs have proven useful biomarkers and hold great promise as potential therapeutics (Rupaimoole & Slack, 2017). Since a sequence-specific mRNA-targeting RNA oligo is far easier to engineer than a peptide, harnessing miRNAs to regulate expression or target mutated transcripts remains an intriguing strategy to combat disease.

Though well studied, the effects that Agos have on mRNA remain elusive, likely due to their manifold regulatory functions (discussed in further detail in following sections). Altogether, Ago is an intriguing candidate to further study, and gaining a better

understanding of Ago's function in miRISC-mediated translation control will contribute important, meaningful information to the scientific community. Many studies over the past two decades have provided insight into how Ago-mediated translation silencing is thought to occur, a summary of which is provided in the following section.

1.2.1 microRNA biogenesis

miRNA are small, non-coding RNAs transcribed from genes by Pol II (Bartel, 2018). Because of this, they can be up- or down-regulated through promoter-driven transcription regulation depending on cell type or in response to stimuli. Precursor miRNA are transcribed as long noncoding RNA hairpins which are exported from the nucleus and cleaved in two steps to form ~22 nucleotide RNA-RNA duplexes with an overhang. An Ago protein recognizes and melts the miRNA-miRNA duplex, selecting one of the strands to be used in miRNA-directed silencing and releasing the unused strand (called the star strand) to be degraded. The Ago2-miRNA duplex is the core of the miRISC complex and, once formed, can target and initiate miRNA-mediated gene silencing (Bartel, 2018; Jonas & Izaurralde, 2015).

1.2.2 How does miRNA silence a transcript?

The miRNA in a RISC complex serves as a modular template for targeting a wide range of different mRNA sequences yet maintain high specificity and affinity. Thus, the miRNA allows the same population of Ago proteins to target with high specificity a diverse range of transcripts for silencing. When Argonaute interacts with a miRNA to form the miRISC, it pockets the 3' and 5' ends of the miRNA, displaying the nucleic acid

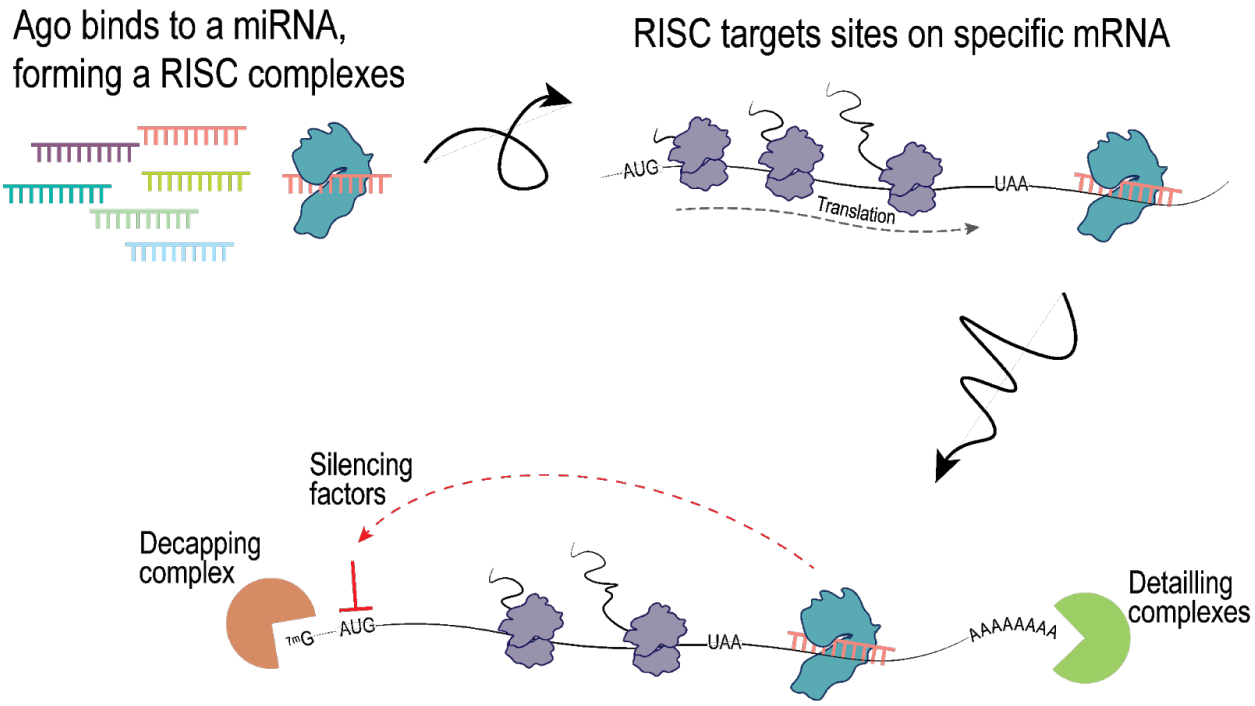

Figure 1.1 The Argonaute mediated miRNA silencing mechanism.

bases of the middle section (Schirle & MacRae, 2012; Sheu-Gruttadauria & MacRae, 2018). This allows for these mid-miRNA residues to interact with a mRNA through Watson-Crick base pairing. The miRISC is thought to form weak, transient interactions with sequence-agnostic regions of the mRNA as it scans sections of a mRNA transcript through 2D facilitated diffusion (sliding along or jumping between nearby regions of an mRNA). This is thought to aid the miRISC in reaching a mRNA location with a strong miRNA-mRNA match, called a miRNA Recognition Element (MRE; Chandradoss et al., 2015; Cui & Joo, 2019). Unlike siRNA, miRNA bind to their target with imperfect

complementarity; however, the more residues that can base-pair between the miRNA and mRNA, the stronger and more stable the interaction. Generally, MREs are no less than 7 nucleotide sequences, usually found in the 3' untranslated region (UTR) of a mRNA. Targeting of the nucleotides in positions 2-8 on the miRNA, termed the seed sequence, are essential for miRNA targeting, and more interactions can lead to more stable binding and stronger targeting (Bartel, 2018).

Once miRNA directs the miRISC to an appropriate transcript through a stable miRNA-MRE interaction, Ago catalyzes silencing of the transcript. There are four Ago proteins in mammals (Ago1-4). However, only Ago1-2 are substantially expressed. Ago3 is expressed at low levels thus minimally contributing to miRNA silencing, and the cellular concentration of Ago4 is thought to be too low to have a significant, measurable impact on gene silencing. Ago proteins are essential to miRNA-mediated silencing – without an Ago protein, miRNA-mediated silencing is not thought to be able to happen.

Once a miRNA-loaded Ago has targeted a mRNA, the overall outcome is reduced protein output, which has been repeated in a wide variety of experiments (Béthune et al., 2012; Djuranovic et al., 2012; Eichhorn et al., 2014; Guo et al., 2010; Hendrickson et al., 2009; Pillai et al. 2004; Tat et al., 2016). However, how exactly this happens is still quite unclear and under debate (Izuaralde & Jonas, 2016).

It is worth noting here that one of the Ago proteins, Ago2, has a functional RNase H-like domain and can perform endonucleolytic cleavage/slicing of the target mRNA. However, Ago2's cleavage activity is thought to be restricted to the siRNA pathway. If Ago2 is in a complex with a small RNA which has perfect base pair complementarity to its target, which is the case for siRNA, it can have the catalytic power to slice the mRNA

strand (Ameres et al., 2007; Chandradoss et al., 2015). The benefits of siRNA-directed Ago2 slicing have been harnessed in biotechnology to rapidly design and create siRNA for knock down assays. This allows for rapidly designing and creating siRNA targeting virtually any transcript sequence (Scherer & Rossi, 2003). However, miRNA bind their mRNA target with imperfect complementarity, usually only base-pairing between a ~7 or 8 nucleotide seed sequence that sometimes has non-contiguous base pair interactions. Thus, an miRNA-directed Ago2 is not thought to catalyze the mRNA slicing reaction (Jonas & Izaurralde, 2015).

The most prominent role of Ago in the miRNA-mediated silencing pathway is thought to be recruiting the large, scaffold-like factor TNRC6 (GW182 in invertebrates). Like Ago2, TNRC6 is required for the miRNA pathway to occur; blocking the Ago-TNRC6 interaction by mutating Agos 1 or 2 blocks silencing (Eulalio et al., 2008; Huntzinger et al., 2013). TNRC6 is a large, mostly unstructured protein that is thought to bridge Ago to the factors which facilitate mRNA destabilization and translation silencing. Ago and TNRC6 interact through tryptophan binding pockets: Ago has three tryptophan binding pockets in its PIWI domain and can bind up to three TNRC6 proteins (Lian et al., 2009; Schirle & MacRae, 2012; Sheu-Gruttadauria & MacRae, 2018). Likewise, TNRC6A has three tryptophan in its Argonaute Binding domain (ABD) which can bind up to three Ago proteins (Elkayam et al., 2017). It is unknown if repeated binding domains are used for Ago and TNRC6 to bind each other at three locations (thus increasing the strength of a single Ago-TNRC6 interaction), or for up to three different Ago proteins to bind one TNRC6 and vice versa (promoting weak, multimeric interactions to increase recruitment of the silencing complex). The crystal structure

suggests that both models are sterically possible. In support of multimeric interactions, multiple proximal MRE in a transcript cooperatively enhance miRNA-mediated silencing (Grimson et al., 2007), which could be from the fact that multiple Agos can bind to the same TNRC6 protein and thereby enhance or expedite downstream silencing effects (Elkayam et al., 2017). Also, weak multimeric interactions between multiple Ago and TNRC6 proteins are the hallmark of phase-separation, a property which Ago and TNRC6 are known to have (Elkayam et al., 2017a, p. 182; Liu, Rivas, et al., 2005; Sheu-Gruttadauria & MacRae, 2018).

After TNRC6 is recruited, it in turn recruits proteins that destabilize the mRNA. It does so through a large, unstructured Silencing Domain (SD) which serves as a platform for interacting with a multitude of factors involved in translational repression and mRNA decay (Chen et al., 2014). Not only is TNRC6 required for miRNA-mediated silencing, but so is its SD (Behm-Ansmant et al., 2006); overexpression of a truncated TNRC6 containing only a SD competes for Ago binding and effectively blocks miRNA-mediated silencing (Eulalio et al., 2008).

The TNRC6 scaffold recruits two different deadenylase complexes, the CCR-NOT and PAN2/3 complexes, which reduce the length of the polyA tail (Aizer et al., 2014; Béthune et al., 2012; Djuranovic et al., 2012). It is under debate how exactly de-tailing plays into the rest of the mRNA-mediated silencing, since mRNA decay eventually happens in the 5’ to 3’ end, not starting at the tail. However, it has repeatedly been shown that the miRNA pathway shortens polyA tails, and that de-adenylated mRNA do not accumulate (in rapidly dividing cells at least) unless de-capping is blocked, suggesting a strong mechanistic link between de-adenylation and de-capping (Behm-

Ansmant et al., 2006; Chen et al., 2009). Further, miRNA-targeted mRNA with no detectable polyA tail accumulated in P-bodies, suggesting that a possible role of de-tailing could be involved in the decision between mRNA decay and silent mRNA storage (Aizer et al., 2014). Interestingly, TNRC6 also contains a PolyA-binding Motif (PAM2), which interacts with PolyA Binding Protein Complex (PABPC). The exact purpose of the TNRC6-PABPC interaction is unknown, but it could facilitate miRISC in interacting with the polyA tail for de-adenylation.

After de-adenylation complex recruitment, translation inhibition and de-capping factors are recruited to the target mRNA. The NOT1 subunit of the CCR-NOT deadenylase complex recruits DDX6 through a direct binding interaction (Chen et al., 2014; Rouya et al., 2014). DDX6 is thought to inhibit translation of a targeted mRNA both by promoting de-capping and by de-capping-independent translation initiation silencing (Fabian et al., 2011). De-capping complex subunits DCP1 and 2 are required for miRNA-mediated mRNA decay, though it is still unclear precisely how they are recruited (Jonas & Izaurralde, 2015). DCP2 cleaves the protective 7-methylguanosine (m^7GpppN) cap from the 5' end of the mRNA transcript, making it vulnerable to decay (Cohen et al., 2005; Mugridge et al., 2016).

The final stage of gene silencing in the miRNA pathway is mRNA decay. Since de-capped transcripts are barely detectable in cells, it is thought that mRNA decay rapidly follows de-capping (Hsu & Stevens, 1993). The de-capped mRNA is thought to be decayed processively, base by base, in the 5'-3' direction by exoribonuclease I (XRN1; Hoek et al., 2019; Jinek et al., 2011). It is known since XRN1 is required for siRNA-mediated mRNA decay to degrade the 5' fragment after Ago2-mediated slicing (Orban

& Izaurralde, 2005). Further, though the link between miRNA-mediated decay pathway and XRN1 is not as clear, several studies found that de-capped, miRNA targeted mRNA do not build up in cells (Eichhorn et al., 2014) and when decay is inhibited the outcome is a buildup of de-capped, miRNA-targeted mRNA .

Though much about mRNA decay is left unknown, XRN1 is known to be the major exoribonuclease in the cytoplasm for RNAs including mRNA (Geisler & Coller, 2012). XRN1 is thought to be recruited to the miRISC through a direct interaction with DCP1 (Braun et al., 2012). The interaction between XRN1 and DCP1 is quite convenient, since capped mRNA are highly resistant to XRN1-mediated decay (Geisler & Coller, 2012). Once XRN1 has identified a de-capped 5' end of an mRNA substrate, it proceeds to decay mRNA in the 5' to 3' direction and do so in a processive manner at a rate of about 0.3 kilobases per minute until the mRNA is completely destroyed (Friedman et al., 2009; Hoek et al., 2019).

1.2.3 The role of P-bodies in miRNA mediated gene silencing

The miRNA-targeted mRNA which are not immediately decayed are thought to be stored in membraneless cytoplasmic organelles called P-bodies (Standart & Weil, 2018). These structures are formed through phase-separation by the weak, multimeric bonds between proteins and RNAs (Lin et al., 2015; Sheu-Gruttadauria & MacRae, 2018). Though P-bodies contain most of the decay factors involved in miRNA-mediated silencing, including the de-capping factors, de-tailing factors, and XRN1, decay of mRNA is not thought to happen within P-bodies. Several single-mRNA studies which labeled both 5' and 3' ends of the mRNA found only intact mRNA within P-bodies (Adivarahan et al., 2018; Horvathova, Voigt, Kotrys, Zhan, Artus-Revel, et al., 2017;

Khong & Parker, 2018). There remains the possibility that decay happens too rapidly to be detected, though this would mean that translationally-silenced mRNA linger in P-bodies long enough to be detected as intact and decay happens rapidly enough to be undetectable.

In addition to decay, translation is thought to be generally repressed within P-bodies. Evidence that P-body-localized mRNA are translationally silent comes from the observation that P-bodies lack key translation machinery requisite for translation to happen (Hubstenberger et al., 2017; Matheny et al., 2019). Further, single-mRNA imaging assays revealed that mRNA are often translationally silenced before entering P-bodies (Moon et al., 2019). Though the role between miRNA-mediated silencing and P-bodies is not yet clear, it is known that mRNA harboring miRNA binding sites are more likely to localize within P-bodies (Hubstenberger et al., 2017; Pillai et al., 2005). For these reasons, the current consensus is that the miRNA-targeted mRNA harbored in P-bodies are thought to be protected from decay in a translationally-silenced state.

1.2.4 miRISC-mediated translation inhibition

The majority of studies on the miRNA silencing mechanism agree that the prevailing outcome to reduced gene expression of a target transcript is due to mRNA decay (Jonas & Izaurralde, 2015). This has been shown through a multitude of methods, including both artificial reporters and endogenous transcripts. In most studies, the cellular concentrations of miRNA-targeted mRNA and its encoded protein were reduced (Jonas & Izaurralde, 2015). However, translation inhibition in the absence of decay is also known to play a role in miRNA-mediated silencing. For example, a seminal study determined that miRNA in the let-7 family inhibited translation initiation, likely by

blocking initiation factors from recognizing the m^7G mRNA cap (Pillai et al., 2005). Several studies since then have shown that bypassing the cap recognition step of translation initiation, e.g. through a synthetic cap-like structure or an Internal Ribosome Entry Site (IRES), also relieved miRNA-mediated translation inhibition (Humphreys et al., 2005; Mathonnet et al., 2007; Ricci et al., 2013; Wakiyama et al., 2007). More recently, it was shown that blocking a step in multivesicular body formation increased the stability of miRNA-targeted transcripts yet maintained miRNA-mediated translational repression, thus showing that decay and translation repression can become uncoupled and act independently (Bose et al., 2017). In contrast to initiation inhibition, multiple studies have presented evidence that elongation, by means of premature ribosome dropoff, may also be affected by miRNA targeting (Nottrott et al., 2006; Petersen et al., 2006). However, another report contested these results by showing that only the first step of initiation (40S ribosomal targeting), and not any of the downstream initiation or elongation steps (formation of the 60S ribosomal subunit, elongation or termination) was affected by miRNA targeting (Ricci et al., 2013). Thus, it is quite well established that miRNA-targeting represses translation at the ribosome initiation step.

In addition to a convoluted role of translation inhibition in the miRNA silencing pathway, the timeframe of translation repression is also unclear. When and how long is translation inhibited in the timeline of miRNA-mediated silencing? This has been studied by inducing miRNA targeting of a transcript by either loading/expressing miRNA or a mRNA reporter and then monitoring the subsequent changes to mRNA level and translation output over time. To monitor how mRNA decay and translation repression contributed to silencing, these experiments simultaneously measured the levels of

translation (via luciferase expression or ribosome footprints) versus the level of mRNA (via RT-qPCR or mRNA sequencing; Béthune et al., 2012; Djuranovic et al., 2012; Eichhorn et al., 2014; Guo et al., 2010; Hendrickson et al., 2009; Tat et al., 2016). With this general strategy, the relative silencing contributions of translation inhibition versus decay could be quantified. In this way, the results from these studies suggest that translational inhibition occurs for a brief period of time (~2 hours) before substantial mRNA decay began. The existence of a period of time where translation inhibition prevailed before decay took over thus reinforced the idea that translation silencing was occurring. However, since this time period was so short and directly followed by substantial mRNA decay, it suggested that translation inhibition likely acts on an intermediary step in the decay pathway.

Interestingly, however, not all miRNA-targeted transcripts were silenced in the same way. For example, a study found that a reporter containing 6 let-7 miRNA target sites was translationally inhibited without decay soon after miRNA targeting (1-2 hours post-induction), and substantial mRNA decay began at 4 hours post-induction. In contrast, a single miRNA-21 binding site resulted in decay of the transcript without non-decayed translational silencing (Béthune et al., 2012). At steady-state timepoints (24 and 48 hours post-induction), the study found that though the primary mechanism of silencing was mRNA decay, a sizeable fraction of let-7-targeted transcripts were translationally inhibited without being decayed, whereas mRNA decay was the only silencing mechanism for the miR-21-targeted transcript. Similar heterogeneous results were obtained when miRNA-mediated silencing was studied by ribosome footprinting/mRNA sequencing assays (Eichhorn et al., 2014; Guo et al., 2010). At early timepoints,

ribosomal footprints per miRNA-targeted mRNA decreased without substantial change in the number of mRNA transcripts, suggesting translational repression without mRNA decay. At steady state, however, ribosome footprints and mRNA sequencing reads were reduced, suggesting that the predominant effect of silencing was from mRNA decay. Even so, a fraction of transcripts not associated with ribosomes remained decay-resistant. When mRNA silencing was broken into relative contributions of translation inhibition and mRNA decay, translation inhibition was found to play a small yet significant (6-26%) role in the overall silencing effect (Eichhorn et al., 2014; Guo et al., 2010).

Taken together, these studies suggest that miRNA represses translation ~0.5 - 2 hours after targeting, at which point mRNA decay takes over as the prevailing silencing mechanism. However, not all mRNA undergo the same silencing by miRNA targeting – some are decayed whereas some are repressed without decay. The yet unknown cause of this dissimilitude could be from a number of factors, including the frequency, proximity or sequence context of MREs in the transcript or inherent differences between miRNAs which could, for example, interact with Ago or other miRISC factors in different ways.

1.2.5 miRISC-mediated silencing: decay or translation inhibition?

The current consensus in the field is that the primary outcome of miRNA-targeting is mRNA decay, as described above; however, the minor but measurable contribution of translation repression to silencing remains obscure. Translation repression could be achieved through multiple mechanisms, each supported by somewhat conflicting lines of evidence.

Some studies suggest that translation repression is a direct consequence of mRNA decay. In their models, ribosomes are potently, permanently blocked from initiating by de-capping or physical destruction of the 5' end of the mRNA by XRN1, which could cause mRNA decay to happen co-translationally. Evidence for this model came from co-sedimentation of polysomes with partially decayed, miRNA-targeted mRNA in polysome profiling assays (Tat et al., 2016). Since the rate of XRN1 is thought to be faster than ribosome elongation and both processes are thought to be processive, XRN1 could even potentially catch up with the last translating ribosome (Tat et al., 2016). Another mechanism is that translation repression occurs subsequent to mRNA decay. In this model, translation initiation blocking (by the factor DDX6 or as a result of de-capping) is coupled to decay, but the two events happen stepwise. Evidence for this model came from the fact that translation was repressed for 1 or more hours before detection of mRNA decay (Bazzini et al., 2012; Béthune et al., 2012; Djuranovic et al., 2012; Eichhorn et al., 2014; Guo et al., 2010; Hendrickson et al., 2009; Subtelny et al., 2014; Wilczynska et al., 2019). This timeframe outlasts how long it would take to translate a typical open reading frame and therefore does not support co-translational mRNA decay. A third mechanism is that miRNA targeting can trigger silencing through decay and translation repression separately. Perhaps both decay and translation repression act in a stochastic manner independent of each other, and the delay in mRNA decay comes from that mechanism taking longer to occur. Evidence supporting this model came from the findings that miRNA-mediated translation repression and decay can be uncoupled, suggesting that at least repression can occur independently of decay (Bose et al., 2017).

To add to the complexity, a standard miRNA-mediated silencing mechanism may not exist. One study suggested that transcripts expressed at high levels were silenced by a mixture of translation repression and decay, whereas low-expression transcripts were silenced by decay without detectable translation repression (Béthune et al., 2012). Another study measured that varying levels of Argonaute targeting came from differences such as extent of miRNA-mRNA binding and proximity of other Argonaute binding sites in the same transcript, and the extent to which the mRNA is translated (Ruijtenberg et al., 2020). Moreover, Ago and TNRC6 are mediated by several post-translational modifications and therefore do not act in a uniform, standard way. For example, phosphorylating Ago2's Ser387 residue promotes its localization to P-bodies and reduces its RNaseH slicing activity, both outcomes favoring translation repression over mRNA decay (Zeng et al., 2008). If heterogeneity of miRISCs causes different types of silencing for different transcripts, the outcome of the aforementioned bulk-cell experiments may actually represent multiple, different silencing mechanisms or timelines. Overall, the complexity and likely heterogeneity in miRNA-mediated silencing have obscured our understanding of this process and left many mechanistic questions unanswered.

CHAPTER 2
Advancements in technology for imaging single mRNA-translation dynamics in live cells

This chapter discusses the advances in live-cell, single-mRNA imaging of translation technology. Over the past five years, many technological advances have made it possible to image the translation of single mRNA in the natural context of living cells. With these advances, researchers are beginning to shed light on when, where, and to what degree mRNA are translated with single-molecule precision. These works provide insight into the heterogeneity of translation amongst single transcripts, behavior that is averaged out in complementary bulk assays. This chapter begins with a brief overview of recent technological advances. The chapter then reviews and lists the new biological insights gained from NCT-based technologies.[2]

2.1 Lighting up Single-mRNA Translation Dynamics in Living Cells

Translation is the process by which a ribosome decodes an mRNA codon by codon to synthesize a nascent polypeptide chain. The process has traditionally been studied in cells by detecting expression levels via radiolabeling, fluorescence or bioluminescence (reviewed in Tahmasebi et al., 2019). More recently, the technique ribosome profiling has also been used to detect where translating ribosomes are distributed across each mRNA in the transcriptome (Ingolia, 2016; Ingolia et al., 2019). While powerful, a drawback of these assays is their reliance on population averaging, which limits their temporal resolution and convolves any heterogeneity in translation that

[2]Much of the text of **Chapter 2** is based on the following work (Cialek et al., 2020), of which I was a co-first author with A.L.K. Listed are author contributions: A.L.K., C.A.C. and T.J.S wrote the manuscript. G.G. designed and created the figures. A.L.K., C.A.C., G.G. and T.J.S edited the manuscript and figures.

might exist between individual mRNA (Chao et al., 2012). Complementary techniques are therefore required to study translation at the single-mRNA level with higher temporal resolution, preferably in the natural context of living cells.

2.1.1 The Nascent Chain Tracking assay

In an eventful few months in 2016, five publications announced the development of similar technologies to visualize translation in living cells at the single-molecule level (Morisaki et al., 2016; Pichon et al., 2016; Wang et al., 2016; Wu et al., 2016; Yan et al., 2016). The technology, which we refer to collectively as Nascent Chain Tracking (NCT) for simplicity here, uses complementary probes to label mRNA and nascent polypeptide chains in translation sites with different colored fluorophores (**Figure 2.1**). mRNA are labeled with the MS2 or PP7 systems (Reviewed in Coulon et al., 2013). Similarly, nascent chains are labeled by fluorescent antibody-based probes, either single-chain variable fragments (scFv; Tanenbaum et al., 2014) or fragmented antibodies (Fab; Hayashi-Takanaka et al., 2011; Morisaki et al., 2016). These probes bind short, repeated epitopes fused to the N-terminus of a protein of interest. Unlike more traditional fluorescent fusion tags such as GFP, which take minutes to fold and become fluorescent, the major advantage of using fluorescent Fab or scFv is they can light up a nascent polypeptide chain co-translationally, within seconds of its emergence from the exit tunnel (Morisaki et al., 2016). With NCT, it is now possible to visualize where the translating mRNA are in cells, the heterogeneity in translation dynamics between single mRNA, and the specific kinetics of translation initiation and elongation.

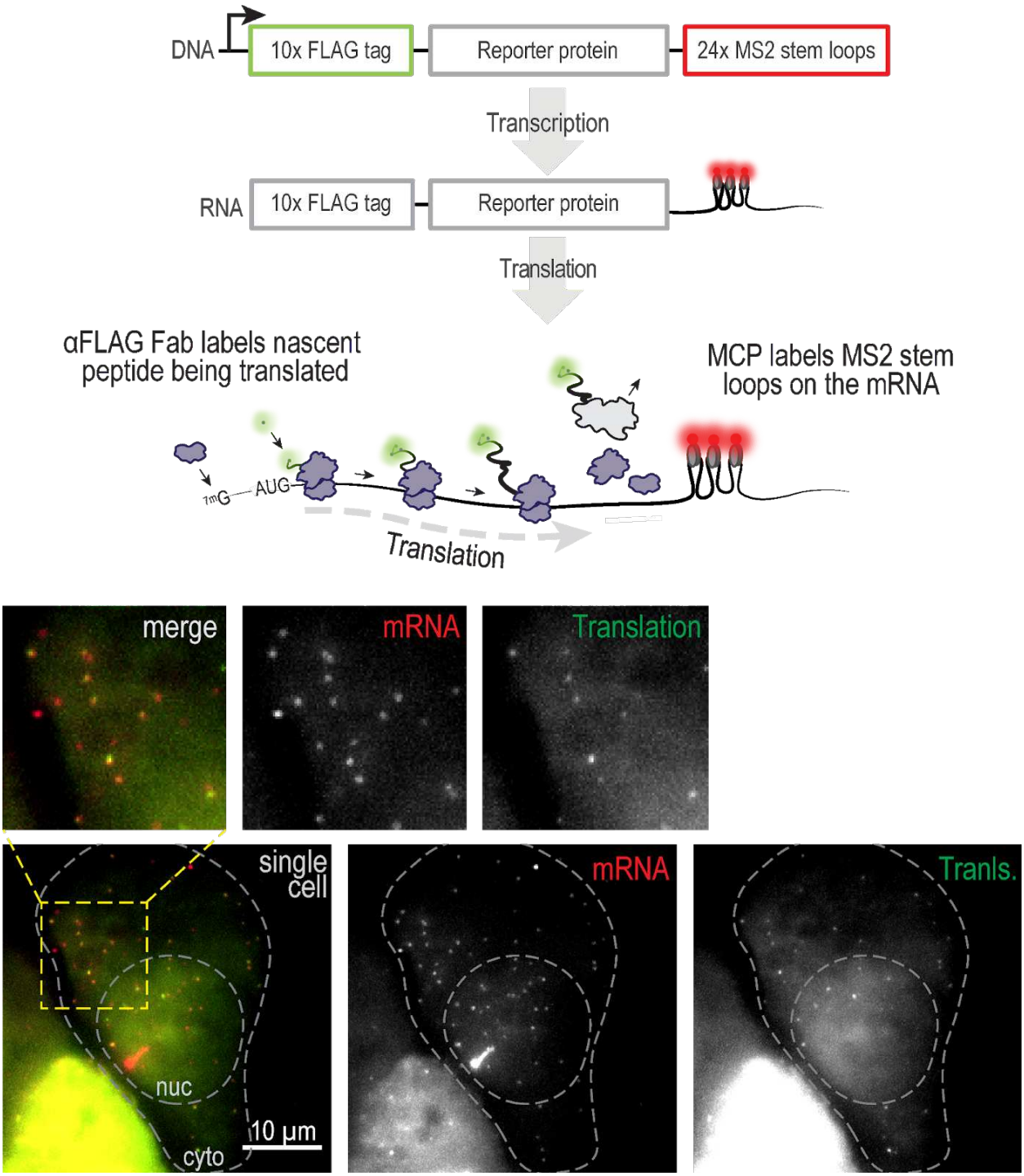

Figure 2.1. The nascent chain tracking system for real-time translation in live human cells at single reporter mRNA. "Nuc", nucleus and "Cyto", cytoplasm.

This sudden burst of NCT-based technology papers from several different labs signifies the need and power of NCT. Since NCT has been cross-verified across research labs, several groups are now starting to use it to extend what we know about translation. In what follows, we highlight the most recent advances of NCT and discuss how the technology is being used to dissect the kinetics of translational gene regulation with unprecedented spatiotemporal resolution.

2.1.2 Recent technology advancing Nascent Chain Tracking

Since 2016, a couple of significant advances have made NCT more versatile and user-friendly, as summarized in **Figure 2.2**. First, considerable effort has been made to make more genetically encoded antibody-based probes. To complement the popular anti-SunTag scFv (Tanenbaum et al., 2014), the anti-MoonTag probe (Boersma et al., 2019) was derived from a camelid nanobody that binds the HIV gp41 epitope (KNEQELLELDKWASL, referred to as the MoonTag; Hulsik et al., 2013). Likewise, to complement the HA spaghetti monster tag (Viswanathan et al., 2015), the anti-HA frankenbody was developed to bind the classic HA epitope (YPYDVPDYA; Zhao et al., 2019). Since the SunTag scFv, MoonTag nanobody, and frankenbody can be encoded in plasmids, they are cheap, easy to use, and can be further genetically engineered to bind their target epitopes with higher affinity or bind new epitopes entirely. Concurrent with the development of these probes, new repeat epitope tags were designed to simultaneously visualize translation in different reading frames (Boersma et al., 2019; Lyon et al., 2019). In the MoonTag and SunTag Hybrid (MASH) tag

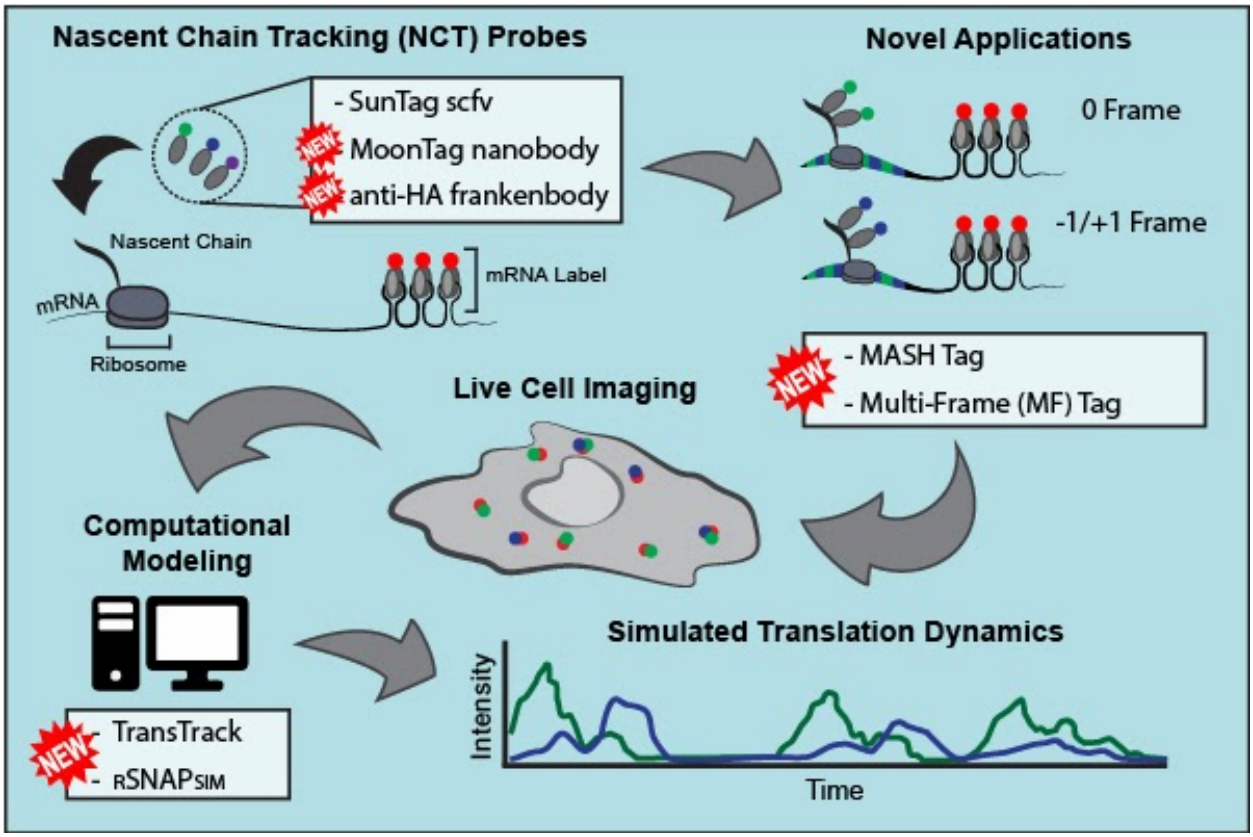

Figure 2.2. Advances in single-mRNA translation imaging technology.
In the Nascent Chain Tracking (NCT) assay, mRNA (red) and nascent polypeptide chains (green or blue) in translation sites co-move in live cells. New probes, including the MoonTag nanobody and anti-HA frankenbody, can be used to label translation sites in different colors. Together with new reporter tags, including the MoonTag and SunTag Hybrid (MASH) tag and the multi-frame tag, translation sites in live cells can be lit up in different colors depending on what frame is being translated. Translation intensity signals over time can be modeled using new software, including TransTrack or RNA Sequence to NAscent Protein SIMulator (RSNAPSIM).

(Boersma et al., 2019) and the multi-frame tag (Lyon et al., 2019), epitopes of one type are interspersed between epitopes of another type encoded in a different frame. In this way, as translation progresses, nascent chains are bound and lit up by different

fluorescent probes depending on which frame is being translated (Boersma et al., 2019; Lyon et al., 2019).

Another significant advance in NCT has been computational in nature. Translation is inherently a stochastic process that requires sophisticated modeling to accurately fit and predict single-mRNA dynamics. To make this easier, several labs have now published their modeling software alongside methods papers (Aguilera et al., 2019; Fonkeu et al., 2019; Voigt et al., 2019). RSNAPSIM, for example, includes an interface that allows users to design translation imaging plasmids and simulate common experiments such as FRAP (fluorescence recovery after photobleaching), FCS (fluorescence correlation spectroscopy), and translation inhibitor experiments (Aguilera et al., 2019).

2.2 New applications of Nascent Chain Tracking

Recently, NCT has been applied to answer numerous biological questions, from the mechanistic details of canonical, endogenous translation to non-canonical viral translation. The NCT assay has helped illuminate not only how translation is activated, but also how cells turn off translation and regulate aberrant mRNA. Here we summarize recent NCT applications to investigate translation control.

2.2.1 Viral translation

Viruses are known to hijack host machinery for the purpose of translating their own viral RNA (vRNA). This phenomenon was recently studied using a NCT-based assay. Boersma et al. adapted a coxsackievirus B3 to contain SunTag epitopes to specifically monitor translation of its vRNA (Boersma et al., 2020). This system allowed

for visualizing the entire viral life cycle during mammalian cell infection, starting with the translation of the first vRNA, shutdown of translation during vRNA replication, then a burst of translation of newly synthesized vRNA. Importantly, this NCT-based system allowed for discerning heterogeneity between single-cell infection, including instances where vRNA replication failed and was restarted, and quantify single-vRNA dynamics, such as distinct vRNA localizations during different phases of the viral life cycle.

2.2.2 mRNA structure during translation

During canonical translation, interactions between initiation factors bound to the 5' cap and poly-A tail have led researchers to believe mRNA exist in a stable closed-loop conformation (Svitkin et al., 2009). Recent single-molecule experiments are beginning to question this model. Specifically, Adivarahan et al. and Khong et al. used smFISH (Femino et al., 1998; Raj et al., 2008; Reviewed in Taliaferro, 2019) to precisely measure distances from the 5' to 3' end of single mRNA in untreated and translation inhibited cells (**Figure 2.3A**; Adivarahan et al., 2018; Khong & Parker, 2018). These studies revealed mRNA ends are further apart in translating versus non-translating mRNA species. Furthermore, by using NCT, these studies in fixed cells and more recently Koch et al. in live cells showed that mRNA become more spread out as more ribosomes load (Adivarahan et al., 2018; Khong & Parker, 2018; Koch et al., 2020), indicating the translation machinery is responsible for the spreading out. These data suggest either mRNA is not in a closed loop during translation or the closed-loop conformation is a transient event (Vicens et al., 2018).

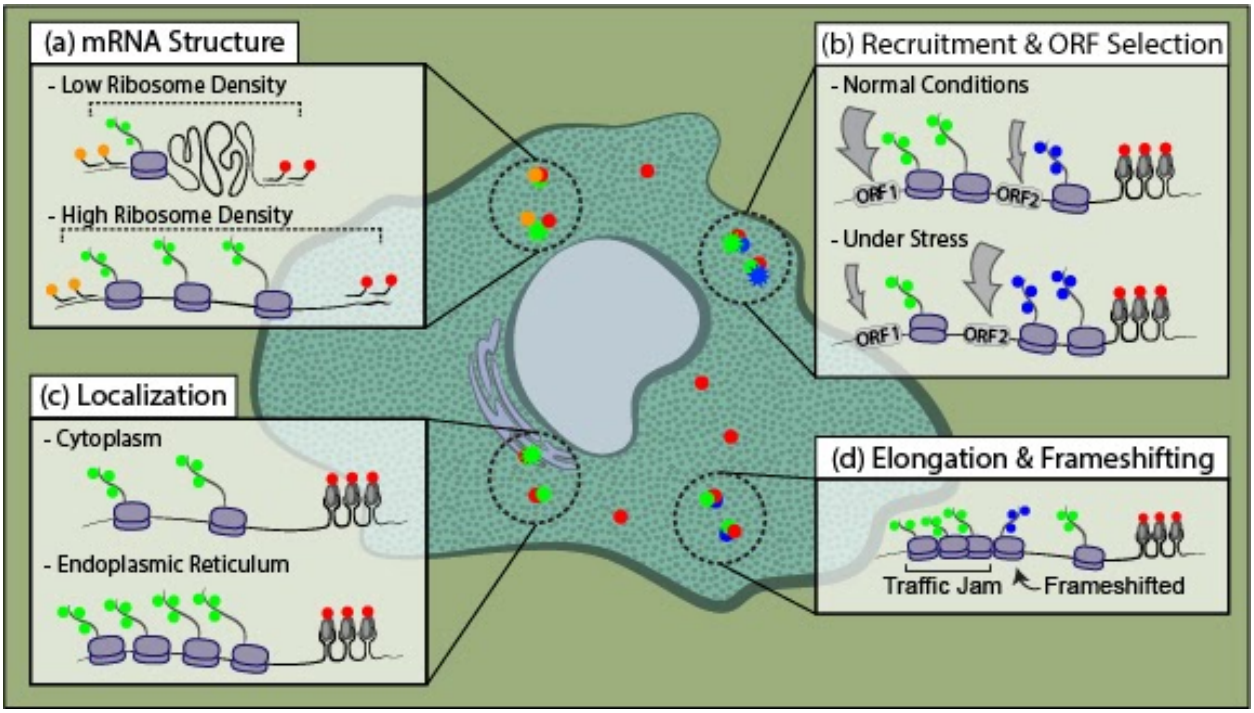

Figure 2.3. Recent applications of NCT to study active translation dynamics
A NCT was combined with Single-Molecule Fluorescence In Situ Hybridization (smFISH) in fixed cells to measure the distance between the ends of the mRNA (red and orange). This was combined with antibody staining of nascent polypeptide chains (green) to count the translating ribosomes. By measuring the distance between 3' (red) and 5' (orange) mRNA probes and counting the number of translating ribosomes, 2D mRNA structures were quantified.
B Two NCT systems were used to measure ribosome recruitment kinetics to a canonical (green) and non-canonical (blue) Open Reading Frame (ORF) and how ribosomes pick a start site once recruited to the mRNA. These assays were also conducted under stress conditions and differences in ribosome recruitment and ORF selection were measured.
C By combining endoplasmic reticulum staining with NCT, mRNA localization and ribosomal content were determined.
D NCT was used to investigate the heterogeneity of ribosomal elongation kinetics, including stalling at specific pause sites or frameshifting at a frameshift sequence. Both of which were associated with ribosomal traffic jams.

2.2.3 Ribosome recruitment mechanisms

Different mechanisms have evolved to recruit ribosomes to mRNA and facilitate translation. The canonical mechanism employed by most eukaryotic transcripts relies on the Cap Binding Complex (CBC) to recruit the first round of ribosomes after nuclear export (Gonatopoulos-Pournatzis & Cowling, 2014). To investigate this at the single-molecule level, Hoek et al. used NCT to image translation in wildtype cells and cells with eIF4E inactivated by ha4EBP1 over-expression (leaving only CBC for ribosome recruitment; Hoek et al., 2019). According to this work, CBC can recruit multiple ribosomes in bursts during early rounds of translation before being replaced by eIF4E. This work highlights how NCT can be combined with inactivation/knock-down assays to dissect the contribution of a specific factor to translational gene regulation.

In addition to cap-dependent ribosome recruitment, other non-canonical mechanisms have evolved to recruit ribosomes. One mechanism used by a wide range of viruses to hijack host ribosomes is an Internal Ribosomal Entry Site (IRES), an mRNA sequence that attracts ribosomal initiation factors (Filbin & Kieft, 2009; Gebauer & Hentze, 2004). Through the development of an NCT bicistronic reporter, Koch et al. uncovered the translation kinetics of cap-dependent versus IRES-mediated translation (**Figure 2.3B**; Koch et al., 2020). According to this work, the IRES recruits two to three times fewer ribosomes than the cap in normal conditions, but the balance shifts dramatically in favor of the IRES during stress.

2.2.4 Open reading frame selection

Once the ribosome is recruited to an mRNA, it must scan the 5’ untranslated region (UTR) to find a start codon and thereby choose an open reading frame (ORF) for

translation. Dr. Marilyn Kozak showed in classic bulk studies that the eukaryotic ribosome typically recognizes an AUG start codon within specific nucleotide contexts, which helps initiation to occur at a specific location and in a specific ORF (Kozak, 1986, 1987). However, some transcripts have multiple ORFs and/or multiple AUGs, so the ribosome must decide where to initiate translation. NCT is now being used to investigate the stochasticity and heterogeneity of this choice. In one study, NCT was used to examine the regulation of the stress-response gene *ATF4*, the transcript of which contains two upstream ORFs (Wang et al., 2016). According to this work, the third ORF, which codes for the ATF4 protein, was rarely chosen by ribosomes under normal conditions but was dramatically upregulated in a short-lived burst upon stress. NCT revealed these bursts were initiated in a matter of seconds and lasted for minutes at a time.

More recently, Boersma et al. used the MASH tag to investigate ribosomal start-site selection (**Figure 2.3B**; Boersma et al., 2019). In their MASH reporter, nascent chains were labeled in different colors depending on the start site chosen. This revealed a surprising degree of heterogeneity amongst mRNA, with multiple start sites used intermittently and to varying degrees. Different 5' UTRs resulted in different start site preferences, directly demonstrating a role for 5' UTRs in dictating which start site is chosen. In addition, computational fits suggested ribosomes often reinitiate after upstream ORF translation.

2.2.5 Subcellular localization and translation

To regulate genes in a spatiotemporal manner, mRNAs are localized to specific cellular compartments for translation. Multiple groups have now used NCT to study

translation dynamics in neurons (Cioni et al., 2019; Fonkeu et al., 2019; Langille et al., 2019; Wu et al., 2016; Reviewed in Latallo et al., 2019). In particular, Wu et al. showed that translation is not necessarily repressed during active mRNA transport in neurons (Wu et al., 2016). More recently, Cioni & Lin et al. showed that endosome-associated mRNA are actively translated (Cioni et al., 2019). Further, blocking the maturation of endosomes with a drug mutating an important endosomal protein inhibited translation without disrupting the mRNA association with endosomes.

Translation can also be targeted to specific subcellular locations. mRNAs encoding membrane and secreted proteins are translated mainly in the endoplasmic reticulum (ER), whereas mRNAs encoding cytosolic proteins are translated mainly in the cytosol. To further study this, Voigt et al. combined ER staining with NCT to track mRNA encoding cytosolic proteins (**Figure 2.3C**; (Voigt et al., 2019). Surprisingly, they found that a subset of these mRNA were localized to the ER during translation. Furthermore, they showed that mRNA localized to the ER were translated by more ribosomes on average, directly demonstrating subcellular localization can alter translation efficiency.

2.2.6 Heterogeneity in ribosome elongation and frameshifting

The regulation of ribosomal elongation rates is an important form of translation control. For example, ribosomes could pause or stall at specific nucleotide sequences to modulate the folding of nascent chains (Reviewed in Collart & Weiss, 2020). Pausing can also lead to ribosomal traffic jams that are known to trigger quality control and the unfolded protein response (Juszkiewicz et al., 2018). NCT is now being used to investigate ribosome elongation dynamics in the context of specific mRNA sequences.

First, Yan et al. demonstrated that ribosomes pause for extended times at the XBP1 pause site (which is known to induce ribosome pausing; Ingolia et al., 2011), after which they exit together in bursts (**Figure 2.3D**; Yan et al., 2016). More recently, Lyon et al. used the multi-frame tag to visualize frameshifting dynamics at the HIV-1 frameshift sequence (**Figure 2.3D**; Lyon et al., 2019). This sequence contains a ribosomal pause site and a slippery sequence that causes ribosomes to occasionally slip from the 0 frame to the -1 frame. NCT revealed frameshifting occurs in bursts and is associated with long pauses at the frameshift sequence that induce ribosomal traffic jams.

2.2.7 Nonsense-mediated mRNA decay

Cells govern which mRNA should be translated by using mechanisms called mRNA surveillance to “survey” and eliminate wrong or mismanufactured mRNA. One type of mRNA surveillance called Nonsense-Mediated Decay (NMD) targets and destroys mRNA containing a Premature Termination Codon (PTC; Shoemaker & Green, 2012). To study how ribosomes impact NMD, Hoek et al. used NCT to detect ribosomes at reporter mRNA targeted for NMD by a PTC (**Figure 2.4**, Above; Hoek et al., 2019). They used variations of mRNA reporters to test the impact of PTC location and context. Strikingly, NMD-triggered mRNA cleavage was found to be induced with equal probability by each translating ribosome. Also, some mRNA (10-20%, depending on the mRNA reporter) were completely NMD-resistant, suggesting heterogeneity in mRNA sensitivity to NMD.

2.2.8 siRNA-mediated mRNA surveillance

Another type of mRNA surveillance is the small-interfering RNA (siRNA) pathway. To silence translation, siRNA locates a binding site on a target mRNA and slices it in half, promoting rapid mRNA degradation (Fire et al., 1998; Hamilton & Baulcombe, 1999). Horvathova et al. first demonstrated that siRNA-mediated mRNA silencing could be seen in real-time in a live-cell, single-mRNA assay called 3′-RNA End Accumulation during Turnover (TREAT), gaining insight into the timing and subcellular localization of these events (Horvathova, Voigt, Kotrys, Zhan, Artus-Revel, et al., 2017). More recently, Ruijtenberg et al. used NCT to show that siRNA silenced an mRNA most efficiently after a ribosome translated across the siRNA binding site (Ruijtenberg et al., 2020). Further, they showed that this was most likely due to translating ribosomes disrupting weak, intra-mRNA interactions, thereby changing the mRNA structure. These structural changes exposed binding sites for siRNA-enzyme complexes, promoting siRNA silencing.

2.2.9 Integrated stress response

To conserve resources during stress, cells repress translation and target mRNA to membraneless organelles called stress granules or P-bodies (Reviewed in Treeck & Parker, 2019). Moon et al. and Wilbertz et al. used NCT to study the dynamics of this process (**Figure 2.4**, Below; Moon et al., 2019; Wilbertz et al., 2019). They showed translationally active mRNA can transiently interact with stress granules and P-bodies, but only for a few seconds at a time. In contrast, non-translating mRNA can stably enter stress granules in a “dock and lock” model (Moon et al., 2019; Pitchiaya et al., 2019). During stress, mRNA decay was inhibited, and mRNA immobilized within granules

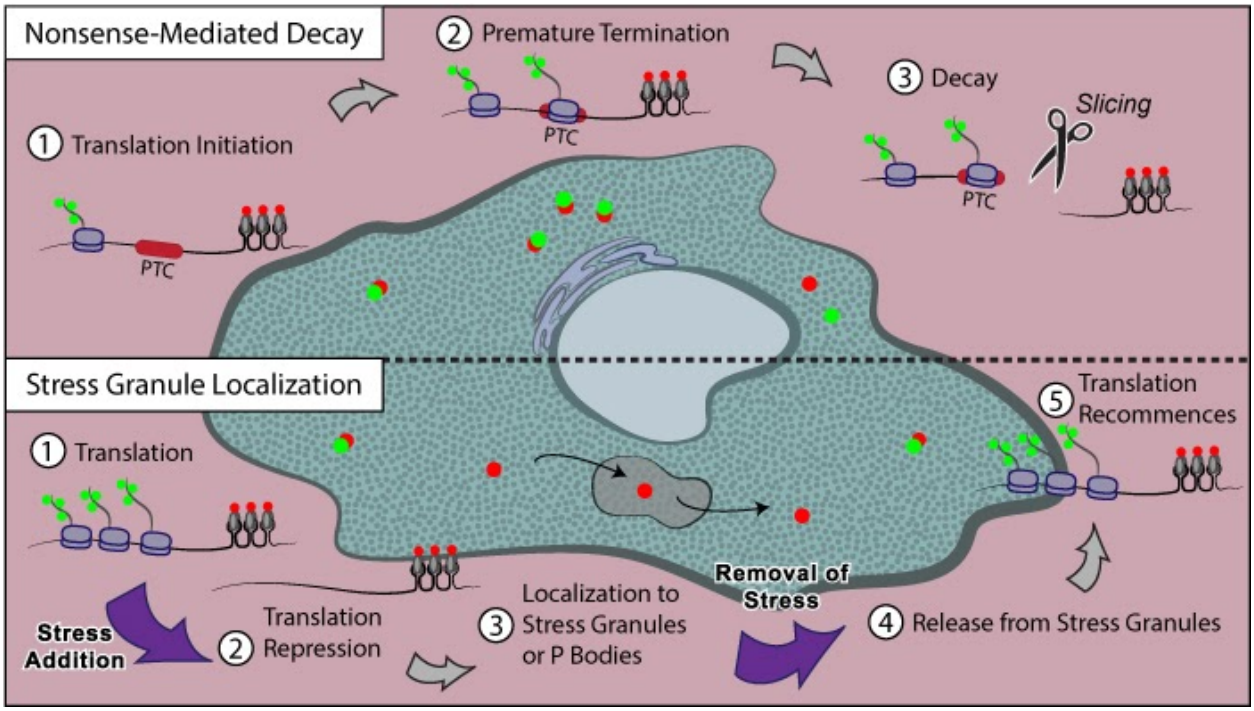

Figure 2.4 Recent applications of NCT to study translation repression dynamics
Above: When a ribosome initiates translation, a green signal appears at a red-labeled mRNA (1). Once translating ribosomes reach a Premature Termination Codon (PTC), they can trigger Nonsense-Mediated Decay (NMD)(2). NMD slices an mRNA in half, which physically separates the green translating ribosome signal on the upstream half of the mRNA from the red mRNA tag signal (3). The count and dwell time of ribosomes and the mRNA slicing event can be determined from the green signal location and intensity.
Below: After adding acute cell stress, translation is repressed, seen in the cell as loss of green translation signal (1-2). Translationally-silent, red signal-only mRNA can enter stress granules or P-bodies (3). After the stress is removed, stress granules dissolve, releasing the mRNA (4). Then, translation recommences, as seen in the cell by green-labeled nascent peptide colocalizing with red mRNA (5).

rarely transferred to other granules (Horvathova, Voigt, Kotrys, Zhan, Artus-Revel, et al., 2017; Wilbertz et al., 2019). After stress, stress granules dissolved and released the mRNA back into the cytoplasm. After this happened, translation returned to near pre-stress levels (Moon et al., 2019; Wilbertz et al., 2019). These data suggest mRNA that have been in stress granules can reinitiate translation once stress is relieved.

Interestingly, a more recent NCT-based study found that not all granule-localized mRNA are translationally repressed. Mateju et al. used a NCT reporter on an ATF4 transcript's upstream open reading frame (uORF), which is known to be preferentially translated during cell stress. They found that every step of the translation cycle--initiation, elongation, and termination--could occur while the reporter transcript was localized inside a stress granule (Mateju, Eichenberger, Voigt, et al., 2020), adding further support to an idea that was difficult, if not impossible, to study via bulk-cell assays.

Table 2.1. Major applications and advancements in Nascent Chain Tracking (NCT) technology

Advance / application	Reference	Summary
NCT application	Hoek 2019 (NMD)	NCT was used to visualize Nonsense Mediated Decay (NMD) of mRNA. Decay was triggered when ribosomes reached a premature stop codon in a reporter mRNA.
NCT application	Boersma 2020 (Viral translation)	This study added a NCT biosensor to a virus to study translation of viral RNA during host-cell infection. They found that infection followed a timeline of distinct steps, each with distinct impacts to viral RNA translation.
NCT application	Moon & Morisaki 2019 (Stress granules)	Using NCT, the authors visualized translating mRNA in cells undergoing stress. They saw translation shutoff before mRNA localized to stress granules, and some mRNA form stable docking interactions with the granules. After stress relief, the stress granules dissolved then translation resumed. Their results corroborate (Wilbertz et al., 2019).
NCT application	Wilbertz 2019 (Stress granules)	This work saw that translation shut down at NCT reporter mRNA soon after cell stress was induced. Stress granules stored mRNA during stress but did not impact mRNA decay. Their results corroborate (Moon et al., 2019).
NCT application	Mateju 2020 (Stress granules)	Using NCT on an upstream open reading frame, this study found evidence that translation can occur inside stress granules to a subset of specialized mRNA.
Technology advance	Horathova 2017 (mRNA decay)	This work developed a single-mRNA biosensor for mRNA decay via fluorescence imaging. They used the biosensor to visualize various types of decay in live human cells, including siRNA-mediated mRNA silencing.
NCT application	Voigt et al. (2017), (local translation)	Here, the authors used NCT to investigate translation at different subcellular locations. They revealed that cytoplasmic proteins can localize and translate at the endoplasmic reticulum and those translation sites were loaded by more ribosomes than the cytoplasmic mRNA.
NCT application	Ruijentenburg, 2019 (siRNA - mediated decay)	Using NCT, this work studied the impact of translating ribosomes on siRNA/Argonaute-mediated mRNA decay. They found that translation increased the probability of Argonaute targeting an mRNA, thus increasing mRNA decay (Currently a preprint).

NCT application and technology advance	Boersma, 2019 (Novel probe development, open reading frame selection)	To study translation start site selection, this work first created a new translation labeling system called the MoonTag. With the SunTag and the MoonTag systems in alternate reading frames, they discovered that alternative start site selection happens frequently. Different 5' UTRs resulted in different start site preferences, directly demonstrating a role for 5' UTRs in dictating which start site is chosen. In addition, computational fits suggested ribosomes often reinitiate after upstream ORF translation.
NCT application	Khong 2018 (mRNA structure)	Here, the distances between the ends of mRNA were measured using fluorescent probes. They determined that mRNA take on an open conformation when translated. Their results corroborate (Adivarahan et al., 2018).
NCT application	Adivarahan 2018 (mRNA structure)	Here, the distances between the ends of mRNA were measured using smFISH. They discovered that mRNA are stretched out while being translated. Further, more translating ribosomes on an mRNA correlated with the mRNA ends being further apart. Their results corroborate (Khong & Parker, 2018).
NCT application	Lyon 2019 (Frameshifting)	To study ribosomal frameshifting, this work created an NCT multi-frame tag with a frameshift sequence from HIV. A small number of mRNA frameshifted for extended times in bursts, and frameshifting was associated with ribosomal traffic jams and mRNA-mRNA dimers.
Technology advance	Zhao 2019 (Novel probe development)	Here, a new genetically encodable scFv probe called the anti-HA frankenbody was developed. This probe can be expressed in cells and was used for imaging and tracking HA-tagged proteins *in vivo* and for performing NCT with the HA-spaghetti monster tag.
NCT application	Cioni, 2019 (Neurons)	Here, the authors studied endosomal trafficking to mitochondria in neurons. Among other results, they used NCT to discover that endosome maturation drove translation of specific mRNA docked to endosomes.
NCT application	Sepulveda 2018 (Centrosomes)	During mitosis, the translation of localized mRNA causes a local enrichment of the cytoplasmic PCNT protein at centrosomes. This work used antibodies to label both ends of endogenous PCNT proteins to study native translation.
NCT application	Koch 2020 (Ribosome recruitment, mRNA structure)	Here, a bicistronic NCT biosensor was developed to light up in different colors depending on whether or not translation occurred in a cap-dependent or IRES-mediated manner. This revealed the EMCV IRES recruits fewer ribosomes than the cap in normal conditions, but that balance shifts to favor the IRES during stress. Also, the biosensor was used to demonstrate that actively translating mRNA become more stretched out as more ribosomes load.

CHAPTER 3
Imaging translational control by Argonaute with single-molecule resolution in live cells

This chapter describes developing technology to directly visualize and quantify the impact of human Argonaute2 (Ago2) on the translation and subcellular localization of individual reporter mRNAs in living cells. The system allowed for quantifying the Ago2-mediated silencing mechanism with unprecedented spatiotemporal resolution. This tethering-based, single-molecule reporter system was designed to be adaptable for wide-ranging application in studying general RNA-protein interactions.[3]

3.1 Motivation

Translation is the culmination of gene expression, whereby genetic information encoded in nucleic acids is converted into proteins. This basic process is fundamental to all life, giving cells the ability to rapidly establish and maintain diverse phenotypes in response to the environment (Buxbaum et al., 2015; Sonenberg & Hinnebusch, 2009). A multitude of factors work in concert to control which mRNAs are translated, how much peptide product is synthesized, and when to halt erroneous translation (Heck & Wilusz, 2018; Hershey et al., 2019). These regulatory factors are activated by broad cell signaling pathways that respond to stimuli including stress, growth conditions, and development (Roux & Topisirovic, 2018).

[3]This chapter is based on a manuscript, currently under review, for which I will be the first-author (Cialek et al., 2021). C.A.C. performed all experiments. C.A.C. performed all data analysis, except for the python analysis in Fig. 3.13 and Fig. 3.16, which was done by T.J.S. Some code and functions were written by T.M. The anti-HA frankenbody was purified by N.Z. Dr. O'Neil Wiggan and Nick Flint helped optimize the fixed-cell immunofluorescence and smiFISH assays.

The dynamics of translational control have traditionally been studied in living cells at the bulk level (e.g. Western blots, polysome/ribosome profiling) or at the single-cell level (e.g. fluorescent/bioluminescent reporters; Biswas et al., 2019; Kuersten et al., 2013, 2013). However, these assays lack spatiotemporal resolution, which has made it hard to decipher complex gene regulatory mechanisms (Chao et al., 2012). More recently, it has become possible to explore translation dynamics in living cells at the single-molecule level (Morisaki et al., 2016; Pichon et al., 2016; Wang et al., 2016; Wu et al., 2016; Yan et al., 2016). These single-molecule technologies, which we collectively refer to as Nascent Chain Tracking (NCT), all use repeat mRNA and protein tags to brightly label and track single mRNA using one fluorophore and elongating nascent peptide chains using another fluorophore (reviewed in Morisaki & Stasevich, 2018).

The ability to image translation at single mRNA makes it possible to quantify individual translation events, measure ribosome initiation and elongation rates, and discern the heterogeneity in translation between mRNA. Since data from this technique are acquired on a microscope, spatial information is naturally embedded. Further, several recent advances in NCT technology have made it possible to study changes in translation at individual mRNA in response to stress (Mateju, Eichenberger, Eglinger, et al., 2020; Moon, 2020; Moon et al., 2019; Wilbertz et al., 2019), mRNA subcellular location (Voigt et al., 2017), mRNA sequence composition (Aguilera et al., 2019; Boersma et al., 2019; Hoek et al., 2019; Koch et al., 2020; Lyon et al., 2019), and more (Reviewed in Cialek et al., 2020).

While powerful, one shortcoming of NCT technology has been visualizing how specific regulatory factors impact translation. Because NCT only amplifies signals from the elongating nascent peptide chain and the mRNA reporter, it is difficult to simultaneously monitor relatively weak signals from individual regulatory factors. Sometimes this difficulty can be avoided if a regulatory factor produces a strong and consistent molecular phenotype that immediately impacts the reporter or its translation. For example, siRNA-directed cleavage of a reporter by Argonaute2 (Ago2) could be detected and quantified using NCT alone because it happened rapidly (seconds to minutes) and resulted in a strong molecular phenotype (the physical splitting of fluorescence signals; Ruijtenberg et al., 2020).

However, translation is often controlled by regulatory factors that act in more subtle ways, for example by inhibiting translation initiation, stalling elongation, or promoting mRNA decay. These modes of regulation tend to have a progressive phenotype that requires extended observation with high sensitivity. To illustrate, in addition to siRNAs, Ago2 binds miRNAs that target mRNAs through partial sequence complementarity and direct gene silencing through a distinct cleavage-independent mechanism (Bartel, 2018). The miRNA-induced silencing complex (miRISC) consists of a miRNA and an Argonaute protein, such as Ago2, along with additional downstream effectors that together promote translational repression and mRNA decay (Jonas & Izaurralde, 2015). Because miRNA-mediated gene silencing and many other gene regulatory mechanisms are likely more gradual and variable than silencing directed by siRNAs, exploring their impact on translation at the single-molecule level is inherently more difficult.

To confront this problem, we developed a “Translation and Tethering” (TnT) single-molecule biosensor that extends NCT technology. As the name implies, the TnT biosensor builds on NCT by adding a tethering cassette that stochastically recruits a fluorescently labeled regulatory factor with controllable stoichiometry. By tracking tethered mRNA through time, the specific and direct impact and regulatory timeframe of the factor can be discerned and quantified. The optimized signal-to-noise ratio of the TnT biosensor makes it possible to continually monitor in 3 colors single-mRNA silencing events that occur on a wide range of timescales, from seconds to hours. Thus, our TnT biosensor provides a route to do highly controlled biochemical experiments with single-molecule spatial resolution and high temporal resolution inside living cells.

Here we introduce the TnT biosensor and demonstrate its functionality by exploring miRNA-mediated gene silencing involving Ago2. We find that within minutes of tethering, Ago2 inhibits the initiation of new translation events, leading to ribosome runoff. Early occurring translational repression is likely independent of mRNA decay, as we sometimes see translation reinitiate in the presence of tethered Ago2. On longer timescales, we find evidence that tethered Ago2 interacts with endogenous miRISC machinery that accumulate at the mRNA and maintain a translationally silent state. Collectively, our data support a model in which Ago2 mediates translational repression largely through reversible inhibition of translation initiation within the cytosol followed by aggregation of mRNA-Ago2 complexes in what are likely P-bodies for sustained silencing.

3.2 A live cell, single-molecule assay to monitor translation and protein tethering in real time

To controllably tether factors to reporter mRNA and simultaneously visualize their impact on mRNA localization, stability, and translation, we constructed a translation and tethering (TnT) biosensor (**Figure 3.1A**). As with standard NCT (**Figure 2.1**), each TnT biosensor contains 24 MS2 RNA stem loops which recruit fluorescent MS2 Coat Proteins (JF646 HaloTag-MCP) to label the mRNA. Translation is monitored by the localized accumulation of Cy3-conjugated α-FLAG fragmented antibodies (Fab) which can bind 10 FLAG epitopes at the N-terminus of a reporter protein. With this arrangement, as a ribosome begins to translate the TnT biosensor, the nascent protein that emerges from the ribosomal exit tunnel is rapidly labeled by Fab (Morisaki et al., 2016). As multiple ribosomes engage the reporter and begin to translate through the FLAG epitopes in the ORF, the Fab signal intensifies and colocalizes with the mRNA signal.

In addition to the mRNA and nascent chain tags, the TnT biosensor also contains a tethering cassette consisting of 15 BoxB RNA stem loops adjacent to the 24 MS2 stem loops in the 3' UTR. Similar to MCP binding to MS2 stem loops, a 22-amino acid λN protein binds a 19-nucleotide BoxB stem loop with high affinity and specificity (Baron-Benhamou et al., 2004). Thus, by fusing a protein of interest to λN labeled with a distinct fluorophore, it can be recruited and tethered to the BoxB stem loops within an mRNA reporter with high specificity (Coller & Wickens, 2007; Eckhardt et al., 2011).

With this arrangement of tags, it is possible to compare individual TnT biosensors tethered to a protein of interest to those that are untethered. Furthermore, since the TnT biosensor can theoretically tether up to 15 proteins, the tethering signal is strongly

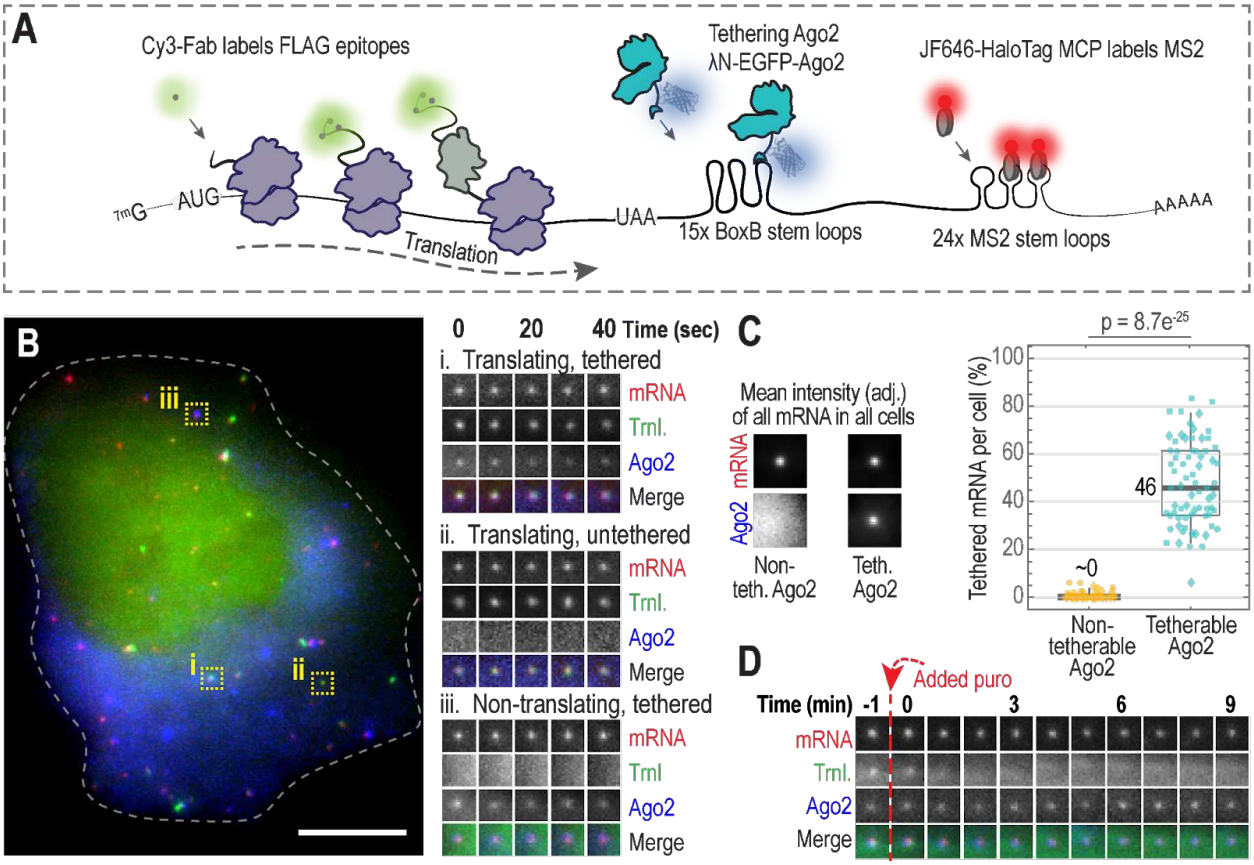

Figure 3.1 Tracking single-mRNA translation and Argonaute tethering with the TnT biosensor.

A Schematic of the Translation and Tethering (TnT) biosensor.

B A representative cell expressing the TnT biosensor to monitor translation (Trnl.) and Ago2-tethering. Single cells were imaged 4 hours after loading plasmids encoding tetherable Ago2 (λN-EGFP-Ago2), the TnT reporter mRNA (smFLAG-KDM5B-15xBoxB-24xMS2), Cy3-FLAG-Fab, and JF646 HaloTag-MCP. The cropped images (15 x 15 pixels^2; 130 nm/pixel) show single mRNA across a 40 second (sec) interval: (i) translating, tethered; (ii) translating, untethered; and (iii) non-translating, tethered. The dashed line marks the cell outline. Scale bar, 10 μm.

C The percentages of mRNAs co-localizing with tetherable (λN-EGFP-Ago2) or non-tetherable (EGFP-Ago2) Ago2 6-8 hours after loading was calculated. Left, intensity-rescaled crops showing the average mRNA and Ago2 channels of all detected mRNA foci (18 x 18 pixels^2; 130 nm/pixel). Right, box plot showing the percentage of mRNA foci colocalizing with Ago2. Each point corresponds to a single cell (shapes denote 3 replicate experiments). The P value was calculated using the Mann-Whitney test. N = 71 (3712) and 65 (7249) cells (mRNA foci) using tetherable and non-tetherable Ago2, respectively.

D A representative 9 minute (min) track of a single mRNA from a cell (loaded as in B) following puromycin treatment (Time = 0, indicated by the dashed vertical red line). Crops (15 x 15 pixels^2; 130 nm/pixel) show the mRNA, translation, and Ago2 signal intensities.

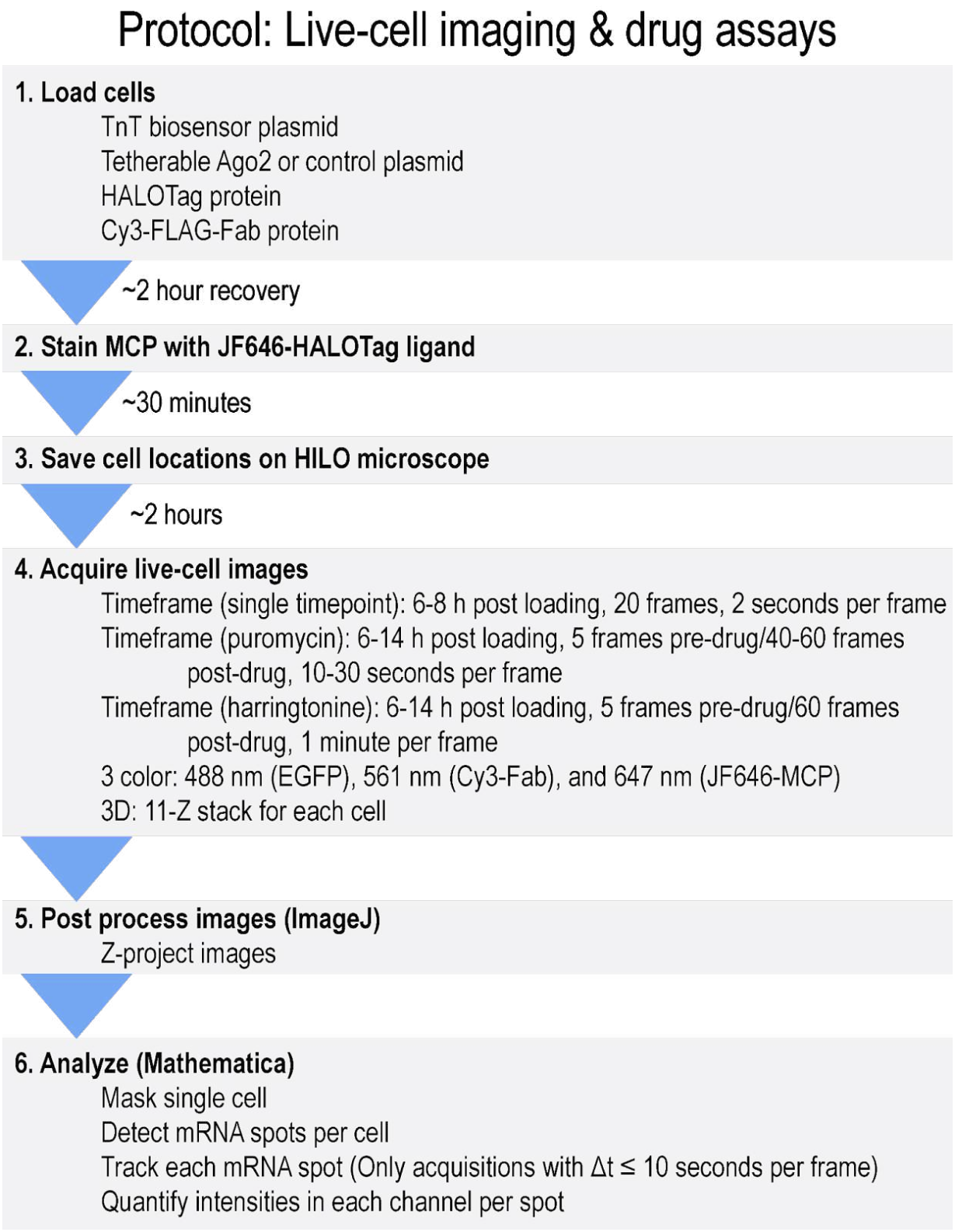

Figure 3.2 Workflow for single-mRNA imaging experiments.
The step-by-step workflow is shown here for live-cell imaging and drug assays. Further details are provided in **Methods**.

amplified so that tethered mRNA can be tracked for relatively long periods of time without substantial photobleaching or loss of signal within a noisy background.

To demonstrate the power of the TnT biosensor, we used it to investigate the miRNA-mediated gene silencing pathway. We focused on Ago2, one of the core proteins in the pathway, because others had already shown that tethering it to an mRNA can faithfully recapitulate miRNA-mediated gene silencing (Golden et al., 2017; Liu, Rivas, et al., 2005; Piao et al., 2010; Pillai et al., 2004). While there is a substantial body of evidence that miRNAs regulate gene expression at the level of translation initiation, mRNA decay, and to a lesser extent translation elongation (Reviewed in Jonas & Izaurralde, 2015), the timing and spatial organization of these regulatory events and their relative contributions to gene silencing are unclear.

To better deconvolve these complex dynamics, we engineered a tetherable Ago2 construct (λN-EGFP-Ago2). We then loaded this construct into human U2OS cells along with the other TnT biosensor components (the reporter mRNA, Cy3-labeled α-FLAG Fabs to monitor translation at the reporter, and JF646 HaloTag-MCP to monitor localization of the reporter mRNA). Cells were imaged 4-6 hours after introducing the TnT components (described in **Figure 3.2**). Within a single cell, mRNA could be visualized with or without colocalization with translation and/or Ago2 tethering signals, and these mRNA could be tracked over time (**Figure 3.1B**).

In order to isolate impacts on the translation of the TnT biosensor to Ago2, we also designed constructs to controls for tethering and Ago2 overexpression (**Figure 3.3A**). To control for non-specific silencing that might occur from tethering a protein to the TnT biosensor, we tethered the inert bacterial protein β-gal (λN-EGFP-β-gal), which

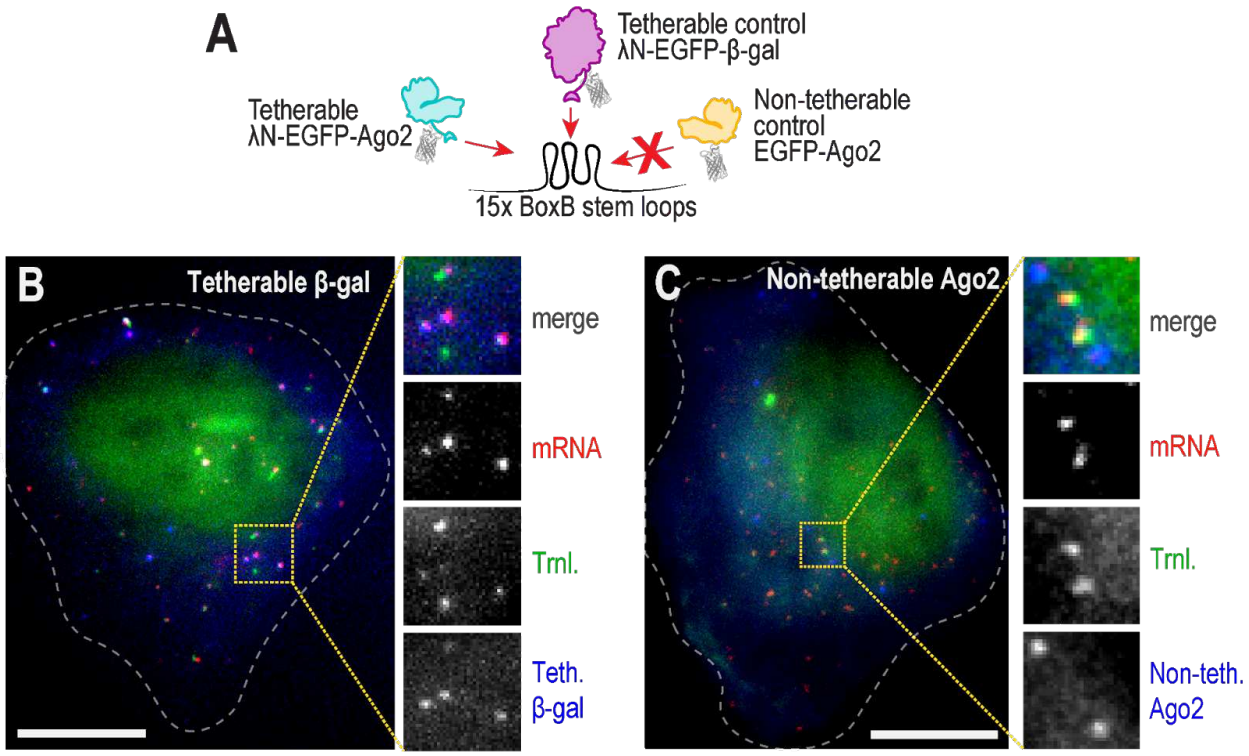

Figure 3.3 The tetherable and non-tetherable controls for the TnT biosensor.
A Cartoon of tetherable Ago2 and the controls non-tetherable Ago2 and tetherable β-gal.
B A representative cell expressing non-tetherable Ago2 (EGFP-Ago2), prepared as described in **Figure 3.2**. The image was acquired approximately 4 hours after loading the TnT components (smFLAG-KDM5B-15xBoxB-24xMS2 mRNA reporter, Cy3-FLAG-Fab, and JF646 HaloTag MCP). The dashed line marks the cell boundary. Scale bar, 10 μm.
C A representative cell expressing tetherable β-gal (λN-EGFP-β-gal), prepared as described in **Figure 3.2**. The image was acquired approximately 4 hours after loading the TnT components. The dashed line marks the cell boundary. Scale bar, 10 μm.

was previously shown to have a negligible impact on translation (Pillai et al., 2004). Like Ago2, β-gal-tethered mRNAs could be actively translated and tethered (**Figure 3.3B**). To control for non-specific effects related to Ago2 overexpression, we also designed another control construct with a non-tetherable form of Ago2 (EGFP-Ago2) which still

had detectable translation at TnT mRNA but showed little to no visible tethering (**Figure 3.3C**). We quantified the fraction of mRNA with detectable tethering and found that ~46% of the TnT biosensors colocalized with tetherable Ago2 (**Figure 3.1C**). We did not observe non-tetherable Ago2 at the TnT biosensor, indicating that the colocalization we observed was indeed due to tethering (**Figure 3.1C**, **Figure 3.3A**).

We next treated cells with the translational inhibitor puromycin. Consistent with the premature release of puromycylated peptide chains during active elongation (Nathans, 1964; Yarmolinsky & Haba, 1959), this led to a rapid loss in translation signals irrespective of whether the mRNA were tethered by Ago2 (**Figure 3.1D**, **Figure 3.4A**). Translation was similarly sensitive in control cells expressing tetherable β-gal or non-tetherable Ago2 (**Figure 3.4B-C**). These data therefore demonstrate the functionality of our TnT biosensor, proving it can be used to tether a specific regulatory factor to a trackable mRNA undergoing active translation.

3.3 Ago2 tethering to the TnT reporter mRNA inhibits its translation

Confident in our ability to simultaneously visualize translation and tethering at the single mRNA level, we next explored the impact of Ago2 tethering on translation. First, we set out to confirm that Ago2 tethering reduces total reporter protein synthesis within cells, as previously seen in bulk cell assays (Golden et al., 2017; Liu, Rivas, et al., 2005; Pillai et al., 2004). In each experiment, we quantified total protein production from the TnT biosensor by measuring the accumulation of reporter protein KDM5B (Lysine Demethylase 5B, a nuclear protein) in the nucleus over time (**Figure 3.5A**, described in **Figure 3.6**). According to this metric, cells expressing tetherable Ago2 accumulated

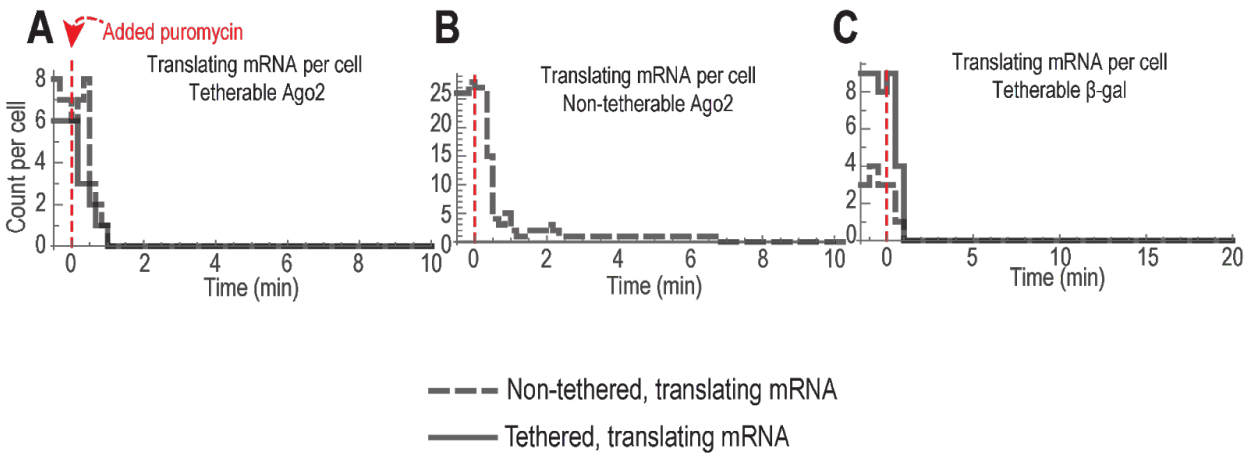

Figure 3.4 The TnT biosensor can be used to simultaneously track translation and tethering to reporter mRNA.
A-C Line plots showing the number of mRNA actively being translated in a single, TnT-loaded cell expressing tetherable Ago2 (A) non-tetherable Ago2 (B), or tetherable β-gal (C), prepared as described in **Figure 3.2**. Cells were treated with puromycin at Time = 0, as indicated by the dashed, vertical red line, and imaged for 10-20 minutes (min). Solid and dashed lines correspond to tethered and untethered mRNA, respectively.

~30% less KDM5B in the nucleus than cells expressing tetherable β-gal or non-tetherable Ago2 (**Figure 3.5B, left**). Importantly, this result was not due to artifactual Fab accumulation in the nucleus (**Figure 3.5B, right**). As a further test, we repeated this experiment in fixed cells (looking only at a 24-hour time point). Similar to live cells, protein accumulation was reduced 37-55% in fixed cells expressing tetherable Ago2 relative to cells expressing tetherable β-gal or non-tetherable Ago2 (**Figure 3.5C**, left). We included an additional control in this experiment in which a non-tetherable reporter mRNA lacking BoxB stem loops was coexpressed with each tetherable and non-tetherable protein construct (**Figure 3.5C, right**). Protein accumulation from this non-tetherable reporter was indistinguishable between the different protein constructs,

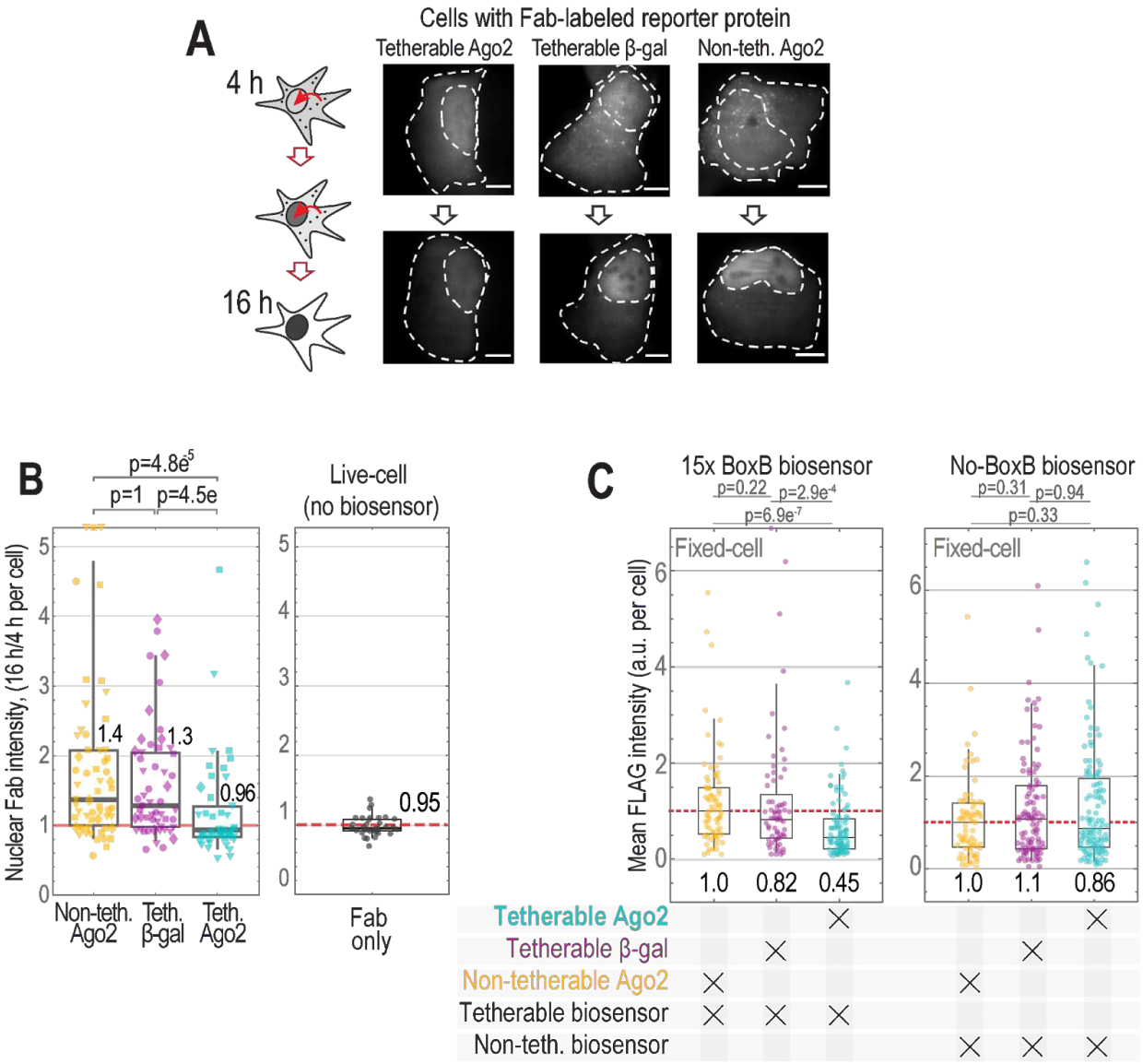

Figure 3.5 Ago2 tethering represses translation.
(Legend on next page)

Figure 3.5 Ago2 tethering represses translation.
A Schematic (above) and representative cells (below) showing the accumulation of the TnT reporter protein KDM5B (as marked by Fab) in the nucleus over time (4 and 16 hour time points shown) after loading tetherable Ago2 or controls with the TnT components (smFLAG-KDM5B-15xBoxB-24xMS2 mRNA reporter, Cy3-FLAG-Fab, and JF646 HaloTag MCP). The experiment is described in **Figure 3.6**. Dashed lines mark the cell and nucleus (the nuclear border was defined using cytoplasmic Ago2 or β-gal staining). Scale bars, 10 μm.
B, left Box plot displaying data from B. Each data point is the ratio of KDM5B nuclear intensity at 16 hours to 4 hours post-loading of the TnT components. Data from 4 replicate experiments were combined (replicates indicated by marker shape). P values were calculated using the Mann-Whitney test. N = 58 (non-tetherable Ago2), 82 (tetherable β-gal), and 66 (tetherable Ago2) cells.
B, right: Box plot displaying nuclear accumulation of Fab in the absence of the TnT biosensor. Each data point is the ratio of Fab nuclear intensity at 16 hours to 4 hours after Fab loading in a single cell.
C Box plot showing the mean intensity of the TnT reporter protein KDM5B (as marked by Fab) in fixed cells expressing the TnT biosensor (with or without the BoxB tethering cassette) as well as non-tetherable Ago2, tetherable β-gal, or tetherable Ago2. Cells were fixed 24 hours after TnT biosensor loading and stained with α-FLAG Fab. The mean cellular intensity was measured. N=77 non-tetherable, 67 β-gal-tetherable, and 97 Ago2-tetherable cells (left), and N=70 non-tetherable, 102 β-gal-tetherable, and 114 Ago2-tetherable cells (right).

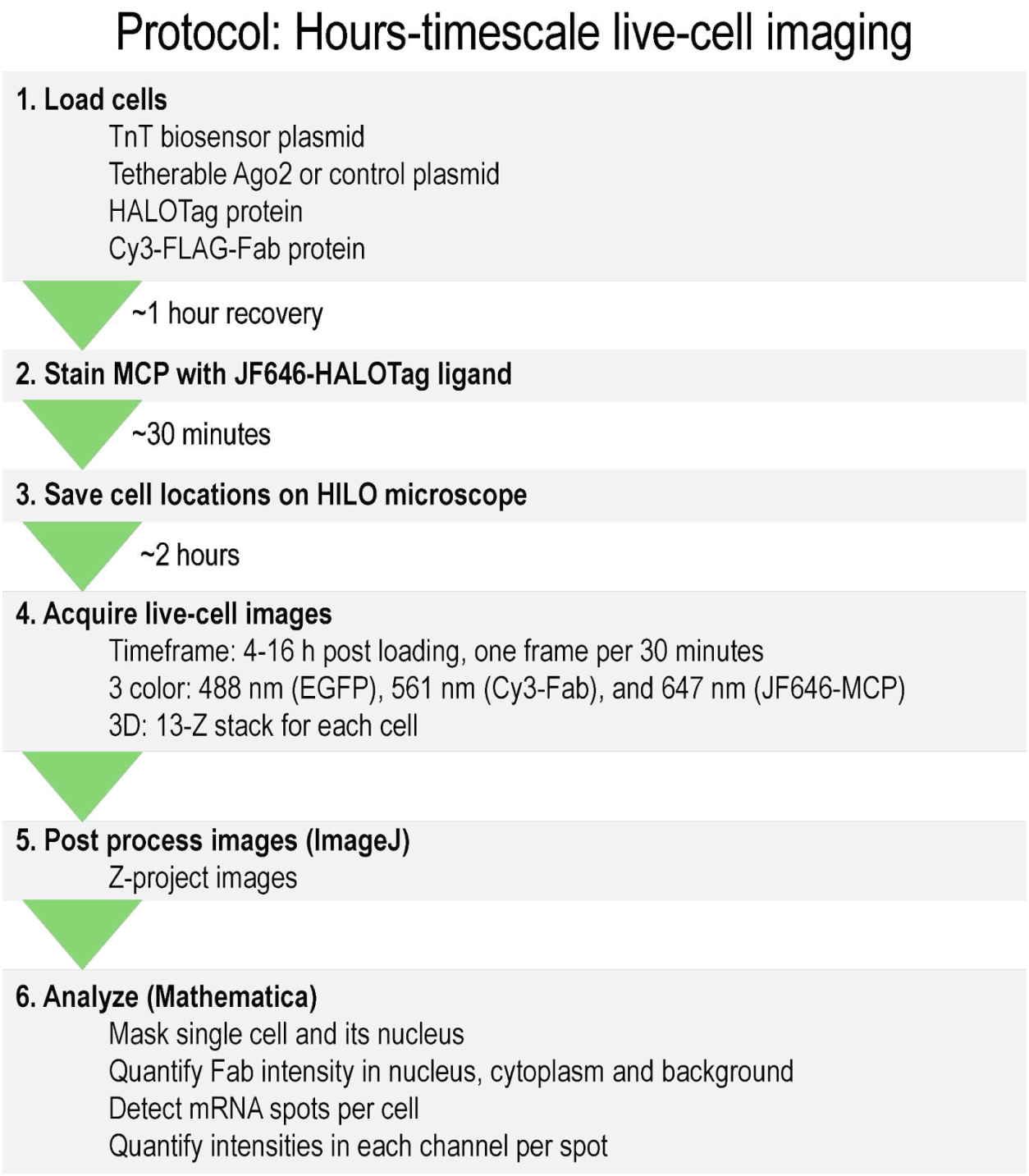

Figure 3.6 Workflow for hours-timescale live cell imaging experiments.
The step-by-step workflow is shown here. Further details are provided in **Methods**.

indicating that Ago2 tethering is directly responsible for the reduction in protein output we observed with the TnT biosensor. Thus, these data demonstrate that Ago2 tethering leads to a global reduction in mature protein accumulation, consistent with (Golden et al., 2017; Liu, Rivas, et al., 2005; Pillai et al., 2004).

The main advantage of using the TnT biosensor is the ability to visualize the impact of Ago2 tethering on translation at the individual mRNA level. For this, we reimaged cells expressing both the TnT biosensor and tetherable Ago2 approximately 6 hours after loading, when tethered and translating mRNA could easily be detected (as in **Figure 3.1B**). To track individual mRNA for many timepoints, we imaged full cell volumes at a rate of 0.5 frames per second for 20 frames total. Averaging the signals from these short tracks increased the sensitivity and accuracy of translation and tethering detection. To control for tethering and Ago2 overexpression artifacts, we again imaged control cells loaded with either non-tetherable Ago2 or tetherable β-gal. For each condition, we quantified the number of mRNA that were tethered/untethered and translating/silent (**Figure 3.7**).

In line with the low levels of mature reporter protein accumulation we observed in the nucleus, cells expressing tetherable Ago2 had, on average, the fewest mRNAs being translated (**Figure 3.7**). In fact, just ~24% of Ago2-tethered mRNAs were being translated compared to ~55% of β-gal-tethered mRNAs (**Figure 3.8A**). There was also a ~30-50% reduction in the total number of mRNA foci per cell using tetherable Ago2 (**Figure 3.7**), indicating a shortened mRNA half-life, although we could not rule out the reduction was in part caused by mRNA clustering and transcriptional stochasticity. Lastly, there were less ribosomes translating each mRNA; in cells expressing tetherable

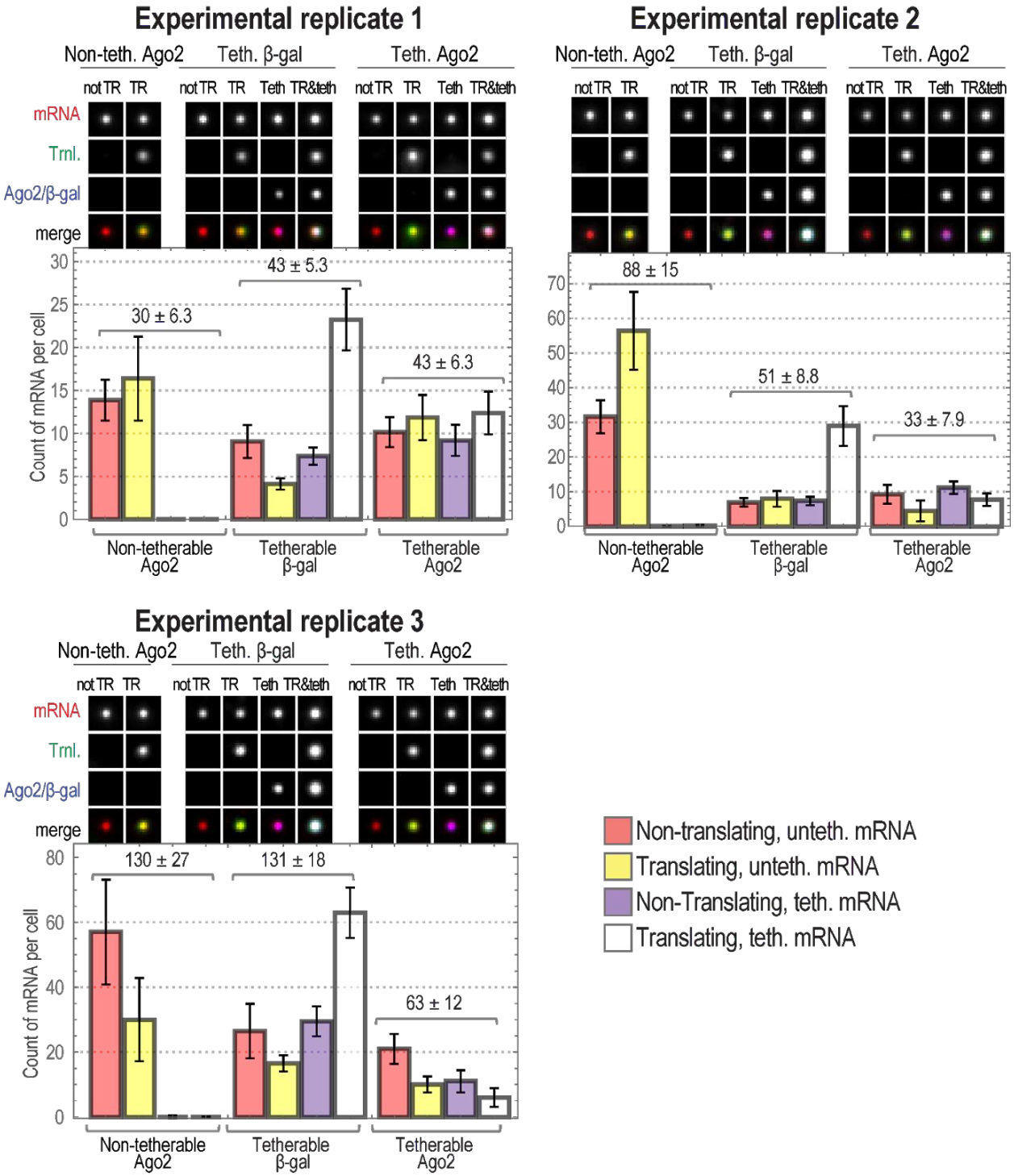

Figure 3.7 Counts of translating and/or tethered mRNA puncta per cell.
(Legend on next page)

Figure 3.7 Counts of translating and/or tethered mRNA puncta per cell.
Bar charts of all mRNA per live, TnT-loaded cells (3 experimental replicates). The experiment is outlined in **Figure 3.2**. The mRNA were categorized based on the presence or absence of detectable translation (TR) and/or Ago2/β-gal tethering (Teth) signals. Above each chart are the background-subtracted and auto-adjusted mean crops from each category (18 x 18 pixels^2; 130 nm/pixel). Note, because very few non-tetherable Ago2 cells had tethering signals, crops showing tethering in this case are not shown. Below, mean counts per cell for each category (color-coded bars). Error bars show SEM.
Replicate 1: The total number of mRNA particles per cell were N_{total} = 30 ± 5.3 (mean±SEM), 43 ± 5.3, and 43 ± 6.3 for non-tetherable Ago2, tetherable β-gal and tetherable Ago2, respectively. 8 (242), 17 (744), 21 (915) cells (mRNA) for non-tetherable Ago2, tetherable β-gal, and tetherable Ago2, respectively.
Replicate 2: The total number of mRNA particles per cell were N_{total} = 88 ± 15 (mean±SEM), 51 ± 8.8, and 33 ± 7.9 for non-tetherable Ago2, tetherable β-gal and tetherable Ago2, respectively. 18 (1590), 28 (1432), 18 (586) cells (mRNA) for non-tetherable Ago2, tetherable β-gal, and tetherable Ago2, respectively
Replicate 2: The total number of mRNA particles per cell were N_{total} = 130 ± 27 (mean±SEM), 131 ± 18, and 63 ± 12 for non-tetherable Ago2, tetherable β-gal and tetherable Ago2, respectively. 13 (1690), 10 (1306), 13 (817) cells (mRNA) for non-tetherable Ago2, tetherable β-gal, and tetherable Ago2, respectively

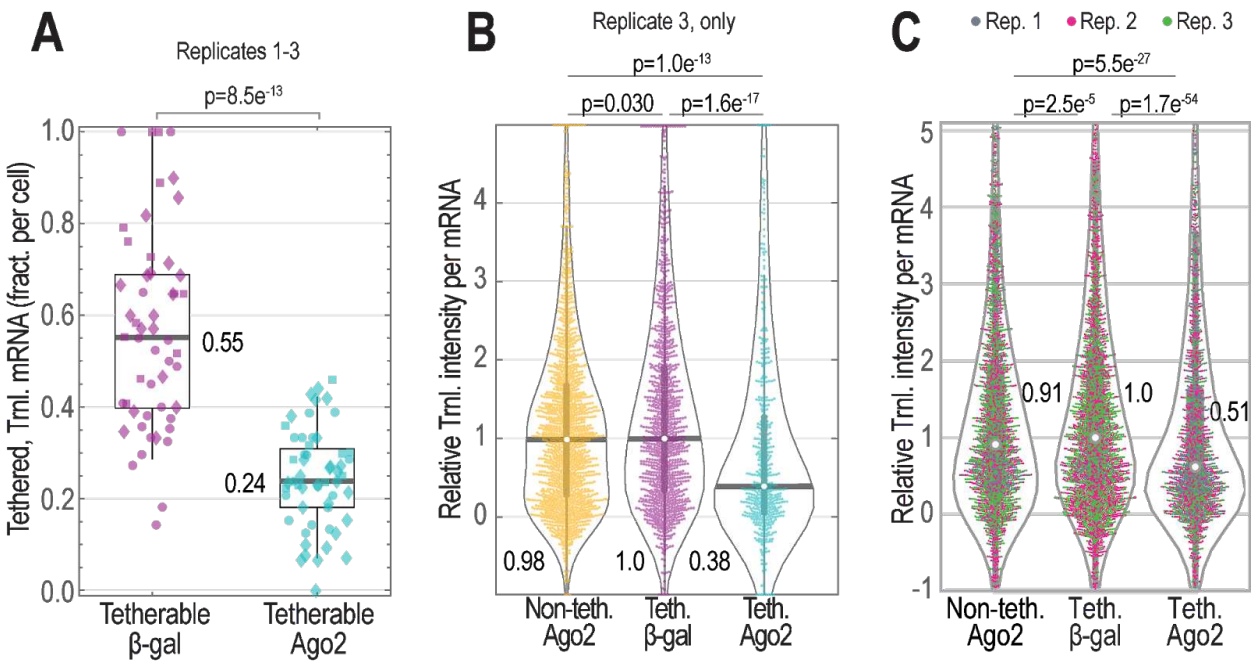

Figure 3.8 Ago2 tethering represses translation at the mRNA level.

A Box plot showing the fraction (frac.) per cell of Ago2- or β-gal-tethered mRNA actively translating 6-8 hours after TnT component loading, as described in **Figure 3.2**. Data from 3 replicate experiments were combined (replicates indicated by marker shape). The P value was calculated using the Mann-Whitney test. N = 55 (tetherable β-gal) and 52 (tetherable Ago2) cells.

B-C Violin plots displaying TnT reporter translation signal intensity in the presence of tetherable Ago2 or control constructs. The data came from the experiments in **Figure 3.7**. The Fab signal intensity was measured for only single mRNA foci, as shown in **Figure 3.8**.

B One representative replicate experiment is shown. P values were calculated using the Bonferroni-corrected Mann-Whitney test. N=18 (1513), 28 (1158), 18 (521) cells (mRNA) for non-tetherable Ago2, tetherable β-gal, and tetherable Ago2, respectively.

C Violin plot showing all experimental replicates (discernable by marker color). P values were calculated using the Bonferroni-corrected Mann-Whitney test. N = 55 (3,153), 39 (4,947) and 52 (3,959) cells (mRNA) for non-tetherable Ago2, tetherable β-gal, and tetherable Ago2, respectively.

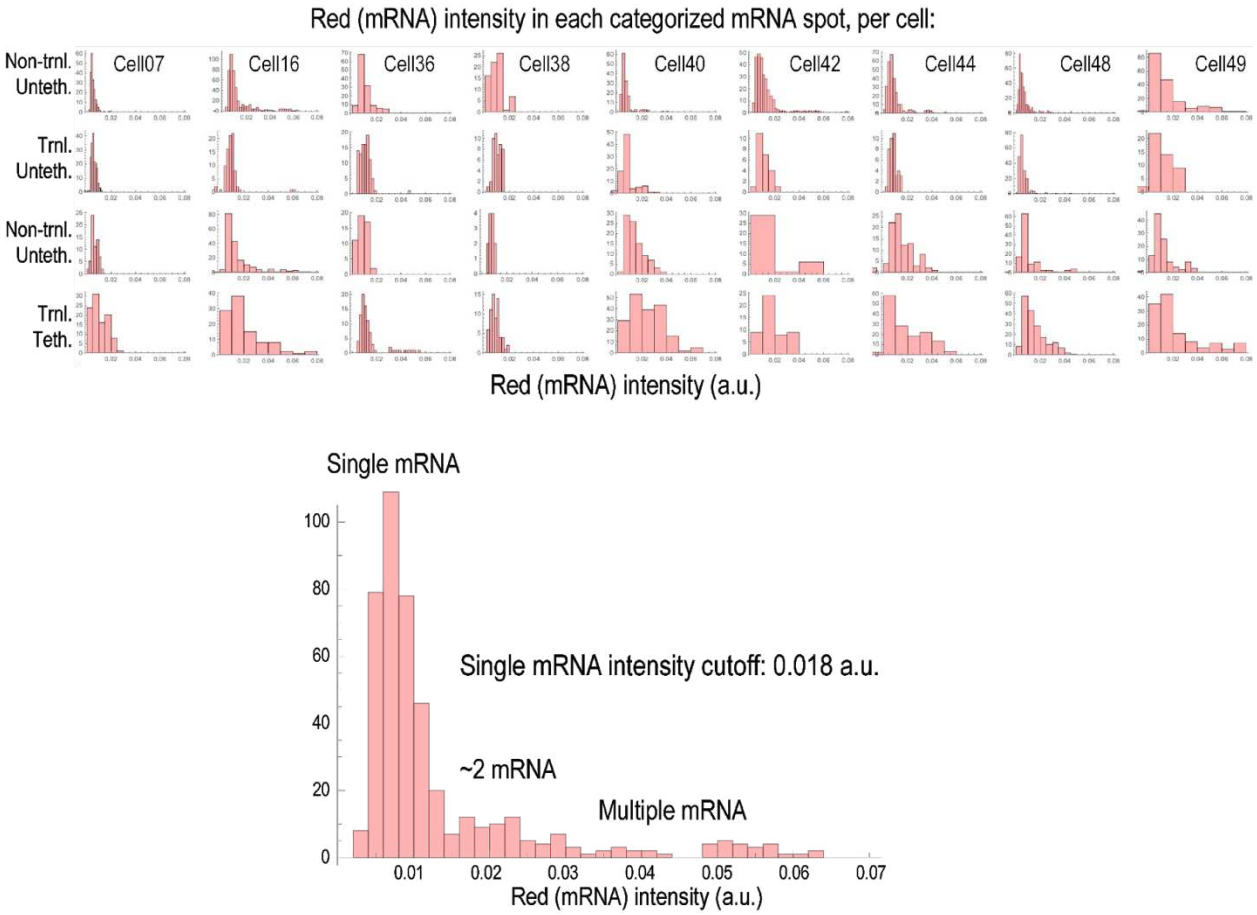

Figure 3.9 Determining the single-mRNA intensity cutoff value.
Histograms visualize the red (mRNA) channel intensity for each mRNA puncta from a random subset of cells in Experimental Replicate 2 in **Figure 3.7** per cell (above) or for all cells (below). Above, the mRNA were categorized on whether or not they were translating (Trnl.) or tethered (Teth.). All cells were imaged on the same day using the same laser power. An intensity cutoff value for single mRNA was determined based on the first peak. Single mRNA in **Figure 3.8B-C** were determined by this intensity cutoff value. This visualization strategy was used for each experimental repeat day of data.

Ago2 had translation signals that were 40-60% as bright as those in cells expressing tetherable β-gal (**Figure 3.8B-C**). Only single mRNA were used in this analysis, since multiple mRNA could overestimate the number of ribosomes per mRNA. Single mRNA were selected by using an mRNA-channel intensity cutoff (**Figure 3.9**). Taken together, these data demonstrate that Ago2 tethering not only reduces the fraction of mRNA being translated, but also reduces the number of translating ribosomes on individual mRNAs.

3.4 Ago2-tethered mRNA coalesce in the cytoplasm

Due to the exceptional signal-to-noise of the TnT biosensor, we could monitor individual mRNA in living cells for extended periods of time, ranging from seconds to hours. By following mRNA in single cells over a period of 12+ hours, we noticed that translationally silenced, Ago2-tethered mRNA tended to cluster over time (**Figure 3.10A**). These mRNA clusters remained translationally silenced and colocalized with bright cytoplasmic Ago2 foci for hours. Notably, they also exhibited behaviors characteristic of phase-separation, such as coalescence. The average intensity of mRNA foci in cells expressing tetherable Ago2 steadily increased with time (**Figure 3.10B**). In contrast, the average intensity of mRNA foci in cells expressing tetherable β-gal or non-tetherable Ago2 slightly decreased with time, which was likely due to photobleaching or probe decay (**Figure 3.10B**).

Based on these observations, we wondered if Ago2 tethering caused the TnT biosensor to relocalize to specific subcellular locations or compartments. Ago2 is known to interact directly with TNRC6 (Elkayam et al., 2017; Liu, Rivas, et al., 2005; Sheu-Gruttadauria & MacRae, 2018) and indirectly with other downstream effectors in the

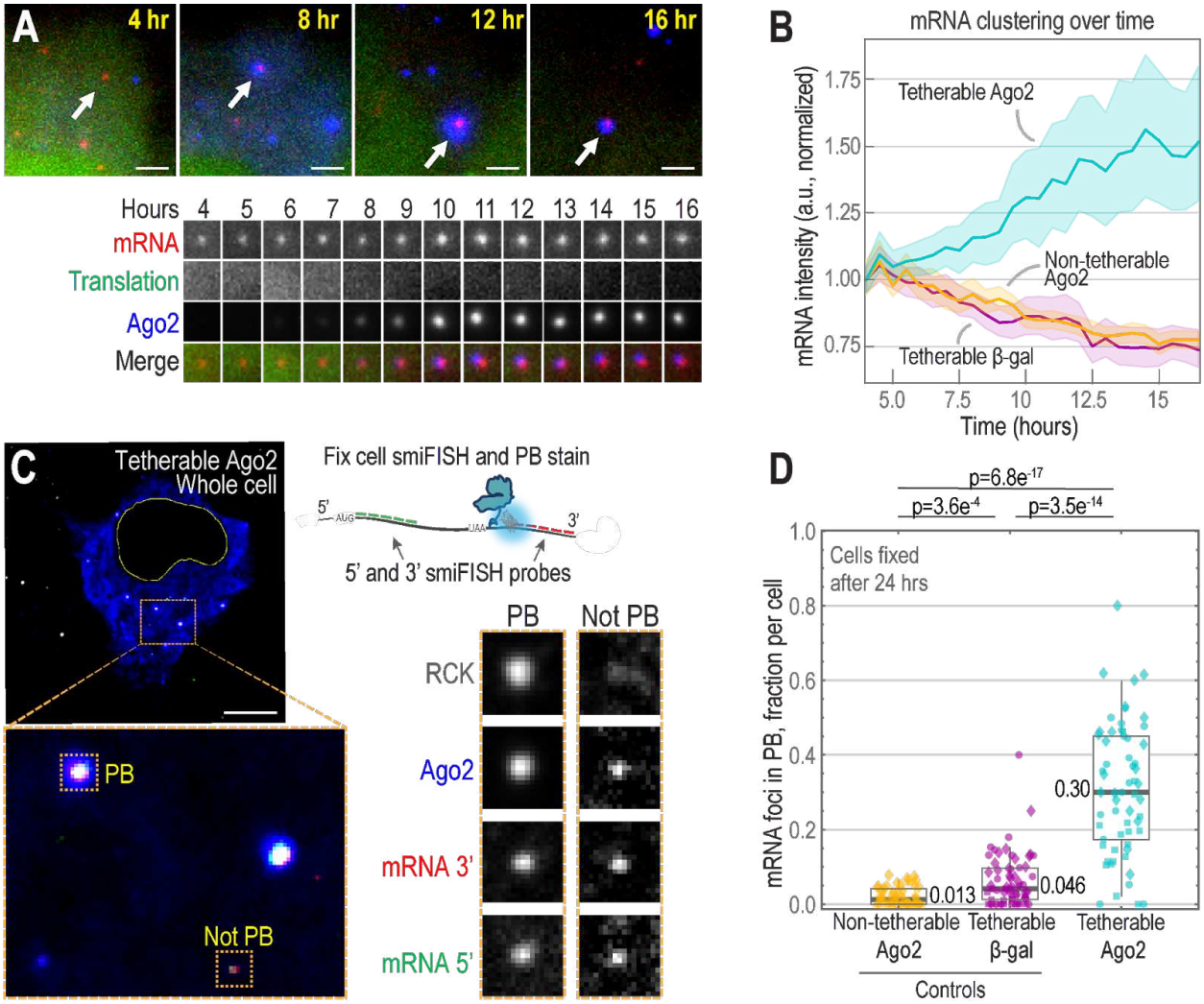

Figure 3.10 Intact Ago2-tethered TnT biosensors cluster and accumulate in P-bodies after translational silencing.
(Legend on following page)

Figure 3.10 Intact Ago2-tethered TnT biosensors cluster and accumulate in P-bodies after translational silencing.
A A representative cytoplasmic patch from a live cell expressing tetherable Ago2 and the TnT biosensor and components (smFLAG-KDM5B-15xBoxB-24xMS2 mRNA reporter, Cy3-FLAG-Fab, and JF646 HaloTag MCP) was imaged 4-16 h post loading, as described in **Figure 3.6**. The mRNA identified by arrows is shown over time below in crops (15 x 15 pixels^2; 130 nm/pixel). Scale bars, 2.5 μm.
B The line plot displays mRNA clustering over time. Cells were imaged as in **A** with either tetherable Ago2, tetherable β-gal, or non-tetherable Ago2. The mean MCP signal of all mRNA in all cells was measured over time and normalized to 1 at the first time point. N = 35 (17,367), 46 (32,666) and 44 (19,236) cells (mRNA foci) for non-tetherable Ago2, tetherable β-gal, and tetherable Ago2, respectively. Shaded region, 95% CI.
C-D The TnT biosensor plasmid plus either the tetherable Ago2, tetherable β-gal, or non-tetherable Ago2 plasmid were loaded into cells. After 24h, cells were fixed. The 5' and 3' mRNA ends were labeled with smiFISH probes, and P-bodies were stained with α-RCK antibodies.
C Representative tetherable-Ago2 cell, cytoplasmic patch, and mRNAs displaying P-body (PB) localization. Colors show P-bodies (α-RCK, gray; not shown on left), expressed tetherable Ago2 (blue), and TnT mRNA smiFISH probes (5', green; 3', red). Crops (17 x 17 pixels^2; 130 nm/pixel) were autoscaled. Scale bar, 10 μm.
D Box plots showing the fraction per cell of mRNA with 5' and 3' smFISH signals that were colocalized with P-bodies. Each point represents the fraction from a single cell (yellow, non-tetherable Ago2; purple, tetherable β-gal; cyan, tetherable Ago2; different shapes mark 1 of 3 replicate experiments). N = 56 (3,655), 63 (3,958), 61 (2,999) cells (mRNA foci) for non-tetherable Ago2, tetherable β-gal, and tetherable Ago2, respectively. P values were calculated from Bonferroni-corrected Mann-Whitney tests.

miRISC complex, including factors required for P-body assembly, such as RCK/DDX6 (Ayache et al., 2015; Chen et al., 2014; Rouya et al., 2014; Standart & Weil, 2018). Thus, we hypothesized progressive mRNA clustering could arise from multivalent interactions with endogenous miRISC machinery and/or P-bodies. Consistent with our observations of coalescing mRNAs, this machinery can exhibit phase-separation

behavior both *in vitro* and *in vivo* (Lin et al., 2015; Moon et al., 2019; Pitchiaya et al., 2019; Sheu-Gruttadauria & MacRae, 2018).

To test this hypothesis, we costained fixed cells expressing the TnT biosensor with smiFISH probes (Tsanov et al., 2016) complementary to the 3' and 5' ends of mRNA in separate colors and with an α-RCK antibody to label P-bodies (although we note RCK foci could also be in complex with Ago2 outside of P-bodies). As we hypothesized, the bright mRNA-Ago2 foci did indeed colocalize with RCK (**Figure 3.10C**). Further, the localization was dependent on Ago2-tethering. About 30% of mRNA was colocalized with RCK in cells expressing tetherable Ago2, compared to less than 5% in control cells (**Figure 3.10D**).

Interestingly, the majority of mRNAs we observed contained both 5' and 3' smiFISH signals, regardless of tethering or colocalization with RCK (**Figure 3.11A**). While this would suggest that at least some mRNAs in P-bodies are intact, as seen previously (Horvathova, Voigt, Kotrys, Zhan, Stadler, et al., 2017), it was difficult to know for sure since each cluster contained many mRNAs and the 5' and 3' signals could therefore come from different molecules. Furthermore, since the distinct smiFISH probes bind with different affinities and have fluorophores with distinct properties, it was also difficult to say if the 5' and 3' signals were present at a one-to-one stoichiometry, although we did observe a similar ratio of signals at mRNA both inside and outside of RCK foci (**Figure 3.11B**).

Collectively, these data show that tethering Ago2 to an mRNA is sufficient to recruit endogenous downstream factors involved in miRNA-mediated translational repression. Furthermore, the recruitment we observed can lead to unique mRNA

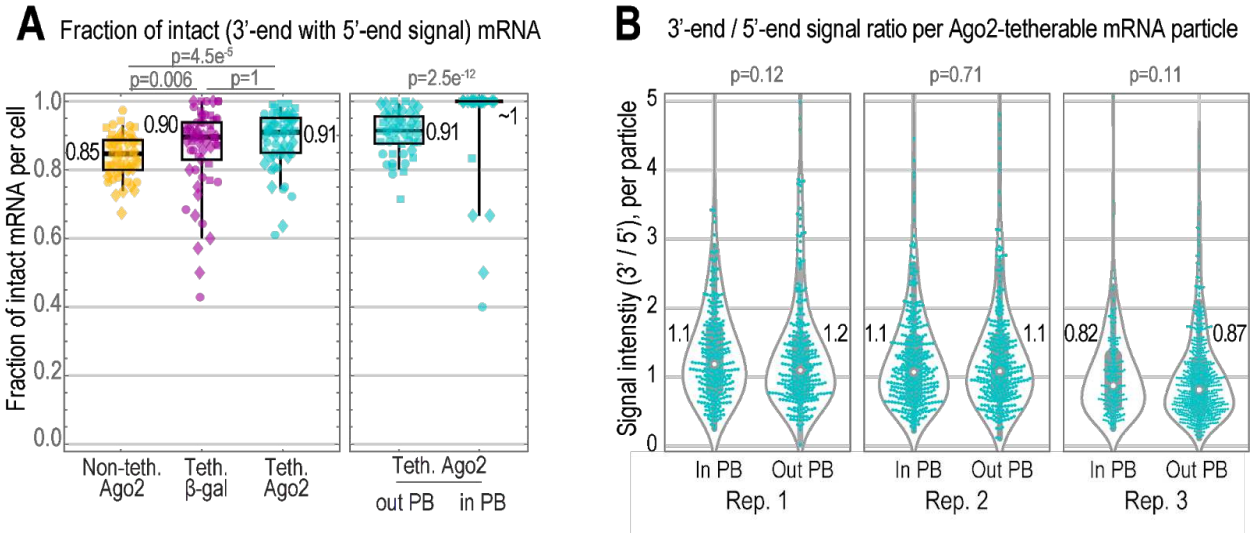

Figure 3.11 Most TnT biosensors in cells have 5' and 3' smiFISH signals
These data come from the experiment shown in **Figure 3.10C-D**.
A Box plots quantifying the fraction of mRNA per cell that were detected by their 3' smiFISH signal and also had a 5' smiFISH signal (yellow, non-tetherable Ago2; purple, tetherable β-gal; cyan, tetherable Ago2; different shapes mark 1 of 3 replicate experiments). Left, tetherable Ago2 versus controls. Right, tetherable Ago2 signals in P-bodies (PBs) versus out. P values were calculated from Mann-Whitney tests (A, left was Bonferroni-corrected).
B Violin plots showing the ratio of 3' to 5' smiFISH signals per each mRNA focus (including multi-mRNA clusters) in or out of PBs in all cells expressing tetherable Ago2 over three experimental replicates. The median ratio value per replicate experiment was calculated. P values were calculated from Mann-Whitney tests.

behaviors, including long-term translational silencing, as well as mRNA clustering and coalescence reminiscent of phase-separation. More generally, these data demonstrate how the TnT biosensor can be used to target mRNA to specific subcellular locations or microenvironments to better understand how they affect translation dynamics.

3.5 Progressive loss of translation upon Ago2 tethering

Thus far we have shown that Ago2-tethered TnT biosensors are translationally silenced and ultimately cluster into RCK foci that are presumably P-bodies. With this in mind, we next sought to zoom in on the kinetics of translation silencing by tracking single TnT biosensors prior to their clustering. According to several lines of work, Ago2 is thought to silence mRNA in part by inhibiting ribosome initiation (Jonas & Izaurralde, 2015). However, direct visual evidence for this has been lacking due to the limited spatiotemporal resolution of earlier experiments. Assuming ribosome initiation is inhibited, we would expect the TnT translation signal to dim after an Ago2 tethering event. Dimming would be gradual as elongating ribosomes finish translating the open reading frame and run off the transcript one by one. Other mechanisms of translational repression are also possible and can be discerned using the TnT biosensor. For example, if ribosomes prematurely abort translation after Ago2 tethering, the translation signal would rapidly disappear, as occurs when cells are treated with puromycin (**Figure 3.1D**, **Figure 3.4B,C,E**). Also, if translation elongation is repressed, ribosome progression could be slowed or halted, in which case the translation signal would persist beyond the time it takes to translate the open reading frame. Finally, if an mRNA were sliced, as in siRNA-mediated translational silencing, this would result in the physical separation of the translation and mRNA signals (Ruijtenberg et al., 2020).

To distinguish between these possibilities, we developed an imaging strategy to track freely diffusing TnT biosensors with high temporal resolution for upwards of 90 minutes. Specifically, we imaged whole cell volumes every 10 seconds in the mRNA channel, allowing us to track a single mRNA for well over an hour. Concurrently, we

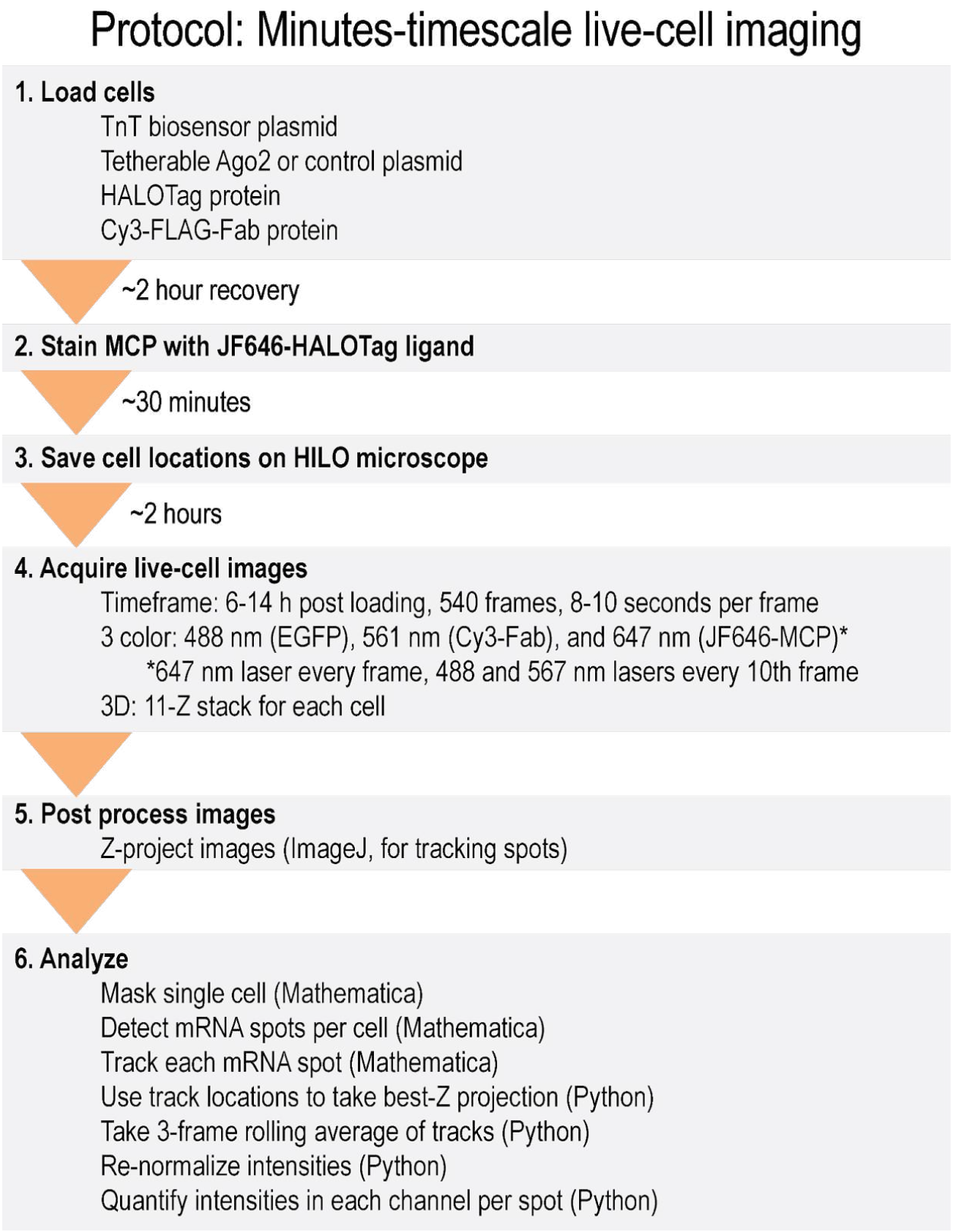

Figure 3.12 Workflow for minutes-timescale live cell imaging experiments.
The step-by-step workflow is shown here. Further details are provided in **Methods**.

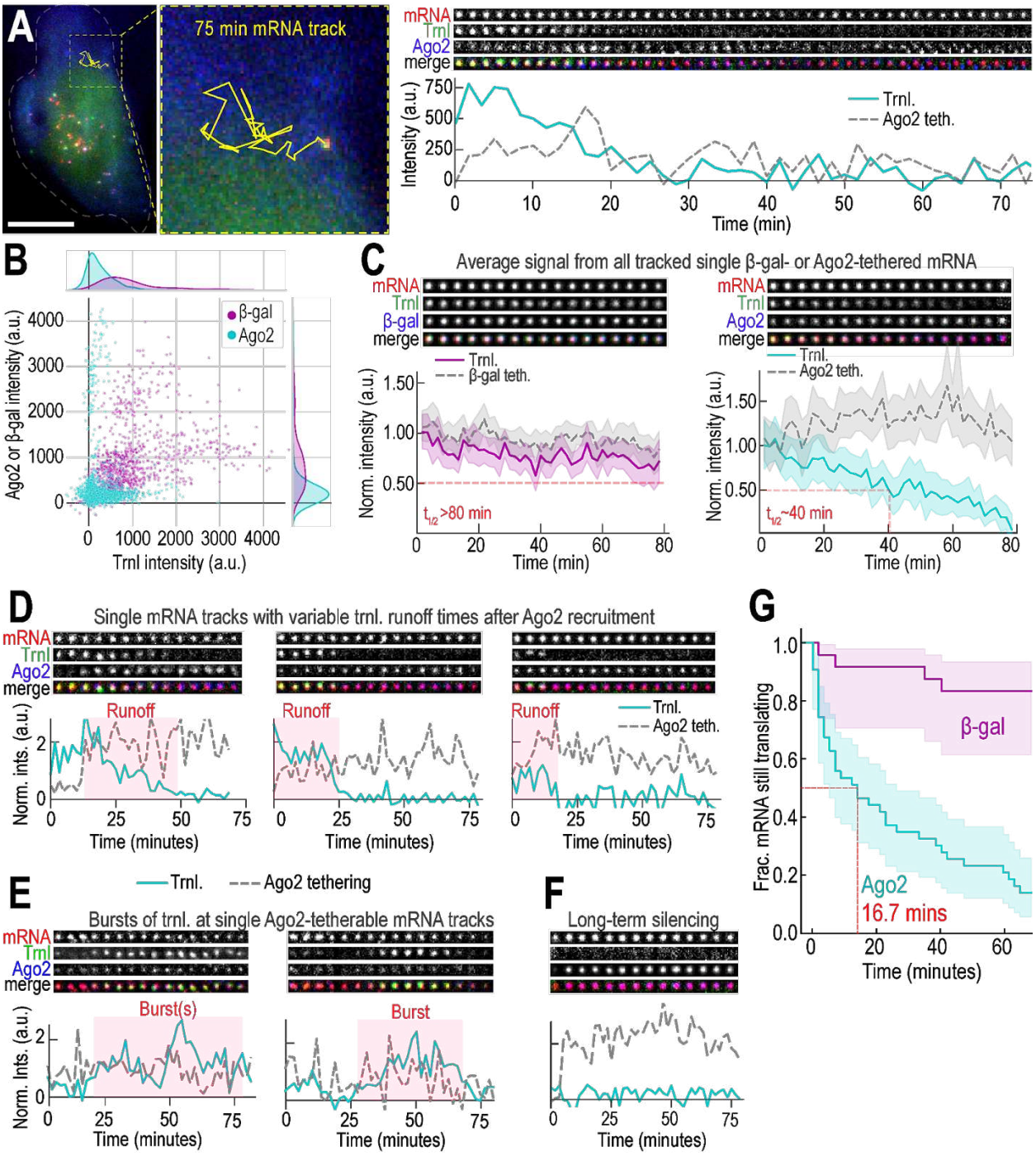

Figure 3.13 Progressive loss of translation upon Ago2 tethering.
(Legend on following page)

Figure 3.13 Progressive loss of translation upon Ago2 tethering.
A A representative track of a single TnT biosensor in a cell expressing tetherable Ago2 and loaded with TnT components (smFLAG-KDM5B-15xBoxB-24xMS2 mRNA reporter, Cy3-FLAG-Fab, and JF646 HaloTag MCP) over a 75-minute interval, described in **Figure 3.12**. Left, the track of the mRNA (yellow line) is overlaid on the cell image. Right, crops (11 x 11 pixels^2; 130 nm/pixel) of this track are displayed over time to show the mRNA, translation (Trnl), and Ago2 tethering signals every 100 seconds. These signals are plotted over time below (Trnl, solid cyan line; Ago2, dashed gray line). Scale bar, 10 μm.
B Scatter plot showing single-mRNA tethering signals (β-gal, purple; Ago2, cyan) versus translation signals (Trnl) for all tracked TnT biosensors at all timepoints (β-gal, 21 tracks, 11 cells; Ago2, 25 tracks, 11 cells). The Spearman Correlation Coefficient was calculated from this data (0.55 for β-gal, $p=2x10^{-81}$; -0.10 for Ago2, $p=2x10^{-4}$).
C Line plots, as in A, showing average signals from multiple TnT biosensor tracks through time. Signals from individual β-gal or Ago2 tetherable tracks were normalized from 0 to 1 and then averaged, so no one track would dominate. The resulting average curves were then renormalized (using the first four timepoints) so they started from ~1. Left, average translation (Trnl.) and tethering (Teth.) signals from cells expressing tetherable β-gal (β-gal-teth., dashed gray line; Trnl, solid purple line). Right, average translation and tethering signals from cells expressing tetherable Ago2 (Ago2-teth., dashed gray line; Trnl, solid cyan line). Shaded regions, 95% CIs. Solid red lines denote the runoff halftime $t_{1/2}$.
D Sample tracks of single TnT biosensors (renormalized as in B; every 3rd crop is shown after a 3-frame rolling average). Runoff times shorten from left to right.
E Sample tracks of single TnT biosensors showing bursts of translation, plotted as in D.
F Sample track showing long-term silencing with high Ago2 tethering signals, plotted as in D.
G Survival plots of translation events for tetherable Ago2 or tetherable β-gal tracks. For the tracks from B, the duration of each translation event was measured. The median survival time for translation at Ago2-tethered TnT reporter mRNA was estimated using the Kaplan-Meier survival function.

imaged translation and tethering once every 100 seconds (described in **Figure 3.12**). This staggered approach allowed us to follow the translation and tethering signals of individual mRNAs with minimal photobleaching. From 11 cells over 5 days, we identified 25 mRNA that were trackable for 35-90 minutes and that had at some point both tethering and translation signals (**Figure 3.13**). We repeated the experiment in 11 cells expressing tetherable β-gal over 4 days, finding 21 such control-tethered mRNA.

For each tracked mRNA, we measured the intensities of the mRNA, translation, and tethering signals through time. Consistent with an inhibition of translation initiation and ribosome runoff, we could observe a slow and steady decline of the translation signal from individual Ago2-tethered mRNA (**Figure 3.13A**). Moreover, a scatterplot of translation signals versus tethering signals for all data points revealed a striking pattern: translation signals were strongest when Ago2 tethering signals were weakest, and vice versa (**Figure 3.13B, cyan**). In stark contrast, this inverse relationship between translation and tethering signals (Spearman correlation coefficient = -0.10; $p = 1.7x10\text{-}4$) was not observed when mRNA were tethered to control β-gal (**Figure 3.13B, purple**). In fact, β-gal tethering signals were correlated with translation (Spearman correlation coefficient = 0.55; $p = 2.4x10^{-81}$). This suggested that the more Ago2 present, the less likely it is that the mRNA is actively translating. To visualize this over time, we normalized all tracked signals and averaged them together (so each mRNA would have equal weight, **Figure 3.13C**). This revealed translation signals steadily and significantly decreased with time (t1/2 ~40 minutes), while Ago2 tethering signals steadily increased (**Figure 3.13C, right**). The corresponding signals in control cells expressing tetherable β-gal remained steady (**Figure 3.13C, left**). These data strongly

suggest Ago2 tethering leads to a gradual runoff of ribosomes, as would be expected if ribosomal initiation were inhibited.

We next examined the individual mRNA tracks in greater detail. In line with the average behavior in **Figure 3.13C**, the translation signals at many steadily declined as in **Figure 3.13C**, although the rate of runoff was variable from mRNA to mRNA (**Figure 3.13D**). This variability most likely reflected stochasticity in the start of our imaging as well as in the positioning of individual ribosomes along an mRNA upon Ago2 tethering. In particular, we noticed runoffs could be delayed by late Ago2 tethering (**Figure 3.13D, left**) and runoffs with low initial translation signal intensities could be faster (**Figure 3.13D, middle vs. right**), presumably because they were already in progress when imaging began.

We also observed occasional bursts of translation despite the presence of low-levels of Ago2 tethering (**Figure 3.13E**). This would suggest the repression of translation initiation by Ago2 is incomplete or reversible. Further, we observed Ago2-tethered, translationally-silent mRNA (**Figure 3.13F**) coalesce to form large clusters that were similar to the P-bodies we identified in **Figure 3.10**. These mRNA were associated with exceptionally bright Ago2 foci that likely contained many Ago2 proteins.

To study all the translation events at tethered mRNA, we visualized the impact to Ago2 tethering to translation events at single mRNA. To do this, we measured the translation run length, the “survival time” of translation, in Ago2-tetherable versus β-gal tetherable cells for all long tracks. This included bursts of translation which initiated in the middle of a track. We found that though translation events sometimes end on control β-gal-tethered mRNA (median translation event length > 60 minutes), the median

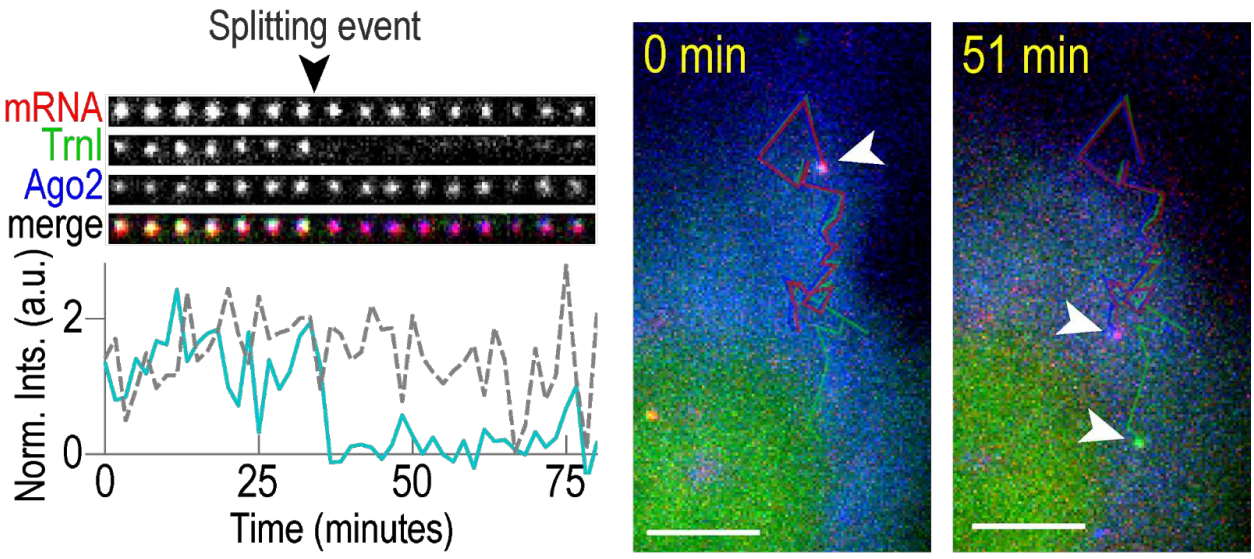

Figure 3.14 Example of a rare event showing the splitting of mRNA and translation signals

One of two example tracks from **Figure 3.13C**, right where the translation signal split from the mRNA. Plotted as in **Figure 3.13D**. Right, two sample images are shown with the tracks overlaid (mRNA, red; translation, green; Ago2, blue). Arrows indicate the current location of the biosensor at the displayed times (yellow text). Scale bar, 5 μm.

survival time of a translation event in an Ago2-tetherable cell was just 16.7 minutes (**Figure 3.13G**). Further, almost all (~85%) of translation events ended during acquisition of the track.

Finally, on two occasions we observed physical separation of the translation and mRNA signals, possibly indicating some form of mRNA cleavage (**Figure 3.14**; Horvathova et al., 2017; Ruijtenberg et al., 2020). Given the scarcity of this type of event (2/25; <8% of observations), we conclude it is not a dominant form of translation repression in our system.

3.6 Translational repression at Ago2-tethered mRNA is consistent with inhibition of translation initiation

Our analysis of the individual mRNA tracks above provides further support for a model in which Ago2 tethering strongly inhibits translation initiation. To further confirm this model, we performed Harringtonine experiments (HT). HT inhibits translation initiation while allowing already-initiated, elongating ribosomes to continue translation and run off the transcript (**Figure 3.15A**; Huang, 1975). The ribosome elongation rate can be quantified by measuring the rate at which the translation signals dim and disappear (**Figure 3.15A,B**). If Ago2 tethering inhibits initiation as potently as HT, we would predict Ago2-tethered ribosome runoff times should be on the same timescale as HT-induced runoff times.

To test this prediction, we added HT to cells expressing the TnT biosensor and either tetherable Ago2 or tetherable β-gal (outlined in **Figure 3.2**). This led to less mRNA being translated over time and a steady loss in the average translation signal from mRNA (**Figure 3.15B** and **Figure 3.16A**). In cells expressing tetherable Ago2, the HT-induced ribosome runoff halftime was ~29 minutes, with the majority of signal lost in ~60 minutes (**Figure 3.16A left, B**). This timescale is similar but a bit faster than what we observed when tracking individual Ago2-tethered mRNA in the absence of HT (**Figure 3.12C, right**). These data indicate Ago2-tethering is nearly as strong at inhibiting translation initiation as HT.

Interestingly, in cells expressing tetherable β-gal, the HT-induced runoff appeared faster (**Figure 3.16A right, B**). This overall faster runoff time could be seen in the average, photobleach-corrected runoff curves from multiple experiments, although

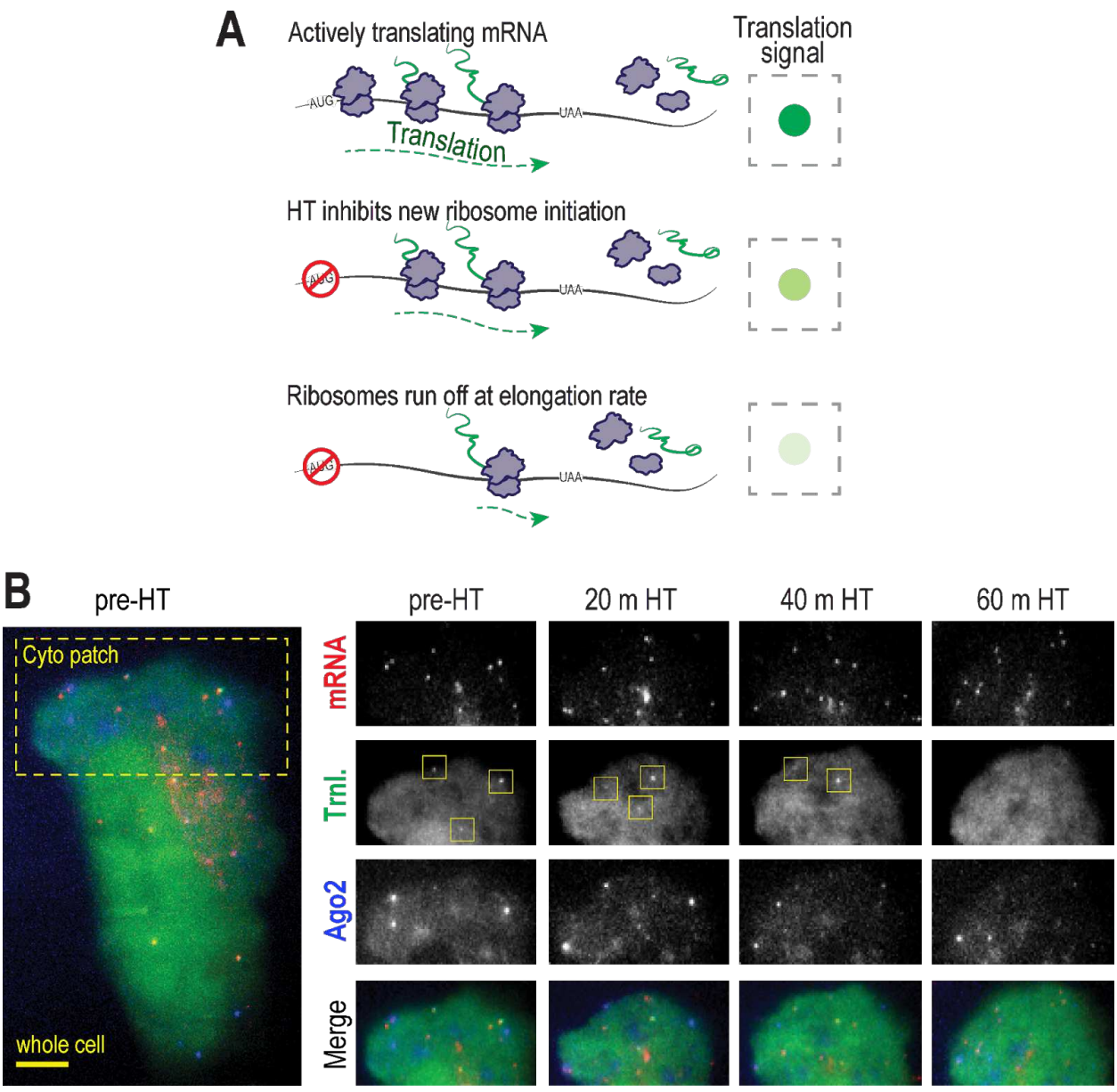

Figure 3.15 Harringtonine experiments
Harringtonine (HT) ribosome runoff assays were performed on TnT loaded cells, as described in **Figure 3.2**.
A Cartoon of measuring ribosome runoff rate using nascent chain tracking.
B Example cell undergoing a HT ribosome runoff assay. A single, Ago2-tetherable cell was imaged before and up to 60 minutes after being dosed with HT. Yellow boxes mark translation sites. The same intensities are used in each image over time. Cytoplasmic patch: 100 x 200 pix (130 nm/pixel). Scale bar, 5 μm.

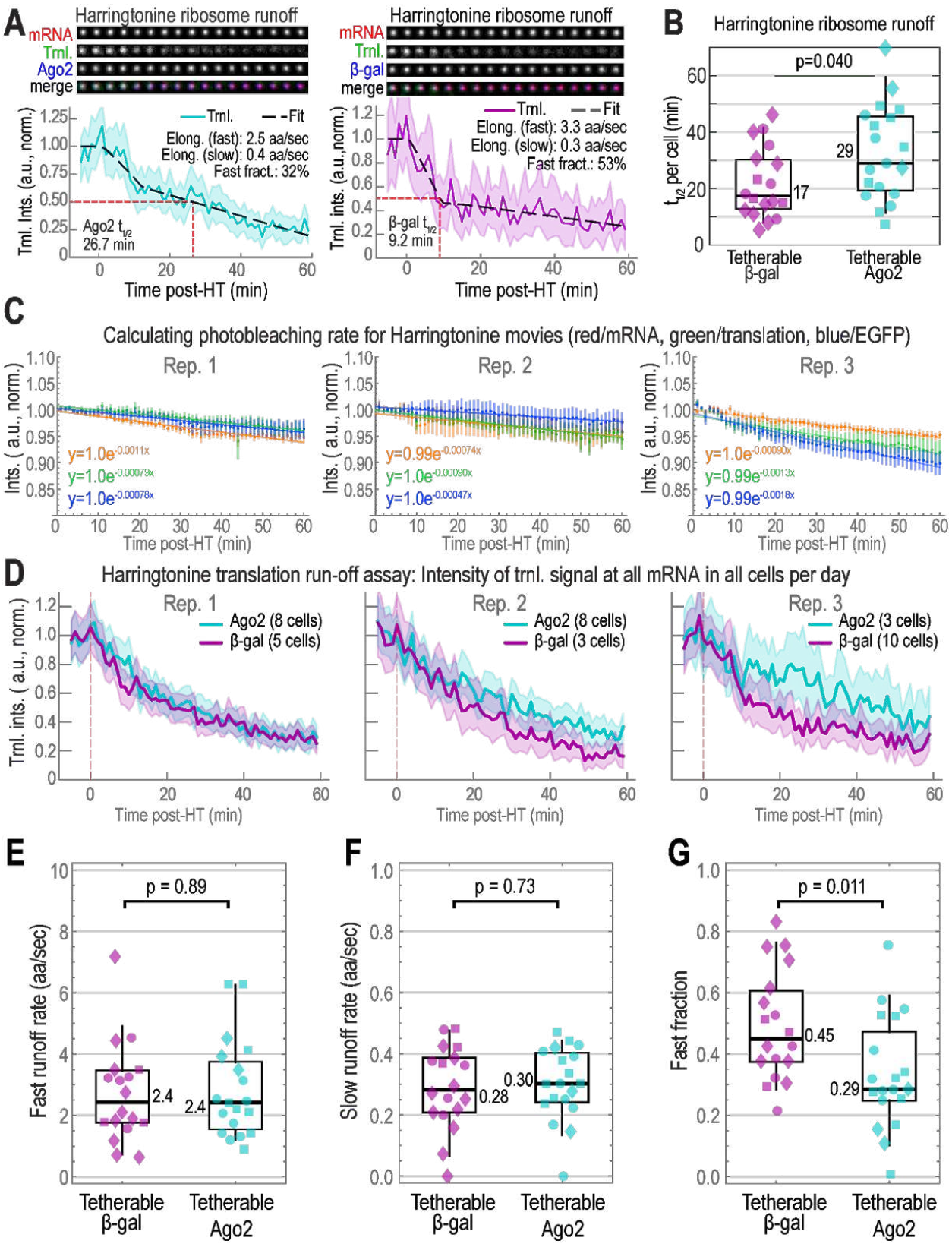

Figure 3.16 Harringtonine experiments analyses (legend on next page)

Figure 3.16 Harringtonine experiments analyses
Harringtonine (HT) ribosome runoff assays were performed on 18 cells expressing tetherable Ago2 and 17 cells expressing tetherable β-gal from 3 replicate experiments. HT was added to cells at time = 0.
A Average single-molecule signals from all detected TnT biosensors in a single representative cell expressing tetherable Ago2 (left) or β-gal (right) and exposed to HT (Time = 0), plotted as in C. The average translation signal (solid line) showing ribosome runoff was fit to a biphasic model (dashed line; fitted parameters displayed). Red line denotes the runoff halftime $t_{1/2}$.
B Box plot showing all fitted single-cell HT-runoff halftimes. N=18 cells expressing tetherable Ago2; N = 17 cells expressing tetherable β-gal (marker shapes denote 3 replicate experiments).
C Signal photobleaching over time in HT replicate experiments was measured, plotted, normalized to start at 1 and fit to a single exponential decay (mRNA, red; translation, green; tethering, blue; error bars show SEM; fit denoted with solid lines). For each replicate experiment, mean background-subtracted, whole-cell intensity was measured at each timepoint and plotted.
D Average signals from TnT biosensors through time for each replicate HT-runoff experiment, plotted as in **Figure 3.16A** (Ago2; cyan, β-gal, purple). HT was added at Time = 0, denoted by vertical, dashed red lines. Shaded regions, 95% CIs.
E-G Box plots showing the fitted parameters from the biphasic HT-runoff model (left, fast elongation rate in amino acids per sec, aa/sec; middle, slow elongation rate; right, fast fraction; shapes denote 1 of 3 replicate experiments). P values were calculated using the Mann-Whitney test.

the difference was not always as significant due to high cell-to-cell variability (**Figure 3.16C,D**). To quantify the difference, we fit each single-cell HT runoff curve to a biphasic model (dashed line in **Figure 3.16A**) in which a fraction of elongating ribosomes run off with relatively fast kinetics and the remaining fraction run off with relatively slow kinetics (see **Methods** for model details). According to the individual fits, the Ago2 slowdown arises because there are fewer ribosomes in the faster elongating state (~29% vs. ~45%; **Figure 3.16E-G**). These results therefore provide evidence that Ago2 not only

inhibits translation initiation, but also leads to a moderate but measurable slowdown in elongation.

3.7 Ago2 tethering mimics miRNA-mediated translational repression at the single-molecule level

Although previous work provided convincing evidence that Ago2 tethering recapitulates natural miRNA-mediated translational silencing (Eckhardt et al., 2011; Golden et al., 2017; Liu, Rivas, et al., 2005; Pillai et al., 2004), we wanted to confirm this at the single-molecule level to further validate our TnT biosensor data. To achieve this, we developed a strategy to recruit endogenous Ago through miRNA-directed targeting, rather than tethering, to a modified TnT reporter. Two methodologies we developed recruited Ago2 by (1) an introduced synthetic miRNA mimic that could target the NCT reporter's 3'UTR (described in Appendix 1), or by (2) adding miRNA response elements (MREs) targetable by endogenous miRNA to the TnT reporter.

For reasons discussed in described in Appendix 1, we followed the second option and created modified TnT biosensors containing MREs in place of the tethering cassette. For MREs, we chose the 3'UTR of the POLR3G gene, which is predicted by TargetScan (TargetScanHuman 7.2, n.d.) to contain three endogenous MREs targeted by miR-26-5p. To confirm these MREs repress translation in our cells, we first placed them in the 3'UTR of a simpler reporter that encodes sfGFP-H2B (**Figure 3.17A**). Cells loaded with the MRE-containing reporter produced ~40% less sfGFP-H2B after 24 hours than cells loaded with a reporter containing mutated MREs, indicating that the intact MREs promote miRNA-mediated silencing (**Figure 3.17B**).

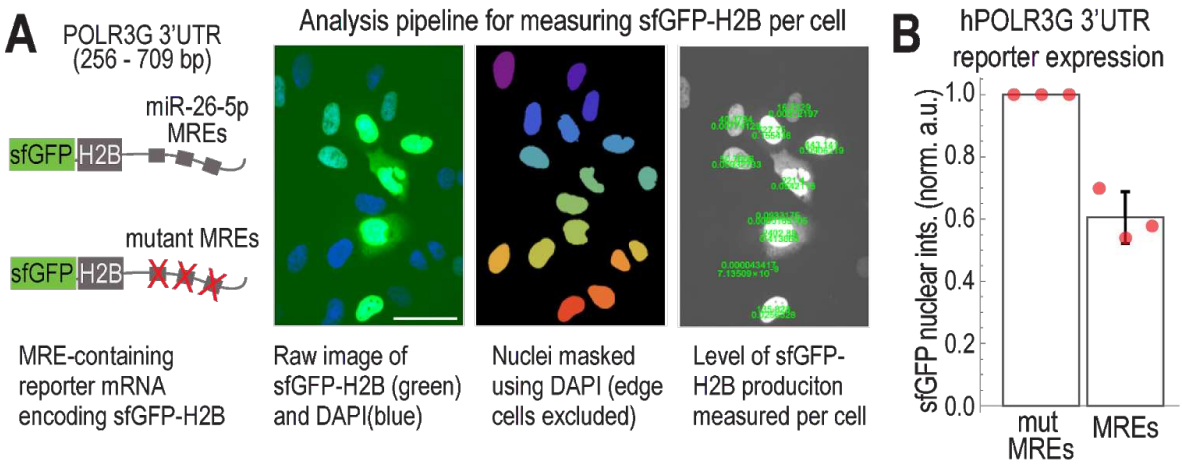

Figure 3.17 Intact miRNA response elements in the POLR3G 3'UTR are sufficient for silencing a reporter.
A Schematic of the sfGFP-H2B-POLR3G-3'UTR reporter, which contains either miRNA Response Element (MRE) or mutated MREs, and analysis pipeline. Scale bar, 25 μm. **B** The nuclear GFP intensity of cells expressing sfGFP-H2B-hPOLR3G 3'UTR with endogenous or mutated (mut) miRNA Response Elements (MREs) was quantified. Points represent the medians per replicate experiment. N = 366, 325, and 1258 nuclei for each replicate experiment for the mutated-MRE-containing reporter (mut MREs) and N = 883, 458, and 1803 nuclei for each replicate experiment for the MRE-containing reporter (MREs).

We then introduced the MRE cassette in place of the BoxB hairpins in our TnT biosensor as well as a similar biosensor that encoded 10 HA instead of 10 FLAG epitopes. In addition, we introduced the mutated MREs into both of these biosensors (**Figure 3.18**). These miRNA-based biosensors provide a more natural context than the TnT biosensor, but with the drawback that we can no longer track Ago2 association. Nevertheless, the miRNA-based biosensors can still be tracked at the single-molecule

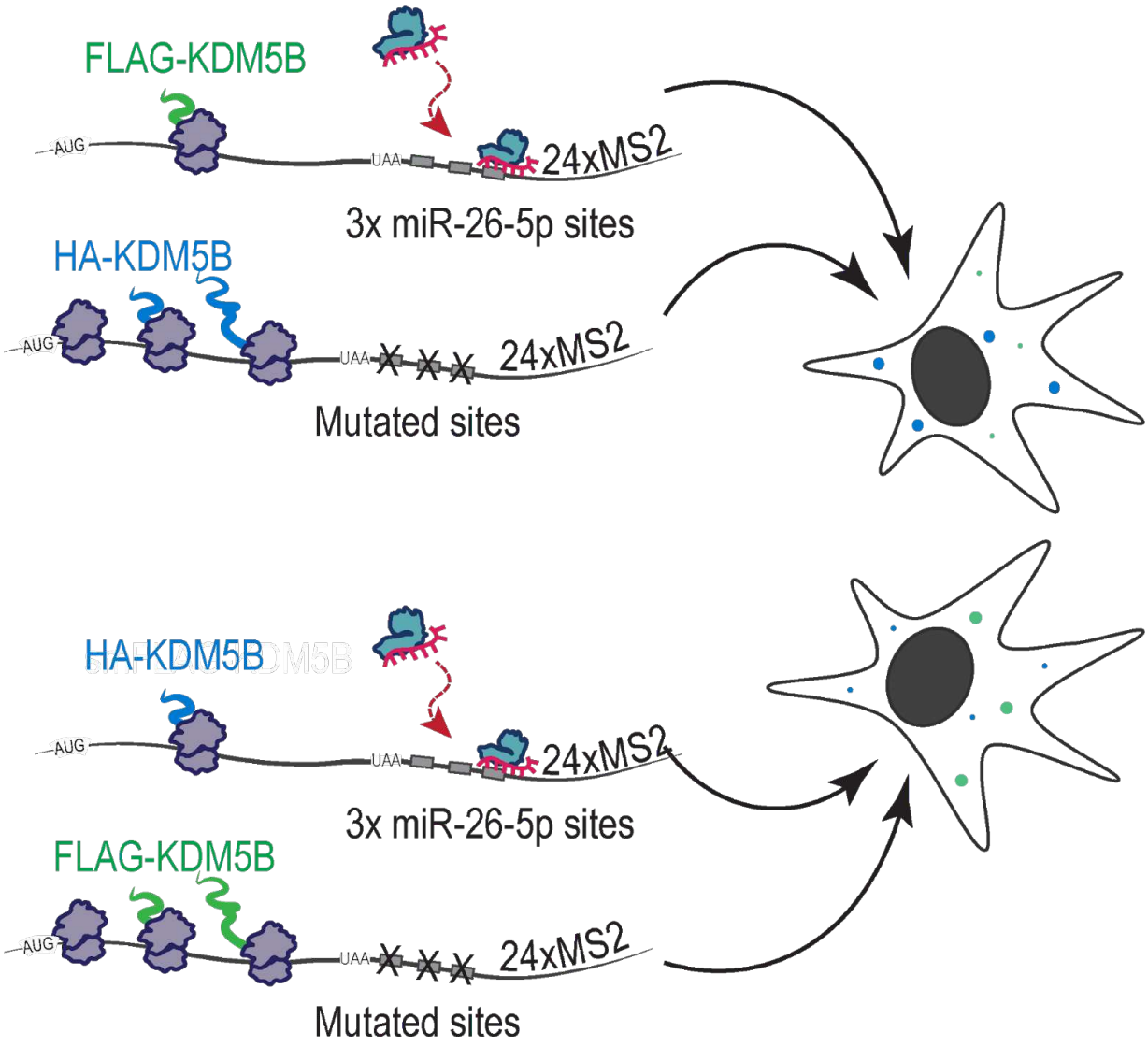

Figure 3.18 Experimental design for assay detecting miRNA-directed Ago targeting represses translation at the single-mRNA level.
Cartoon of modified TnT biosensors with either endogenous miRNA Response Elements (MREs) or mutated, miRNA-untargetable versions (MUT) inserted in place of the TnT tethering cassette. In each experiment, two modified biosensors (one FLAG- and one HA-tagged) were coexpressed in single cells. FLAG-FLAG (or HA-HA) signals were compared across experiments. Translation level here is represented by puncta size.

level, allowing us to measure translation at individual reporter foci. Assuming our original TnT biosensor recapitulates natural miRNA-mediated silencing, we would predict that our new biosensors containing endogenous MREs would on average have lower translation signals (presumably due to ribosome runoff) than those containing mutated MREs.

To test this, we coloaded cells with one of two combinations of biosensors: either a FLAG miRNA-biosensor with endogenous MREs and an HA miRNA-biosensor with mutated MREs, or the reciprocal pair of biosensors in which FLAG and HA were swapped (**Figure 3.18**). This allowed us to directly compare endogenous and mutant MRE-containing biosensors in the same cells (**Figure 3.19A,B**). We then quantified the translation signals at individual biosensors in live cells. Translation was reduced by 38-57% (across 3 replicates) in cells containing our FLAG-based biosensors with endogenous MREs relative to cells containing the mutant versions and by 0-54% (across 3 replicate) in the reciprocal situation with HA-based biosensors (**Figure 3.19C-E**). Thus, in agreement with our prediction, endogenous MREs do significantly reduce the translation signals of individual reporter mRNAs. Moreover, the overall 37-57% reduction in translation in all but one replicate is in good agreement with the 40-60% reduction we observed when tethering Ago2 to the original TnT biosensor (**Figure 3.8B-C**). Taken together, these data provide additional single-molecule evidence that tethering Ago2 to the TnT biosensor recapitulates endogenous miRNA-mediated Ago2 translational repression.

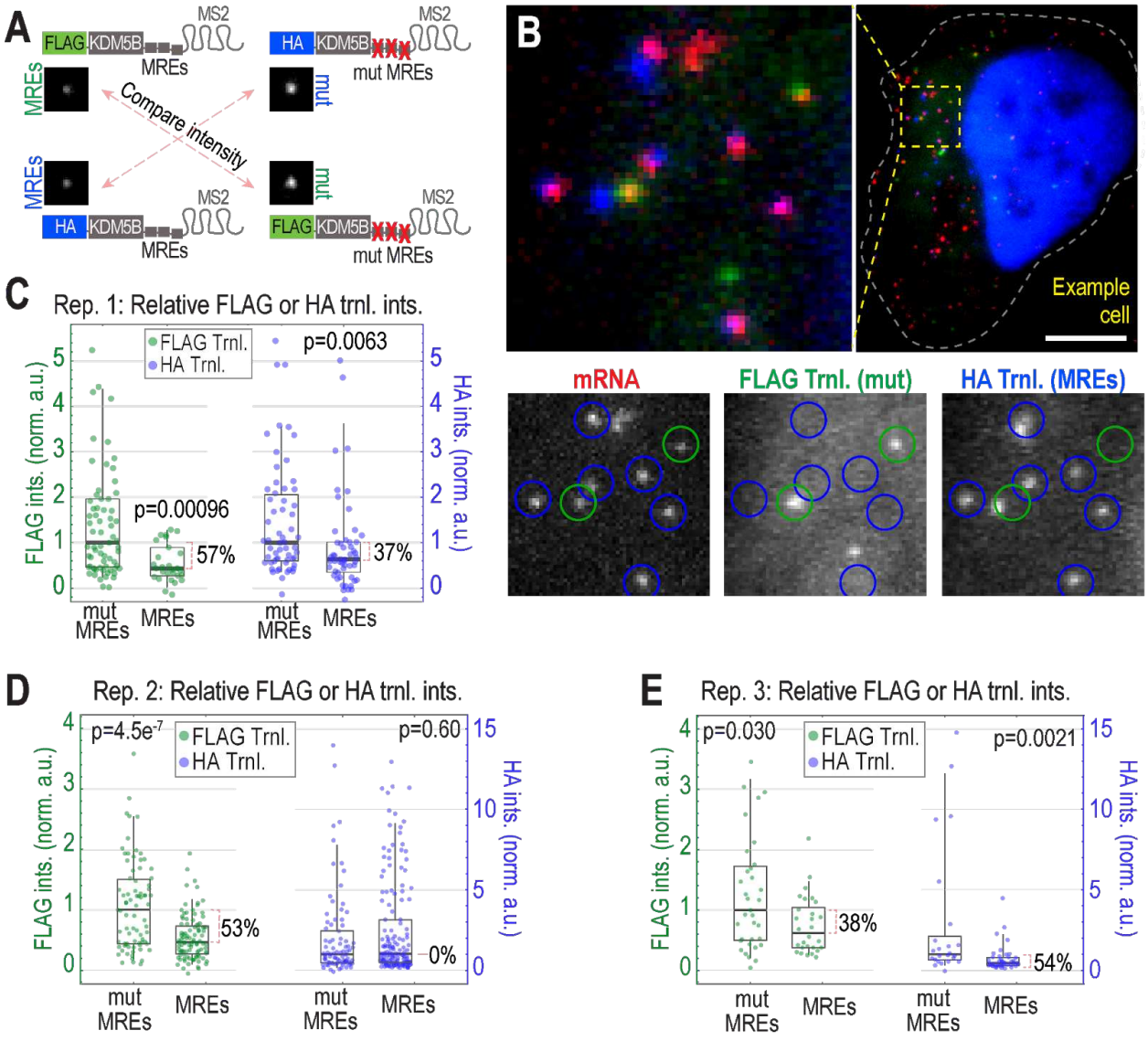

Figure 3.19 miRNA-directed Ago targeting represses translation at the single-mRNA level.
(Legend on next page)

Figure 3.19 miRNA-directed Ago targeting represses translation at the single-mRNA level.
A Schematic of modified TnT biosensors with either endogenous miRNA Response Elements (MREs) or inactive, mutated versions (MUT) inserted in place of the tethering cassette. In each experiment, two modified biosensors (either top two or bottom two) were coexpressed in single cells. To fairly gauge relative translation signals, FLAG (or HA) signals were compared across experiments (red, dashed arrows).
B An example cell loaded with the top two biosensors in A. Image above shows a whole cell and a representative cytoplasmic patch. Image below shows each separated channel from the patch (intensity auto-adjusted), with detected translating (TrnI) mRNA circled in blue (indicating translation of HA) or green (indicating translation of FLAG). Scale bar, 10 μm.
C-E Box plots showing the relative intensity (ints.) of the mutated MREs (mut MREs) and endogenous MREs (MREs) containing modified biosensors from 3 replicate experiments. Each point represents the measured translation signal from a single detected biosensor
C N = 69 mut MREs and 30 MREs for FLAG; N = 58 mut MREs and 54 MREs for HA). P values were calculated using the Mann-Whitney test.
D N = 79 mut and 99 MRE green spots for FLAG; N = 85 mut and 153 MRE blue spots for HA.
E N = 35 mut and 28 MRE green spots for FLAG; N = 24 mut and 44 MRE blue spots for HA.

3.8 Materials and Methods

Plasmid construction

All expression vectors were designed using SnapGene software. The TnT biosensor construct (smFLAG-KDM5B-15xBoxB-24xMS2) was cloned using the smFLAG-KDM5B-24xMS2 plasmid from (Morisaki et al., 2016) and the pRL-5xBoxB construct from (Pillai et al., 2004). First, using restriction cloning, 5x BoxB repeats were copied from the pRL plasmid with AgeI sites on each end using PCR and inserted into the KDM5B reporter plasmid's 3' UTR at AgeI. Next, two 5x BoxB repeats were isolated from the pRL plasmid and added at the XbaI site, creating the final construct smFLAG-

KDM5B-15xBoxB-24xMS2. The orientation of inserted BoxB stem loops was confirmed by Sanger sequencing (Quintara Biosciences). The plasmids were purified via midi-prep (Machery-Nagel) before loading.

The tetherable Ago2 (λN-EGFP-Ago2), non-tetherable Ago2 (EGFP-Ago2), and tetherable β-gal (λN-EGFP-β-gal) constructs were made by first swapping HA for EGFP in the plasmids λN-HA-hAgo2 or λN-HA-β-gal from (Pillai et al., 2004) using isothermal assembly. The EGFP sequence was obtained from the EGFP-hAgo2 plasmid (Addgene plasmid # 21981), which was a gift from Dr. Phil Sharp (Leung et al., 2006). Next, the entire open reading frame was inserted into the plasmid backbone from pFN24A HaloTag CMV*d3* Flexi Vector (Promega) so that the ORF was under a CMV-d3 minimal expression promoter. Lastly, we verified the plasmid sequence using whole-plasmid sequencing via de novo assembly (Gallegos et al., 2020).

The “MRE" insert was created from a gene block containing the nucleotides 256-706 of the POLR3G 3’UTR, which was predicted to contain three miR-26-5p MREs with 50 nucleotides of endogenous UTR context flanking the first and last MRE. The mutant “mut MREs” insert additionally had two nucleotide mutations for each MRE (sequence and MRE locations obtained from TargetScan; *TargetScanHuman 7.2*, n.d.). The insert’s orientation was verified by Sanger sequencing (Quintara Biosciences).

The MRE-containing sfGFP-H2B reporters were constructed from the plasmid sfGFP-H2B-C-10 (Addgene 56367, which was a gift from Dr. Michael Davidson) by inserting a UTR sequence at MfeI and HpaI in its 3’UTR. The MRE-containing translation reporters used SpaghettiMonsterHA or SpaghettiMonsterFLAG constructs (sm**FLAG**-KDM5B-24xMS2 or sm**HA**-KDM5B-24xMS2 from Morisaki et al., 2016). The

MRE or mutant POLR3G 3'UTR gene blocks were inserted at AgeI and XmaI sites in the 3'UTR of each FLAG and HA reporter. The insert orientation was verified by Sanger sequencing (Quintara Biosciences).

PolR3G 3'UTR sequence (256 – 706 nucleotides):

256 TGAATATGAATGTGCCTAAAGAATTTTTGCTCTCTTAATCTATGTATACA
TA(C/t)T(T/c)GAACAAATCATTCTTGCTTAACTGCTGATCTTTTGTA
AAACTATTGCTAGTCATAATGGATTTCTATAACCTGAAAGTTGATATAAT
ACAGCACGTGGAGCACTTTAAAAACAAAGAAA(C/t)T(T/c)GAAAATA
ATTTTATTTTTTACCTTTACATGGTGTGTTCTAGACTACTGCATTATGAC
TACATAAACCTACCTGAGCTCTTACAAGTACAGAATTGTGAGACAGAGGT
TTTGTGATGGAAAACATACACATAGGGAAAAATACCAAACTGAGCAATAT
AAATTTCACAGCTCACATCTTAGCCAGTACAAAGAAACTTTCACATGGGG
TGAATATTATAATA(C/t)T(T/c)GAATTTGAGACTTAATACTGTATAT
GAATTAATCATCCCACTGTAATAACTGA *706*

Gold highlight: human miR-26-5p predicted recognition sites
Red text: (endogenous / mutated) nucleotide
Sequence source: TargetScan

Fab/Frankenbody Generation and MCP Purification

The Cy3 α-FLAG-Fab were generated and affinity purified as previously described (Morisaki et al., 2016). Briefly, Fab were generated from monoclonal α-FLAG antibodies (Wako, 012-22384 Anti DYKDDDDK mouse IgG2b) using the Pierce Mouse IgG1 Fab and F(ab')2 Preparation Kit (ThermoFisher). First, α-FLAG antibody were digested into Fab in a Zeba Desalt Spin Column (ThermoFisher) containing immobilized Ficin undergoing gentle rotation for 3-5 hours at 37°C. Fab were purified from the digest by centrifugation in a NAb Protein A column. Eluted Fab were concentrated to about 1 mg/mL and either conjugated with Cy3 or stored at 4°C. Cy3 labeling was performed in small batches of 100 µg Fab at a time. The dye was Cy3 *N*-hydroxysuccinimide ester (Invitrogen) dissolved in DMSO and either used immediately or stored at -20°C. For

labeling, 100 µg of Fab was dissolved in a final volume of 100 µL of 100 mM NaHCO3 (pH 8.5) plus 1.33 µl of Cy3 dye. Fabs were labeled for about 2 hours at room temperature during gentle rotation and agitation. The Fab were separated from unconjugated dye in an equilibrated PD MiniTrap G-25 desalting column (GE Healthcare). Fab were concentrated in an Amicon Ultra-0.5 Centrifugal Filter Unit (NMWL 10 kDa; Millipore) to about 1 mg ml^{-1}. The degree of labeling (*DOL*) was calculated using the following equation:

$$DOL = \frac{\varepsilon_{Fab}}{\varepsilon_{dye}} \times \frac{1}{A_{280}/A_{dye} - CF} \quad (1)$$

where ε_{Fab} is the extinction coefficient of Fab (70,000 M^{-1} cm^{-1}), ε_{dye} is the extinction coefficient of the dye used for conjugation (150,000 M^{-1} cm^{-1} for Cy3), A_{280} and A_{dye} are the measured absorbances of dye-conjugated Fab fragments at 280 nm and at the peak of the emission spectrum of the dye (570 nm for Cy3), respectively, and *CF* is the correction factor of the dye (the ratio of the absorbances of the dye alone at 280 nm to at the peak; 0.08 for Cy3). If the DOL was less than 0.8, this protocol was repeated on the same Fab to increase their DOL to approximately 1. Fab were stored at 4°C.

MCP was generated as previously described (Morisaki et al., 2016). Briefly, MCP (His-HaloTag-2xMCP) was purified using its histidine tag with Ni-NTA Agarose (Qiagen) following the manufacturer's instructions with minor modifications. The bacteria were lysed in a PBS-based buffer containing a complete set of protease inhibitors (Roche). In a gravity-flow column, binding to the Ni-NTA resin was carried out in the presence of 10 mM imidazole. After washing with 20 and 50 mM imidazole in PBS, the protein was

eluted with 300 mM imidazole in PBS. The eluted protein was dialyzed against a HEPES-based buffer (10% glycerol, 25 mM HEPES pH 7.9, 12.5 mM $MgCl_2$, 100 mM KCl, 0.1 mM EDTA, 0.01% NP-40 detergent, and 1 mM DTT) and stored at –80°C after snap-freezing by liquid nitrogen.

The GFP-tagged α-HA Frankenbody was generated and purified as previously described (Zhao et al., 2019). Briefly, α-HA Frankenbody was expressed in *E. coli* BL21 (DE3) pLysS cells transformed with pET23b-FB-GFP (Addgene plasmid 129593), induced with IPTG at O.D. ~0.6, and expressed at 18°C overnight. The protein was purified in two steps, first with HisTrap HP 5 mL columns (GE Healthcare) and next with a size-exclusion HiLoad Superdex 200 PG column (GE healthcare) in a HEPES-based buffer (25 mM HEPES pH 7.9, 12.5 mM $MgCl_2$, 100 mM KCl, 0.1 mM EDTA, 0.01% NP40, 10% glycerol, and 1 mM DTT). Eluted α-HA Frankenbody was flash-frozen in liquid nitrogen and stored at -80°C. Only α-HA Frankenbody and MCP with 1-2 freeze-thaws were used in experiments.

Cell culture

Human U2OS osteosarcoma cells were grown in 10% (v/v) FBS (Atlas) media DMEM (Thermo Scientific) supplemented with 1 mM L-glutamine (Gibco) and 1% (v/v) Pen/Strep (Invitrogen/Gibco) and grown at 37°C in 5% CO_2. Cell density was maintained between 20-80%. U2OS cells were purchased from ATCC and were authenticated by STR profiling by ATCC and morphological assessments. We also confirmed that the cell line tested negative for mycoplasma contamination.

Bead loading and transfection

To bead load TnT plasmid and protein components, cells were plated at 70% confluency on 35 mm glass bottom chambers (MatTek) 1-2 days before imaging. Cells were bead loaded as described previously (Hayashi-Takanaka et al., 2011; McNeil & Warder, 1987; Cialek et al. 2021). Briefly, the media was changed to 10% FBS Opti-MEM (Thermo Scientific) before bead loading. The components were mixed together in a total volume of 4-8 µL: ~100 µg/mL of Cy3 α-FLAG Fab, ~33 µg/ml of purified HaloTag-2xMCP protein, plasmids, and 1x PBS if needed to fill to volume. Concentrations of 1.5 or 1.75 µg of DNA were used for the GFP-containing plasmids (either λN-EGFP-Ago2, λN-EGFP-β-gal, or EGFP-Ago2) or the reporter plasmid (pUb-smFLAG-KDM5B -15xBoxB-24xMS2), respectively. After removing the media, the 4 µL mixture of protein and DNA were pipetted on top of the cells, followed by sprinkling a monolayer of ~106 µm glass beads on top of the cells (Sigma Aldrich). The chamber was tapped ~20 times gently, then the media were replaced. After ~2.5 hours, cells were washed three times in phenol-free DMEM with 10% FBS and 1 mM L-glutamine. Before imaging, cells were stained with 200 nM JF646 HaloTag ligand for 15 minutes, followed by three washes in DMEM with 10% FBS and 1 mM L-glutamine. Cells were moved to the microscope stage-top incubator for imaging ~3 h post bead loading.

Transfection was performed in the fixed cell experiments where no protein loading was needed. All transfections were performed with the LTX Lipofectamine with Plus Reagent kit (Thermo Fisher), per the manufacturer's instructions. Briefly, cells were washed and the media was replaced with 1.75 mL Opti-MEM (Thermo Scientific) directly before transfection. The transfection solution included 2.5 µg DNA plasmid, 7.5

μL Plus reagent, and 7.5 μL Lipofectamine and Opti-MEM brought the solution to 250 μL. This solution was incubated for 5-15 minutes at room temperature before being added to the cell chamber. Cells were incubated in this transfection solution for 2-4 hours before the media was changed back to 10% FBS-DMEM. For the TnT biosensor, 1.5 μg smFLAG-KDM5B-15xBoxB-24xMS2 or smFLAG-KDM5B-24xMS2 plasmid plus 1.0 μg of either λN-EGFP-Ago2, λN-EGFP-β-gal, or EGFP-Ago2 plasmid were used. For sfGFP-H2B reporter assays, 2.5 μg plasmid was used.

Cell Imaging with the confocal microscope

Fixed-cell images were acquired on an Olympus (IX83) Inverted Spinning Disk Confocal Microscope with a cascade II EMCCD camera. The objectives used were the 40x oil-immersion (0.24 μm per pixel) and the 100x oil-immersion (0.096 μm per pixel). For smiFISH experiments, the 405 nm, 488 nm, 561 nm, and 647 nm lasers were used. Each location captured a 15 image Z-stack with a step size of 0.35 μm which was max-projected. For the sfGFP-H2B reporter assay, the 405 nm, 488 nm lasers were used. Each location captured a 15 image Z-stack with a step size of 0.35 μm which was max-projected.

Cell Imaging with the HILO microscope

All live-cell imaging was performed on a custom built widefield fluorescence microscope with a highly inclined thin illumination scheme (Tokunaga et al., 2008) described previously (Morisaki et al., 2016). Briefly, the microscope equips three solid-state laser lines (488, 561, and 637 nm from Vortran) for excitation, an objective lens

(60X, NA 1.49 oil immersion, Olympus), an emission image splitter (T660lpxr, ultra-flat imaging grade, Chroma), and two EMCCD cameras (iXon Ultra 888, Andor). Achromatic doublet lenses with 300 mm focal length (AC254-300-A-ML, Thorlabs) were used to focus images onto the camera chips instead of the regular 180 mm Olympus tube lens to satisfy Nyquist sampling (this lens combination produces 100X images with 130 nm/pixel). The far-red signal of mRNA visualized by JF646 HaloTag MCP was imaged on one camera, and the red signal of translation visualized by Cy3 α-FLAG-Fab and the green signal of GFP-tagged Ago2, β-gal, or α-HA Frankenbody were imaged on the other camera. A high-speed filter wheel (HS-625 HSFW TTL, Finger Lakes Instrumentation) was placed in front of the second camera to minimize the bleed-through between the red and the green signals (593/46 nm BrightLine for the red and 510/42 nm BrightLine for the green, Semrock). The focus was maintained throughout the experiments with the CRISP Autofocus System (CRISP-890, Applied Scientific Instrumentation). The Z-stack images were taken with a piezoelectric stage (PZU-2150, Applied Scientific Instrumentation). The laser emission, the camera integration, the piezoelectric stage movement, and the emission filter wheel position change were synchronized by an Arduino Mega board (Arduino). Image acquisition was performed using open source Micro-Manager software (version 1.4.22; Edelstein et al., 2010).

Live cells were placed into a stage-top environmental chamber at 37°C and 5% CO_2 (Okolab) to equilibrate for at least 30 minutes before image acquisition. Imaging size, exposure time, and the vertical shift speed was set to 512 x 512 pixels^2, 53.64 msec, and 1.13 microsec, respectively. This resulted in the imaging rate of 13 Hz (70 msec per image). To capture the whole thickness of the cytoplasm of U2OS cells, 13 Z-

stack of step size 500 nm were imaged such that the Z-position changed every 2 images (for the red and the green signals at each stack). This resulted in a maximal cellular imaging rate of 0.5 Hz (2 sec per volume). When needed, delays between volume captures were used to image at lower frame rates. For longterm single molecule tracking (**Figure 3.13**, **Figure 3.14**, described in **Figure 3.12**), photobleaching was minimized by imaging mRNA (JF646) every 10 seconds, while imaging tethering and translation (GFP and Cy3) every 100 seconds. Laser powers for all movies were: 15-20 mW for 637 nm, 9-20 mW for 488 nm and 5-15 mW for 561 nm with an ND10 neutral density filter at the beam expander.

TetraSpeck Fluorescent Microspheres (100 nm, ThermoFisher Scientific) mounted on a MatTek chamber were imaged at the end of each imaging session in order to correct for the slight shift in the alignment of the two cameras. These images of beads were used to generate a transformation matrix using either the GeometricTransformation function in Mathematica (Wolfram Research) or the ProjectiveTransform function in scikit-image in Python to correct for offsets in detected particle positions in each channel.

Co-Immunofluorescence and RNA smiFISH

Single-Molecule Inexpensive Fluorescent In Situ Hybridization (smiFISH) plus Immunofluorescence (IF) experiments were performed as previously described (LGC Biosearch Technologies, n.d.; Tsanov et al., 2016). Briefly, cells were transfected (as described in the “Bead loading and transfection” section). After 24 hours, cells were washed 3 times in PBS and fixed in 4% paraformaldehyde (Sigma Alrich) PBS for 20

minutes at 37°C. Cells were washed then permeabilized in 0.1 mM TritonX (Sigma Alrich) in PBS for 20 minutes.

Next, smiFISH was performed at room temperature unless otherwise specified. The smFISH hybridization and wash buffers were from Biosearch Technologies Stellaris buffers (SMF-HB1-10, SMF-WA1-60, and SMF-WB1-20) and used as stated in the Stellaris protocol for adherent cells. The probe hybridization was performed for ~12 hours at 37°C. The probe set for smFLAG (5') was designed using the open-source R script Oligostan (Tsanov et al., 2016), and the probe set for MS2 (3') was copied from (Tsanov et al., 2016).

Lastly, immunostaining was performed at room temperature unless otherwise specified. Cells were blocked with 1:4 diluted Blocking One-P (Nacalai Tesque) in PBS for 1 h, then stained with a 1:500 dilution of α-RCK antibody (MBL, PD009) in 1:4 diluted Blocking One-P for 1 h. Cells were washed for 30 minutes four times in 0.1% Tween-20 PBS, blocked as above for 1 h, then incubated in DyLight 405-AffiniPure F(ab')2 α-Rabbit antibody (Jackson ImmunoResearch) diluted 1:2000 in 1:4 diluted blocking buffer. Cells were washed for 30 minutes four times in 0.1% Tween-20 PBS and mounted in ProLong Diamond AntiFade Mountant (Thermo Fisher). Following these procedures, fixed cells were imaged as described in "Cell Imaging with the confocal microscope".

Live-cell nuclear reporter accumulation assay

For experiments in **Figure 3.5A,B**, cells were bead loaded with 0.5 μg of purified Cy3 α-FLAG Fab, 130 nm of purified HaloTag-2xMCP, 1.5 μg of the TnT biosensor

plasmid (smFLAG-KDM5B-15xBoxB-24xMS2) and 1.0 μg of either tetherable Ago2 (λN-EGFP-Ago2), tetherable β-gal (λN-EGFP-β-gal), or non-tetherable Ago2 (EGFP-Ago2), as described in the “Bead loading and transfection” section. The HaloTag was labeled for 15 minutes with JF646 HaloTag Ligand 1 hour after bead loading, after which cells were moved to the microscope stage-top incubator. At 4 hours post-bead loading, the microscope was programmed to visit multiple locations and take one full cell volume (13 Z-planes with a 0.5 μm step size) every 30 minutes. This continuous imaging was important to identify and exclude cells that died or divided, or moved away.

All videos were max-Z projected. Masks were hand-drawn on the 4 hour (early) and 16 hour (late) frames to isolate the nucleus and cytoplasm and used to measure the mean intensity of Cy3 α-FLAG Fab in these locations. Reporter accumulation in the nucleus was calculated:

$$Accumulation = \frac{I_{nuc}^{late}}{I_{nuc}^{early}} / \frac{I_{cyto}^{late}}{I_{cyto}^{early}} \quad (2)$$

where I_{nuc}^{early} and I_{cyto}^{early} were the measured intensity of the nucleus or cytoplasm, respectively, at the 4 hour time point, while I_{nuc}^{late} and I_{cyto}^{late} were the measured intensity of the nucleus or cytoplasm, respectively, at the 16 hour time point. Two of three experimental days were performed blinded.

Fixed-cell TnT nuclear reporter accumulation assay

For experiments in (**Figure 3.5C**), cells were transfected with the plasmid smFLAG-KDM5B-15xBoxB-24xMS2 and with either tetherable Ago2 (λN-EGFP-Ago2), tetherable β-gal (λN-EGFP-β-gal), or non-tetherable Ago2 (EGFP-Ago2), as described in the "Bead loading and transfection" section above. After 24 hours, cells were fixed in 4% paraformaldehyde-PBS for 20 minutes at 37°C then permeabilized in 0.1% TritonX100 for 20 minutes at 37°C.

Cells were blocked with 1:4 diluted Blocking One-P (Nacalai Tesque) in PBS for 1 h, then stained with 0.5 µg Cy3 α-FLAG Fab diluted to 100 µL in 1:4 diluted Blocking One-P. Cells were washed for 30 minutes four times in PBS and imaged directly, as described in the "Cell Imaging with the HILO microscope" section. Any images with multiple cells were cropped such that in the end each image showed a single cell, and a mask was hand-drawn around each cell. The mean Fab signal in the masked cell was measured per image. The imaging and analysis of all three experiments were performed blinded.

Fixed-cell miRNA target site reporter nuclear accumulation assay

For experiments in (**Figure 3.17**), cells were transfected with 2.5 ug of the plasmid sfGFP-H2B-MRE-POLR3G-3'UTR or sfGFP-H2B-mut-POLR3G-3'UTR, as described in the "Bead loading and transfection" section above. After 24 hours, cells were fixed in 4% paraformaldehyde-PBS for 20 minutes at 37°C then stained in 1:2000 diluted Hoechst 33232 (ThermoFisher) for 10 mins.

Image analysis was performed using custom code in Mathematica (Wolfram Research) to detect and measure the fluorescence intensities of all nuclei. Each background subtracted image in the Hoechst channel was binarized (using a sensible threshold) to create a nuclear mask. Using Mathematica's built-in function "ComponentMeasurements," nuclei that crossed the image edge were discarded, and masks were shape- and size-selected so that only whole, single nuclei were detected. The mask was applied to the 488 nm channel of the image and the total sfGFP fluorescence signal of each nucleus was measured. The imaging and analysis of all three experiments were performed blinded. All code is available on Github.

MRE-reporter assay

This experiment (**Figure 3.18, 3.19**) used a modified TnT reporter using endogenous MREs instead of BoxB tethering cassette. Using TargetScan (TargetScanHuman 7.2, n.d.), we chose a stretch of the POLR3G 3'UTR that had three miR-26-5p sites targeted by miRNA that are abundant in U2OS cells (Jerez et al., 2019). As a control (called the MUT reporter), we mutated two nucleotides in each miR-26-5p site, rendering them untargetable by Ago2 ((Mayr et al., 2007), plasmids are further described above in "Plasmid construction"). Each experiment used two cell chambers. Cells were loaded with the plasmids described below, along with 0.5 µg of Cy3 α-FLAG Fab, 0.5 µg of GFP-tagged α-HA Frankenbody, and 130 nm of HaloTag-2xMCP (further description of loading in the section "Bead Loading and transfection"). Each replicate experiment used one chamber loaded with 1 µg of smFLAG-KDM5B-MRE-POLR3G-3'UTR-24xMS2 and 1 µg of smHA-KDM5B-mut-POLR3G-3'UTR-

24xMS2 and a second chamber loaded with the reversed combination of smHA-KDM5B-MRE-POLR3G-3'UTR-24xMS2 plus 1 μg of smFLAG-KDM5B-mutPOLR3G-3'UTR-24xMS2. Both chambers were then imaged on our custom HILO microscope. For each cell, 20 frames (11-13 Z-stacks with a 0.5 μm vertical step size) were imaged at a 2 frames*s^{-1} frame rate. Two of the three experiments were performed blinded.

Puromycin translation inhibition assay

Puromycin assays (**Figure 3.1D**, **Figure 3.4**) were performed as previously described (Morisaki et al., 2016). Briefly, cells were bead loaded with the TnT components along with either tetherable Ago2 (λN-EGFP-Ago2), tetherable β-gal (λN-EGFP-β-gal), or non-tetherable Ago2 (EGFP-Ago2). While on the microscope, cells were treated with 50 μg/mL of puromycin. Cells were imaged continuously for 5 frames before and up to 60 frames aftertreatment at a rate of one full cell volume (11-13 Z-planes with a 0.5 μm step size) per 10 or 30 seconds. All mRNA foci colocalized with a Cy3 α-FLAG Fab translation signal were detected by hand and further categorized by colocalized tethering signal. The count of tethered/untethered, translating mRNA per cell were quantified per frame.

Single particle detection, tracking, and intensity measurement

Image processing was done in the software program Fiji (Schindelin et al., 2012) by Z-projecting each time frame of the 3-dimensional movie. These images were then analyzed using custom Mathematica code (Wolfram Research, available on GitHub) to detect single particles in a semi-automated fashion. Briefly, for each image the

background was masked by a hand-drawn outline of the cell and each image was binarized using a bandpass filter to highlight particles between 1 and 7 pixels in size (96 nm/pixel for the confocal, 130 nm/pixel for our custom HILO microscope). The mRNA channel was used to detect spots agnostic to tethering or translation status. Mathematica's built-in "ComponentsMeasurements" function was used to select and filter out larger aggregates from single particles and to categorize mRNA into groups based on the presence of detectable particles with signals above background in each channel. When needed, particles were tracked. Briefly, detected mRNA were linked to the closest mRNA in the next time frame, with a maximum step size of 10 pixels and a shortest track length of 5 frames. All detected particles and tracks were confirmed by hand when necessary.

To quantify particle intensities in each channel, intensities were local-background subtracted. This involved three steps using a 15 x 15 pixel crop (130 nm/pixel) of each detected particle: (1) the central signal was calculated as the mean intensity in a centered disc of diameter 3 pixels; (2) the background signal was quantified by measuring the median intensity in four 9-pixel quadrants in the corners of the 15 x 15 pixel crop; (3) The particle's signal intensity in each channel was computed by subtracting the background signal from the central signal. For fixed cell images using the confocal microscope (**Figure 3.10C,D**, **Figure 3.11**), steps 1 and 2 were modified such that the central disc was 5 pixels in diameter to accommodate larger P-bodies (96 nm/pixel), and the background was the mean intensity in an outer ring of diameter 15 pixels and width 2 pixels (96 nm/pixel).

For the long-term, single-molecule tracking experiments (**Figure 3.13**, **Figure 3.14**, described in **Figure 3.12**), intensity measurements were further refined to get the highest possible signal to noise. For this, we used custom Python code to do “best-Z” projections rather than max-Z projections. This was achieved using the positions of particles tracked in 2D to make a set of 3D crops around each detected particle at each timepoint. Each 3D crop had an XYZ dimension of 11 x 11 x 3 voxels, respectively, where each voxel had an XYZ dimension of 130 nm x 130 nm x 500 nm, respectively. In these 3D crops, the 3 chosen Z-slices were $Z_{best} \pm 1$ such that Z_{best} was the Z-slice having a maximal mean mRNA intensity inside a central disc of diameter 6 pixels (130 nm/pixel). Four steps were then used to quantify the signal intensities in each channel from individual 3D crops: (1) the 3 best Z slices were max-Z projected (3-frame moving averages of these best-Z projected crops are displayed in **Figure 3.13**, **Figure 3.14**; the only exception is **Figure 3.13A**, where every frame is shown); (2) the central signal was calculated as the mean intensity in a centered disc of diameter 6 pixels (130 nm/pixel); (3) The background signal was calculated as the mean intensity in a surrounding ring of diameter 10 pixels and width 1 pixel (130 nm/pixel); and (4) The signal intensity was computed by subtracting the background signal from the central signal. To aid in this analysis, each step was viewed using Napari (napari contributors, 2019). From the measured signal intensities, CSV files were generated and Seaborn (Waskom, 2020) was used to create scatter plots and intensity vs. time plots. All Python code for this analysis is available on Github.

Harringtonine ribosome runoff assay

To generate Harringtonine (HT) runoff curves, cells were bead loaded with the TnT components along with either tetherable Ago2 (λN-EGFP-Ago2), tetherable β-gal (λN-EGFP-β-gal), or non-tetherable Ago2 (EGFP-Ago2). While on the microscope, cells were treated with 3 μg/mL of Harringtonine (Cayman Chemical) to inhibit translation initiation (Huang, 1975). Cells were continuously imaged for 5 minutes before and 60 minutes after addition of HT, at a rate of one full cell volume (11-13 Z-planes with a 0.5 μm step size) per minute. For photobleach correction, a hand-drawn mask was used to find the mean, background subtracted whole-cell intensity through time (**Figure 3.16C**). The single exponential fit of the signal decay was calculated per channel and divided from single mRNA translation intensities through time. Images were preprocessed and all mRNA in cells were detected as described in the “Single particle detection, tracking, and intensity measurement” section. Intensities of particles in 3D were quantified using best-Z projections rather than max-Z projections. From these, we plotted the average single-molecule signals from single cells treated with HT through time (with the corresponding average best-Z projected crops shown above in **Figure 3.16A**). The average of the first four timepoints was used to normalize single-cell runoff curves so they began at a value of one.

Each runoff curve was fit to a biphasic model. In the model, a fraction f of ribosomes run off transcripts with an elongation rate v1 and the remaining fraction (1-f)run off transcripts with an elongation rate v2. The full model as a function of time t can be written as:

$$Runoff(f, v_1, v_2, t) = f \times I(v_1, t) + (1 - f) \times I(v_2, t) \quad (3)$$

Here I(v,t)describes a monophasic ribosome runoff curve in which all ribosomes are assumed to run off the transcript with an average elongation rate of v (Pichon et al., 2016):

$$I(v,t) = \begin{cases} 1 & t \leq 1 \\ \frac{1}{L_1+2\times L_2} \times \left\{ \left[1 - (\frac{v\times t}{L_1})^2 \right] \times L_1 + 2 \times L_2 \right\} & 0 < t < \frac{L_1}{v} \\ \left[1 - \frac{v}{L_2} \times (t - \frac{L_1}{v}) \right] \times \frac{2\times L_2}{L_1+2\times L_2} & \frac{L_1}{v} \leq t < \frac{L_1+L_2}{v} \\ 0 & t \geq \frac{L_1+L_2}{v} \end{cases} \quad (4)$$

where L1 is the length of the tagged portion of the ORF in our TnT reporter (336 AA) and L2 is the length of the untagged portion (1549 AA). After fitting, the runoff halftime $t_{1/2}$ was determined by setting the fitted runoff curve to 0.5. Fitting was performed with Python using the command scipy.optimize.curve_fit from SciPy. All code is available on Github.

Data availability

A collection containing the data used to generate figures is available in the public repository: “Datasets associated with ‘Imaging translational control by Argonaute with single-molecule resolution in live cells’". https://doi.org/10.6084/m9.figshare.c.5395800.v1 (Cialek, 2021). All other data

supporting the findings of this study are available from the corresponding author on request.

CHAPTER 4
Bead loading proteins and nucleic acids into adherent human cells

This chapter discusses the technique bead loading, which introduces proteins, plasmids, and particles into adherent mammalian cells. This cell loading technique is inexpensive, rapid, and does not substantially affect cell health. It is best suited for live-cell imaging. Here, we adapted bead loading to introduce and express plasmids. Further, we quantified efficiencies and variance for loaded proteins and expressed plasmids. This is useful for the TnT assay, which loaded all protein and plasmids simultaneously into the same cell using bead loading.[4]

4.1 How to introduce plasmids and proteins into cells

Loading macromolecules into mammalian cells necessitates methodology which allows them to croßss the cell's plasma membrane (Stewart et al., 2016). Several methods can introduce plasmids into mammalian cells through transfection, including liposomal transfection (Felgner et al., 1987) and DEAE-dextran transfection (Schenborn & Goiffon, 2000). However, methods for loading proteins or membrane-impermeable particles into cells are more limited.

Several techniques have bypassed this difficult hurdle using various strategies. First, microinjection delivers particles through a micropipette into cells live on a

[4]**Chapter 4** is based on a manuscript, currently under review, of which I was the first author (Cialek et al., 2021). Listed are author contributions: C.A.C. acquired/analyzed all data, did all experiments and analyses (except imaging HeLa and RPE1 cells in **Figure 4.4A**,**B**, contributed by M.N.S.), and made **Table 4.1**. A.L.K., C.A.C. M.N.S. and T.J.S. wrote the manuscript. G.G. and M.N.S. designed and created the figures. A.L.K., C.A.C., G.G., M.N.S. and T.J.S. edited the manuscript and figures. Dr. Phil Fox and Dr. Linda Forero gave valuable advice on bead loading different cell types.

microscope (Celis, 1984). While arguably the most controlled and least invasive method, this technique is relatively low throughput because cells must be loaded one-by-one. Further, microinjection requires specialized equipment and is technically demanding. Second, electroporation is a way to electro-inject proteins into cells via voltage-induced membrane disruption (Chakrabarti et al., 1989; Potter, 2003; Wilson et al., 1991). However, this method again requires specialized, expensive equipment and the shock can cause cell stress and mortality. Further, cells must be trypsinized before electroporation and subsequently replated, limiting the timeframe at which cells can be investigated post-electroporation. Third, cell membranes may be chemically modified for temporary reversible permeabilization (Fawell et al., 1994; Prior et al., 1992). Steptolysin-O (SLO) loading inserts an endotoxin into cell membranes which forms temporary pores, allowing exogenous membrane-impermeable particles, including proteins and DNA plasmids, to enter cells (Walev et al., 2001). After a 2 hour recovery, about half the cells repair these pores and halt internalizing particles from the solution. However, this technique requires a long recovery time and is incompatible with cell types that cannot tolerate endotoxins. Fourth, mechanical disruption loads particles into cells through physical perturbation of the cell membrane (Pitchiaya et al., 2012). This can be done in multiple ways, including scratching, scraping, and rolling beads atop cells (McNeil et al., 1984; Ortiz et al., 1987). As early as 1987, beads have been used to mechanically load proteins into cells (McNeil & Warder, 1987). More recently, we have optimized and adapted the bead loading technique beyond proteins to include loading of plasmids and RNA, as described here.

Bead loading is an easy, inexpensive, and fast method for loading protein and plasmids into adherent human cells. Glass beads are briefly rolled atop cells, temporarily disrupting their cellular membrane. This allows particles in solution to enter. Since bead loading has low efficiency, it is best suited for single-molecule or single-cell microscopy experiments. Bead loading can introduce a wide variety of proteins, including fragmented antibodies (Fab; Hayashi-Takanaka et al., 2011; Morisaki et al., 2016) purified proteins like scFvs (Tanenbaum et al., 2014), intrabodies (Jedlitzke & Mootz, 2021), or mRNA coat proteins like MCP (Coulon et al., 2014; Pichon et al., 2020). Plasmid expression vectors can also be added to the protein solution and bead loaded simultaneously (Koch et al., 2020; Moon, 2020; Moon et al., 2019). Beyond proteins and plasmids, molecules as large as 250 nm polystyrene beads have been introduced into cells via bead loading (personal correspondence). Bead loading is incredibly inexpensive, costing less than a penny per experiment in materials and requiring no additional expensive equipment. The cost is further reduced by minimizing the amount of probes used per experiment, since only the cells in the center 14 mm-diameter microwell of an imaging chamber are loaded. It should be noted that the limited loading area means that bead loading is not ideal for bulk-cell loading.

In this chapter, we demonstrate the bead loading process, including both how to construct the bead loading apparatus and how to perform an experiment (**Figure 4.1**). We show that proteins, RNA, and DNA can be loaded into various cell types. Further, we demonstrate both by representative images and quantification that two different proteins simultaneously bead loaded have highly correlated cellular concentrations and relatively low variance. We discuss variations in the protocol based on cell type and

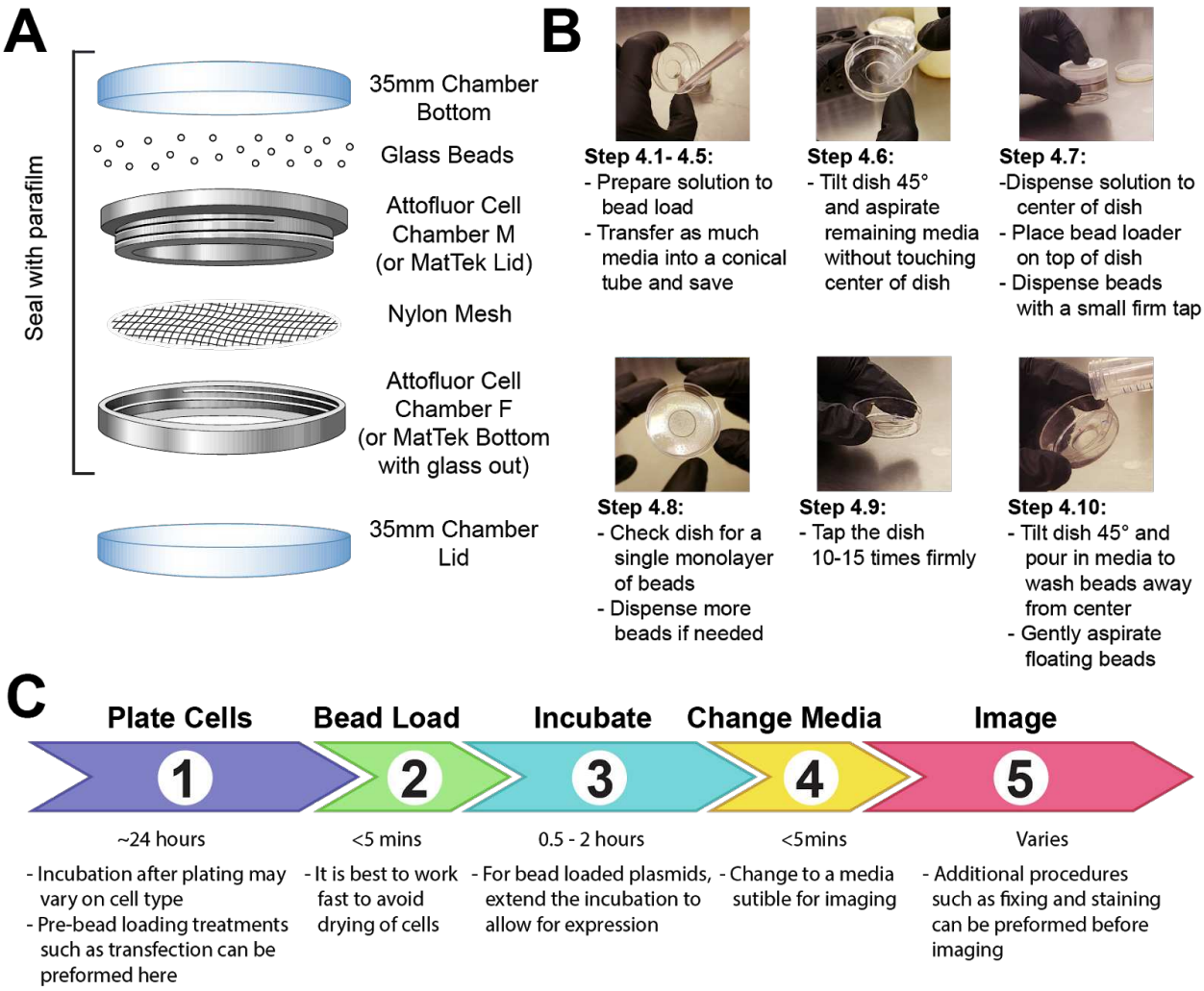

Figure 4.1. Bead loading apparatus, technique, and timeline.[5]

loading of protein, plasmid or RNA. Though beads are thought to perforate and disrupt the cell membrane, when performed properly, the bead loading process dislodges only a small number of cells from the bottom of the imaging chamber and after a short

[5] G.G. designed and created the figure. C.A.C. and G.G. took the images in **B.**

recovery period cells continue to grow and divide. This methodology is ideal for live-cell microscopy experiments, including single-molecule protein and RNA tracking, post-translational modification detection, observation of dynamic cellular mechanisms, or subcellular localization monitoring (Forero-Quintero et al., 2020; Hayashi-Takanaka et al., 2011; Koch et al., 2020; Lyon et al., 2019; Morisaki et al., 2016).

4.2 Bead loading proteins and plasmids into adherent human cells

The most common application of bead loading is to introduce one or more types of protein into adherent human cells. To illustrate this, we bead loaded cells with a solution of a Cy3- and Alexa488-conjugated Fab protein. Though not every cell in the microwell was bead loaded, the cells that were loaded almost always had both Cy3- and Alexa488-labeled proteins together (**Figure 4.2A**). According to an earlier estimate, when 1 µL of 0.5 mg/mL (~2.5 µM) Fab is bead loaded (Hayashi-Takanaka et al., 2009), as in **Figure 4.2A**, each cell is loaded with roughly a million Fab molecules.

Plasmid DNA encoding GFP (1 µg of plasmid DNA, 1.8 microliters of 557 ng/µl) added with 0.5 µg Cy3-labeled protein was also introduced into cells via bead loading and subsequently expressed and visualized (**Figure 4.2B**). The GFP fluorescence represented that the GFP-encoded plasmid was not only loaded into cells but also expressed. Thus, in the same cell, bead loading can introduce a protein probe (like Cy3-labeled Fab) and reporter plasmid (like GFP), as performed in our lab previously (Koch et al., 2020; Moon, 2020; Moon et al., 2019). We quantified 40% of cells were bead loaded with Fab protein and 21% of the bead-loaded cells expressed the co-loaded plasmid, as shown in the representative fields-of-view in **Figure 4.2B**. We typically load

each chamber with 1-2 μg of plasmid, approximately the same amount as lipofections. Bead-loaded cells express widely varying levels of plasmids (**Figure 4.2C,D**). To specifically measure this, we used the Fisher Ratio test to compare the distributions of protein and plasmid intensity data. We found that though the protein 1 and 2 had similar intensity distributions to one another ($p = \sim 1$) each protein had a significantly smaller distribution than the plasmid ($p = 3.2e-6$ and $1.8e-5$). Though this could be from variability in how many plasmids are loaded per cell, we suspect that the greater source of variability comes from the many steps required for plasmid expression -- including being imported into the cell nucleus, transcription, and translation -- that are likely to vary greatly between cells. In contrast, the levels of bead-loaded proteins had little cell-to-cell variance, and the levels of two simultaneously loaded proteins highly correlated with each other (**Figure 4.2C-E**). Plasmid expression can be seen as early as 2-4 hours post bead loading but may occur later depending on when optimal plasmid expression is obtained. We recommend performing a time course to determine the best window of expression for a specific plasmid spanning 2-24 hours post bead loading. This can be done in one chamber with long timeframe imaging or by bead loading and staggering multiple chambers.

4.3 Bead loading and cell health

Bead-loaded cells remain adherent and are healthy enough to grow and divide. Bead-loaded human U2OS cells were imaged directly before, directly after, and 24 hours after bead loading. Proper bead loading had almost no noticeable effect on the number of cells or their morphology, as shown in this representative field of view (**Figure 4.3A**, left, middle). In contrast, poor bead loading with too many beads and

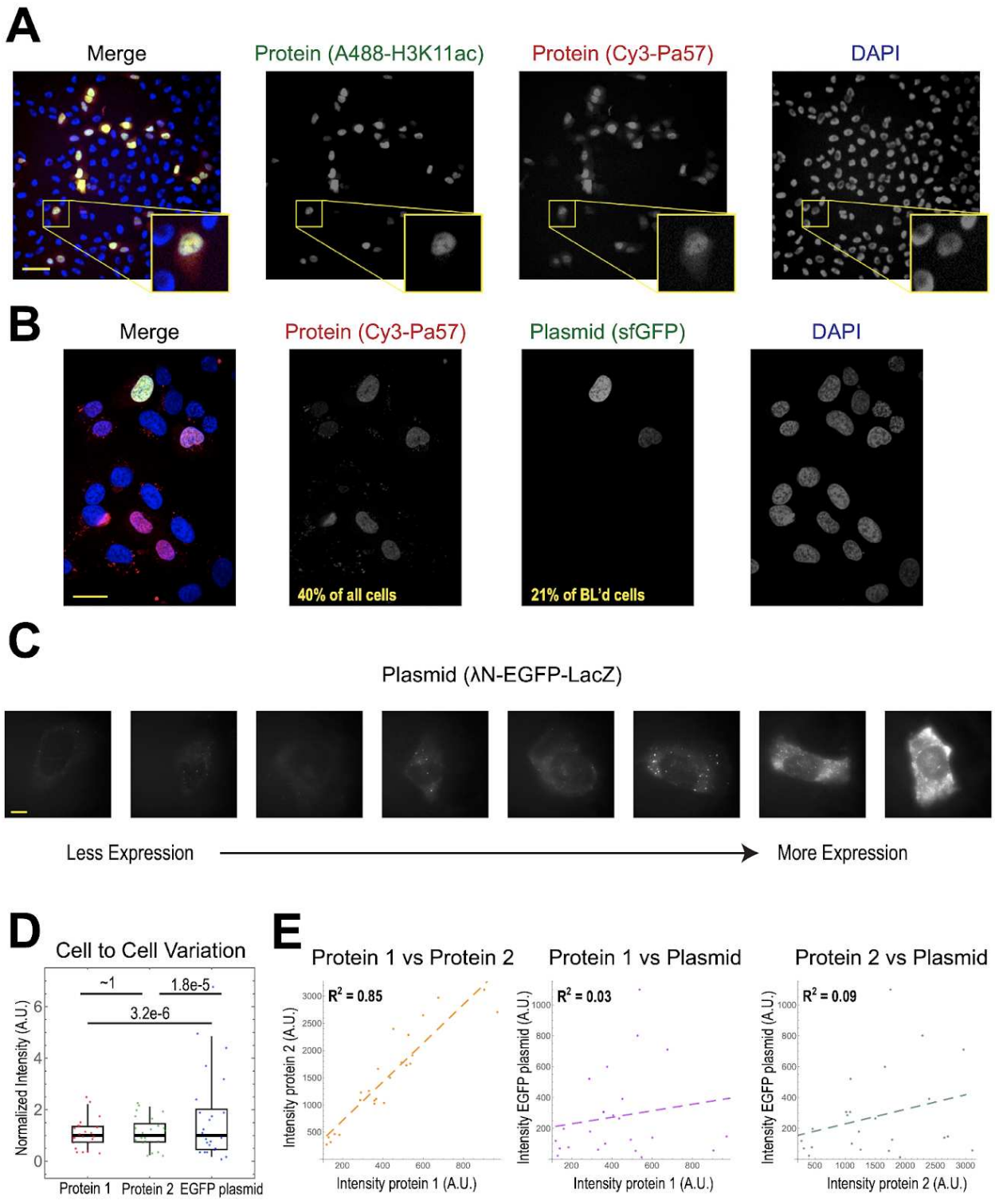

Figure 4.2. Bead loading introduces low variability in protein concentration but high variability in plasmid expression. (Legend on next page)

Figure 4.2. Bead loading introduces low variability in protein concentration but high variability in plasmid expression.[6]

A Cells were bead loaded with 0.5 µg of each of the proteins Alexa488-conjugated anti-H3K27Acetyl Fab (green) and Cy3-conjugated anti-RNAPII-Serine5phosphorylation Fab (red) in 4 µL of bead loading solution. Cells were DAPI-stained (blue) then live-imaged immediately. Scale bar measures 20 µm.

B Cells were bead loaded with 0.5 µg of Fab protein (Cy3-conjugated anti-RNAPII-Serine5phosphorylation, red) and 1 µg of plasmid encoding superfoldGFP-H2B (green) in 4 µL of bead loading solution. After 24 hours, cells were DAPI-stained (blue) and imaged live. Scale bar measures 30 µm.

C-E Protein 1 (JF646-HaloLigand-labeled HaloTag-MCP), protein 2 (Cy3-conjugated anti-FLAG Fab) and a plasmid encoding EGFP (λN-EGFP-LacZ) were bead loaded together into cells. The total intensity in each fluorescent channel was measured in a 1.3 x 1.3 µm patch in the cytoplasm of each cell. N = 25 cells.

C Representative cells expressing the bead loaded plasmid, λN-EGFP-LacZ. The same imaging conditions and intensities were used for all cells. Spots are aggregates of the expressed protein. Scale bar measures 10 µm.

D The chart shows each cell's total intensity of either protein 1, protein 2, or EGFP expressed from the plasmid. Each channel was normalized to the median. Bonferroni-corrected P values were calculated by the Fisher Ratio test, comparing if the distribution of protein or plasmid intensity data has the same variability. Each point represents a cell.

E The total intensities for either both proteins, protein 1 and the plasmid, or protein 2 and the plasmid are plotted against each other. Calculated R2 values are displayed. Each point represents a cell.

excessive tapping force is depicted in **Figure 4.3B**. This caused much cell loss (large patches of the coverglass without cells and detached, floating, out-of-focus cells), poor cell morphology (cells appearing rounded up and poorly adhered), and clusters of beads remaining on the coverglass after bead loading. Though cells are thought to undergo mechanical damage during bead loading, cells grew and proliferated in the properly

[6] G.G. and C.A.C designed the figure, and G.G. created the figure. C.A.C. acquired data, made graphs, and performed the analysis.

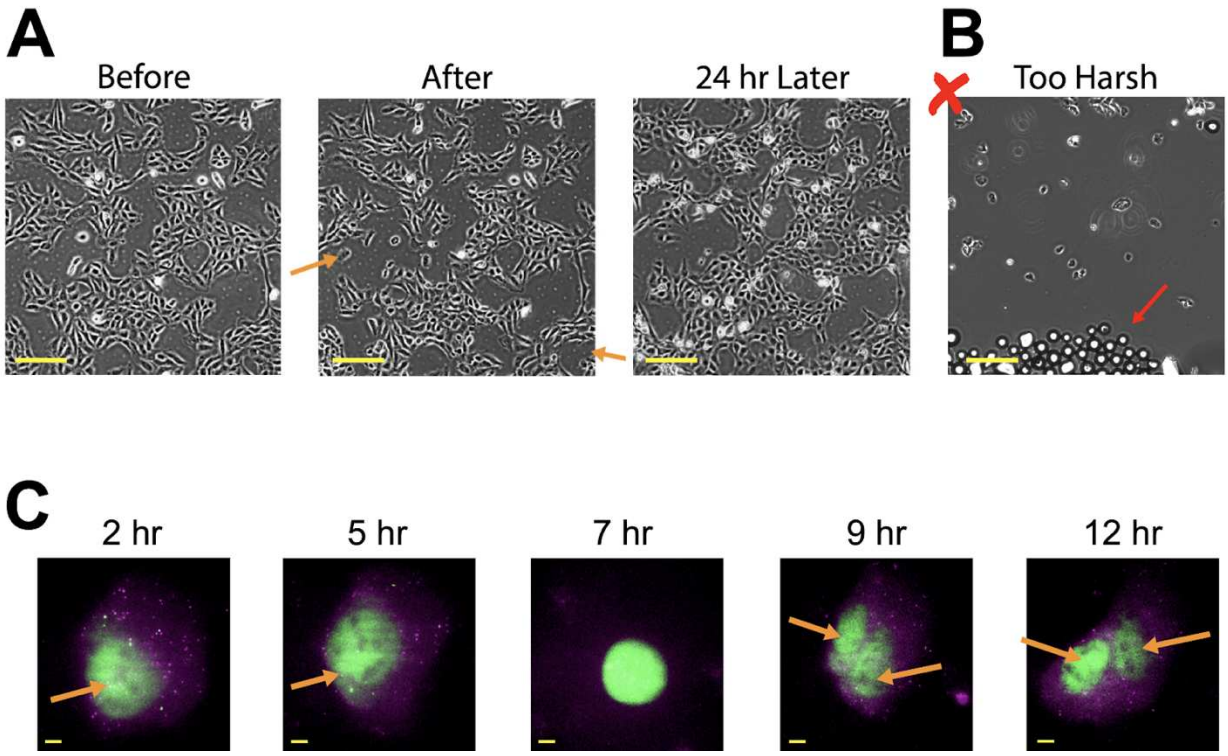

Figure 4.3. Bead loaded cells remain adherent and are healthy enough to grow and divide.[7]

A U2OS cells were bead loaded with 0.5 µg of Cy3 conjugated anti-FLAG Fab in 4 µL of bead loading solution. The cells were imaged directly before, directly after bead loading, and 24 h after bead loading. Orange arrows identify areas where cells peeled off during bead loading. Scale bar measures 2 mm.

B Representative image of U2OS cells bead loaded with components from A but with harsh tapping and too many beads. The red arrow identifies extra glass beads. Scale bar measures 2 mm.

C U2OS cells were loaded with 1.5 µg of the 14.4 kbp plasmid smFLAG-KDM5B-15xBoxB-24xMS2, 0.5 µg of Cy3 conjugated anti-FLAG Fab (green), 130 ng HaloTag-MCP (magenta) in 8 µL of bead loading solution. Directly before imaging, the HaloTag was stained with JF646-HaloLigand. The MS2 stem loops of the mRNA transcribed from the reporter plasmid are labeled by MCP (magenta spots), and FLAG-tagged translated reporter protein is labeled via anti-FLAG Fab (green colocalization to mRNA). Mature Fab-labeled protein localizes to the nucleus. This cell was imaged 4-15 hours after bead loading. Yellow arrows identify the cell nucleus before and nuclei after cell division. Scale bar measures 5 µm.

[7] This figure was designed by G.G. and C.A.C. and created by G.G. C.A.C. acquired data.

bead loaded chamber, as evidenced by the increased number of cells 24 hours after bead loading (**Figure 4.3A, right**). The magnitude of the effect to cell viability can be assessed through a variety of assays, such as a MTT assay, to compare bead-loaded to mock loaded cells (Kumar et al., 2018). Further, we show here and previously that the bead loaded cells, themselves, undergo cell divisions (**Figure 4.3C**) and the timing of mitosis was not affected by bead loading (Stasevich et al., 2014), which serves as further evidence to sustained cell health after bead loading.

4.4 Loading different cell types and materials via bead loading

Bead loading is a versatile technique, accommodating several types of adherent cell lines and various types of macromolecules. We demonstrate this variety by loading RPE1 and HeLa cell lines with Fab (**Figure 4.4A,B**). **Table 4.1** provides further examples of bead loading in different cell lines, in our lab and beyond, and points out some of the

nuanced differences between bead loading protocols from other labs. Of note, the diameter of glass beads used for loading varies greatly between labs, though most efficient loading was found for small, 75 μm diameter beads in several cell lines (McNeil & Warder, 1987). Further, our lab has begun bead loading RNA as well (currently unpublished). **Figure 4.4C** displays a representative U2OS cell bead-loaded with a Cy5-RNA 9mer and Cy3-DNA 28mer together.

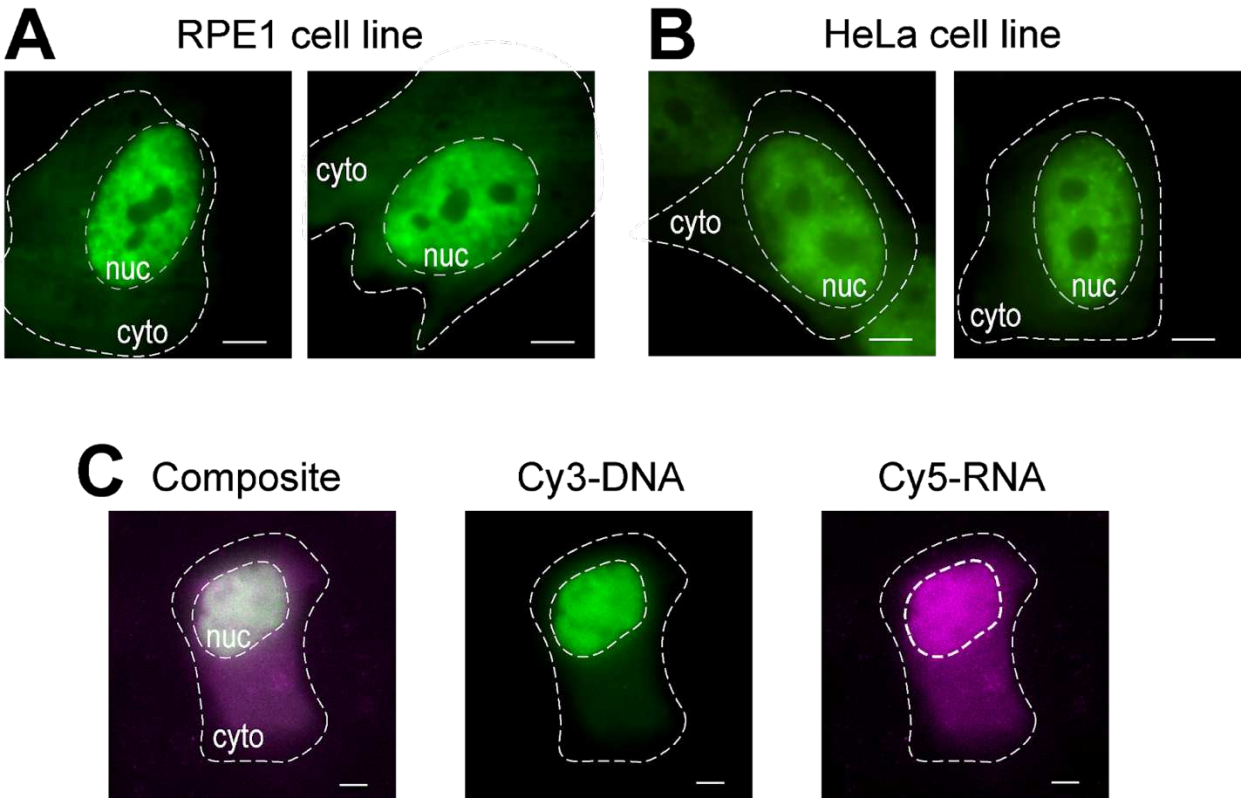

Figure 4.4. Variations in cell type loading material of the bead loading protocol.
A-B RPE1 (A) and HeLa (B) cells were bead loaded with 1.5 µg of a nuclear Fab protein (anti-RNAPII-Serine5-phosphorylation) in a 4 µL loading solution. Each cell's nucleus (nuc) and cytoplasm (cyto) are marked. Cells were imaged 6 hours after being bead loaded. Scale bars measure 5 µm.
C Human U2OS cells were bead loaded with both Cy5-RNA 9mer (magenta) and Cy3-DNA 28mer (green) oligos, 10 picomoles of each, in 4 µL bead loading solution. Cells were imaged 4 hours after being bead loaded. All cell nuclei are highlighted by a dashed line. The cell's nucleus (nuc) and cytoplasm (cyto) are marked. Scale bar measures 5 µm.[8]

[8] M.N.S., C.C. and G.G. designed and created the figure. M.N.S. acquired the data in **A** and **B**. C.A.C. acquired the data in **C**.

4.5 Bead loading of live, adherent cells is inexpensive and versatile

The bead loading technique described here is a cost-effective and time-efficient method for introducing macromolecules and other types of particles into adherent cells. This versatile process can load protein (**Figure 4.2A**; Forero-Quintero et al., 2020; Hayashi-Takanaka et al., 2011; Lyon et al., 2019; Morisaki et al., 2016), a combination of protein and plasmids (**Figure 4.2B-E**; Koch et al., 2020), RNA (**Figure 4.4C**), 100 and 250 nm polystyrene beads (Ashok Prasad lab, unpublished), synthetic dyes (Jones et al., 2011) or quantum dots (Sabri, 2020; Emerson et al., 2014). Bead loading may have the capability to load other types of membrane-impermeable particles as well. Its most-used application is for loading antibodies or Fabs to target endogenous epitopes, like post-translational modifications (PTMs), in live cells. Targets like PTMs are often difficult to label in live cells without established PTM-specific genetically encoded tags, such as a mintbodies (Sato et al., 2013, 2018). In contrast, bead loading can introduce multiple types of probes, reporters, or other molecular tools together into the same cell for monitoring multiple readouts simultaneously. We anticipate that bead loading will be a useful technique for loading a variety of macromolecules or particles.

A major advantage of bead loading is the low cost: each experiment costs less than a penny. A bead loader apparatus can be made easily using inexpensive materials costing in total about $150, which is significantly less expensive than any other cell loading method. The cost of a bead loader apparatus can be further reduced to under $10 by replacing the metal reusable chamber with a plastic one. For this, either drill a hole in a 35 mm chamber or remove the glass from a 35 mm glass-bottom chamber, then securely fasten the mesh in place with tape. In lieu of an apparatus, bead loading

can even be performed using a wide-bore p-1000 pipette tip to scoop and sprinkle beads onto cells, though this variation adds variability in the size and number of beads.

A major benefit of bead loading is that cells retain normal overall morphology, recover rapidly, and continue to grow and divide for the U2OS, RPE1, and HeLa cells studied here and other cell lines studied elsewhere (**Figure 4.3**, **Figure 4.4A,B**, **Table 4.1**; Stasevich et al., 2014). During bead loading, cells undergo physical stress and sometimes dislodge and peel (~5% of cells peel under optimal conditions, but greater cell loss can happen if bead loading is performed too forcefully or too many glass beads are loaded atop the cells, depicted in **Figure 4.3B**). However, cells appear healthy and can be imaged as soon as 30 minutes after bead loading (**Figure 4.3A**). We generally give cells a 30-minute recovery period but anticipate that imaging sooner post-bead loading is feasible. A major drawback of this technique is that the cells need to be capable of withstanding minor physical stress during loading and remain securely adhered to the coverslip. Poorly/non-adherent cell lines or cells grown on coated plates (e.g. HEK and stem cells) detach upon the gentle tapping during bead loading. Further, in our experience, primary neurons are too sensitive for bead loading.

Bead loading is best for single-cell or single-molecule experiments due to its low efficiency. In our experience, bead loading demonstrated around 20-40% protein loading efficiency, and about 20% of the bead loaded cells also expressed a co-loaded plasmid (**Figure 4.2A,B**). We speculate that bead loaded plasmids had low efficiency because plasmids must not only enter cells but also be expressed. Increasing the amount of plasmid in the bead loading solution may increase how many cells express the plasmid, yet also could increase the level of expression per transfected cell and

cause overexpression. The low efficiency of bead loaded plasmid expression can be circumvented by using alternative transfection protocols, such as lipofection, prior to bead loading the proteins or probes (Lyon et al., 2019; Morisaki et al., 2016). Additionally, we noticed that incubating cells in optimal media for 30 minutes before bead loading may assist plasmid expression. Due to low plasmid expression, we do not use bead loading as an alternative method to lipofection exogenous expression. However, for cells that are unresponsive or intolerant to lipofection, bead loading may provide an alternate, albeit low-efficiency, method for transient plasmid expression.

4.6 Protocol

1. Clean, sterilize and dry glass beads so that they do not clump and can spread evenly atop cells.

   1.1 Sterilize approximately 5 mL glass beads in NaOH. Measure the beads in a 50 mL conical tube. Add 25 mL of 2 M NaOH and mix gently using a shaker or rotator for 2 hours.

   1.2 Decant the NaOH, retaining as many beads as possible. If the beads are in suspension, spin down the tube of beads briefly in a centrifuge (1 minute at ~1000 rcf).

   1.3 Wash the beads thoroughly with cell culture-grade water until the pH is neutral (use pH test strip on the eluent to confirm a neutral pH). Decant the wash water each time, as before.

   1.4 Wash the beads thoroughly with 100% ethanol 2-3 times. Decant the ethanol each time, as before.

   1.5 Dry the beads. Sprinkle the beads to form a thin layer inside a sterile container (such as a 10 cm petri dish). Leaving the container open, let the beads air dry in a biosafety cabinet overnight. Ensure that the beads are completely dry by tapping or gently shaking the container and checking that the beads have a sandy texture with no clumping or flaking.

   1.6 UV-sterilize the dry beads for 15 minutes.

2. Assemble the bead loader apparatus.

   2.1 Fasten a patch of mesh (polypropylene or equivalent material, 105 μm openings to allow beads to pass through) to cover the entire opening of the beads holding chamber with either tape or clamping the mesh between male and female ends of a metal reusable imaging chamber (**Figure 4.1A**).

   2.3 UV-sterilize the apparatus for 15 minutes.

   2.4 Add beads to the apparatus and seal tightly with parafilm.

   NOTE: It is essential that the beads are completely clean and dry at this step. They should be loose and look sandy with no clumps. If they do not appear so, re-wash and completely dry the beads.

   2.5 Store the apparatus in a sealed, dry container desiccated by silica gel or other desiccant medium. If the beads become damp, which will be apparent by bead clumping, thoroughly dry and sterilize the bead loader and replace with fresh beads. This will prevent any mold or bacteria from growing on or around the beads within the bead loader.

   NOTE: *The bead loader apparatus can be made in different ways. See details in* ***Chapter 4.5***.

3. Prepare glass-bottom chambers of adherent cells

   3.1 Seed adherent mammalian cells onto a 35 mm glass-bottom chamber. Ensure cells are approximately 80% confluent at the time of bead loading. (See **Table 4.1** for more information on various cell types and notes on the effectiveness of bead loading in different cell types.)

   NOTE: Cells can be seeded in only the microwell in the center of the chamber to conserve how many cells are used.

   3.2 Incubate the cells under normal conditions until they are completely adhered to the glass.

   NOTE: It is essential that cell density is high enough and that the cells are securely adhered to the glass. If these requirements are not met, cells will likely peel off during bead loading. The timeline between cell seeding and bead loading can be lengthened to ensure proper cell adhesion and confluency.

4. Bead loading cells

   Optional: Wash cells briefly with PBS then add 2 mL optimal media. Incubate for at least 30 m.

4.1 Make a solution of 3-8 µL containing desired plasmids, protein, and/or particles. Use ~1 µg (0.1 - 1 pmol) of each type of plasmid and ~0.5 µg (0.01 nmol) protein, depending on experimental requirements. Use a low-retention tube for proteins so that they are not left behind on tube walls. Bring the solution up to a minimum of 3 µL with PBS. Adjust solution volume as necessary to coat the entire area of cells to be loaded (i.e. chamber's microwell, **Figure 4.1B**).

4.2 Mix the solution thoroughly by pipetting up and down and/or flicking the tube.

4.3 Briefly spin the solution down to the bottom of the tube in a tabletop microfuge.

4.4 Move bead loading solution and chamber of cells into a tissue culture hood. Perform the remaining steps in the tissue culture hood using sterile technique.

4.5 Remove media from cells and temporarily store it in a sterile tube.

4.6 Gently suck off all media from around the edges of the chamber. Tilt the chamber at approximately a 45° angle and suck off the remaining drop of media in the center microwell. During media removal, make sure not to let the pipette tip touch the glass, which may result in cell peeling and loss. Move quickly to the next step so that the cells are not dry for long.

4.7 Gently pipette the bead loading solution onto the glass microwell in the center of the chamber.

Optional: Incubate with gentle rocking for ~30 seconds, without allowing the chamber to dry up completely.

4.8 Gently disperse a monolayer of glass beads on top of the cells, preferably using a bead loading apparatus (**Figure 4.1A**). The beads should cover the cells in the glass-bottom microwell completely.

4.9 Pinching the chamber with two fingers, tap it against the hood surface by lifting it ~2 inches and bringing it down firmly. Use a force approximately equivalent to dropping the dish from that height. Repeat for ~10 taps total.

Note: Ensure that taps do not substantially peel the cells. Tapping can be optimized for cell type. If cells load poorly, tap harder, but if many cells peel off, tap more lightly.

4.10 Gently add media back into the chamber by pipetting slowly onto the plastic side of the chamber. Try to suck off any floating beads without disturbing cells. Add more pre-warmed media at this step if too much was removed.

4.11 Incubate cells for 0.5 - 2 hours in the incubator.

4.12 UV-sterilize the bead loader for 15 minutes before returning it to storage under desiccating conditions.

4.13 Add dye (e.g. DAPI or HaloTag ligand stain, if required by experiment) as per manufacturer's recommended protocol.

4.14 Wash the cells 3 times with media before imaging to remove beads and excess loading components in solution. Avoid pipetting directly onto cells to keep them from peeling.

5. Imaging the bead loaded cells

5.1 Image the cells immediately or when required by the experiment. Use a microscope capable of capturing fluorescence (lasers or monochromatic light source). Ensure that the excitation wavelengths are appropriate for the chosen fluorophore or dye (e.g. 488 nm wavelength light for GFP).

*Note: Bead loaded proteins may be imaged once the cells have recovered (as soon as 30 minutes post loading for the cell lines described here). Plasmid expression takes 2 or more hours depending on expression vector elements (**Figure 4.1C**, and further explanation in the **Chapter 4.5**).*

Note: Imaging of bead-loaded cells can be performed on any microscope equipped with the appropriate fluorescent sources associated with loaded probes, a camera capable of capturing fluorescence images, such as an EMCCD or sCMOS camera, and an incubator to control temperature, humidity and carbon dioxide. A guide to fluorescence microscopy can be found here: (*Introduction to Fluorescence Microscopy | Protocol*, n.d.).

Table 4.1. Bead loading in different cell lines. For the cell lines not yet bead loaded in our lab, references and notes on variations in the protocol are provided.[9]

Cell line	Cell type	Bead loading effectiveness	Notes/reference
Stem cells (human)	Embryonic stem cells	Difficult	*Many cells peel off during bead loading if plated on gelatin-coated plates
HEK 293	Human embryonic kidney cells	Difficult	*Need to lay down a gel matrix to imaging chamber surface before beadloading. Tap gently when beadloading at first.
Neurons (rat)	Primary embryonic neurons (e-18), dissociated	Very inefficient	*We were unable to efficiently bead load neurons using our standard bead loading protocol. This could be due to the non-adherent nature of neurons or from consequent damage to neural processes.
MDCK (canine)	Madin-Darby canine kidney cells	See McNeil and Warder (1987)	*Low efficiency bead loading in (McNeil & Warder, 1987)
U2OS (human)	Osteosarcoma	Standard bead loading protocol	
HeLa (human)	Cervical cancer	Standard bead loading protocol	
RPE1 (human)	Epithelial cells immortalized with hTERT	Standard bead loading protocol	
HFF (human)	Primary foreskin fibroblasts	See Besteiro *et al.* (2009)	*Modified protocol of tilting instead of tapping in (Besteiro et al., 2009)
BALB/c 3T3, NIH 3T3, and Swiss 3T3 (mouse)	Embryonic fibroblasts	See Gilmore and Romer (1996), Emerson *et al*. (2014) and McNeil and Warder (1987)	*425-600-μm glass beads reported in (Gilmore & Romer, 1996) *Used 200–300 μm glass beads reported in (Emerson et al., 2014)

[9] C.A.C. created **Table 4.1**.

			*75 um glass beads bad better results than 400 µm in (McNeil & Warder, 1987)
DM (Indian muntjac)	Skin fibroblasts	See Manders, Kimura and Cook (1999)	
CHO (hamster)	Epithelial-like ovary cells	See Memedula and Belmont (2003)	*Used 425-600-µm glass beads in (Memedula & Belmont, 2003)
BAE (bovine)	Bovine aortic endothelial cells (BAEC-11)	See McNeil and Warder (1987)	*75 um glass beads bad better results than 400 µm in (McNeil & Warder, 1987)
PtK-2 (Potomus tridaclylis)	Epithelial kidney cells	See McNeil and Warder (1987)	*75 um glass beads bad better results than 400 µm in (McNeil & Warder, 1987)
HUVEC (human)	Umbilical vein endothelial cells	See Gilmore and Romer (1996)	*Used 425-600 µm glass beads in (Gilmore & Romer, 1996)
J774 and J774.2 (mouse)	monocyte macrophage cells	See Becker *et al.* (2005) and McNeil and Warder (1987)	*Gentle agitation (instead of tapping) and 425-600-µm glass beads reported in (Becker et al., 2005)
MS-5 (mouse)	bone marrow stromal cells	See Molenaar et al. (2003)	
WPE1-NB11 (human)	prostate epithelial cells	See Gilmore and Romer (1996) and Emerson *et al.* (2014)	*Used 425-600-µm glass beads in (Gilmore & Romer, 1996) *Used 200–300 µm glass beads reported in (Emerson et al., 2014)

CHAPTER 5
Discussion and future directions

This section discusses the meaning impact and big picture of the results obtained throughout this document. First, the results are related and woven into a story of what was learned about Ago2-mediated silencing using the TnT. Next, the broader impacts to the NCT field are suggested. Lastly, this section speculates at the future development and purpose of NCT to the field of translation control.[10]

5.1 Adapting Nascent Chain Tracking for studying translation control at the live-cell, single-mRNA level

The more we learn about translation control, the more we discover specific, nuanced regulatory mechanisms that are key to maintaining healthy gene expression (Hershey et al., 2019). Though informative, the median outcome of millions of cells in a bulk-cell assay does not always describe how the individual events of a mechanism take place. For the whole picture, assays at the single-cell and single-molecule levels can compliment those at the bulk-cell level to describe the precise timeline of individual events and heterogeneity in individual cell or molecule responses. Nascent Chain Tracking (NCT; **Figure 2.1**) can resolve precisely when, where, and to what degree single mRNA are translated in living cells, making it ideally suited to address questions of heterogeneity and stochasticity in translation control.

[10]This chapter includes short excerpts and ideas from the following two manuscripts: (Cialek et al., 2020), of which I was a co-first author with A.L.K, with writing contributions from A.L.K., C.A.C. and T.J.S.; and (Cialek et al. 2021, currently under review), of which I am the first author, with discussion section writing contributions from C.A.C., T.A.M. and T.J.S.

As the breadth of recent applications indicates, NCT is a rapidly maturing technology that is now beginning to shed light on traditionally hard-to-see aspects of translational control (**Figure 2.2**). Since this assay can visualize differences between single mRNA, we anticipate that it will be a key assay in measuring specific impacts of translation control to single mRNA. In the future we anticipate NCT will be used to clarify the how various post-transcriptional mRNA modifications (Hoernes et al., 2016; Simms et al., 2014), subcellular localization and higher-order structure (Babendure et al., 2006; Buxbaum et al., 2015; Jung et al., 2014; Wen et al., 2008), and bound regulatory factors (Simsek & Barna, 2017; Wu et al., 2015) -- all impact translational control.

Many recent improvements have aided and expanded the breadth of applications of NCT. Here, we present Translation and Tethering (TnT) assay, methodology which builds upon NCT to study a specific regulatory factor (**Chapter 3**). Further, we have adapted a cell loading technique, bead loading, into a method for loading both proteins and reporter plasmids (**Chapter 4**). We hope these technologies will contribute to the design and application of future NCT-based studies.

To fully exploit NCT and better decipher translational regulatory mechanisms, it will be important to combine it with other technologies. For example, combining NCT with a depletion assay like siRNA knockdown, could be a valuable method of studying a specific factor's contribution to translation control. A large portion of what we know about molecular mechanisms comes from knockdown and knockout assays, which study how the mechanism changes in the absence of a specific factor. This line of thought was used, for example, to distinguish translation initiation from the Cap Binding Complex (CBC) from the initiation factor eIF4E. The study overexpressed the factor

hyper-active 4E-BP1, which greatly reduced the activity of eIF4E and allowed for isolating CBC-initiated translation events (further discussed in **Chapter 2**; Hoek et al., 2019). Beyond this eIF4E-specific study, we have not yet seen NCT combined with knockdown or knockout assays, which would have the advantage of being more versatile than hyper-active 4E-BP1 overexpression. Combining NCT with a CRISPR knockout, siRNA knockdown, temporally-controlled degradation such as Auxin Inducible Degron, or sequestration from chemicals (e.g. rapamycin) or light (e.g. optogenetics) induced tethering will open the door to studying contributions of translation control factors at the single-mRNA level.

To address this, the TnT assay developed in **Chapter 3** offers a similar solution from the opposite approach. Instead of applying a bulk-cell knockdown, knockout, or sequestration assay, the TnT assay instead allows for studying the impacts of a specific factor recruited to single mRNA.

NCT-based assays studying canonical translation require marking translation sites in two fluorescent colors, one for detecting mRNA and another for translation (**Figure 2.1**). The TnT assay introduced a specific translational regulatory factor tagged in a third color for visualizing and monitoring its direct impact on translation dynamics. This was achieved by tethering the factor to a reporter TnT biosensor, which allowed for directly visualizing its perturbative effect on the biosensor's translation.

There are several benefits to using a tethering-based strategy to selectively recruit a factor to an mRNA. First, a single-molecule based tethering strategy allows for comparing tethered and untethered mRNA in the same cell. Tracking an mRNA over time can monitor impacts to translation before and after being tethered. These

advantages serve as built-in controls to correct for cell-to-cell or mRNA-to-mRNA heterogeneity. Further, since recruitment by tethering is specific to reporter mRNA, the endogenous mRNA population is left unaffected. Thus, a tethering strategy does not suffer from secondary effects that come from whole-cell strategies. For example, removing a key or essential factor from a cell can dramatically affect general translation and mRNA localization, induce cell stress, and risk causing an environment not suitable for collecting canonical translation information. For example, inactivating eIF4E by hyper-active 4E-BP1, as mentioned above, most likely caused whole-cell changes in the translation landscape since global canonical translation becomes blocked.

Thus, we offer the TnT assay as methodology to circumvent this problem and study a specific factor in a natural way.

5.2 Development and impact of the TnT assay

The Translation and Tethering (TnT) biosensor reported here allows for direct visualization of specific regulatory factors and quantification of their impact on translation at individual mRNA molecules in living cells. The innovation of the TnT biosensor builds off of Nascent Chain Tracking technology, adding an independent tethering cassette composed of repeat BoxB stem loops in the 3' UTR of the biosensor (Baron-Benhamou et al., 2004). These stem loops are bound by λN, a short, 21-amino acid peptide tag which can be fused to a protein of interest to tether it to the mRNA (Baron-Benhamou et al., 2004). This makes it possible to track individual mRNA molecules and simultaneously monitor their translational status both before and after tethering events. Since tethering is highly specific and the tethering signal is amplified by repeat epitopes, a tethered regulatory factor's impact on translation can be

quantified, and its actions on timescales ranging from seconds to hours can be deconvolved. We anticipate the TnT biosensor will be a valuable new tool in the microscopy toolbox to investigate broad protein-mRNA interactions with unprecedented spatiotemporal resolution. The TnT biosensor therefore brings us one step closer to performing controlled, single mRNA biochemical reactions in the natural environment of living cells.

5.2.1 The TnT system elucidated Argonaute2-mediated translational silencing

To demonstrate the applicability of the TnT biosensor, we used it to deconvolve the complex translational regulatory dynamics of Argonaute2 (Ago2). There has been a long-term debate about the precise temporal ordering of translational silencing by Ago2 (Jonas & Izaurralde, 2015). Multiple models have been proposed, some stating decay occurs co-translationally, others stating translational repression and mRNA decay occur sequentially, and still others stating silencing and decay can be uncoupled (Bazzini et al., 2012; Béthune et al., 2012; Bose et al., 2017; Djuranovic et al., 2012; Eichhorn et al., 2014; Guo et al., 2010; Pillai et al., 2005; Subtelny et al., 2014; Tat et al., 2016; Wilczynska et al., 2019). According to our data, within minutes of Ago2 tethering to an mRNA, translation initiation is strongly inhibited, leading to a gradual loss of translating ribosomes as they run off the transcript. Collectively, our data support a model in which the inhibition of translation initiation is an early step in the miRNA-mediated silencing pathway, one that can act independently of other steps, such as mRNA decay. Two lines of evidence support this model: first, we observed that translational bursts could occur after an mRNA was silenced by Ago2 tethering (**Figure 3.13E**); second, it

appeared that nearly all TnT biosensors had 5' and 3' ends according to smiFISH (**Figure 3.11**). Together, this evidence suggests an mRNA that has been translationally silenced by Ago2 tethering can remain intact and later, at least in some cases, reinitiate translation. Thus, inhibition of translation initiation can be uncoupled from mRNA decay, at least in our Ago2-tethering system.

5.2.2 Ago2 modestly slows the translation elongation rate

In addition to the clear impact Ago2 tethering had on translation initiation, we also measured a moderate impact on translation elongation via Harringtonine (HT) assays (**Figure 3.15**). This was especially interesting because a slowdown to elongation based on Ago2-tethering has not been shown by Ago2 or in the miRNA-mediated silencing pathway. In fact, since it is very difficult to discern modest slowdowns in translation, especially those that occur transiently or only impact a small population of mRNA, we speculate that there is much left undiscovered about how elongation rate contributes to translation control.

When we fit the translation runoff signal with two separate rates to accommodate fast- and slow-moving ribosomes, Ago2-tethering did not appear to affect the translation rate (2.4 amino acids sec-1 for mRNA in cells expressing either tetherable Ago2 or β-gal, **Figure 3.15**). However, the fraction of mRNA translating at the fast rate was reduced from 45% to 28%. Of note, the elongation rate of ribosomes in the fast fraction was consistent with previous findings in our lab and others (2.4 amino acids sec^{-1} measured here, 1-10 amino acids sec^{-1} measured in other NCT-based assays; Koch et al., 2020; Lyon et al., 2019; Morisaki et al., 2016; Viswanathan et al., 2015; Wang et al., 2016; Yan et al., 2016). The fact that not all translation spots disappeared in NCT-based

HT assays has been widely reported, with these drug-resistant translation sites being deemed the “immobile fraction”. Perhaps the immobile fraction of ribosomes contain interesting information about translation dynamics that has thus far been overlooked. In our data, we wonder if the increased fraction of slowly-translating ribosomes in Ago2-tethering cells is a consequence of Ago2-mediated translation silencing. Further, in the drug-free experiments, though Ago2-tethering inhibited translation at most mRNA, some of the Ago2-tethered single mRNA never ended translation over the 75 minutes monitored (**Figure 3.13C,G**). Before analyzing the HT data, we had speculated that these mRNA were resistant to Ago2-mediated translation silencing and were being actively translated. However, in light of the slowed rate of translation in Ago2-tetherable cells, we now wonder if some of these mRNA have slowed or stalled ribosome elongation, thus preventing translation signal runoff.

While it remains unclear how this slight slowdown in elongation would impact translational silencing, in principle the slowly moving ribosomes would increase the probability of incidental ribosomal collisions (Hickey et al., 2020; Juszkiewicz et al., 2020). If this were to happen, these collisions could be sensed by quality control machinery. According to recent work from the Hegde and Green labs, this machinery can inhibit translation initiation so that additional ribosomal collisions do not occur and elongation can proceed (Hickey et al., 2020; Juszkiewicz et al., 2020). While it remains unclear if similar coupling between elongational and initiation repression is occurring in our system, it could be one more contributing factor in Ago2-dependent translational silencing. In the future, a more precise ribosome runoff time could be measured by tracking single mRNA puncta after HT dosing. Tracking was not possible for the 1-

minute-interval imaging performed here, since mRNA moved too much between frames to connect timepoints of a track to faithfully track the same mRNA without adding error of switching to another nearby. Increasing the imaging frame rate could allow for faithful tracking, however we observe that mRNA diffusion rate increases during HT assays, most likely because the polysome size decreases as ribosomes run off the transcript and make the mRNA increasingly difficult to track. To help solve this problem, we adapted NCT to slow the diffusion of mRNA by membrane tethering (Appendix 3; adapted from technology developed in Yan et al., 2016). Slowed mRNA diffusion could improve the accuracy of tracking and translation measurement during long-timeframe imaging such as HT assays and allow for studying heterogeneity of single mRNA over time during ribosome runoff.

A puzzling observance was the lack of agreement between ribosomal runoff half-times in **Figure 3.13C** (t1/2 = ~40 minutes; translation intensity of all mRNA puncta over tracks up to 75 minutes), **Figure 3.13G** (t1/2 = 16.7 minutes; translation survival of all translation events over tracks up to 75 minutes) and **Figure 3.15B** (t1/2 = 29 minutes; translation intensity after Harringtonine, HT, initiation inhibition). It makes sense that **Figure 3.13C** had the longest runoff time, since Ago2-tethering did not completely inhibit translation inhibition. This allowed late bursts of initiation (**Figure 3.13E**) to contribute to the intensity of the translation signal at later time points, delaying the t1/2. This most likely explains the longer ribosome runoff time, as compared to the HT assay runoff time. For the survival plot in **Figure 3.13G**, many of the tracks were already bound by Ago2 and therefore, we speculate, already undergoing translation initiation inhibition. This would result in a prematurely early ribosome runoff, which could

contribute to the shortened ribosome runoff time as compared to the HT ribosome runoff time.

The optimal way to determine how long translation lasts after Ago2 tethering would be to collect long timeframe tracks with a detectable Ago2-tethering event, align tracks where Ago2-tethering was at time point 0, and measure the subsequent translation survival. However, we were unable to take this measurement since we found very few tracks with an Ago2 tethering event. Increasing the throughput (**Chapter 5.4**) or tracking capabilities (**Appendix 3**) of the TnT assay so that more mRNA can be tracked could generate enough data to make such an analysis possible.

5.2.3 P-bodies and long-timescale translational silencing

By tracking the TnT biosensor over longer timescales, we also discovered both Ago2 and mRNA signals progressively increased with time. The buildup in Ago2 signals began during ribosome runoff (**Figure 3.13C, right**), while the buildup in mRNA signals occurred over many hours as mRNA and Ago2 molecules coalesced (**Figure 3.10A,B**). These P-body-localizing, multi-mRNA clusters were, as far as we saw, permanently translationally silenced while in P-bodies. However, we should note that we could not detect if mRNA were allowed to exit P-body to reinitiate translation. Since Ago2 is a component of P-bodies, it was unclear whether P-body localization was through Ago2-tethering itself or due to the Ago2 silencing mechanism.

The nature of this progressive accumulation of signals is consistent with diverse, multivalent interactions of endogenous miRISC machinery. In particular, a single tethered Ago2 protein can theoretically bind up to three TNRC6B proteins via three distinct binding pockets (Schirle & MacRae, 2012; Sheu-Gruttadauria & MacRae, 2018).

Likewise, a single TNRC6A protein can bind up to three Ago2 proteins via three distinct binding sites (Elkayam et al., 2017). In turn, TNRC6 proteins contain long, unstructured domains that can recruit other, more downstream miRISC effectors, such as deadenylases, de-capping complexes, and translational repression factors like RCK/DDX6 (Jonas & Izaurralde, 2015). Such diverse, multivalent protein-protein and protein-RNA interactions are hallmarks of phase separation (Lin et al., 2015; Moon et al., 2019; Pitchiaya et al., 2019; Sheu-Gruttadauria & MacRae, 2018), and minimal Ago2-TNRC6 complexes have in fact been observed to phase separate both *in vivo* and *in vitro* (Lin et al., 2015; Meister et al., 2005; Pillai et al., 2005; Sen & Blau, 2005), leading to increased sequestration of miRNA target mRNAs and deadenylases (Sheu-Gruttadauria & MacRae, 2018). It therefore seems likely the TnT biosensor serves as a proxy for these large ribonuclear complexes.

While the presence of RCK would suggest some are mature P-bodies, it is possible that Ago2 and RCK interact outside of P-bodies. It has been previously proposed that P-bodies can exist in a wide range of sizes, from conventional large aggregates of many P-body proteins to foci that have so few P-body proteins that they are microscopically invisible above background signal (Pitchiaya et al., 2019). This would further blur delineation between a P-bodies, a microenvironment, and factor recruitment. The slow and progressive accumulation in mRNA and Ago2 we observed would imply that our TnT biosensor offers a live-cell, single-molecule window into the seeding of phase-separated bodies.

5.2.4 Dynamics of BoxB-λN tethering

An unexpected finding was that the BoxB-λN tethering interaction seemed to be variable and dynamic. This dynamism of tethering was serendipitous, in fact, because it allowed us to capture tethering events as they happened and to study tethered versus untethered mRNA in the same cell. In addition, it was curious to us that only about half of the MCP-labeled TnT biosensors in a cell were λN-tethered, which was the case in Ago2- or β-gal-tetherable cells. Though fortunate for our TnT application, we wondered why BoxB-λN tethering behaved so differently than MS2-MCP tethering.

The interaction of tethering MCP to MS2 stem loops is well-studied. MCP labels MS2 elements in nascent mRNA co-transcriptionally (Forero-Quintero et al., 2021). The MS2-MCP tethering we used to label TnT mRNA showed low-variability of MCP-signal in **Figure 3.9**. When using 12 mW power of our 647 nm laser, we consistently saw a single peak at ~0.012 a.u. (likely representing one MCP-saturated MS2 tag), a peak at twice this intensity (likely representing two colocalizing MS2 tags), and some higher intensity signals (likely multi-mRNA, such as a transcription site, or non-mRNA aggregates). The distribution of MCP intensities was not affected by translation or tethering (**Figure 3.9, above**).

However, only about half the MS2-labeled mRNA were β-gal or Ago2-tethered (**Figure 3.1C**). The β-gal- or Ago2-tethered mRNA had variable intensities of EGFP, unlike the defined peak in the histogram of MCP signals (**Figure 3.9**, **Figure 3.13**), such that we were not able to similarly quantify how many BoxB tags were present. Furthermore, when we tracked an mRNA over long timeframes, its tethering signal was highly dynamic, especially so for Ago2-tethering (**Figure 3.13A, D-F**). Thus, we wondered why λN tethering, unlike MCP tethering, was so variable and dynamic.

Though we cannot provide any concrete answers to this question at this time, we have generated interesting data that may help elucidate the picture. Interestingly, our data suggested that higher translation leads to more BoxB-λN tethering interactions. To demonstrate, β-gal-tethering was strongly correlated with translation (**Figure 3.13B**). This could, however, be from a direct correlation (e.g. translation causes increased tethering) or indirect correlation (e.g. tethering takes a long time, and highly translated mRNA are older). We should note here that β-gal tetramerizes, which could artificially strengthen tethering or cause a brighter EGFP signal at the mRNA; a better tethering control would be an inert, monomeric protein.

If translation and λN-tethering are, indeed, directly correlated, one explanation for this could be related to mRNA structure. It has been shown that increased translation of an mRNA changes its shape by stretching the mRNA molecule out in both fixed-cell (Adivarahan et al., 2018; Khong & Parker, 2018) and live-cell (Koch et al., 2020) experiments. More ribosomes translating on a single mRNA was also shown to cause higher probability of targeting and repression by RNA-Binding Proteins (RBPs; Hoek et al., 2019; Ruijtenberg et al., 2020). These studies suggested that during translation, ribosomes unfold the mRNA, which breaks many weak mRNA-mRNA intramolecular bonds, which in turn uncovers mRNA elements for RBP targeting. They further supported this claim by showing that blocking predicted mRNA-mRNA intramolecular interactions through silent mutations resulted in mRNA that were targeted by RBPs with higher likelihood (Ruijtenberg et al., 2020). Further, these intramolecular interactions could be long-ranging (Ruijtenberg et al., 2020), which could describe the crumpled, compact shape of an mRNA with low or no translation (Adivarahan et al., 2018; Khong

& Parker, 2018; Koch et al., 2020). This shape-based phenomenon could be mediating the dynamics of tethering seen here for the TnT sensor. Though this is only speculation, it would be interesting if highly translated mRNA were unfolded, displaying BoxB stem loops in a way that are more targetable by λN.

Unlike the strong correlation between tethering and translation of the inert protein β-gal, we measured an inverse correlation between translation and Ago2-tethering (**Figure 3.13B**; a similar trend was seen for Ago2- or β-gal-tetherable mRNA at ~6 hours post-loading mRNA from **Figure 3.7**, data not shown here). The mRNA with the brightest Ago2-tethering signals also had the dimmest translation signals, following the idea that mRNA were not being translated when localizing in Ago2-rich, mRNA-rich P-bodies (**Figure 3.10**). The mRNA colocalizing with dim or nonexistent Ago2-tethering signals also had the brightest translation signals, following the idea that Ago2 represses translation (**Figure 3.13B**).

However, in our 75-minute tracks, we observed interesting temporal-based correlation between Ago2-tethering and translation. Overall, we observed an average trend of Ago2 increasing as translation decreased (**Figure 3.13C, right**). However, at single mRNA tracks, we often saw Ago2 tethering signals increase at mRNA being translated. This was, in turn, associated with a decrease in translation signals, presumably by tethered-Ago2 blocking translation. Interestingly, for many mRNA tracks with weak Ago2 signals, when translation signals were completely shut off we saw a loss of Ago2 signal, which in some cases resulted in a subsequent burst of translation (**Figure 3.13E**). We speculate that this burst of translation could be from de-repression of translation from a loss of tethered Ago2. Altogether, we find it possible that these

observations come from the combination of translation enhancing tethering, for example due to ribosome-mediated changes in mRNA structure, and Ago2-tethering subsequently repressing translation. Though the dynamics of λN-BoxB tethering are still quite unclear at this point, overall we are glad that this tethering system operated in a way that caused dynamic fluctuations in tethering at single mRNA, which enhanced the TnT system's ability to study the impact of Ago2 on translation.

5.2.5 Validation of the TnT biosensor

Our design for the tethering module of the TnT biosensor was based off of earlier work from the Filipowicz and Parker labs, which pioneered the use of the Ago2 tethering system to investigate miRNA-directed Ago2 translational silencing (Eckhardt et al., 2011; Liu, Valencia-Sanchez, et al., 2005; Pillai et al., 2004, 2005). Using the TnT biosensor, we corroborated their finding that tethering Ago2 to a reporter mRNA leads to a global reduction in reporter protein synthesis (**Figure 3.7**, **Figure 3.8**). Furthermore, by comparing the TnT biosensor to a more natural one with endogenous MREs, we demonstrated that Ago2 tethering remains a good model of miRNA-directed translational silencing at the single-cell and single-molecule level (**Figure 3.15**, **Figure 3.16**).

This work is similar to a companion study by Kobayashi and Singer (manuscript under review) that developed a different miRNA-based reporter to investigate translational silencing by Ago2 with single-molecule precision *in situ*. Their measurements also indicate Ago2 silences mRNA translation on the 30-40 minute timescale, prior to mRNA decay. Although the two reporter systems are similar, a

unique advantage of ours is the amplified tethering signal, which allowed us to track the dynamics of Ago2-tethered mRNA for long periods of time in living cells.

5.3 Caveats to consider for the TnT assay

Despite these reassuring results, there are several important caveats to studying translation using the TnT approach that we should point out. These caveats apply to both the Ago2-related results reported here and future TnT assay applications. As with using any molecular biology tool, using the TnT assay for examining the translational impact of Ago2 or other control factors requires careful review of all caveats and considerations, such as those listed here.

First, fusion of λN-EGFP to a factor has the potential to alter its conformation or folding. This could potentially hinder its natural ability to control translation, e.g. inhibit binding of a cofactor or downstream effector or block an important post translational modification. This was not an issue for Ago2, as it has been validated to accept an N-terminal fusion of λN or EGFP through thorough biochemical validation of activity in vitro (Leung et al., 2006; Pillai et al., 2004). However, other factors may not accept a bulky polypeptide sequence to their N-terminal and should be validated before being used in a TnT assay.

Additionally, the artificial nature of the TnT assay may cause unwanted, artifactual impacts to translation or the mRNA. For example, MS2 stem loops used in the TnT reporter were found to be resistant to XRN1-mediated decay in yeast cells. The partially decayed stem loop fragments consequentially accumulated in P-bodies, giving the false appearance of mRNA localized to P-bodies as a real, biological phenomenon (Tutucci et al., 2018). It should be noted that decay resistance of MS2 stem loops was

only in yeast and was not detected in mammalian cells, as yeast XRN1 is less robust and cannot catalyze decay of higher-ordered RNA structure (Tutucci et al., 2018). Thus, we found it essential to control for tethering-induced effects with a tetherable, non-Ago2 control protein, β-gal. For each experiment, we consistently compared tetherable Ago2 to the control to ensure that the effects we saw were, in fact, due to Ago2-specific tethering. Though there were no noteworthy differences between tethered and untethered mRNA in β-gal-tetherable control cells in our experiments, suggesting tethering does not have a noticeable impact on translation or mRNA, we still recommend this control for future studies as a precaution from tethering-specific effects, especially when using yeast cells. In addition, a non-tetherable Ago2 control was important for measuring the effects of overexpressed Ago2. As with the tethering control, in most cases the effects of non-tetherable Ago2 were not noticeable. However, while studying P-bodies we found twice as many P-body foci (stained by α-RCK) in cells expressing non-tetherable and tetherable Ago2, as compared to cells expressing non-tetherable β-gal (data not shown). Including the non-tetherable Ago2 control protected us from misinterpreting results by attributing this effect to Ago2-tethering. This further confirmed the importance of including tetherable and non-tetherable controls in future TnT studies.

A third consideration is that the artificial tethering of Ago2 to mRNA bypasses the natural interaction mediated by miRNA base-pairing. This could misorient tethered Ago2 so that it does not behave in a completely natural way. Nonetheless, the consistency of translation silencing between the TnT biosensor and the more natural miRNA-based

biosensors we tested suggests that tethered Ago2 retains its core silencing functionality.

Fourth, our tethering cassette was quite large, requiring 15 BoxB stem loops to track tethering for extended periods of time above background. Note, we were unable to detect tethering at a 5x BoxB tethering cassette (data not shown). Thus, there is some unknown threshold of tethered Ago2 protein that is required for their signal to become detectable. While the threshold is probably below 15 EGFP-tagged Ago2 or β-gal proteins (given the wide range we observed in EGFP intensities at single mRNA), a bright TnT biosensor is nonetheless a very large complex composed of many natural and unnatural proteins whose size could interfere with or alter underlying biological processes. For example, the clustering and P-body localization we observed may not occur with such high probability when just one or two Ago2 proteins are recruited to an endogenous mRNA target. This is relevant since it is known that multiple miRISC cooperatively silence their target (**Chapter 1.2.2**; Grimson et al., 2007), and 15 proximal miRNA binding sites is more than what is commonly found in endogenous transcripts (Friedman et al., 2009). Therefore the silencing seen by the TnT biosensor may be different (e.g. stronger or more rapid) than from endogenous miRNA-site targeting. To remedy this, it may be useful to use a different tethering strategy with a smaller footprint than 15 BoxB stem loops. One possible strategy for miRNA would be the use of fluorescently conjugated miRNA rather than EGFP-Ago2, similar to the strategy employed in (Appendix 1). The Walters lab demonstrated individual miRNA can be tracked in living cells (Pitchiaya et al., 2012, 2019), so in theory their method could be

combined with ours to visualize both miRISC and translation dynamics in a more natural setting.

Fifth, although our TnT biosensor associates with Ago2 independent of its interaction with a miRNA, it is likely that tetherable Ago2 can still bind to miRNA. If so, tetherable Ago2 could potentially engage endogenous mRNA targets in *cis* while tethered to the TnT reporter. This could also be the case when tethering other, non-Ago RBPs. It is not clear what impact this might have on its functionality. Given the multivalent nature of Ago2 interactions with the miRISC machinery, it may be that even under natural conditions Ago2 interacts, albeit indirectly, with multiple mRNAs. Since endogenous mRNA are not MCP-labeled, the TnT system cannot tell of tetherable Ago2 associates with endogenous mRNA through miRNA binding. It should be noted that nearby ribosomes on endogenous, colocalizing transcripts would not cause a brighter translation signal since only FLAG-tagged reporter nascent chains can be visualized by Fab.

Another major drawback of the current TnT system is that tethering happens spuriously and infrequently. As a remedy, the TnT biosensor could be coupled with optogenetic dimerization domains to enable precision tethering (Benedetti et al., 2020; Kawano et al., 2015; Spiltoir & Tucker, 2019; Taslimi et al., 2014). Tethering could even be made inducible by chemicals (Stanton et al., 2018) or light (Spiltoir & Tucker, 2019) to perturb translation in a controlled, reversible fashion. This assay modification would increase the spatiotemporal control and dramatically increase the count of tethered mRNA per experiment. Further, it would allow for studying many mRNA before and after a controlled tethering event.

Overall, the fact that the TnT system works at all is, to be frank, quite lucky. Specific cellular concentrations are required for each reporter and probe involved in this complicated assay for accurate reporting of translation, mRNA, and tethering. These reporter/probe parameters include TnT biosensor expression level, Fab and MCP concentration, mature reporter protein level, and expressed level of tetherable Ago2 per cell. The TnT assay cannot be performed in a cell with inadequate levels of any of these parameters, rendering the majority of loaded cells as unusable due to one or more of the concentrations being too high, too low or not present.

We explored the possibility of increasing the throughput of the TnT assay by generating stable cell lines expressing one or multiple TnT protein components. This would remove variability from transiently loading and transfecting cells by generating stable cell lines, as proposed in Appendix 2. However, we note that though generating stable cell line expressing tetherable β-gal at the optimal concentration for the TnT assay was quite straightforward, doing so for tetherable or non-tetherable Ago2 cells proved more difficult, most likely due to the repressive impact of Ago2 on global cellular growth and functions (Appendix 2).

An arduous amount of optimization needed to be performed to create the conditions necessary for even visualizing tethering at an mRNA. During this time we found that, even after tripling the number of BoxB stem loops, only one of the three promoters driving tetherable Ago2 produced an Ago2 concentration low enough to be seen tethering over the background yet high enough to be visible at all. Beyond Ago2 levels, each of the assay parameters have high variability at the single-cell level, and variable concentration of probes and reporters combinatorially contribute to the assay's

low-efficiency. Thus, finding cells with optimal levels of each of the several parameters is quite difficult: even after optimization of the TnT and bead loading assays, the TnT assay still only yielded 25-50 imageable cells per dish. Taking measures to reduce the variability of parameters or decreasing the number of parameters altogether would greatly increase throughput of the TnT assay, allowing for more usable data and thus better statistics and more impactful results.

5.4 Controlled biochemistry in a living cell

The majority of our understanding of cellular regulatory mechanisms and gene expression control comes from bulk-cell and in vitro assays. A whole-picture understanding can be obtained by studying these mechanisms using endogenous machinery in a live cell context. The TnT assay is a powerful tool to study a factor's impact on the natural process of translation in real time inside a living cell. In this way, the TnT biosensor brings us one step closer to performing controlled, single mRNA biochemical reactions in the natural environment of living cells.

Moving beyond Ago2, our overall goal for the TnT biosensor is that it can now easily be adapted to tether other proteins of interest to the translation reporter. Other NCT-based methods studying the impact of a factor on translation used a strategy that is not adaptable for other factors, e.g. a siRNA target site to specifically recruit Ago2 or a premature stop codon to specifically recruit nonsense mediated decay factors (Hoek et al., 2019; Ruijtenberg et al., 2020). The advantage of tethering is that virtually any factor that can accept an N-terminal addition can be incorporated into the TnT assay. Indeed, tethering has frequently been used in the literature to study a wide variety of RNA binding proteins in diverse biological settings. For example, tethering has been

used to investigate nonsense-mediated decay (Hickey et al., 2020), to screen for effects caused by RNA binding proteins (Luo et al., 2020), and to study specific protein domains (Fabian et al., 2011; Liu, Valencia-Sanchez, et al., 2005; Piao et al., 2010) or specific amino acid modifications (Golden et al., 2017). With the TnT biosensor, these studies can be expanded to the single-molecule level, where their impact can be more thoroughly investigated with higher spatiotemporal resolution.

A further use of the TnT assay is to study the effects on translation in the context of directed mRNA localization. Using tethered Ago2, we observed re-localization of the TnT biosensor to presumed P-bodies upon Ago2 tethering (**Figure 3.10C,D**), we believe our approach will be generally useful in targeting a biosensor to a specific subcellular environment, such as the nucleus, the ER, or mitochondria, where local translation can be studied (Buxbaum et al., 2015; Voigt et al., 2017).

Collectively, mRNA behave in a way that is easy to monitor using bulk-cell assays, such as blots or RNAseq. However, single mRNA work on individual timescales that can be highly variable. Using NCT-based assays capable of detecting and studying this heterogeneity has provided major contributions to the fields of translation and its control (covered in **Chapter 2**). The impacts and discoveries could be even greater on a high-throughput scale, such as screening for effects on translation. This could be useful to either endogenous, non-canonical (such as uORF translation, see section **Chapter 2.2.9** or viral translation (see **Chapter 2.2.1**). Using TnT in a screen could screen for specific impacts to translation on a panel of λN-tagged candidate factors. Adapting TnT for such an application would make it possible to rapidly discover novel translational control factors which have specific impacts on translation. For example, factors could be

tested to modify subcellular localization, repress translation, increase translation or modify how a mRNA is translated, such as ribosomes per polysome.

However, at this point, live-cell TnT or NCT-based assays are currently in an early stage of development. These assays are still quite low-throughput, with limited technology capable single-molecule detection and tracking. To maximize benefit, increasing the throughput and automating image collection and data analysis of NCT-based assays would allow for these methodologies to have a much greater impact.

This dream is lofty but may not be too futuristic. Presently, several biotechnology companies, including Recursion, Eikon, insitro, Spring Discovery, Allcyte, and Soley, are moving towards using single-cell imaging technologies to study disease. These companies have made this possible by improving the throughput, automation and analysis of their imaging assays. Since these assays are imaging-based, they can monitor additional parameters, such as colocalization, subcellular localization, cell-to-cell variability, and cell morphology, which are convoluted or unmeasurable using bulk-cell, lysis-based assays.

Further, studying impacts to translation have proven key for significant medical advances. Take, for example, the mRNA vaccine developed by Moderna. After studying the impacts of modifications and sequence composition on translation, Moderna was able to incorporate these results into novel mRNA vaccine technology and rapidly design and develop an mRNA vaccine against SARS-CoV-2. This shows that studying translation is of great interest not only for academic acquisition of knowledge but also for biotechnology and medical advances. The interest and investment from the

biotechnology sector in high-throughput single-cell image assays paves the way for a future for similar imaging-based assays at the single-molecule level.

5.5 The future of Nascent Chain Tracking

As described in detail in **Chapter 3**, the expanded resources for NCT-based applications have increased the breadth and capabilities of how and which translation processes can be studied. The original NCT technology publications almost exclusively studied translation in two channels, marking the mRNA and translation (Morisaki et al., 2016; Pichon et al., 2016; Wang et al., 2016; Wu et al., 2016; Yan et al., 2016). However, several works have since multiplexed the NCT assay to study translation of different transcripts or ORFs in the same cell (Boersma et al., 2019; Koch et al., 2020; Lyon et al., 2019). This includes the work presented here (**Figure 3.15**, **Figure 3.16**), where multiplexing FLAG- or HA-tagged translation at MRE-containing or control mRNA allowed for studying the impacts of miRNA-targeting to translation at a population of mRNA in the same cell. Multiplexing has now become possible using a combination of new translation-sensing probes, such as the MoonTag nanobody (Boersma et al., 2019) and frankenbody (Zhao et al., 2019). To further facilitate multiplexed imaging, additional probes binding complementary epitopes are still needed. Since the frankenbody is modular, loop grafting can be used to generate new probes quickly, as was the strategy performed in Zhao et al. 2019. New nanobodies continue to be developed to bind epitopes *in vivo*, such as the BC2 (M. B. Braun et al., 2016) and ALFA nanobodies (Götzke et al., 2019). A larger toolkit of probes could be incorporated into NCT-based assays, expanding the type or number of ORFs that could be studied simultaneously using multiplexing.

As well, additional new RNA tags could be incorporated into NCT to enhance multicolor applications. In **Figure 3.15** and **Figure 3.16**, since we used the same MS2 tag for MRE and control mRNA, we could only distinguish mRNA that were being translated. Multiplexing mRNA labels, instead of or as well as translation signals, could expand the capabilities of multiplexed assays as in **Figure 3.15** and **Figure 3.16** or increase the number of mRNA to be studied. For this, riboglow (Braselmann et al., 2019) and fluorogenic Mango arrays (Cawte et al., 2019) show great promise. Finally, as the probe and tag sets for NCT continue to expand, software will also need to improve to assist with the increased complexity of experimental design and interpretation. Single-particle detection and tracking programs like TrackMate (ImageJ) and FISH-quant (Mueller et al., 2013) exist for counting, measuring, and, for TrackMate, tracking single particles. The field would greatly benefit from improving these programs to have higher automation, be more customizable, have increased sensitivity for noisy images, and diversified built-in data visualization functions. As machine learning-based image analysis grows for microscopy data, we anticipate that so too will it revolutionize single-molecule detection and tracking.

Ultimately, the final frontier for NCT is to move closer to imaging native translation *in vivo*. Introducing the NCT-based reporter mRNA using genetic modification, such as CRISPR or viral transduction, is quite straightforward for cultured cells and some whole organisms, C. elegans. As an alternative to studying reporter mRNA translation, a more natural approach would be to develop a reporter system monitoring endogenous translation. This could be achieved by raising antibodies against endogenous epitopes to light up native translation. A proof-of-concept of this

approach was used to image the translation of endogenous PCNT protein in fixed cells (Sepulveda et al., 2018). The optimal ORF for visualizing endogenous translation would contain naturally occurring, targetable repeat epitopes in the N-terminal region, allowing for rapid and multiplied signal upon translation.

Alternatively, if repeated epitopes do not exist for the protein of interest, a cocktail of multiple antibodies targeting different locations on an endogenous peptide could similarly amplify the translation signal. Once development of these probes and reporters are designed and created, we anticipate that the limiting factor will be the microscopy. We predict that advanced light-sheet microscopy (Power & Huisken, 2017) with adaptive optics (Ji, 2017) will likely be necessary to focus deep within a specimen while maintaining good signal-to-noise and spatiotemporal resolution with minimal phototoxicity.

Regardless of how NCT precisely evolves or which biological questions it eventually helps tackle, its unique ability to light up single mRNA translation in living cells means its future will undoubtedly be bright.

REFERENCES

Adivarahan, S., Livingston, N., Nicholson, B., Rahman, S., Wu, B., Rissland, O. S., & Zenklusen, D. (2018). Spatial Organization of Single mRNPs at Different Stages of the Gene Expression Pathway. *Molecular Cell*, *72*(4), 727-738.e5. https://doi.org/10.1016/j.molcel.2018.10.010

Aguilera, L. U., Raymond, W., Fox, Z. R., May, M., Djokic, E., Morisaki, T., Stasevich, T. J., & Munsky, B. (2019). Computational design and interpretation of single-RNA translation experiments. *PLOS Computational Biology*, *15*(10), e1007425. https://doi.org/10.1371/journal.pcbi.1007425

Aizer, A., Kalo, A., Kafri, P., Shraga, A., Ben-Yishay, R., Jacob, A., Kinor, N., & Shav-Tal, Y. (2014). Quantifying mRNA targeting to P-bodies in living human cells reveals their dual role in mRNA decay and storage. *Journal of Cell Science*, *127*(20), 4443–4456. https://doi.org/10.1242/jcs.152975

Ameres, S. L., Martinez, J., & Schroeder, R. (2007). Molecular Basis for Target RNA Recognition and Cleavage by Human RISC. *Cell*, *130*(1), 101–112. https://doi.org/10.1016/j.cell.2007.04.037

Ayache, J., Bénard, M., Ernoult-Lange, M., Minshall, N., Standart, N., Kress, M., & Weil, D. (2015). P-body assembly requires DDX6 repression complexes rather than decay or Ataxin2/2L complexes. *Molecular Biology of the Cell*, *26*(14), 2579–2595. https://doi.org/10.1091/mbc.E15-03-0136

Babendure, J. R., Babendure, J. L., Ding, J.-H., & Tsien, R. Y. (2006). Control of mammalian translation by mRNA structure near caps. *RNA*, *12*(5), 851–861. https://doi.org/10.1261/rna.2309906

Baron-Benhamou, J., Gehring, N. H., Kulozik, A. E., & Hentze, M. W. (2004). Using the λN Peptide to Tether Proteins to RNAs. In D. R. Schoenberg (Ed.), *MRNA Processing and Metabolism: Methods and Protocols* (pp. 135–153). Humana Press. https://doi.org/10.1385/1-59259-750-5:135

Bartel, D. P. (2018). Metazoan MicroRNAs. *Cell*, *173*(1), 20–51. https://doi.org/10.1016/j.cell.2018.03.006

Bazzini, A. A., Lee, M. T., & Giraldez, A. J. (2012). Ribosome profiling shows that miR-430 reduces translation before causing mRNA decay in zebrafish. *Science (New York, N.Y.)*, *336*(6078), 233–237. https://doi.org/10.1126/science.1215704

Becker, T., Volchuk, A., & Rothman, J. E. (2005). Differential use of endoplasmic reticulum membrane for phagocytosis in J774 macrophages. *Proceedings of the National Academy of Sciences*, *102*(11), 4022–4026. https://doi.org/10.1073/pnas.0409219102

Behm-Ansmant, I., Rehwinkel, J., Doerks, T., Stark, A., Bork, P., & Izaurralde, E. (2006). MRNA degradation by miRNAs and GW182 requires both CCR4:NOT deadenylase and DCP1:DCP2 decapping complexes. *Genes & Development*, *20*(14), 1885–1898. https://doi.org/10.1101/gad.1424106

Benedetti, L., Marvin, J. S., Falahati, H., Guillén-Samander, A., Looger, L. L., & De Camilli, P. (2020). Optimized Vivid-derived Magnets photodimerizers for

subcellular optogenetics in mammalian cells. *ELife*, *9*, e63230. https://doi.org/10.7554/eLife.63230

Besteiro, S., Michelin, A., Poncet, J., Dubremetz, J.-F., & Lebrun, M. (2009). Export of a Toxoplasma gondii Rhoptry Neck Protein Complex at the Host Cell Membrane to Form the Moving Junction during Invasion. *PLOS Pathogens*, *5*(2), e1000309. https://doi.org/10.1371/journal.ppat.1000309

Béthune, J., Artus-Revel, C. G., & Filipowicz, W. (2012). Kinetic analysis reveals successive steps leading to miRNA-mediated silencing in mammalian cells. *EMBO Reports*, *13*(8), 716–723. https://doi.org/10.1038/embor.2012.82

Biswas, J., Liu, Y., Singer, R. H., & Wu, B. (2019). Fluorescence Imaging Methods to Investigate Translation in Single Cells. *Cold Spring Harbor Perspectives in Biology*, *11*(4), a032722. https://doi.org/10.1101/cshperspect.a032722

Boersma, S., Khuperkar, D., Verhagen, B. M. P., Sonneveld, S., Grimm, J. B., Lavis, L. D., & Tanenbaum, M. E. (2019). Multi-Color Single-Molecule Imaging Uncovers Extensive Heterogeneity in mRNA Decoding. *Cell*, *178*(2), 458-472.e19. https://doi.org/10.1016/j.cell.2019.05.001

Boersma, S., Rabouw, H. H., Bruurs, L. J. M., Pavlovič, T., van Vliet, A. L. W., Beumer, J., Clevers, H., van Kuppeveld, F. J. M., & Tanenbaum, M. E. (2020). Translation and Replication Dynamics of Single RNA Viruses. *Cell*, *183*(7), 1930-1945.e23. https://doi.org/10.1016/j.cell.2020.10.019

Bose, M., Barman, B., Goswami, A., & Bhattacharyya, S. N. (2017). Spatiotemporal Uncoupling of MicroRNA-Mediated Translational Repression and Target RNA Degradation Controls MicroRNP Recycling in Mammalian Cells. *Molecular and Cellular Biology*, *37*(4). https://doi.org/10.1128/MCB.00464-16

Braselmann, E., Stasevich, T. J., Lyon, K., Batey, R. T., & Palmer, A. E. (2019). Detection and quantification of single mRNA dynamics with the Riboglow fluorescent RNA tag. *BioRxiv*, 701649. https://doi.org/10.1101/701649

Braun, J. E., Truffault, V., Boland, A., Huntzinger, E., Chang, C.-T., Haas, G., Weichenrieder, O., Coles, M., & Izaurralde, E. (2012). A direct interaction between DCP1 and XRN1 couples mRNA decapping to 5′ exonucleolytic degradation. *Nature Structural & Molecular Biology*, *19*(12), 1324–1331. https://doi.org/10.1038/nsmb.2413

Braun, M. B., Traenkle, B., Koch, P. A., Emele, F., Weiss, F., Poetz, O., Stehle, T., & Rothbauer, U. (2016). Peptides in headlock – a novel high-affinity and versatile peptide-binding nanobody for proteomics and microscopy. *Scientific Reports*, *6*(1), 1–10. https://doi.org/10.1038/srep19211

Buchan, J. R., & Parker, R. (2009). Eukaryotic Stress Granules: The Ins and Outs of Translation. *Molecular Cell*, *36*(6), 932–941. https://doi.org/10.1016/j.molcel.2009.11.020

Buxbaum, A. R., Haimovich, G., & Singer, R. H. (2015). In the right place at the right time: Visualizing and understanding mRNA localization. *Nature Reviews Molecular Cell Biology*, *16*(2), 95–109. https://doi.org/10.1038/nrm3918

Buccitelli, C. and Selbach, M., 2020. mRNAs, proteins and the emerging principles of gene expression control. *Nature Reviews Genetics*, 21(10), pp.630-644. https://doi.org/10.1038/s41576-020-0258-4

Cawte, A. D., Unrau, P. J., & Rueda, D. S. (2019). Live Cell Imaging of Single RNA Molecules with Fluorogenic Mango II Arrays. *BioRxiv*, 840082. https://doi.org/10.1101/840082

Celis, J. E. (1984). Microinjection of somatic cells with micropipettes: Comparison with other transfer techniques. *Biochemical Journal*, *223*(2), 281–291. https://doi.org/10.1042/bj2230281

Chakrabarti, R., Wylie, D. E., & Schuster, S. M. (1989). Transfer of monoclonal antibodies into mammalian cells by electroporation. *Journal of Biological Chemistry*, *264*(26), 15494–15500.

Chandradoss, S. D., Schirle, N. T., Szczepaniak, M., MacRae, I. J., & Joo, C. (2015). A Dynamic Search Process Underlies MicroRNA Targeting. *Cell*, *162*(1), 96–107. https://doi.org/10.1016/j.cell.2015.06.032

Chao, J. A., Yoon, Y. J., & Singer, R. H. (2012). Imaging Translation in Single Cells Using Fluorescent Microscopy. *Cold Spring Harbor Perspectives in Biology*, *4*(11), a012310. https://doi.org/10.1101/cshperspect.a012310

Chen, C.-Y. A., Zheng, D., Xia, Z., & Shyu, A.-B. (2009). Ago–TNRC6 triggers microRNA-mediated decay by promoting two deadenylation steps. *Nature Structural & Molecular Biology*, *16*(11), 1160–1166. https://doi.org/10.1038/nsmb.1709

Chen, Y., Boland, A., Kuzuoğlu-Öztürk, D., Bawankar, P., Loh, B., Chang, C.-T., Weichenrieder, O., & Izaurralde, E. (2014). A DDX6-CNOT1 Complex and W-Binding Pockets in CNOT9 Reveal Direct Links between miRNA Target Recognition and Silencing. *Molecular Cell*, *54*(5), 737–750. https://doi.org/10.1016/j.molcel.2014.03.034

Choy, E., Chiu, V. K., Silletti, J., Feoktistov, M., Morimoto, T., Michaelson, D., Ivanov, I. E., & Philips, M. R. (1999). Endomembrane Trafficking of Ras: The CAAX Motif Targets Proteins to the ER and Golgi. *Cell*, *98*(1), 69–80. https://doi.org/10.1016/S0092-8674(00)80607-8

Cialek. (2021). *Datasets associated with "Imaging translational control by Argonaute with single-molecule resolution in live cells."* https://doi.org/10.6084/m9.figshare.c.5395800.v1

Cialek, C. A., Galindo, G., Koch, A., Saxton, M., & Stasevich, T. (2021). Bead Loading Proteins and Nucleic Acids into Adherent Human Cells. *J. Vis. Exp*. https://doi.org/10.3791/62559

Cialek, C. A., Koch, A. L., Galindo, G., & Stasevich, T. J. (2020). Lighting up single-mRNA translation dynamics in living cells. *Current Opinion in Genetics & Development*, *61*, 75–82. https://doi.org/10.1016/j.gde.2020.04.003

Cialek, C. A., Morisaki, T., Zhao, N., Montgomery, T. A., & Stasevich, T. J. (2021). Imaging translational control by Argonaute with single-molecule resolution in live cells. *BioRxiv*, 50.

Cioni, J.-M., Lin, J. Q., Holtermann, A. V., Koppers, M., Jakobs, M. A. H., Azizi, A., Turner-Bridger, B., Shigeoka, T., Franze, K., Harris, W. A., & Holt, C. E. (2019). Late Endosomes Act as mRNA Translation Platforms and Sustain Mitochondria in Axons. *Cell*, *176*(1), 56-72.e15. https://doi.org/10.1016/j.cell.2018.11.030

Cohen, L. S., Mikhli, C., Jiao, X., Kiledjian, M., Kunkel, G., & Davis, R. E. (2005). Dcp2 Decaps m2,2,7GpppN-Capped RNAs, and Its Activity Is Sequence and Context Dependent. *Molecular and Cellular Biology*, *25*(20), 8779–8791. https://doi.org/10.1128/MCB.25.20.8779-8791.2005

Collart, M. A., & Weiss, B. (2020). Ribosome pausing, a dangerous necessity for co-translational events. *Nucleic Acids Research*, *48*(3), 1043–1055. https://doi.org/10.1093/nar/gkz763

Coller, J., & Wickens, M. (2007). Chapter Fourteen - Tethered Function Assays: An Adaptable Approach to Study RNA Regulatory Proteins. In J. Lorsch (Ed.), *Methods in Enzymology* (Vol. 429, pp. 299–321). Academic Press. https://doi.org/10.1016/S0076-6879(07)29014-7

Coulon, A., Chow, C. C., Singer, R. H., & Larson, D. R. (2013). Eukaryotic transcriptional dynamics: From single molecules to cell populations. *Nature Reviews Genetics*, *14*(8), 572–584. https://doi.org/10.1038/nrg3484

Coulon, A., Ferguson, M. L., de Turris, V., Palangat, M., Chow, C. C., & Larson, D. R. (2014). Kinetic competition during the transcription cycle results in stochastic RNA processing. *ELife*, *3*. https://doi.org/10.7554/eLife.03939

Cui, T. J., & Joo, C. (2019). Facilitated diffusion of Argonaute-mediated target search. *RNA Biology*, *16*(9), 1093–1107. https://doi.org/10.1080/15476286.2019.1616353

Darnell, J. C., Van Driesche, S. J., Zhang, C., Hung, K. Y. S., Mele, A., Fraser, C. E., Stone, E. F., Chen, C., Fak, J. J., Chi, S. W., Licatalosi, D. D., Richter, J. D., & Darnell, R. B. (2011). FMRP Stalls Ribosomal Translocation on mRNAs Linked to Synaptic Function and Autism. *Cell*, *146*(2), 247–261. https://doi.org/10.1016/j.cell.2011.06.013

Djuranovic, S., Nahvi, A., & Green, R. (2012). MiRNA-mediated gene silencing by translational repression followed by mRNA deadenylation and decay. *Science (New York, N.Y.)*, *336*(6078), 237–240. https://doi.org/10.1126/science.1215691

Eckhardt, S., Szostak, E., Yang, Z., & Pillai, R. (2011). Artificial Tethering of Argonaute Proteins for Studying their Role in Translational Repression of Target mRNAs. In T. C. Hobman & T. F. Duchaine (Eds.), *Argonaute Proteins: Methods and Protocols* (pp. 191–206). Humana Press. https://doi.org/10.1007/978-1-61779-046-1_13

Edelstein, A., Amodaj, N., Hoover, K., Vale, R., & Stuurman, N. (2010). Computer Control of Microscopes Using μManager. *Current Protocols in Molecular Biology*, *92*(1), 14.20.1-14.20.17. https://doi.org/10.1002/0471142727.mb1420s92

Eichhorn, S. W., Guo, H., McGeary, S. E., Rodriguez-Mias, R. A., Shin, C., Baek, D., Hsu, S., Ghoshal, K., Villén, J., & Bartel, D. P. (2014). MRNA Destabilization Is the Dominant Effect of Mammalian MicroRNAs by the Time Substantial Repression Ensues. *Molecular Cell*, *56*(1), 104–115. https://doi.org/10.1016/j.molcel.2014.08.028

Elkayam, E., Faehnle, C. R., Morales, M., Sun, J., Li, H., & Joshua-Tor, L. (2017). Multivalent Recruitment of Human Argonaute by GW182. *Molecular Cell*, *67*(4), 646-658.e3. https://doi.org/10.1016/j.molcel.2017.07.007

Eulalio, A., Huntzinger, E., & Izaurralde, E. (2008). GW182 interaction with Argonaute is essential for miRNA-mediated translational repression and mRNA decay. *Nature Structural & Molecular Biology*, *15*(4), 346–353. https://doi.org/10.1038/nsmb.1405

Fabian, M. R., Cieplak, M. K., Frank, F., Morita, M., Green, J., Srikumar, T., Nagar, B., Yamamoto, T., Raught, B., Duchaine, T. F., & Sonenberg, N. (2011). MiRNA-mediated deadenylation is orchestrated by GW182 through two conserved motifs that interact with CCR4–NOT. *Nature Structural & Molecular Biology*, *18*(11), 1211–1217. https://doi.org/10.1038/nsmb.2149

Fawell, S., Seery, J., Daikh, Y., Moore, C., Chen, L. L., Pepinsky, B., & Barsoum, J. (1994). Tat-mediated delivery of heterologous proteins into cells. *Proceedings of the National Academy of Sciences*, *91*(2), 664–668. https://doi.org/10.1073/pnas.91.2.664

Felgner, P. L., Gadek, T. R., Holm, M., Roman, R., Chan, H. W., Wenz, M., Northrop, J. P., Ringold, G. M., & Danielsen, M. (1987). Lipofection: A highly efficient, lipid-mediated DNA-transfection procedure. *Proceedings of the National Academy of Sciences of the United States of America*, *84*(21), 7413–7417.

Femino, A. M., Fay, F. S., Fogarty, K., & Singer, R. H. (1998). Visualization of Single RNA Transcripts in Situ. *Science*, *280*(5363), 585–590. https://doi.org/10.1126/science.280.5363.585

Filbin, M. E., & Kieft, J. S. (2009). Toward a structural understanding of IRES RNA function. *Current Opinion in Structural Biology*, *19*(3), 267–276. https://doi.org/10.1016/j.sbi.2009.03.005

Fire, A., Xu, S., Montgomery, M. K., Kostas, S. A., Driver, S. E., & Mello, C. C. (1998). Potent and specific genetic interference by double-stranded RNA in Caenorhabditis elegans. *Nature*, *391*(6669), 806–811. https://doi.org/10.1038/35888

Fonkeu, Y., Kraynyukova, N., Hafner, A.-S., Kochen, L., Sartori, F., Schuman, E. M., & Tchumatchenko, T. (2019). How mRNA Localization and Protein Synthesis Sites Influence Dendritic Protein Distribution and Dynamics. *Neuron*, *103*(6), 1109-1122.e7. https://doi.org/10.1016/j.neuron.2019.06.022

Forero-Quintero, L. S., Raymond, W., Handa, T., Saxton, M., Morisaki, T., Kimura, H., Bertrand, E., Munsky, B., & Stasevich, T. J. (2020). Live-cell imaging reveals the spatiotemporal organization of endogenous RNA polymerase II phosphorylation at a single gene. *BioRxiv*, 2020.04.03.024414. https://doi.org/10.1101/2020.04.03.024414

Forero-Quintero, L. S., Raymond, W., Handa, T., Saxton, M., Morisaki, T., Kimura, H., Bertrand, E., Munsky, B., & Stasevich, T. J. (2021). Live-cell imaging reveals the spatiotemporal organization of endogenous RNA polymerase II phosphorylation at a single gene. *BioRxiv*, 2020.04.03.024414. https://doi.org/10.1101/2020.04.03.024414

Friedman, R. C., Farh, K. K.-H., Burge, C. B., & Bartel, D. P. (2009). Most mammalian mRNAs are conserved targets of microRNAs. *Genome Research*, *19*(1), 92–105. https://doi.org/10.1101/gr.082701.108

Gallegos, J. E., Rogers, M. F., Cialek, C. A., & Peccoud, J. (2020). Rapid, robust plasmid verification by de novo assembly of short sequencing reads. *Nucleic Acids Research*, *48*(18), e106–e106. https://doi.org/10.1093/nar/gkaa727

Gebauer, F., & Hentze, M. W. (2004). Molecular mechanisms of translational control. *Nature Reviews Molecular Cell Biology*, *5*(10), 827–835. https://doi.org/10.1038/nrm1488

Geisler, S., & Coller, J. (2012). Chapter Five - XRN1: A Major 5′ to 3′ Exoribonuclease in Eukaryotic Cells. In G. F. Chanfreau & F. Tamanoi (Eds.), *The Enzymes* (Vol. 31, pp. 97–114). Academic Press. https://doi.org/10.1016/B978-0-12-404740-2.00005-7

Gilmore, A. P., & Romer, L. H. (1996). Inhibition of focal adhesion kinase (FAK) signaling in focal adhesions decreases cell motility and proliferation. *Molecular Biology of the Cell*, *7*(8), 1209–1224. https://doi.org/10.1091/mbc.7.8.1209

Golden, R. J., Chen, B., Li, T., Braun, J., Manjunath, H., Chen, X., Wu, J., Schmid, V., Chang, T.-C., Kopp, F., Ramirez-Martinez, A., Tagliabracci, V. S., Chen, Z. J., Xie, Y., & Mendell, J. T. (2017). An Argonaute phosphorylation cycle promotes microRNA-mediated silencing. *Nature*, *542*(7640), 197–202. https://doi.org/10.1038/nature21025

Gonatopoulos-Pournatzis, T., & Cowling, V. H. (2014). Cap-binding complex (CBC). *Biochemical Journal*, *457*(2), 231–242. https://doi.org/10.1042/BJ20131214

Götzke, H., Kilisch, M., Martínez-Carranza, M., Sograte-Idrissi, S., Rajavel, A., Schlichthaerle, T., Engels, N., Jungmann, R., Stenmark, P., Opazo, F., & Frey, S. (2019). The ALFA-tag is a highly versatile tool for nanobody-based bioscience applications. *Nature Communications*, *10*(1), 1–12. https://doi.org/10.1038/s41467-019-12301-7

Grimson, A., Farh, K. K.-H., Johnston, W. K., Garrett-Engele, P., Lim, L. P., & Bartel, D. P. (2007). MicroRNA Targeting Specificity in Mammals: Determinants beyond Seed Pairing. *Molecular Cell*, *27*(1), 91–105. https://doi.org/10.1016/j.molcel.2007.06.017

Guo, H., Ingolia, N. T., Weissman, J. S., & Bartel, D. P. (2010). Mammalian microRNAs predominantly act to decrease target mRNA levels. *Nature*, *466*(7308), 835–840. https://doi.org/10.1038/nature09267

Hamilton, A. J., & Baulcombe, D. C. (1999). A Species of Small Antisense RNA in Posttranscriptional Gene Silencing in Plants. *Science*, *286*(5441), 950–952. https://doi.org/10.1126/science.286.5441.950

Hayashi-Takanaka, Y., Yamagata, K., Nozaki, N., & Kimura, H. (2009). Visualizing histone modifications in living cells: Spatiotemporal dynamics of H3 phosphorylation during interphase. *Journal of Cell Biology*, *187*(6), 781–790. https://doi.org/10.1083/jcb.200904137

Hayashi-Takanaka, Y., Yamagata, K., Wakayama, T., Stasevich, T. J., Kainuma, T., Tsurimoto, T., Tachibana, M., Shinkai, Y., Kurumizaka, H., Nozaki, N., & Kimura,

H. (2011). Tracking epigenetic histone modifications in single cells using Fab-based live endogenous modification labeling. *Nucleic Acids Research*, *39*(15), 6475–6488. https://doi.org/10.1093/nar/gkr343

Heck, A. M., & Wilusz, J. (2018). The Interplay between the RNA Decay and Translation Machinery in Eukaryotes. *Cold Spring Harbor Perspectives in Biology*, *10*(5), a032839. https://doi.org/10.1101/cshperspect.a032839

Hendrickson, D. G., Hogan, D. J., McCullough, H. L., Myers, J. W., Herschlag, D., Ferrell, J. E., & Brown, P. O. (2009). Concordant Regulation of Translation and mRNA Abundance for Hundreds of Targets of a Human microRNA. *PLoS Biology*, *7*(11), e1000238. https://doi.org/10.1371/journal.pbio.1000238

Hershey, J. W. B., Sonenberg, N., & Mathews, M. B. (2019). Principles of Translational Control. *Cold Spring Harbor Perspectives in Biology*, *11*(9), a032607. https://doi.org/10.1101/cshperspect.a032607

Hickey, K. L., Dickson, K., Cogan, J. Z., Replogle, J. M., Schoof, M., D'Orazio, K. N., Sinha, N. K., Hussmann, J. A., Jost, M., Frost, A., Green, R., Weissman, J. S., & Kostova, K. K. (2020). GIGYF2 and 4EHP Inhibit Translation Initiation of Defective Messenger RNAs to Assist Ribosome-Associated Quality Control. *Molecular Cell*, *79*(6), 950-962.e6. https://doi.org/10.1016/j.molcel.2020.07.007

Hinnebusch, A. G., Ivanov, I. P., & Sonenberg, N. (2016). Translational control by 5′-untranslated regions of eukaryotic mRNAs. *Science*, *352*(6292), 1413–1416. https://doi.org/10.1126/science.aad9868

Hoek, T. A., Khuperkar, D., Lindeboom, R. G. H., Sonneveld, S., Verhagen, B. M. P., Boersma, S., Vermeulen, M., & Tanenbaum, M. E. (2019). Single-Molecule Imaging Uncovers Rules Governing Nonsense-Mediated mRNA Decay. *Molecular Cell*, *75*(2), 324-339.e11. https://doi.org/10.1016/j.molcel.2019.05.008

Hoernes, T. P., Hüttenhofer, A., & Erlacher, M. D. (2016). mRNA modifications: Dynamic regulators of gene expression? *RNA Biology*, *13*(9), 760–765. https://doi.org/10.1080/15476286.2016.1203504

Horvathova, I., Voigt, F., Kotrys, A. V., Zhan, Y., Artus-Revel, C. G., Eglinger, J., Stadler, M. B., Giorgetti, L., & Chao, J. A. (2017). The Dynamics of mRNA Turnover Revealed by Single-Molecule Imaging in Single Cells. *Molecular Cell*, *68*(3), 615-625.e9. https://doi.org/10.1016/j.molcel.2017.09.030

Horvathova, I., Voigt, F., Kotrys, A. V., Zhan, Y., Stadler, M. B., Giorgetti, L., & Chao, J. A. (2017). The Dynamics of mRNA Turnover Revealed by Single-Molecule Imaging in Single Cells. *Molecular Cell*, *68*(3), 615-625.e9. https://doi.org/10.1016/j.molcel.2017.09.030

Hsu, C. L., & Stevens, A. (1993). Yeast cells lacking 5'—>3' exoribonuclease 1 contain mRNA species that are poly(A) deficient and partially lack the 5' cap structure. *Molecular and Cellular Biology*, *13*(8), 4826–4835. https://doi.org/10.1128/mcb.13.8.4826

Huang, M.-T. (1975). Harringtonine, an Inhibitor of Initiation of Protein Biosynthesis. *Molecular Pharmacology*, *11*(5), 511–519.

Hubstenberger, A., Courel, M., Bénard, M., Souquere, S., Ernoult-Lange, M., Chouaib, R., Yi, Z., Morlot, J.-B., Munier, A., Fradet, M., Daunesse, M., Bertrand, E.,

Pierron, G., Mozziconacci, J., Kress, M., & Weil, D. (2017). P-Body Purification Reveals the Condensation of Repressed mRNA Regulons. *Molecular Cell*, *68*(1), 144-157.e5. https://doi.org/10.1016/j.molcel.2017.09.003

Hulsik, D. L., Liu, Y., Strokappe, N. M., Battella, S., Khattabi, M. E., McCoy, L. E., Sabin, C., Hinz, A., Hock, M., Macheboeuf, P., Bonvin, A. M. J. J., Langedijk, J. P. M., Davis, D., Quigley, A. F., Aasa-Chapman, M. M. I., Seaman, M. S., Ramos, A., Poignard, P., Favier, A., … Rutten, L. (2013). A gp41 MPER-specific Llama VHH Requires a Hydrophobic CDR3 for Neutralization but not for Antigen Recognition. *PLOS Pathogens*, *9*(3), e1003202. https://doi.org/10.1371/journal.ppat.1003202

Humphreys, D. T., Westman, B. J., Martin, D. I. K., & Preiss, T. (2005). MicroRNAs control translation initiation by inhibiting eukaryotic initiation factor 4E/cap and poly(A) tail function. *Proceedings of the National Academy of Sciences of the United States of America*, *102*(47), 16961–16966. https://doi.org/10.1073/pnas.0506482102

Huntzinger, E., Kuzuoğlu-Öztürk, D., Braun, J. E., Eulalio, A., Wohlbold, L., & Izaurralde, E. (2013). The interactions of GW182 proteins with PABP and deadenylases are required for both translational repression and degradation of miRNA targets. *Nucleic Acids Research*, *41*(2), 978–994. https://doi.org/10.1093/nar/gks1078

Ingolia, N. T. (2016). Ribosome Footprint Profiling of Translation throughout the Genome. *Cell*, *165*(1), 22–33. https://doi.org/10.1016/j.cell.2016.02.066

Ingolia, N. T., Hussmann, J. A., & Weissman, J. S. (2019). Ribosome Profiling: Global Views of Translation. *Cold Spring Harbor Perspectives in Biology*, *11*(5), a032698. https://doi.org/10.1101/cshperspect.a032698

Ingolia, N. T., Lareau, L. F., & Weissman, J. S. (2011). Ribosome Profiling of Mouse Embryonic Stem Cells Reveals the Complexity and Dynamics of Mammalian Proteomes. *Cell*, *147*(4), 789–802. https://doi.org/10.1016/j.cell.2011.10.002

Introduction to Fluorescence Microscopy | Protocol. (n.d.). Retrieved April 19, 2021, from https://www.jove.com/t/5040/introduction-to-fluorescence-microscopy

Jedlitzke, B., & Mootz, H. D. (2021). Photocaged Nanobodies Delivered into Cells for Light Activation of Biological Processes. *ChemPhotoChem*, *5*(1), 22–25. https://doi.org/10.1002/cptc.202000163

Ji, N. (2017). Adaptive optical fluorescence microscopy. *Nature Methods*, *14*(4), 374–380. https://doi.org/10.1038/nmeth.4218

Jin, H. Y., Gonzalez-Martin, A., Miletic, A. V., Lai, M., Knight, S., Sabouri-Ghomi, M., Head, S. R., Macauley, M. S., Rickert, R. C., & Xiao, C. (2015). Transfection of microRNA Mimics Should Be Used with Caution. *Frontiers in Genetics*, *6*. https://doi.org/10.3389/fgene.2015.00340

Jinek, M., Coyle, S. M., & Doudna, J. A. (2011). Coupled 5′ Nucleotide Recognition and Processivity in Xrn1-Mediated mRNA Decay. *Molecular Cell*, *41*(5), 600–608. https://doi.org/10.1016/j.molcel.2011.02.004

Jonas, S., & Izaurralde, E. (2015). Towards a molecular understanding of microRNA-mediated gene silencing. *Nature Reviews Genetics*, *16*(7), 421–433. https://doi.org/10.1038/nrg3965

Jones, S. A., Shim, S.-H., He, J., & Zhuang, X. (2011). Fast, three-dimensional super-resolution imaging of live cells. *Nature Methods*, *8*(6), 499–505. https://doi.org/10.1038/nmeth.1605

Jung, H., Gkogkas, C. G., Sonenberg, N., & Holt, C. E. (2014). Remote Control of Gene Function by Local Translation. *Cell*, *157*(1), 26–40. https://doi.org/10.1016/j.cell.2014.03.005

Juszkiewicz, S., Chandrasekaran, V., Lin, Z., Kraatz, S., Ramakrishnan, V., & Hegde, R. S. (2018). ZNF598 Is a Quality Control Sensor of Collided Ribosomes. *Molecular Cell*, *72*(3), 469-481.e7. https://doi.org/10.1016/j.molcel.2018.08.037

Juszkiewicz, S., Slodkowicz, G., Lin, Z., Freire-Pritchett, P., Peak-Chew, S.-Y., & Hegde, R. S. (2020, July 13). *Ribosome collisions trigger cis-acting feedback inhibition of translation initiation*. ELife; eLife Sciences Publications Limited. https://doi.org/10.7554/eLife.60038

Kawano, F., Suzuki, H., Furuya, A., & Sato, M. (2015). Engineered pairs of distinct photoswitches for optogenetic control of cellular proteins. *Nature Communications*, *6*(1), 6256. https://doi.org/10.1038/ncomms7256

Khong, A., & Parker, R. (2018). MRNP architecture in translating and stress conditions reveals an ordered pathway of mRNP compactionTranslating and nontranslating mRNP architecture. *The Journal of Cell Biology*, *217*(12), 4124–4140. https://doi.org/10.1083/jcb.201806183

Koch, A., Aguilera, L., Morisaki, T., Munsky, B., & Stasevich, T. J. (2020). Quantifying the dynamics of IRES and cap translation with single-molecule resolution in live cells. *Nature Structural & Molecular Biology*, *27*(12), 1095–1104.

Kozak, M. (1986). Point mutations define a sequence flanking the AUG initiator codon that modulates translation by eukaryotic ribosomes. *Cell*, *44*(2), 283–292. https://doi.org/10.1016/0092-8674(86)90762-2

Kozak, M. (1987). At least six nucleotides preceding the AUG initiator codon enhance translation in mammalian cells. *Journal of Molecular Biology*, *196*(4), 947–950. https://doi.org/10.1016/0022-2836(87)90418-9

Kozomara, A., & Griffiths-Jones, S. (2014). miRBase: Annotating high confidence microRNAs using deep sequencing data. *Nucleic Acids Research*, *42*(D1), D68–D73. https://doi.org/10.1093/nar/gkt1181

Kuersten, S., Radek, A., Vogel, C., & Penalva, L. O. F. (2013). Translation regulation gets its 'omics' moment. *WIREs RNA*, *4*(6), 617–630. https://doi.org/10.1002/wrna.1173

Kumar, P., Nagarajan, A., & Uchil, P. D. (2018). Analysis of Cell Viability by the MTT Assay. *Cold Spring Harbor Protocols*, *2018*(6), pdb.prot095505. https://doi.org/10.1101/pdb.prot095505

Langille, J. J., Ginzberg, K., & Sossin, W. S. (2019). Polysomes identified by live imaging of nascent peptides are stalled in hippocampal and cortical neurites. *Learning & Memory*, *26*(9), 351–362. https://doi.org/10.1101/lm.049965.119

Latallo, M. J., Livingston, N. M., & Wu, B. (2019). Translation imaging of single mRNAs in established cell lines and primary cultured neurons. *Methods*, *162–163*, 12–22. https://doi.org/10.1016/j.ymeth.2019.03.021

Leung, A. K. L., Calabrese, J. M., & Sharp, P. A. (2006). Quantitative analysis of Argonaute protein reveals microRNA-dependent localization to stress granules. *Proceedings of the National Academy of Sciences*, *103*(48), 18125–18130. https://doi.org/10.1073/pnas.0608845103

LGC Biosearch Technologies. (n.d.). *Stellaris RNA FISH Protocol for Adherent Cells*. LGC Biosearch Technologies. Retrieved December 6, 2019, from https://www.biosearchtech.com/support/resources/stellaris-protocols

Lian, S. L., Li, S., Abadal, G. X., Pauley, B. A., Fritzler, M. J., & Chan, E. K. L. (2009). The C-terminal half of human Ago2 binds to multiple GW-rich regions of GW182 and requires GW182 to mediate silencing. *RNA*, *15*(5), 804–813. https://doi.org/10.1261/rna.1229409

Lin, Y., Protter, D. S. W., Rosen, M. K., & Parker, R. (2015). Formation and Maturation of Phase-Separated Liquid Droplets by RNA-Binding Proteins. *Molecular Cell*, *60*(2), 208–219. https://doi.org/10.1016/j.molcel.2015.08.018

Liu, J., Rivas, F. V., Wohlschlegel, J., Yates, J. R., Parker, R., & Hannon, G. J. (2005). A role for the P-body component GW182 in microRNA function. *Nature Cell Biology*, *7*(12), 1261–1266. https://doi.org/10.1038/ncb1333

Liu, J., Valencia-Sanchez, M. A., Hannon, G. J., & Parker, R. (2005). MicroRNA-dependent localization of targeted mRNAs to mammalian P-bodies. *Nature Cell Biology*, *7*(7), 719–723. https://doi.org/10.1038/ncb1274

Luo, E.-C., Nathanson, J. L., Tan, F. E., Schwartz, J. L., Schmok, J. C., Shankar, A., Markmiller, S., Yee, B. A., Sathe, S., Pratt, G. A., Scaletta, D. B., Ha, Y., Hill, D. E., Aigner, S., & Yeo, G. W. (2020). Large-scale tethered function assays identify factors that regulate mRNA stability and translation. *Nature Structural & Molecular Biology*, *27*(10), 989–1000. https://doi.org/10.1038/s41594-020-0477-6

Lyon, K., Aguilera, L. U., Morisaki, T., Munsky, B., & Stasevich, T. J. (2019). Live-Cell Single RNA Imaging Reveals Bursts of Translational Frameshifting. *Molecular Cell*, *75*(1), 172-183.e9. https://doi.org/10.1016/j.molcel.2019.05.002

Mateju, D., Eichenberger, B., Eglinger, J., Roth, G., & Chao, J. (2020). Single-molecule imaging reveals translation of mRNAs localized to stress granules. *BioRxiv*, 2020.03.31.018093. https://doi.org/10.1101/2020.03.31.018093

Mateju, D., Eichenberger, B., Voigt, F., Eglinger, J., Roth, G., & Chao, J. A. (2020). Single-Molecule Imaging Reveals Translation of mRNAs Localized to Stress Granules. *Cell*, *183*(7), 1801-1812.e13. https://doi.org/10.1016/j.cell.2020.11.010

Matheny, T., Rao, B. S., & Parker, R. (2019). Transcriptome-Wide Comparison of Stress Granules and P-Bodies Reveals that Translation Plays a Major Role in RNA Partitioning. *Molecular and Cellular Biology*, *39*(24). https://doi.org/10.1128/MCB.00313-19

Mathonnet, G., Fabian, M. R., Svitkin, Y. V., Parsyan, A., Huck, L., Murata, T., Biffo, S., Merrick, W. C., Darzynkiewicz, E., Pillai, R. S., Filipowicz, W., Duchaine, T. F., & Sonenberg, N. (2007). MicroRNA Inhibition of Translation Initiation in Vitro by

Targeting the Cap-Binding Complex eIF4F. *Science*, *317*(5845), 1764–1767. https://doi.org/10.1126/science.1146067

Mayr, C., & Bartel, D. P. (2009). Widespread Shortening of 3′UTRs by Alternative Cleavage and Polyadenylation Activates Oncogenes in Cancer Cells. *Cell*, *138*(4), 673–684. https://doi.org/10.1016/j.cell.2009.06.016

McNeil, P. L., Murphy, R. F., Lanni, F., & Taylor, D. L. (1984). A method for incorporating macromolecules into adherent cells. *The Journal of Cell Biology*, *98*(4), 1556–1564. https://doi.org/10.1083/jcb.98.4.1556

McNeil, P. L., & Warder, E. (1987). Glass beads load macromolecules into living cells. *Journal of Cell Science*, *88*(5), 669–678.

Meister, G., Landthaler, M., Peters, L., Chen, P. Y., Urlaub, H., Lührmann, R., & Tuschl, T. (2005). Identification of Novel Argonaute-Associated Proteins. *Current Biology*, *15*(23), 2149–2155. https://doi.org/10.1016/j.cub.2005.10.048

Memedula, S., & Belmont, A. S. (2003). Sequential Recruitment of HAT and SWI/SNF Components to Condensed Chromatin by VP16. *Current Biology*, *13*(3), 241–246. https://doi.org/10.1016/S0960-9822(03)00048-4

Moon, S. L. (2020). Coupling of translation quality control and mRNA targeting to stress granules. *J Cell Biol*, *219*(8). https://doi.org/10.1083

Moon, S. L., Morisaki, T., Khong, A., Lyon, K., Parker, R., & Stasevich, T. J. (2019). Multicolor single-molecule tracking of mRNA interactions with RNP granules. *Nature Cell Biology*, *21*(2), 162–168. https://doi.org/10.1038/s41556-018-0263-4

Morisaki, T., Lyon, K., DeLuca, K. F., DeLuca, J. G., English, B. P., Zhang, Z., Lavis, L. D., Grimm, J. B., Viswanathan, S., Looger, L. L., Lionnet, T., & Stasevich, T. J. (2016). Real-time quantification of single RNA translation dynamics in living cells. *Science*, *352*(6292), 1425–1429. https://doi.org/10.1126/science.aaf0899

Morisaki, Tatsuya, Lyon, K., DeLuca, K., DeLuca, J., English, B., Zhang, Z., Lavis, L. D., Grimm, J. B., Viswanathan, S., Looger, L. L., Lionnet, T., & Stasevich, T. J. (2016). Real-time quantification of single RNA translation dynamics in living cells. *Science*, *352*(6292), 1425–1429. https://doi.org/10.1126/science.aaf0899

Morisaki, Tatsuya, & Stasevich, T. J. (2018). Quantifying Single mRNA Translation Kinetics in Living Cells. *Cold Spring Harbor Perspectives in Biology*, *10*(11), a032078. https://doi.org/10.1101/cshperspect.a032078

Mueller, F., Senecal, A., Tantale, K., Marie-Nelly, H., Ly, N., Collin, O., Basyuk, E., Bertrand, E., Darzacq, X., & Zimmer, C. (2013). FISH-quant: Automatic counting of transcripts in 3D FISH images. *Nature Methods*, *10*(4), 277–278. https://doi.org/10.1038/nmeth.2406

Mugridge, J. S., Ziemniak, M., Jemielity, J., & Gross, J. D. (2016). Structural basis of mRNA-cap recognition by Dcp1–Dcp2. *Nature Structural & Molecular Biology*, *23*(11), 987–994. https://doi.org/10.1038/nsmb.3301

napari contributors. (2019). *napari: A multi-dimensional image viewer for python*. https://doi.org/10.5281/zenodo.3555620

Nathans, D. (1964). PUROMYCIN INHIBITION OF PROTEIN SYNTHESIS: INCORPORATION OF PUROMYCIN INTO PEPTIDE CHAINS. *Proceedings of*

the National Academy of Sciences of the United States of America, *51*(4), 585–592.

Nottrott, S., Simard, M. J., & Richter, J. D. (2006). Human let-7a miRNA blocks protein production on actively translating polyribosomes. *Nature Structural & Molecular Biology*, *13*(12), 1108–1114. https://doi.org/10.1038/nsmb1173

Ortiz, D., Baldwin, M. M., & Lucas, J. J. (1987). Transient correction of genetic defects in cultured animal cells by introduction of functional proteins. *Molecular and Cellular Biology*, *7*(8), 3012–3017. https://doi.org/10.1128/MCB.7.8.3012

Palmiter, R. D. (1975). Quantitation of parameters that determine the rate of ovalbumin synthesis. *Cell*, *4*(3), 189–197. https://doi.org/10.1016/0092-8674(75)90167-1

Petersen, C. P., Bordeleau, M.-E., Pelletier, J., & Sharp, P. A. (2006). Short RNAs Repress Translation after Initiation in Mammalian Cells. *Molecular Cell*, *21*(4), 533–542. https://doi.org/10.1016/j.molcel.2006.01.031

Piao, X., Zhang, X., Wu, L., & Belasco, J. G. (2010). CCR4-NOT Deadenylates mRNA Associated with RNA-Induced Silencing Complexes in Human Cells. *Molecular and Cellular Biology*, *30*(6), 1486–1494. https://doi.org/10.1128/MCB.01481-09

Pichon, X., Bastide, A., Safieddine, A., Chouaib, R., Samacoits, A., Basyuk, E., Peter, M., Mueller, F., & Bertrand, E. (2016). Visualization of single endogenous polysomes reveals the dynamics of translation in live human cells. *The Journal of Cell Biology*, *214*(6), 769–781. https://doi.org/10.1083/jcb.201605024

Pichon, X., Robert, M.-C., Bertrand, E., Singer, R. H., & Tutucci, E. (2020). New Generations of MS2 Variants and MCP Fusions to Detect Single mRNAs in Living Eukaryotic Cells. In M. Heinlein (Ed.), *RNA Tagging: Methods and Protocols* (pp. 121–144). Springer US. https://doi.org/10.1007/978-1-0716-0712-1_7

Pillai, R. S., Artus, C. G., & Filipowicz, W. (2004). Tethering of human Ago proteins to mRNA mimics the miRNA-mediated repression of protein synthesis. *RNA*, *10*(10), 1518–1525. https://doi.org/10.1261/rna.7131604

Pillai, R. S., Bhattacharyya, S. N., Artus, C. G., Zoller, T., Cougot, N., Basyuk, E., Bertrand, E., & Filipowicz, W. (2005). Inhibition of Translational Initiation by Let-7 MicroRNA in Human Cells. *Science*, *309*(5740), 1573–1576. https://doi.org/10.1126/science.1115079

Pitchiaya, S., Androsavich, J. R., & Walter, N. G. (2012). Intracellular single molecule microscopy reveals two kinetically distinct pathways for microRNA assembly. *EMBO Reports*, *13*(8), 709–715. https://doi.org/10.1038/embor.2012.85

Pitchiaya, S., Mourao, M. D. A., Jalihal, A. P., Xiao, L., Jiang, X., Chinnaiyan, A. M., Schnell, S., & Walter, N. G. (2019). Dynamic Recruitment of Single RNAs to Processing Bodies Depends on RNA Functionality. *Molecular Cell*, *74*(3), 521-533.e6. https://doi.org/10.1016/j.molcel.2019.03.001

Potter, H. (2003). Transfection by Electroporation. *Curr Protoc Mol Biol*, *Chapter 9: Unit9-3*. https://doi.org/doi:10.1002/0471142727.mb0903s62

Power, R. M., & Huisken, J. (2017). A guide to light-sheet fluorescence microscopy for multiscale imaging. *Nature Methods*, *14*(4), 360–373. https://doi.org/10.1038/nmeth.4224

Prior, T. I., FitzGerald, D. J., & Pastan, I. (1992). Translocation mediated by domain II of Pseudomonas exotoxin A: Transport of barnase into the cytosol. *Biochemistry*, *31*(14), 3555–3559. https://doi.org/10.1021/bi00129a001

Raj, A., Bogaard, P. van den, Rifkin, S. A., Oudenaarden, A. van, & Tyagi, S. (2008). Imaging individual mRNA molecules using multiple singly labeled probes. *Nature Methods*, *5*(10), 877–879. https://doi.org/10.1038/nmeth.1253

Ricci, E. P., Limousin, T., Soto-Rifo, R., Rubilar, P. S., Decimo, D., & Ohlmann, T. (2013). MiRNA repression of translation in vitro takes place during 43S ribosomal scanning. *Nucleic Acids Research*, *41*(1), 586–598. https://doi.org/10.1093/nar/gks1076

Richter, J. D., & Coller, J. (2015). Pausing on Polyribosomes: Make Way for Elongation in Translational Control. *Cell*, *163*(2), 292–300. https://doi.org/10.1016/j.cell.2015.09.041

Roux, P. P., & Topisirovic, I. (2018). Signaling Pathways Involved in the Regulation of mRNA Translation. *Molecular and Cellular Biology*, *38*(12), 26.

Rouya, C., Siddiqui, N., Morita, M., Duchaine, T. F., Fabian, M. R., & Sonenberg, N. (2014). Human DDX6 effects miRNA-mediated gene silencing via direct binding to CNOT1. *RNA*, *20*(9), 1398–1409. https://doi.org/10.1261/rna.045302.114

Ruijtenberg, S., Sonneveld, S., Cui, T. J., Logister, I., de Steenwinkel, D., Xiao, Y., MacRae, I. J., Joo, C., & Tanenbaum, M. E. (2020). MRNA structural dynamics shape Argonaute-target interactions. *Nature Structural & Molecular Biology*, *27*(9), 790–801. https://doi.org/10.1038/s41594-020-0461-1

Sabri, A. (2020). Elucidating the origin of heterogeneous anomalous diffusion in the cytoplasm of mammalian cells. *Phys. Rev. Lett.*, *125*(5). https://doi.org/053901

Salomon, W. E., Jolly, S. M., Moore, M. J., Zamore, P. D., & Serebrov, V. (2015). Single-Molecule Imaging Reveals that Argonaute Reshapes the Binding Properties of Its Nucleic Acid Guides. *Cell*, *162*(1), 84–95. https://doi.org/10.1016/j.cell.2015.06.029

Sato, Y., Mukai, M., Ueda, J., Muraki, M., Stasevich, T. J., Horikoshi, N., Kujirai, T., Kita, H., Kimura, T., Hira, S., Okada, Y., Hayashi-Takanaka, Y., Obuse, C., Kurumizaka, H., Kawahara, A., Yamagata, K., Nozaki, N., & Kimura, H. (2013). Genetically encoded system to track histone modification in vivo. *Scientific Reports*, *3*, 2436. https://doi.org/10.1038/srep02436

Sato, Y., Stasevich, T. J., & Kimura, H. (2018). Visualizing the Dynamics of Inactive X Chromosomes in Living Cells Using Antibody-Based Fluorescent Probes. In T. Sado (Ed.), *X-Chromosome Inactivation: Methods and Protocols* (pp. 91–102). Springer. https://doi.org/10.1007/978-1-4939-8766-5_8

Schenborn, E. T., & Goiffon, V. (2000). DEAE-Dextran Transfection of Mammalian Cultured Cells. In M. J. Tymms (Ed.), *Transcription Factor Protocols* (pp. 147–153). Humana Press. https://doi.org/10.1385/1-59259-686-X:147

Scherer, L. J., & Rossi, J. J. (2003). Approaches for the sequence-specific knockdown of mRNA. *Nature Biotechnology*, *21*(12), 1457–1465. https://doi.org/10.1038/nbt915

Schindelin, J., Arganda-Carreras, I., Frise, E., Kaynig, V., Longair, M., Pietzsch, T., Preibisch, S., Rueden, C., Saalfeld, S., Schmid, B., Tinevez, J.-Y., White, D. J., Hartenstein, V., Eliceiri, K., Tomancak, P., & Cardona, A. (2012). Fiji: An open-source platform for biological-image analysis. *Nature Methods*, *9*(7), 676–682. https://doi.org/10.1038/nmeth.2019

Schirle, N. T., & MacRae, I. J. (2012). The Crystal Structure of Human Argonaute2. *Science*, *336*(6084), 1037–1040. https://doi.org/10.1126/science.1221551

Schwanhäusser, B., Busse, D., Li, N., Dittmar, G., Schuchhardt, J., Wolf, J., Chen, W., & Selbach, M. (2011). Global quantification of mammalian gene expression control. *Nature*, *473*(7347), 337–342. https://doi.org/10.1038/nature10098

Sen, G. L., & Blau, H. M. (2005). Argonaute 2/RISC resides in sites of mammalian mRNA decay known as cytoplasmic bodies. *Nature Cell Biology*, *7*(6), 633–636. https://doi.org/10.1038/ncb1265

Sepulveda, G., Antkowiak, M., Brust-Mascher, I., Mahe, K., Ou, T., Castro, N. M., Christensen, L. N., Cheung, L., Jiang, X., Yoon, D., Huang, B., & Jao, L.-E. (2018). Co-translational protein targeting facilitates centrosomal recruitment of PCNT during centrosome maturation in vertebrates. *ELife*, *7*, e34959. https://doi.org/10.7554/eLife.34959

Sheu-Gruttadauria, J., & MacRae, I. J. (2018). Phase Transitions in the Assembly and Function of Human miRISC. *Cell*, *173*(4), 946-957.e16. https://doi.org/10.1016/j.cell.2018.02.051

Shoemaker, C. J., & Green, R. (2012). Translation drives mRNA quality control. *Nature Structural & Molecular Biology*, *19*(6), 594–601. https://doi.org/10.1038/nsmb.2301

Simms, C. L., Hudson, B. H., Mosior, J. W., Rangwala, A. S., & Zaher, H. S. (2014). An Active Role for the Ribosome in Determining the Fate of Oxidized mRNA. *Cell Reports*, *9*(4), 1256–1264. https://doi.org/10.1016/j.celrep.2014.10.042

Simsek, D., & Barna, M. (2017). An emerging role for the ribosome as a nexus for post-translational modifications. *Current Opinion in Cell Biology*, *45*, 92–101. https://doi.org/10.1016/j.ceb.2017.02.010

Sonenberg, N., & Hinnebusch, A. G. (2009). Regulation of Translation Initiation in Eukaryotes: Mechanisms and Biological Targets. *Cell*, *136*(4), 731–745. https://doi.org/10.1016/j.cell.2009.01.042

Spiltoir, J. I., & Tucker, C. L. (2019). Photodimerization systems for regulating protein–protein interactions with light. *Current Opinion in Structural Biology*, *57*, 1–8. https://doi.org/10.1016/j.sbi.2019.01.021

Standart, N., & Weil, D. (2018). P-Bodies: Cytosolic Droplets for Coordinated mRNA Storage. *Trends in Genetics*, *34*(8), 612–626. https://doi.org/10.1016/j.tig.2018.05.005

Stanton, B. Z., Chory, E. J., & Crabtree, G. R. (2018). Chemically induced proximity in biology and medicine. *Science*, *359*(6380). https://doi.org/10.1126/science.aao5902

Stasevich, T. J., Hayashi-Takanaka, Y., Sato, Y., Maehara, K., Ohkawa, Y., Sakata-Sogawa, K., Tokunaga, M., Nagase, T., Nozaki, N., McNally, J. G., & Kimura, H.

(2014). Regulation of RNA polymerase II activation by histone acetylation in single living cells. *Nature*, *516*(7530), 272–275. https://doi.org/10.1038/nature13714

Stewart, M. P., Sharei, A., Ding, X., Sahay, G., Langer, R., & Jensen, K. F. (2016). In vitro and ex vivo strategies for intracellular delivery. *Nature*, *538*(7624), 183–192. https://doi.org/10.1038/nature19764

Stewart, M., 2019. Polyadenylation and nuclear export of mRNAs. *Journal of Biological Chemistry*, 294(9), 2977-2987. https://doi.org/10.1074/jbc.REV118.005594

Subtelny, A. O., Eichhorn, S. W., Chen, G. R., Sive, H., & Bartel, D. P. (2014). Poly(A)-tail profiling reveals an embryonic switch in translational control. *Nature*, *508*(7494), 66–71. https://doi.org/10.1038/nature13007

Svitkin, Y. V., Evdokimova, V. M., Brasey, A., Pestova, T. V., Fantus, D., Yanagiya, A., Imataka, H., Skabkin, M. A., Ovchinnikov, L. P., Merrick, W. C., & Sonenberg, N. (2009). General RNA-binding proteins have a function in poly(A)-binding protein-dependent translation. *The EMBO Journal*, *28*(1), 58–68. https://doi.org/10.1038/emboj.2008.259

Tahmasebi, S., Sonenberg, N., Hershey, J. W. B., & Mathews, M. B. (2019). Protein Synthesis and Translational Control: A Historical Perspective. *Cold Spring Harbor Perspectives in Biology*, *11*(9), a035584. https://doi.org/10.1101/cshperspect.a035584

Taliaferro, J. M. (2019). Classical and emerging techniques to identify and quantify localized RNAs. *WIREs RNA*, *10*(5), e1542. https://doi.org/10.1002/wrna.1542

Tanenbaum, M. E., Gilbert, L. A., Qi, L. S., Weissman, J. S., & Vale, R. D. (2014). A Protein-Tagging System for Signal Amplification in Gene Expression and Fluorescence Imaging. *Cell*, *159*(3), 635–646. https://doi.org/10.1016/j.cell.2014.09.039

TargetScanHuman 7.2. (n.d.). Retrieved January 18, 2021, from http://www.targetscan.org/vert_72/

Taslimi, A., Vrana, J. D., Chen, D., Borinskaya, S., Mayer, B. J., Kennedy, M. J., & Tucker, C. L. (2014). An optimized optogenetic clustering tool for probing protein interaction and function. *Nature Communications*, *5*(1), 4925. https://doi.org/10.1038/ncomms5925

Tat, T. T., Maroney, P. A., Chamnongpol, S., Coller, J., & Nilsen, T. W. (2016). Cotranslational microRNA mediated messenger RNA destabilization. *ELife*, *5*, e12880. https://doi.org/10.7554/eLife.12880

T. Emerson, N., Hsia, C.-H., U. Rafalska-Metcalf, I., & Yang, H. (2014). Mechanodelivery of nanoparticles to the cytoplasm of living cells. *Nanoscale*, *6*(9), 4538–4543. https://doi.org/10.1039/C3NR06468A

Tokunaga, M., Imamoto, N., & Sakata-Sogawa, K. (2008). Highly inclined thin illumination enables clear single-molecule imaging in cells. *Nature Methods*, *5*(2), 159–161. https://doi.org/10.1038/nmeth1171

Treeck, B. V., & Parker, R. (2019). Principles of Stress Granules Revealed by Imaging Approaches. *Cold Spring Harbor Perspectives in Biology*, *11*(2), a033068. https://doi.org/10.1101/cshperspect.a033068

Tsang, B., Arsenault, J., Vernon, R. M., Lin, H., Sonenberg, N., Wang, L.-Y., Bah, A., & Forman-Kay, J. D. (2019). Phosphoregulated FMRP phase separation models activity-dependent translation through bidirectional control of mRNA granule formation. *Proceedings of the National Academy of Sciences*, *116*(10), 4218–4227. https://doi.org/10.1073/pnas.1814385116

Tsanov, N., Samacoits, A., Chouaib, R., Traboulsi, A.-M., Gostan, T., Weber, C., Zimmer, C., Zibara, K., Walter, T., Peter, M., Bertrand, E., & Mueller, F. (2016). SmiFISH and FISH-quant – a flexible single RNA detection approach with super-resolution capability. *Nucleic Acids Research*, *44*(22), e165–e165. https://doi.org/10.1093/nar/gkw784

Tutucci, E., Vera, M., Biswas, J., Garcia, J., Parker, R., & Singer, R. H. (2018). An improved MS2 system for accurate reporting of the mRNA life cycle. *Nature Methods*, *15*(1), 81–89. https://doi.org/10.1038/nmeth.4502

Vicens, Q., Kieft, J. S., & Rissland, O. S. (2018). Revisiting the Closed-Loop Model and the Nature of mRNA 5′–3′ Communication. *Molecular Cell*, *72*(5), 805–812. https://doi.org/10.1016/j.molcel.2018.10.047

Viswanathan, S., Williams, M. E., Bloss, E. B., Stasevich, T. J., Speer, C. M., Nern, A., Pfeiffer, B. D., Hooks, B. M., Li, W.-P., English, B. P., Tian, T., Henry, G. L., Macklin, J. J., Patel, R., Gerfen, C. R., Zhuang, X., Wang, Y., Rubin, G. M., & Looger, L. L. (2015). High-performance probes for light and electron microscopy. *Nature Methods*, *12*(6), 568–576. https://doi.org/10.1038/nmeth.3365

Voigt, F., Gerbracht, J. V., Boehm, V., Horvathova, I., Eglinger, J., Chao, J. A., & Gehring, N. H. (2019). Detection and quantification of RNA decay intermediates using XRN1-resistant reporter transcripts. *Nature Protocols*, *14*(5), 1603–1633. https://doi.org/10.1038/s41596-019-0152-8

Voigt, F., Zhang, H., Cui, X. A., Triebold, D., Liu, A. X., Eglinger, J., Lee, E. S., Chao, J. A., & Palazzo, A. F. (2017). Single-Molecule Quantification of Translation-Dependent Association of mRNAs with the Endoplasmic Reticulum. *Cell Reports*, *21*(13), 3740–3753. https://doi.org/10.1016/j.celrep.2017.12.008

Wakiyama, M., Takimoto, K., Ohara, O., & Yokoyama, S. (2007). Let-7 microRNA-mediated mRNA deadenylation and translational repression in a mammalian cell-free system. *Genes & Development*, *21*(15), 1857–1862. https://doi.org/10.1101/gad.1566707

Walev, I., Bhakdi, S. C., Hofmann, F., Djonder, N., Valeva, A., Aktories, K., & Bhakdi, S. (2001). Delivery of proteins into living cells by reversible membrane permeabilization with streptolysin-O. *Proceedings of the National Academy of Sciences of the United States of America*, *98*(6), 3185–3190. https://doi.org/10.1073/pnas.051429498

Wang, C., Han, B., Zhou, R., & Zhuang, X. (2016). Real-Time Imaging of Translation on Single mRNA Transcripts in Live Cells. *Cell*, *165*(4), 990–1001. https://doi.org/10.1016/j.cell.2016.04.040

Waskom, M. (2020). Mwaskom/seaborn. *Zenodo*, *latest*. https://doi.org/10.5281/zenodo.592845

Wen, J.-D., Lancaster, L., Hodges, C., Zeri, A.-C., Yoshimura, S. H., Noller, H. F., Bustamante, C., & Tinoco, I. (2008). Following translation by single ribosomes

one codon at a time. *Nature*, *452*(7187), 598–603. https://doi.org/10.1038/nature06716

Wilbertz, J. H., Voigt, F., Horvathova, I., Roth, G., Zhan, Y., & Chao, J. A. (2019). Single-Molecule Imaging of mRNA Localization and Regulation during the Integrated Stress Response. *Molecular Cell*, *73*(5), 946-958.e7. https://doi.org/10.1016/j.molcel.2018.12.006

Wilczynska, A., Gillen, S. L., Schmidt, T., Meijer, H. A., Jukes-Jones, R., Langlais, C., Kopra, K., Lu, W.-T., Godfrey, J. D., Hawley, B. R., Hodge, K., Zanivan, S., Cain, K., Le Quesne, J., & Bushell, M. (2019). EIF4A2 drives repression of translation at initiation by Ccr4-Not through purine-rich motifs in the 5′UTR. *Genome Biology*, *20*(1), 262. https://doi.org/10.1186/s13059-019-1857-2

Willyard, C. (2018). New human gene tally reignites debate. *Nature*, *558*(7710), 354–355. https://doi.org/10.1038/d41586-018-05462-w

Wilson, A. K., Horwitz, J., & De Lanerolle, P. (1991). Evaluation of the electroinjection method for introducing proteins into living cells. *American Journal of Physiology-Cell Physiology*, *260*(2), C355–C363. https://doi.org/10.1152/ajpcell.1991.260.2.C355

Wright, L. P., & Philips, M. R. (2006). Thematic review series: Lipid posttranslational modifications. CAAX modification and membrane targeting of Ras. *Journal of Lipid Research*, *47*(5), 883–891. https://doi.org/10.1194/jlr.R600004-JLR200

Wu, B., Buxbaum, A. R., Katz, Z. B., Yoon, Y. J., & Singer, R. H. (2015). Quantifying Protein-mRNA Interactions in Single Live Cells. *Cell*, *162*(1), 211–220. https://doi.org/10.1016/j.cell.2015.05.054

Wu, B., Eliscovich, C., Yoon, Y. J., & Singer, R. H. (2016). Translation dynamics of single mRNAs in live cells and neurons. *Science*, *352*(6292), 1430–1435. https://doi.org/10.1126/science.aaf1084

Yan, X., Hoek, T. A., Vale, R. D., & Tanenbaum, M. E. (2016). Dynamics of Translation of Single mRNA Molecules In Vivo. *Cell*, *165*(4), 976–989. https://doi.org/10.1016/j.cell.2016.04.034

Yarmolinsky, M. B., & Haba, G. L. D. L. (1959). INHIBITION BY PUROMYCIN OF AMINO ACID INCORPORATION INTO PROTEIN*. *Proceedings of the National Academy of Sciences of the United States of America*, *45*(12), 1721–1729.

Zeng, Y., Sankala, H., Zhang, X., & Graves, P. R. (2008). Phosphorylation of Argonaute 2 at serine-387 facilitates its localization to processing bodies. *Biochemical Journal*, *413*(3), 429–436. https://doi.org/10.1042/BJ20080599

Zhao, N., Kamijo, K., Fox, P. D., Oda, H., Morisaki, T., Sato, Y., Kimura, H., & Stasevich, T. J. (2019). A genetically encoded probe for imaging nascent and mature HA-tagged proteins in vivo. *Nature Communications*, *10*(1), 2947.

APPENDIX 1
Designing an NCT-based synthetic miRNA targeting assay

This section discusses developing a strategy to target an NCT-based translation reporter using synthetic miRNA. Though this work was inconclusive, it provides a platform for developing methodology for studying endogenous miRNA targeting of the NCT reporter.[11]

A1.1 Motivation

Though the Tethering and Tracking (TnT) system is powerful, it remains an artificial means of studying translational silencing. Several previous works provided convincing evidence that tethered Ago silences translation of a reporter in a way that recapitulates natural miRNA-mediated translational silencing (Eckhardt et al., 2011; Golden et al., 2017; Liu, Rivas, et al., 2005; Pillai et al., 2004). Further, we controlled for the effects that tethering alone may cause in each experiment by comparing tethered Ago2 to a tethering control protein (λN-EGFP-β-gal, described in **Chapter 3** and discussed in **Chapter 5**). However, this control strategy could not confirm that the impact on translation of tethered Ago2 mimicked that from endogenously targeted Ago. Thus, we wanted to confirm this at the single-molecule level to further validate our TnT biosensor data.

[11]This appendix is not published. It contains ideas inspired by Tatsuya Morisaki, as it was originally based on a project that he had started.

There are several possible reasons that tethered Ago2 may not recapitulate its natural silencing mechanism (discussed in **Chapter 5**). For instance, λN-fused Ago may be unable to adopt the full range of conformations used in its silencing mechanism or force Ago2 to adopt an artificial conformation. Further, it is known that Ago needs to assume a specific conformation to form a chaperone-mediated functional RISC complex with dsRNA (Iwasaki et al., 2015) and that human Ago proteins recruit the scaffold protein TNRC6B with higher efficiency when they are bound to a guide RNA (Elkayam et al., 2017). It is currently unknown to what extent an artificially tethered Ago impacts silencing of an mRNA.

For these reasons, we thought it necessary to examine how a more natural silencing context of miRNA-recruited Ago compares to silencing of Ago-tethered to the TnT biosensor. To do this, we developed a strategy which recruited Ago2 via miRNA targeting using a preexisting miRNA response element (MRE) in the Nascent Chain Tracking (NCT) reporter mRNA.

The 3'UTR of the NCT reporter used in Morisaki et al. 2016 is composed of the human actin (actB) 3'UTR, which harbors an 8mer miRNA MRE predicted to be targeted by miR-145-5p and miR-5195-3p (**Figure A1.1**; *TargetScanHuman 7.2*, n.d.). However, since neither of these miRNAs were found at detectable levels in U2OS cells (Jerez et al., 2019), the untethered NCT-reporter is unlikely targeted naturally. Note, an MRE with predicted miRNA targeting has not been confirmed to be able to be bound by Ago2, as determinable by other methods, such as HITS-CLIP (Moore et al., 2014).

Thus, we purchased a synthetic miRNA mimic of miR-145-5p to target the NCT translation reporter's 3' UTR. We hypothesized that the miRNA mimic would load into

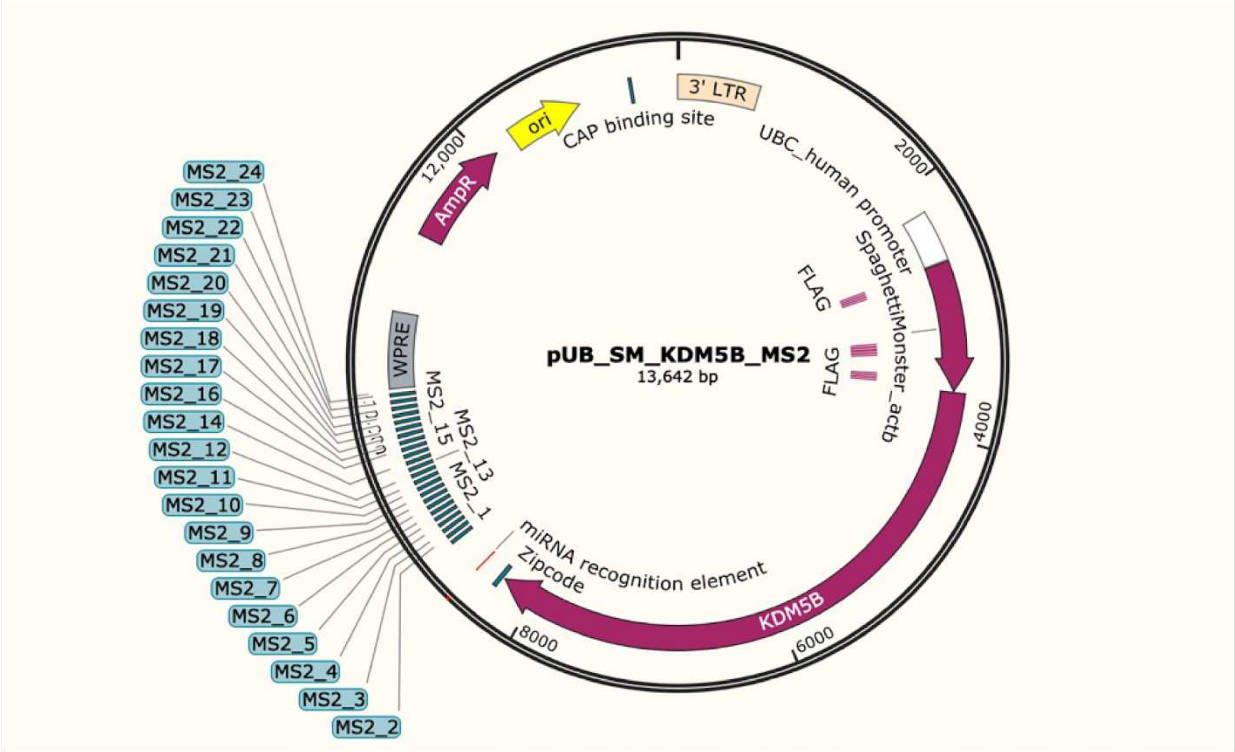

	Predicted consequential pairing of target region (top) and miRNA (bottom)	Site type	Context++ score	Context++ score percentile
Position 145-152 of ACTB 3' UTR	5' ...GACUCAGGAUUUAAAAACUGGAA...	8mer	-0.56	99
hsa-miR-5195-3p	3' UCGGGGGAGUCUCUUGACCUA			
Position 145-152 of ACTB 3' UTR	5' ...GACUCAGGAUUUAAAAACUGGAA...	8mer	-0.47	99
hsa-miR-145-5p	3' UCCCUAAGGACCCUUUUGACCUG			

Figure A1.1. The miRNA recognition element in the NCT translation reporter.
Above: The plasmid map for pUb-smFLAG-KDM5B-actB-3'UTR-24xMS2.
Below: The two miRNA sites located in the actB 3' UTR.

miRISC complexes and thus program endogenous miRISC machinery to target and silence the NCT reporter. In this way, we hoped to increase miRISC-targeting of the NCT reporter sufficiently to visualize translation silencing. By then comparing translation

sites in cells with or without the loaded miRNA mimic, we aimed to isolate the impact of miRNA-targeting on NCT reporter translation. We then aimed to compare the impact to translation from this more endogenous miRISC-targeting strategy to our Ago2-tethering findings in **Chapter 3**.

A1.2 Methods

For the endogenously loaded miRNA, we purchased a synthetic miRIDIAN microRNA (5'-GUCCAGUUUUCCCAGGAAUCCCU-3', Dharmacon) to mimic miR-145-5p and target the 8mer MRE in the NCT translation reporter (**Figure A1.1**). The translation vector used for these experiments, smFLAG-KDM5B-actb-24xMS2, contained a MRE in the 3' UTR shown to be targeted by this miR-145-5p (Morisaki et al., 2016). Note, this reporter did not contain BoxB stem loops. The manufacturer recommends transfection of 10-100 nM synthetic miRNA. The miRNA were added by LTX transfection at 0, 112.5 nM, or 560 nM miRNA.

The NCT assay was performed as described previously (Morisaki et al., 2016). The nucleic acid components (2.5 μg reporter plasmid in a transfection solution of either 0, 112.5 nM, or 560 nM miRNA) were transfected 4 hours before bead loading to allow cells time to express the plasmid and form RISC complexes with the synthetic miRNA. Imaging was performed 2 hours after bead loading Cy3-FLAG-Fab and JF646-stained HaloTag-MCP. Images of cells were acquired as described previously (**Figure 3.2**). Cells without (N=8) and with (N=8) 560 nM co-transfected miRNA were imaged during one day of imaging.

To see if translation was impacted, the fraction of Cells were analyzed with the Mathematica TrackingCode as described (**Figure 3.2**, **Methods**), and intensities of

fluorescent centroids in the NCT mRNA (red) and translation (green) channels were quantified by a local background subtracted centroid measurement. The intensities of translation at all mRNA foci were visualized in a cumulative density histogram to show the relationship between miRNA and no-miRNA translation sites.

A1.3 Results

The NCT-loaded cells performed the translation assay with or without loaded miRNA. Co-transfection with 112.5 or 560 nM miRNA did not appear different by eye, so only 560 nM miRNA was quantified. Co-transfection of miRNA did not affect the ability to find NCT-expressing cells or detect and quantify mRNA and translation. Cells did not have apparent morphology disruption from the added miRNA (**Figure A1.2**). This is noteworthy because miR-145 also targets the 3'UTR of endogenous transcripts encoding actin, an important cytoskeletal protein with essential cellular functions.

When we measured the intensity of mRNA, the histogram showed a single, approximately symmetric peak, which suggests that primarily single mRNA were detected (**Figure A1.3A, above**). Further, the mRNA channel's median intensity, ~0.08 a.u., was similar to that of previous assays using a 24x MS2 tag to label mRNA. There was not a noticeable difference in mRNA intensity between the two conditions.

Next, we measured if translation at the single mRNA was being reduced, which would result in less ribosomes (the Fab signal at nascent chains being our readout) per mRNA focus. For the measured translation intensity at each mRNA, the histogram showed separate populations of non-translating and translating mRNA (**Figure A1.3A, below**). Surprisingly, the distributions of translation signals did not noticeably vary between the miRNA-loaded and control mRNA populations. This would suggest that the

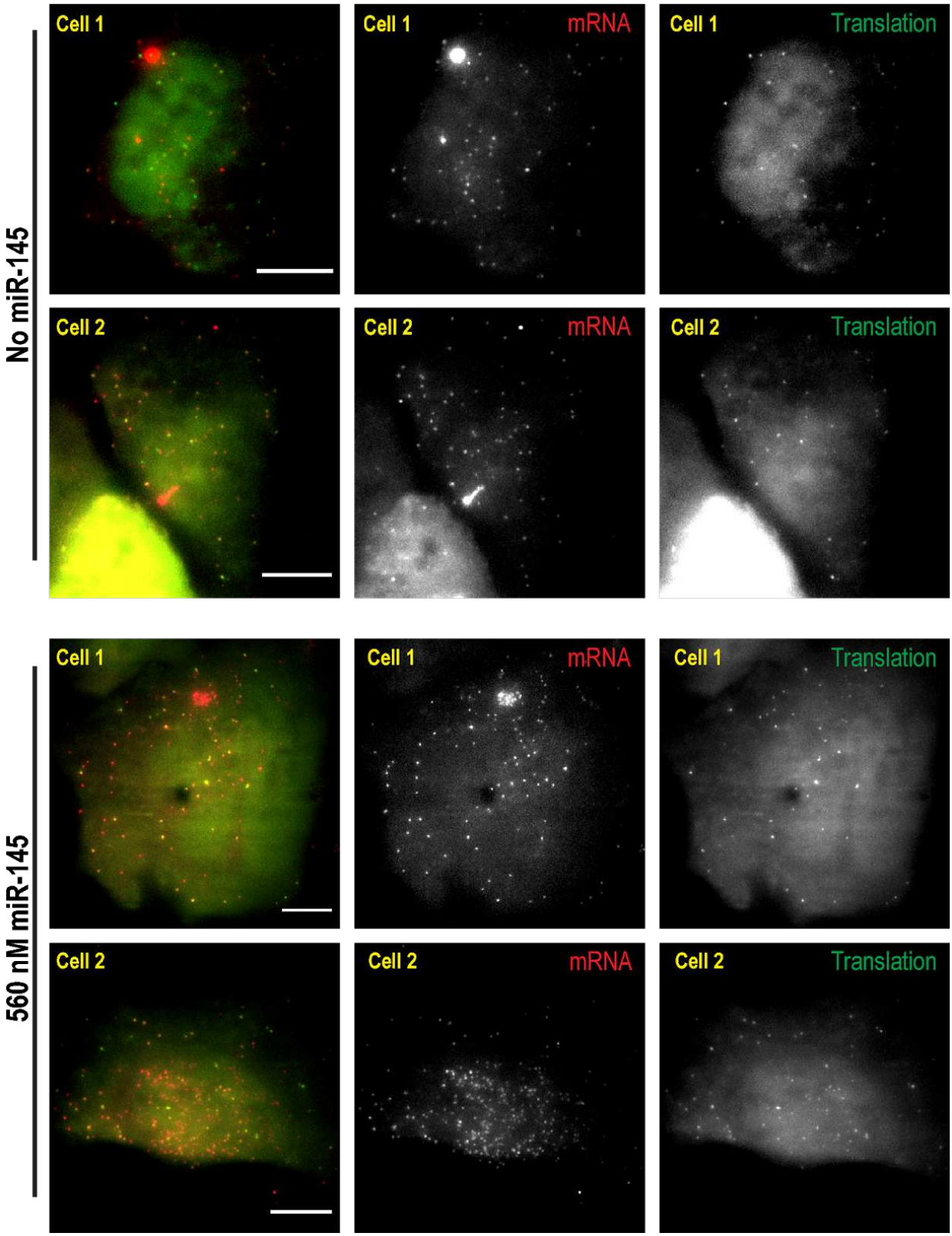

Figure A1.2 Example cells with NCT translation upon miRNA transfection.
(Legend on next page)

Figure A2.2 Example cells with NCT translation upon miRNA transfection.
The NCT assay was performed in cells co-transfected with 0 or 560 nM miR-145. All intensities were auto-adjusted. 2 of 8 representative cells per condition are shown.

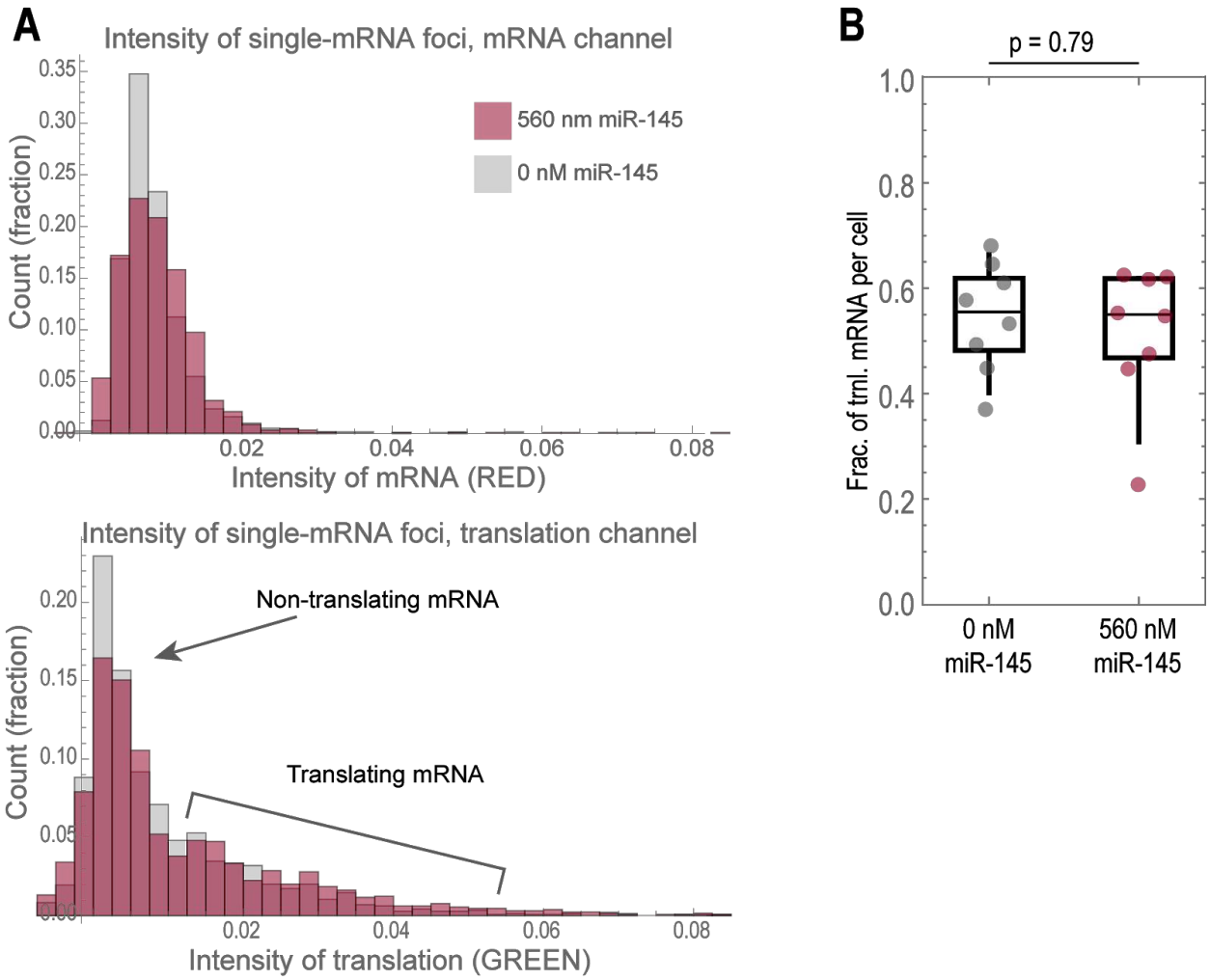

Figure A1.3 The addition of miR-145 is not likely to affect NCT translation at single mRNA.

The NCT assay was performed in cells co-transfected with 0 (gray) or 560 nM miR-145 (red).

A Histograms showing the intensity of each mRNA spot in the mRNA (MCP) channel, above, or the translation (Fab) channel. The count of mRNA quantified were 1128 for 150 nM miRNA-145 and 908 for 0 nM miR-145.

B Box plots showing the fraction of translating mRNA per cell. Error was calculated by the Mann-Whitney test. The median +/- SD is 0.56 +/- 0.10 for 0 nM miR-145 and 0.55 +/- 0.13 for 560 nM miR-145. N of cells were 8 for each 0 nM or 560 nM miR-145.

mRNA in both populations were associated with the same number of nascent chains (i.e. reporter protein being translated).

Lastly, to determine if miRNA-loaded cells had more mRNA with completely shut-off translation, we counted the mRNA associated with or without translation signal per cell (**Figure A1.3B**). For this, the presence of translation signal was automatically detected in the analysis code then curated by hand. The mRNA were translating at typical percentages as seen previously (**Figure 3.7**, ~55% of the mRNA per cell were being translated). The percentage of translating mRNA per cell was statistically the same between miRNA-loaded and control cells, suggesting translation is not being shut down by loaded miRNA.

Together, these results suggest that adding miRNA did not impact the level of translation at NCT reporter mRNA. The mRNA did not coalesce, as seen with Ago2-tethered TnT mRNA (**Figure A1.3A, above**, **Figure 3.10A,B**). The mRNA did not have reduced translation levels at the mRNA level, as seen by similar intensity distributions of ribosomes per mRNA between miRNA-loaded and control cells (**Figure A1.3A, below**). Lastly, the mRNA did not show signs of complete translation inhibition of mRNA, as seen by approximately the same number of mRNA being translated per cell between miRNA-loaded and control cells (**Figure A1.3A, below**). Though the strategy of co-transfecting the NCT assay components and miRNA into cells are promising, this result is currently inconclusive, since several factors should be optimized in further tests.

A1.4 Discussion and future directions

Optimizing this experiment could yield a strategy for easily testing the effects of miRNA-targeting on single mRNA translation. This strategy relies on endogenous Ago

proteins and could therefore be used to compare endogenous Ago targeting to the artificial Ago tethering to the TnT reporter. Moreover, due to the facility of purchasing synthetic miRNA mimics, this strategy could be rapidly adapted for different miRNA/target sequences and therefore expanded to testing different miRNA-mRNA interactions to live-cell single mRNA translation, similar to what has been done *in vitro* (Salomon et al., 2015). This could allow for testing different miRNA sequences, such as a series of miRNA with more or less complementarity to MRE target sites.

The main benefit of this strategy is that it does not rely on endogenous miRNA levels. Endogenous miRNA are known to vary greatly depending on cell type, and the extent to which miRNA levels vary cell-to-cell of the same cell type has not yet been thoroughly studied. Transfecting the miRNA controls how many miRNA are loaded per cell, roughly. Moreover, miRNA loading could provide a straightforward way of studying the impact of the level of miRNA per cell. Varying the concentration of transfected miRNA allows for transfecting different levels of the miRNA to represent a greater or lesser proportion of total cellular miRNA (Jin et al., 2015). It is known that the concentrations of endogenous miRNA species can vary greatly -- for example, in U2OS cells miR-20 makes up ~25% of all miRNAs (~210,000 sequencing reads) as compared to the next highest-expressed miRNA at ~8% (~5,000 sequencing reads; Mayr & Bartel, 2009). It would be interesting to study how these proportions affect the miRNA silencing pathway at the level of translation.

Several reporters using repeated MREs have been constructed and tested in our lab and others. A simple strategy for constructing miRNA targetable reporters would be by copying a sequence from a previously verified MRE reporter and inserting it into the

NCT mRNA reporter by either appending or swapping it with the NCT reporter's 3' UTR. However, careful testing must be done to ensure that these UTR sequences do not disrupt the cytoplasmic localization of NCT mRNA (which is extremely helpful for live-cell single-mRNA tracking and imaging). For example, when we inserted an hmga2 3' UTR sequence into the mRNA reporter for a similar experiment, mRNA were immobilized and localized to the perinuclear region instead of cytoplasm (data not shown). The mRNA were then much more difficult to target and track, since the perinuclear region had high background fluorescence and the lack of movement made the mRNA difficult to discern from autofluorescent debris.

To control for the effects of synthetic miRNA mimic on the NCT reporter, several steps can (and should) be taken. Most importantly, the gold standard in the miRNA field is to control for the effects of loaded miRNAs themselves by comparing reporters with or without intact miRNA sites, not cells with or without loaded miRNA. This can be done by either scrambling or reversing the MRE sequences, as both strategies would render the MRE unbindable by the miRNA mimic. Multiple proximal MREs on the same transcript are thought to have a cooperative effect on silencing (Grimson et al., 2007). This could be from the fact that multiple Agos can bind to the same TNRC6 protein (Elkayam et al., 2017) and thereby enhance or expedite downstream silencing effects.

Another adaptation to this protocol would be to use a fluorescent-tagged miRNA. The benefits are twofold: First, the level of miRNA in cells could be measured, thus ensuring that each cell imaged had a sufficient level of loaded miRNA. This would also add a way to ensure that only miRNA-loaded cells were imaged. Further, previous studies used a 3'-labeled miRNA to track its movement in the cell (Pitchiaya et al.,

2012, 2019). If a reporter with tandem repeated miRNA sites was constructed and could be targeted by multiple miRNA, the enhanced signal from multiple miRNA may be high enough to detect above background. This would provide a method for reporting miRNA-mRNA interactions and discerning miRNA-targeted and untargeted mRNA.

APPENDIX 2
Generating stable cell lines for the Tethering and Tracking biosensor

This section describes developing a strategy to create stable U2OS cell lines to express the tetherable Argonaute or control proteins using FACS. These cell lines were not used in any other sections of this dissertation. However, these cell lines may be valuable in the future for λN-tethering experiments.[12]

A.2.1 Motivation

One drawback of the Translation and Tethering (TnT) system developed and described in **Chapter 3** is the difficulty of finding cells with optimal concentrations of the reporter and various probes. Though it is of great advantage to simply bead load all plasmid and protein components in cells, described in **Chapter 4**, finding optimal expression in a cell is difficult due to the high variability we see when bead loading plasmids. The problem with transiently expressing multiple plasmids is that the probability of finding a cell with good expression of one of the plasmids is low, then the probability of finding a cell with both plasmids is exponentially worse (**Figure 4.2B**, discussed in **Chapter 5**). Further, we could not solve this problem with transfection, since it was still difficult to find cells that (1) had both bead loaded protein probes and transfected reporters and (2) had optimal expression levels of both transfected plasmids in the same cell.

[12]Dr. Chris Allen assisted with cytometric cell sorting, and Dr. O'Neil Wiggan gave advice on generating stable cells. Nick Pollock helped culture stable cells.

As an attempt to remedy these factors lowering the efficiency of the TnT assay, we hypothesized that making stable cells expressing one of the two plasmids would greatly increase the yield of imageable cells. Moreover, sorting the stable based on their fluorescence intensity of expressed protein would allow for a more homogenous expression level in the population. Due to the sensitivity of concentration of TnT components in cells, we theorized that it may be helpful if cells were sorted into different intensity-based populations so that the researcher could choose the level of fluorescent protein expression required for a specific experiment. Though only one fluorescence intensity would be needed for our TnT application, we could imagine future applications may vary depending on, for example, how many stem loops were available for a reporter to bind, which may require higher or lower levels of tetherable protein in the assay.

Thus, we decided to generate a U2OS cell line stably expressing the tetherable Ago2 construct. When deciding which plasmid to use to generate stable cells, we decided upon tetherable Argonaute (λN-EGFP-Ago2) along with the corresponding tetherable and non-tetherable controls for several reasons:

1. First, we hypothesized that stable cells would greatly reduce the variation of expression, which is a key factor of visualizing tethering.

2. On a practical note, though neither of the plasmids contained a mammalian selection marker, the Ago2 construct was much easier to clone. Unlike the Ago2 vector, The TnT vector was quite difficult to incorporate a mammalian cell resistance marker via cloning due to the

plasmid's massive size, many already-used restriction sites, and highly repetitive sections.

3. On a speculative note, stable cells could possibly reduce variability of transiently expressed Ago2. This is important because simply overexpressing Ago could impact translation regulation. To support this, for instance, we saw increased P-body formation about 2-fold in cells transiently expressing Ago2 (data not shown). Stable Ago2 expression could perhaps help maintain equilibrium with endogenous Ago2 and other P-body protein levels.

4. On another speculative note, stably expressed Ago2 could perhaps better reflect the endogenous Ago. A concern of studying transiently expressed Ago2 is that it may not behave completely naturally, since Agos are known to change conformation during miRNA binding, undergo several PTMs and bind to other cytoplasmic proteins. These steps are known to control Ago's ability to form a complex with a miRNA, associate with P-bodies, and Ago's overall stability. Stably expressed, mature tetherable-Ago could, perhaps, better reflect endogenous Ago than newly-synthesized, pre-steady-state, transiently expressed Ago.

Thus, to attempt to ameliorate this problem, we generated stable cell lines via FACS which expressed one of each of the TnT-tetherable factors: tetherable Ago2, tetherable β-gal control, or non-tetherable Ago2 control.

A.2.2 Methods

1 Stable cell line generation.

1.1 The following constructs were cloned into hygromycin-resistant plasmids for stable cell line generation:

i. Tetherable Ago2: CMV-d3 λN-EGFP-Ago2 KAN

ii. Tetherable β-gal control: CMV-d3 λN-EGFP-β-gal KAN

iii. Non-tetherable Ago2 control: CMV-d3 EGFP-Ago2 KAN

1.2 Populations of U2OS cells (grown under conditions as described previously) were transfected (as described previously) with each construct, allowed to recover for 24 hours.

1.3 Cells were then selected using 750 ug/mL hygromycin (Gold Biotechnology) at every media change (every 1-3 days) for 7 days.

1.4 Cells were further grown under 400 ug/mL hygromycin spiked media, which was changed every 1-3 days, for an additional 14 days. From this point on, cells were continuously grown in media containing 400 ug/mL hygromycin.

2 Sorting stable cell lines for GFP expression by FACS

2.1 Cells were grown to 50-90% confluency on a 10 cm cell culture dish.

2.2 Cells were prepared in suspension by being trypsinized, washed one in media and twice in PBS. Cells were then resuspended in PBS at a concentration of 10-20 million cells/mL. Clumps of cells were gently mixed thoroughly.

2.3 Cells were sorted on a FACS Aria-III (BD) based on their fluorescence intensity from 488 nm laser excitation.

2.3.1 The laser voltages were optimized by CS&T beads (BD) by range running the beads through the FACS to determine voltage settings which detected bead emission in the linear range (**Figure A2.1**).

2.3.2 Control U2OS cells were used to set gates partitioning intact, single, GFP- cells (**Figure A2.2**).

2.3.3 Each cell line was sequentially loaded, and intact, single, GFP+ cells were sorted. At this step the gain was significantly adjusted to increase sensitivity in the 488 nm channel (**Figure A2.3**). Sorting results are found in **Table A2.1**.

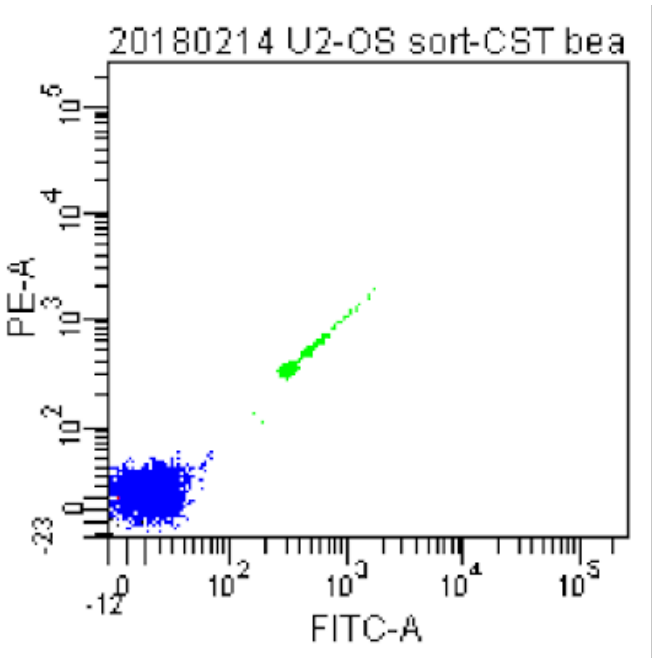

Figure A2.1 Aligning the FACS intensity parameters by CS & T beads. The multicolor beads were measured at various voltages of the FITC (488 nm laser) and PE (561 nm laser) channels to determine the linear range of detection in both channels (green population of beads).

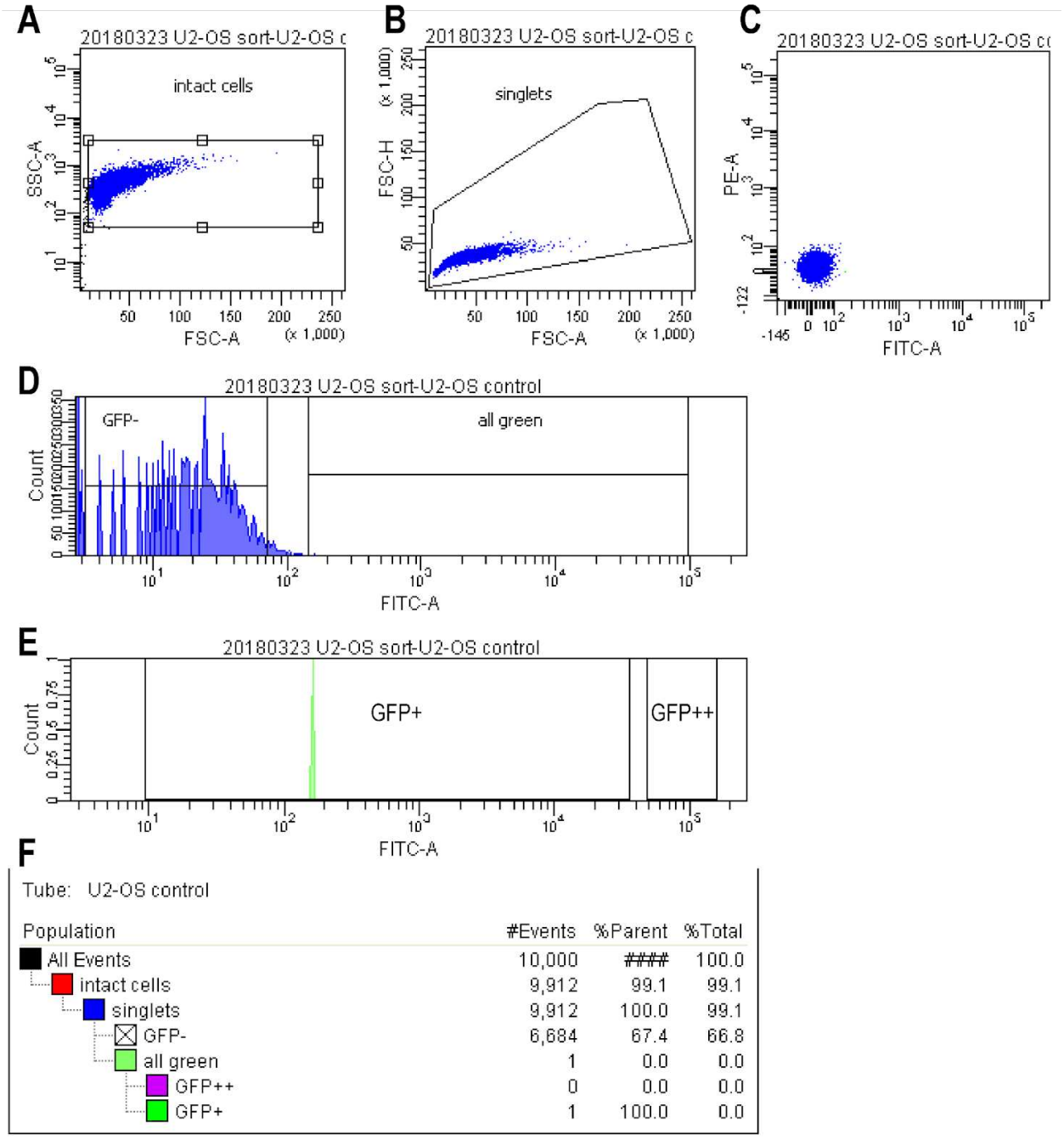

Figure A2.2 Setting FACS parameters with unlabeled U2OS control cells.
(legend on next page)

Figure A2.2 Setting FACS parameters with unlabeled U2OS control cells.
A Scatterplot displaying how the side scatter area (SSC-A) and forward scatter area (FSC-A) per detected event were used to draw a gate for the intact cells.
B Scatterplot displaying how the forward Scatter Height (FSC-H) and forward scatter area (FSC-A) per intact cell were used to draw a gate for single cells.
C Scatterplot displaying the fluorescence intensity per singlet cell in 488 nm (FITC-A) and 561 nm (PE-A) channels.
D Histogram showing 488 nm (FITC-A) intensities per singlet cell which was used to draw gates for GFP- and all green cell populations.
E Histogram showing 488 nm (FITC-A) intensities per all green cells which was used to draw gates for GFP + and GFP ++ cell populations.
F Data results showing the count of cells in each population: intact cells, singlet cells, GFP-/all green cells, and GFP+/GFP++ cells.

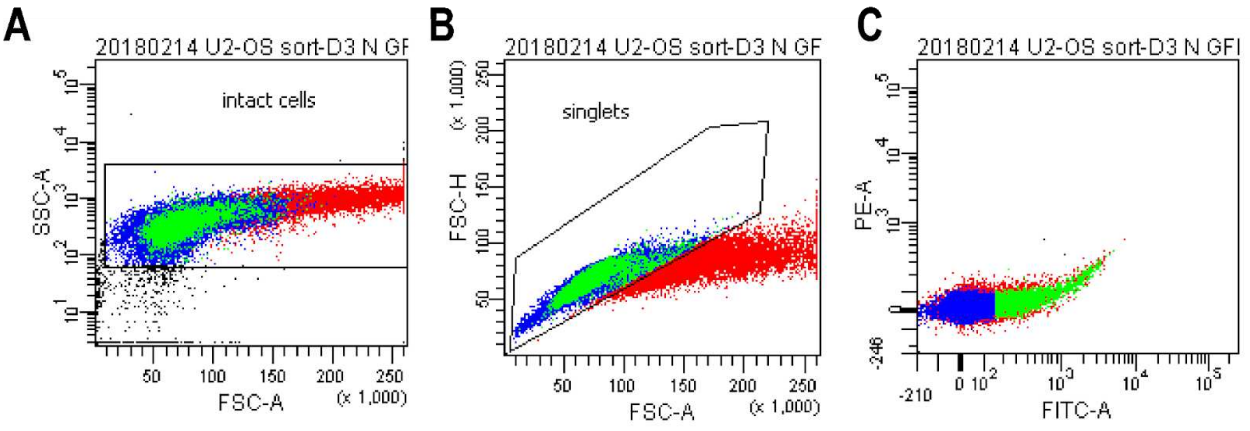

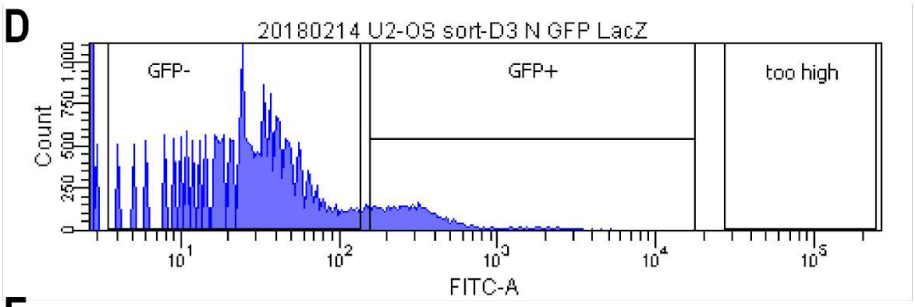

E

Tube: D3 N GFP LacZ

Population	#Events	%Parent	%Total
All Events	50,000	####	100.0
intact cells	49,374	98.7	98.7
singlets	38,069	77.1	76.1
GFP-	22,814	59.9	45.6
GFP+	3,737	9.8	7.5
too high	0	0.0	0.0

Figure A2.3 Example of FACS sorting of λN-EGFP-β-gal cells.
A Scatterplot displaying how the side scatter area (SSC-A) and forward scatter area (FSC-A) per detected event were used to draw a gate for the intact cells.
B Scatterplot displaying how the forward Scatter Height (FSC-H) and forward scatter area (FSC-A) per intact cell were used to draw a gate for single cells.
C Scatterplot displaying the fluorescence intensity per singlet cell in 488 nm (FITC-A) and 561 nm (PE-A) channels.
D Histogram showing 488 nm (FITC-A) intensities per singlet cell which was used to draw gates for collecting populations of GFP-negative, GFP-positive, and cells that had too much GFP-channel fluorescence.
E Table showing the count of cells in each population: intact cells, singlet cells, GFP-/all green cells, and GFP+/too high cells.

Table A2.1 Stable cell lines sorted by FACS.

Construct	Expt.	Date	FITC range	# cells collected:
d3 EGFP-Ago2	1	2/14/18	All	~4,000
d3 λN-EGFP-β-gal	1	2/14/18	All	~200,000
d3 λN-EGFP-Ago2	2	3/23/18	All	4,210
d3 GFP-AGO2	2	3/23/18	All	2,361
d3 λN-EGFP-β-gal	2	3/23/18	Brightest 25%	>10,000
d3 λN-EGFP-β-gal	2	3/23/18	Dimmest 75%	>10,000
d3 λN-EGFP-β-gal	3	5/2/18	GFP+	159246
d3 λN-EGFP-β-gal	3	5/2/18	GFP++	839305
d3 λN-GFP-AGO2	3	5/2/18	GFP+	89522
d3 λN-GFP-AGO2	3	5/2/18	GFP++	29482
d3 GFP-AGO2	3	5/2/18	GFP+	48702
d3 GFP-AGO2	3	5/2/18	GFP++	16788

2.3.4 Data were analyzed by FACSDiva Version 6.1.3 software (BD).

2.4 Sorted cells were re-plated in 10 cm cell culture dishes.

2.5 Cell populations were expanded, and stocks of each cell type were stored in CellBanker at -80 C.

3 Sorting stable cell lines by FACS (second round of sorting)

3.1 Since cells expressing λN-EGFP-Ago2 were very low, sorting by FACS (step 2) was repeated. This time, however, β-gal-expressing cells were sorted into high (top 25% brightest) and low (75% dimmest) populations to test if gating could be optimized.

3.2 Successfully sorting was achieved for all three cell lines (tetherable Ago2, tetherable β-gal, and non-tetherable Ago2). **Sorting results are found in Table A2.1.**

3.3 Cell populations were expanded, and stocks of each cell type were stored in CellBanker at -80 C.

4 Measuring cell fluorescence by microscopy

4.1 To find the efficiency of FACS sorting, cells were imaged on the custom-built HILO microscope FLEXIE.

4.2 Though there was a high proportion of cells expressing tetherable β-gal (~80% cells had visible GFP expression by microscope), few cells were expressing either tetherable or non-tetherable Ago2 constructs (~10% cells had visible GFP expression by microscope).

5 Re-sorting stable cell lines by FACS

5.1 Since the percent of cells stably expressing λN-EGFP-Ago2 were very low, sorting by FACS (step 2) was repeated as described above.

5.1.1 This time, cells were sorted into high and low EGFP level pools for each cell line. These were named GFP++ and GFP+, respectively, as shown in **Figure A2.4**.

5.1.2 Additionally, a portion of cells were plated at low concentrations (~150 cells per 10 cm culture dish) for monoclonal isolation.

5.2 Successfully sorting was achieved for all three cell lines (tetherable Ago2, tetherable β-gal, and non-tetherable Ago2). Sorting results are found in **Table A2.1**.

5.3 Cell populations were expanded, and stocks of each cell type were stored in CellBanker at -80 C.

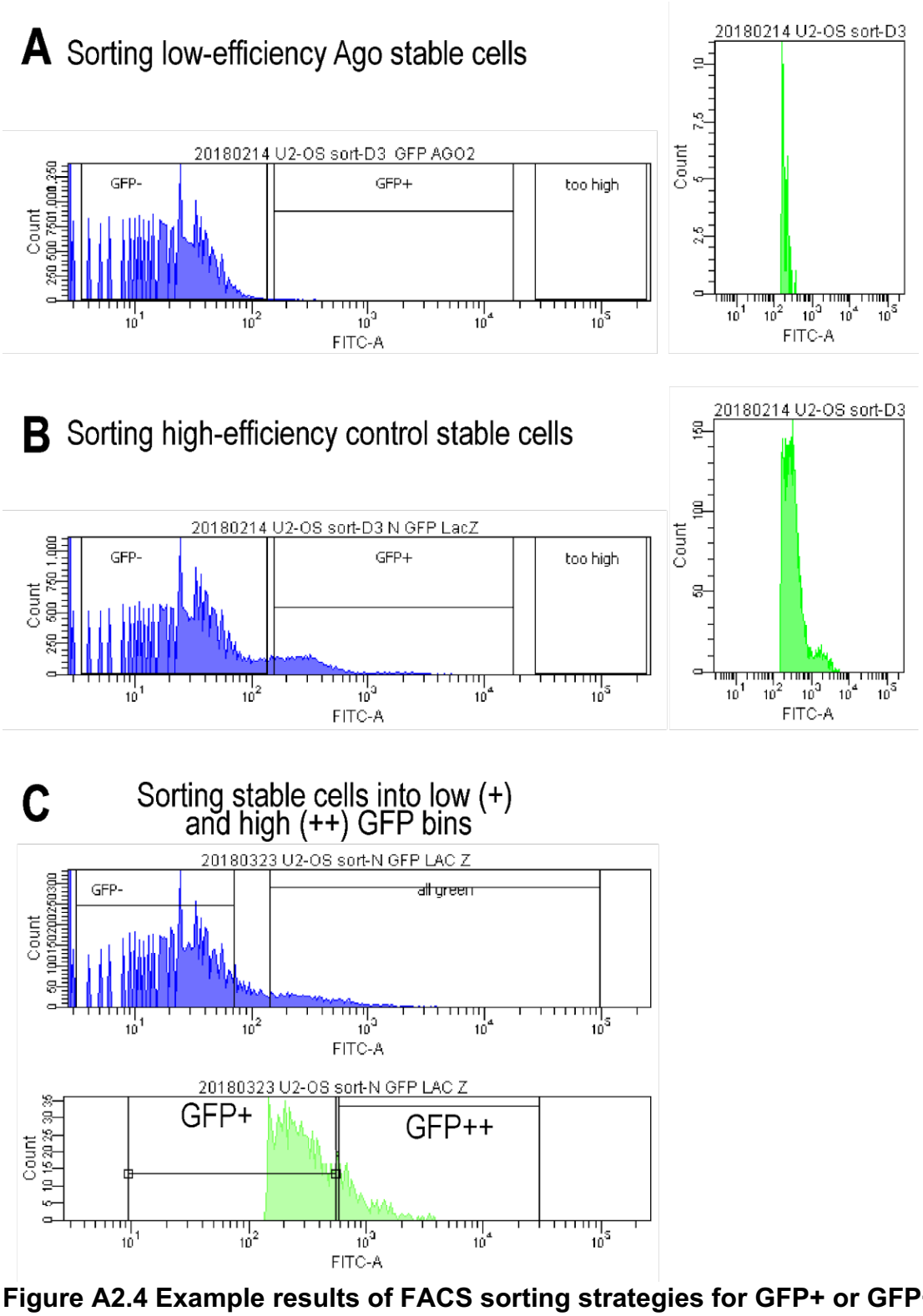

Figure A2.4 Example results of FACS sorting strategies for GFP+ or GFP+/GFP++ binning for stable cells expressing tetherable β-gal and Ago2 (legend on next page)

Figure A2.4 Example results of FACS sorting strategies for GFP+ or GFP+/GFP++ binning for stable cells expressing tetherable β-gal and Ago2.
A Histogram showing 488 nm (FITC-A) intensities per all singlet cells expressing tetherable Ago2 (a low-efficiency stable cell line) which was used to draw gates for GFP+ and >GFP+ (too high) cell populations. Left: histogram visualizes all singlet cells. Right: histogram visualizes only GFP+ cells.
B Histogram showing 488 nm (FITC-A) intensities per all singlet cells expressing tetherable β-gal (a high-efficiency stable cell line) which was used to draw gates for GFP+ and >GFP+ (too high) cell populations. Left: histogram visualizes all singlet cells. Right: histogram visualizes only GFP+ cells.
C Histogram showing 488 nm (FITC-A) intensities per all singlet cells expressing tetherable β-gal which was used to draw gates for GFP+ and GFP++ cell populations. Above: histogram visualizes all singlet cells (blue). Below: histogram visualizes only GFP+ cells (green).

6 Monoclonal isolation on stable, sorted cell lines

6.1 Monoclonal cell populations were achieved by growing the dispersed, single cells into small monoclonal colonies.

6.2 Each colony was transferred to an individual well in a 24 well cell culture dish by transferring the colony onto a trypsin-soaked disk of sterilized blotting paper.

6.3 Monoclonal cell populations were expanded, and stocks of each cell type were stored in CellBanker at -80 C.

A.2.3 Results

Though cell sorting took a considerable amount of time (~5 months due to re-sorting), it generated a population of cells enriched for those which stably expressed tethering constructs. Cells stably expressing tetherable constructs could be bead loaded with the TnT system and display tethering and translation at mRNA foci (**Figure A2.5A**).

For cells binned into low and high GFP populations, the cells best demonstrating tethering in the TnT assay were from the cells from bright populations (GFP++ or 25% bright). Many of the dim populations (GFP+ or 75% dim) had too lowly expressed GFP to see tethering. Some of the cells from bright populations had high GFP background levels which may have blocked visible tethering. However, the bright populations had higher percentages of cells expressing GFP overall.

In all populations, there was a high heterogeneity of GFP expression levels in cells. This was true for heterogeneous populations and monoclonal isolated populations, though the monoclonal cells seemed to have less variability (data not quantified). It was unclear if this heterogeneity was stochastic (for example, a stable cell oscillating between bright and dim GFP levels depending on expression at that time) or stable (for example, each stable cell expressing a constant level of GFP, some of which were bright and some of which were dim). Of note, when cells were tracked over long timeframes, the cells didn't show a noticeable change in GFP fluorescence (not quantified).

Only one round of FACS was needed to generate a population of GFP-expressing cells, for cells stably expressing the inert protein β -gal. However, for cells stably expressing Ago2 proteins (tetherable or non-tetherable), this was not the case. Two rounds of FACS were needed specifically for these cell lines because the percent of positive cells in these populations was too low to be useful. For the Ago2-expressing cell lines, the second round of FACS further enriched the percent of GFP+ cells, and there were enough GFP-positive cells to partition populations of dim and bright GFP expressing cells. However, in the time it took to expand the colony of sorted cells, the

percentage of the population expressing microscopically visible GFP was greatly reduced. This was despite the fact that we maximized the number of sorted cells by plating all sorted cells together (except the small portion that was used for monoclonal isolation).

A.2.4 Discussion and future directions

Generating stable cell lines is a promising idea to bypass low loading efficiency and achieve more cells with optimal imaging parameters (discussed in **Chapter 5**). For experiments requiring the co-loading of multiple plasmids, such as the TnT system, using cells which already stably express one of the constructs would greatly improve the number of cells optimal for imaging per experiment and could reduce search time on the microscope. Furthermore, stably expressing the tethering protein, Ago2 in this case, specifically may improve experiments since it would allow for imaging of mature protein at equilibrium instead of induced expression.

However, several drawbacks kept us from using these stable cell lines for other studies in this project. Most prominently, the stable cells expressing an Ago protein were progressively “self-selected” out of the population. This was apparent since over time the percentage of GFP-positive cells in the Ago2-expressing cell lines decreased over time (data not shown), though the cells were continuously grown under the selection agent 400 ug/mL hygromycin. We speculate that this could be because Ago proteins have repressive cellular functions and could slow cell growth enough to allow for outcompeting by low-expressing or negative cells. Another possible answer could be that cells turn down Ago expression to overcome negative impacts of its overexpression. Further supporting these speculations is the fact that β-gal expressing

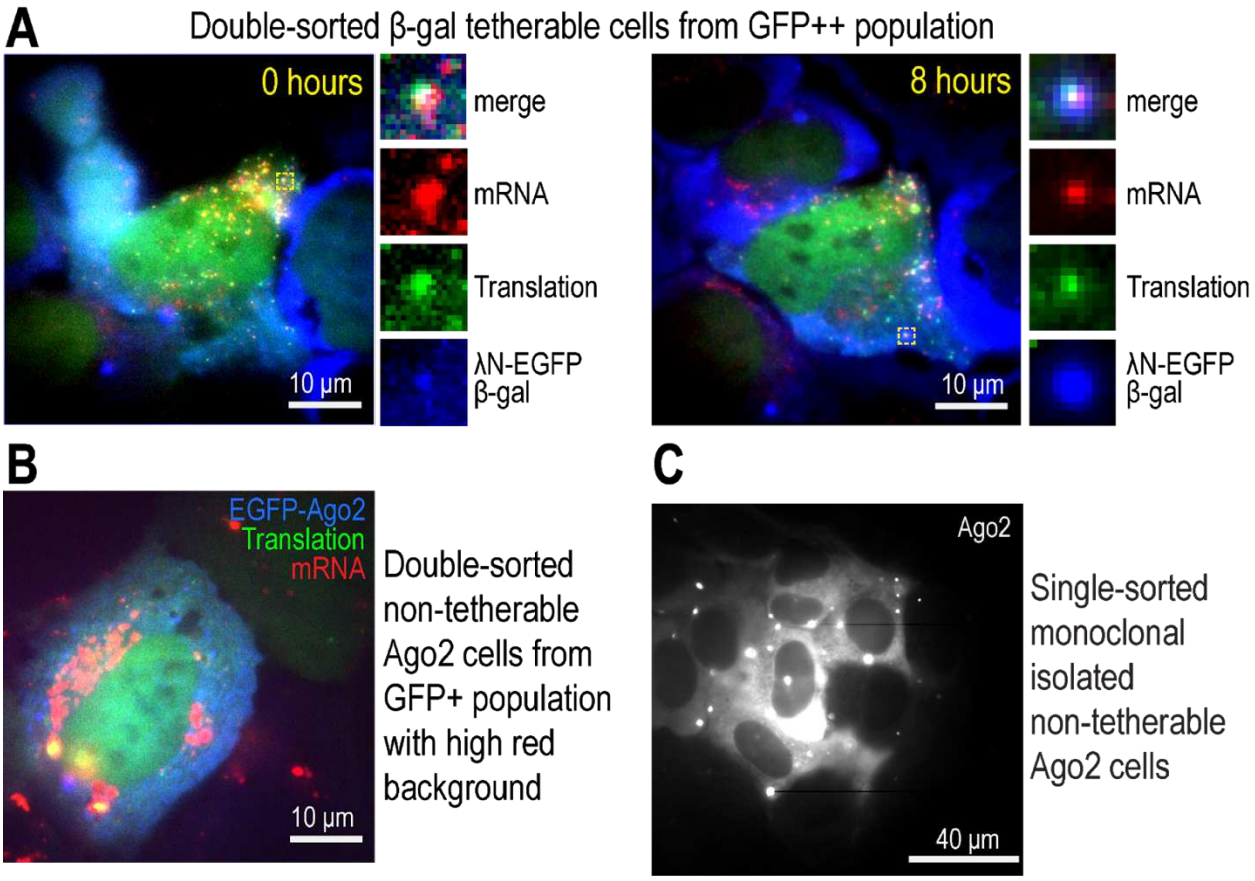

Figure A2.5 Examples of FACS sorted stable cells.
A Representative double-sorted (GFP++ population) cells stably expressing λN-EGFP-β-gal. Cells were loaded with the TnT components (smFLAG-KDM5B-15xBoxB-24xMS2 mRNA reporter plasmid, Cy3-FLAG-Fab, and JF646 HaloTag MCP). Blue, tetherable β-gal; green, translation; red, mRNA.
B Representative double-sorted (GFP+ population) cell stably expressing EGFP-Ago2. Cells were loaded with the TnT components (smFLAG-KDM5B-15xBoxB-24xMS2 mRNA reporter plasmid, Cy3-FLAG-Fab, and JF646 HaloTag MCP). Blue, tetherable Ago2; green, translation; red, mRNA.
C Representative field of view of single-sorted, monoclonal isolated non-tetherable Ago2 cells stably expressing EGFP-Ago2. Grayscale, tetherable Ago2.

cells had higher GFP-expression levels (**Figure A2.4**) and maintained positive percentages in the cell population when continuously grown under the selection agent. This outcome was especially unfortunate for our study, and further optimization would need to be done to obtain a cell line stably expressing Ago2 constructs which was useful. However, we anticipate that this cell sorting strategy could still be useful for other tethering proteins without substantial repressive effects on cell growth. Further, the control cells expressing tetherable β-gal have already proven useful in our lab for optimizing optogenetic control of tethering in a different research project.

A few important points should be noted about FACS sorting for single-molecule imaging experiments. First, sorting cells into different expression level populations was highly useful (**Figure A2.4**). We found that the tetherable protein was over-expressed in the bright population of cells and therefore not useful for TnT experiments. Other imaging experiments most likely require a specific level of fluorescence to achieve the needed function. For example, for λN-BoxB tethering, a specific level of the β-gal protein was essential: If the λN-fused protein was expressed too lowly, it did not tether to the BoxB-mRNA. If it was expressed too highly, tethering was not visible over the GFP-bright background. As such for future cell sorting projects, a similar gating strategy should routinely be performed to separate cells into separately collected bright and dim populations.

Further, adjusting the gain setting on the FACS Aria-III machine was necessary for detecting fluorescence. We discovered this during the first round of FACS. Cells were imaged the day before FACS and showed a percentage of the population had optimal expression levels of GFP. However, when we first tried sorting cells, they all looked

indistinguishable from the no-GFP control cells. We determined that the Ago2 tethering proteins were expressed at too low of levels to be detected under standard gain settings, even under maximal laser intensities. Though the β-gal could be seen, the bright population β-gal expressing cells were over-expressed for TnT experiments, as we later determined when studying the cells on a microscope. Only by adjusting the gain bin size on the FACS machine could we separate and sort the optimally low GFP-expressing cells.

Another thing to note is that background autofluorescence increased for cells grown for many passages (**Figure A.2.5B**). Thus, sorting by FACS twice was not an optimal protocol for cells which would be imaged by fluorescence microscopy. For similar future experiments, optimization could help reduce the passage number of stable, sorted cells. Examples of such optimization could be starting with larger cell populations before FACS sorting or optimizing the selection agent or process.

Lastly, since GFP expression levels were more similar, monoclonal isolation achieved better imaging results than a mixed population of sorted cells (**Figure A.2.5C**). However, even in the monoclonal populations expression levels varied per cell, most likely because expression was so low in the first place. Also, since it took so many passages to expand a colony from a single cell, monoclonal cells also had the high autofluorescence background problem. For future experiments sorting dimly expressed proteins, monoclonal may prove more troublesome and time-consuming than useful.

APPENDIX 3
Tethering TnT mRNA to cell membranes with MCP-CAAX

This section discusses development of methodology to reduce the mobility of TnT mRNA through membrane tethering. With reduced mobility, mRNA are able to be tracked for extended periods of time with higher resolution and lower phototoxicity. We believe this will be a valuable tool for long-timeframe imaging projects in the future.[13]

A3.1 Motivation

A major limiting factor to the Nascent Chain Tracking (NCT) and Tethering and Translation (TnT) assay is generating tracks of sufficient length to capture mechanistic events lasting on the minutes timescale. For example, single-mRNA tracking over tens of minutes to hours was needed to capture Ago2-mediated translation silencing of ribosome initiation (**Chapter 3**). Further, single-mRNA track lengths of tens of minutes are needed to do autocorrelation, which is a drug-free method for quantifying ribosome elongation rate (Morisaki et al., 2016).

Tracking freely-diffusing, fluorescently tagged mRNA is difficult for several reasons. Firstly, long-timeframe imaging may require lengthening the time interval between movie frames (Δt) or dimming the lasers to reduce photobleaching and phototoxicity, both of which increases the difficulty of faithfully tracking the same mRNA. Also, if many mRNA are present within a cell, the longer the Δt the more likely it is for

[13]This project started as a collaboration with Drew Tonsanger, a rotation student whom I mentored, and Dr. Ning Zhao. Ning, Drew and I designed the plasmid and cloning strategy together. After Drew's rotation, I cloned and validated the plasmid. I imaged the plasmid with Gabriel Galindo.

two tracks to cross paths which would make it difficult, if not impossible, to tell which mRNA belongs to which track. Even powerful, flexible single-particle tracking software can lose tracks, resulting in prematurely truncated tracking data and lower quality results. Lastly, if mRNA are moving more distance than their fluorophore's point spread function during the exposure time, they will appear as smears resulting in loss of resolution. This can be remedied by shortening the exposure time, but doing so will also compromise resolution and microscope sensitivity. Slowing or completely stopping movement of mRNA allows for longer exposure times, longer Δt between frames, and higher fidelity of tracking, all of which lead to more sensitive intensity data and increased microscopic resolution.

Single mRNA diffuse rapidly through the cell [ADD HERE: diffusion rate of single mRNA]. In our hands, anything more than 25-50 mRNA per cell becomes un-trackable, at our lab's microscope's fastest imaging settings.

To solve this problem, we developed a system to greatly reduce TnT reporter mRNA diffusion in order to increase their trackability. We accomplished this by tethering reporter mRNA to the plasma membrane, an idea first used in an NCT application by (Yan et al., 2016), which found that membrane tethered mRNA were basically immobilized since diffusion in the membrane is so slow. In our lab, we label NCT mRNA with freely-diffusing, fluorescent MS2 Coat Protein (MCP), which binds to MS2 stem loops on the reporter mRNA. To reduce mRNA diffusion, we introduced a membrane-tethering amino acid sequence, a CAAX box, to the C-terminal end of the MCP construct. This peptide sequence undergoes endoproteolytic cleavage between the C (cystine) and the AAX (two aliphatic amino acids followed by one of many amino acid

residues), allowing the protein to be prenylated at the C. The prenylation is inserted into a membrane, tethering MCP to the golgi, ER, or plasma membranes (Choy et al., 1999). Though CAAX prenylation is thought to happen post-translationally in eukaryotic cells (Wright & Philips, 2006), we did not attempt to recombinantly produce MCP-CAAX due in case recombinant CAAX had lower prenylation and thus decreased membrane localization.

It should be noted that Yan et al. (2016) developed a similar system for the mRNA coat protein PP7 Coat Protein (PCP) expressed stably in cell lines. However, our lab primarily uses MCP transiently, and most of our NCT-based reporters, including the TnT reporter, already contain MS2 stem loops. Since cloning these large reporter constructs is difficult and time-intensive, we thought it would be easier overall to develop an MCP tethering system than to remake the multitude of MS2-containing reporters.

A3.2 Methods

We designed a mammalian expression vector encoding HaloTag-2xMCP-CAAX (**Figure A3.1**). We used a low-copy promoter for minimal CAAX expression. From my experience with λN-BoxB tethering, low expression is necessary to view the signal at a single mRNA over background. Thus, we used a tethering plasmid backbone with a CMV-d3 promoter from CMV.d3-LamndaN-EGFP-LacZ-KAN (a plasmid which I cloned and used in **Chapter 3**). The CAAX domain, Cys-Val-Ile-Met, proceed by a long Gly/Ser rich linker was added to the C-terminal end of the open reading frame of HaloTag-2xMCP via PCR primer using the specified primers:

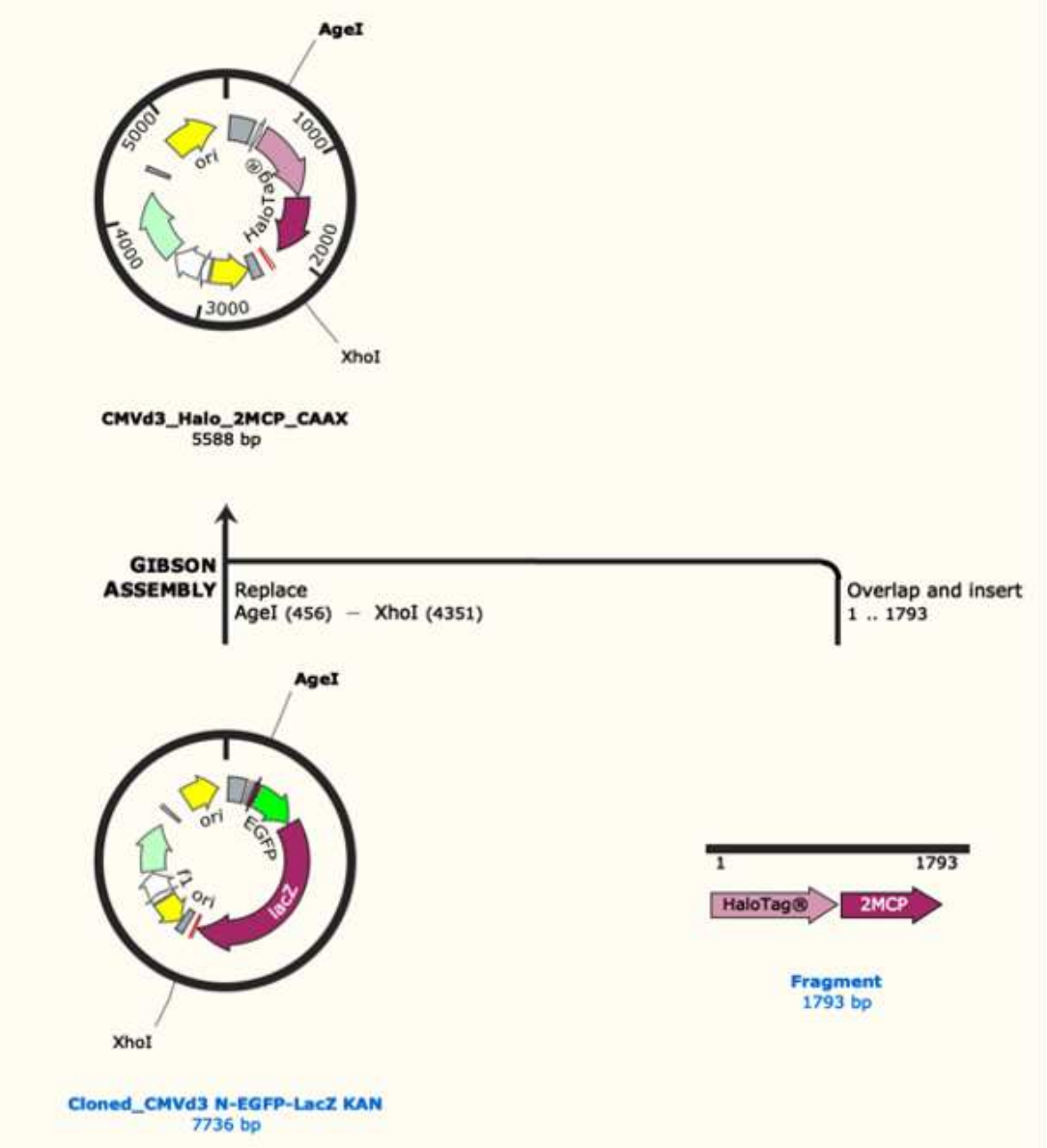

Figure A3.1. Cloning strategy for CMV.d3 HaloTag-2xMCP-CAAX

Forward: “tagtgaaccgGCTAGCGCTACCGGTAGCCACCATGGAAATCGGTACTGGCT
TTCCATTCG”

Reverse: “tatagaatagggccctctagtctcgagTTACATGATAACACACTTGGTTTTTGACTTC
TT”

The resulting amplicon, HaloTag-2xMCP-CAAX, was inserted via isothermal assembly into the AgeI and XhoI cut sites on the backbone of CMV.d3 λN-EGFP-LacZ. The final cloned product was purified by plasmid miniprep kit (Zymo) and verified by both restriction digest and Sanger sequencing (Quintara Biotechnology).

To test MCP-CAAX for membrane localization, we bead loaded 1 µg of the HaloTag-2xMCP-CAAX plasmid into cells along with 1.5 µg of the TnT reporter plasmid, smFLAG-KDM5B-15xBoxB-24xMS2, 1 µg of the plasmid encoding λN-EGFP-β-gal, and 0.5 µg of anti-FLAG-Fab. About 6 hours after bead loading, we imaged cells on FLEXIE, our lab’s HILO microscope. We assessed whether (1) MCP tethered to the cell membrane, (2) if single translation sites could be visualized, and (3) if λN-EGFP-β-gal tethering could be visualized. We imaged cells at FLEXIE’s standard (53.64 msec) and extended (100-200 msec) exposure times.

A3.3 Results, discussion and future directions

As expected, the expressed MCP-CAAX protein localized to the cell membrane (**Figure A3.2A**). Further, most of the MCP-CAAX-labeled mRNA were localized to the bottom of the cell, just above the glass (**Figure A3.2A, left**) and few mRNA puncta were seen in the middle of the cell (**Figure A3.2A, right**). Using CAAX-mediated membrane-tethered TnT reporter mRNA, we were still able to clearly see translation and β-gal

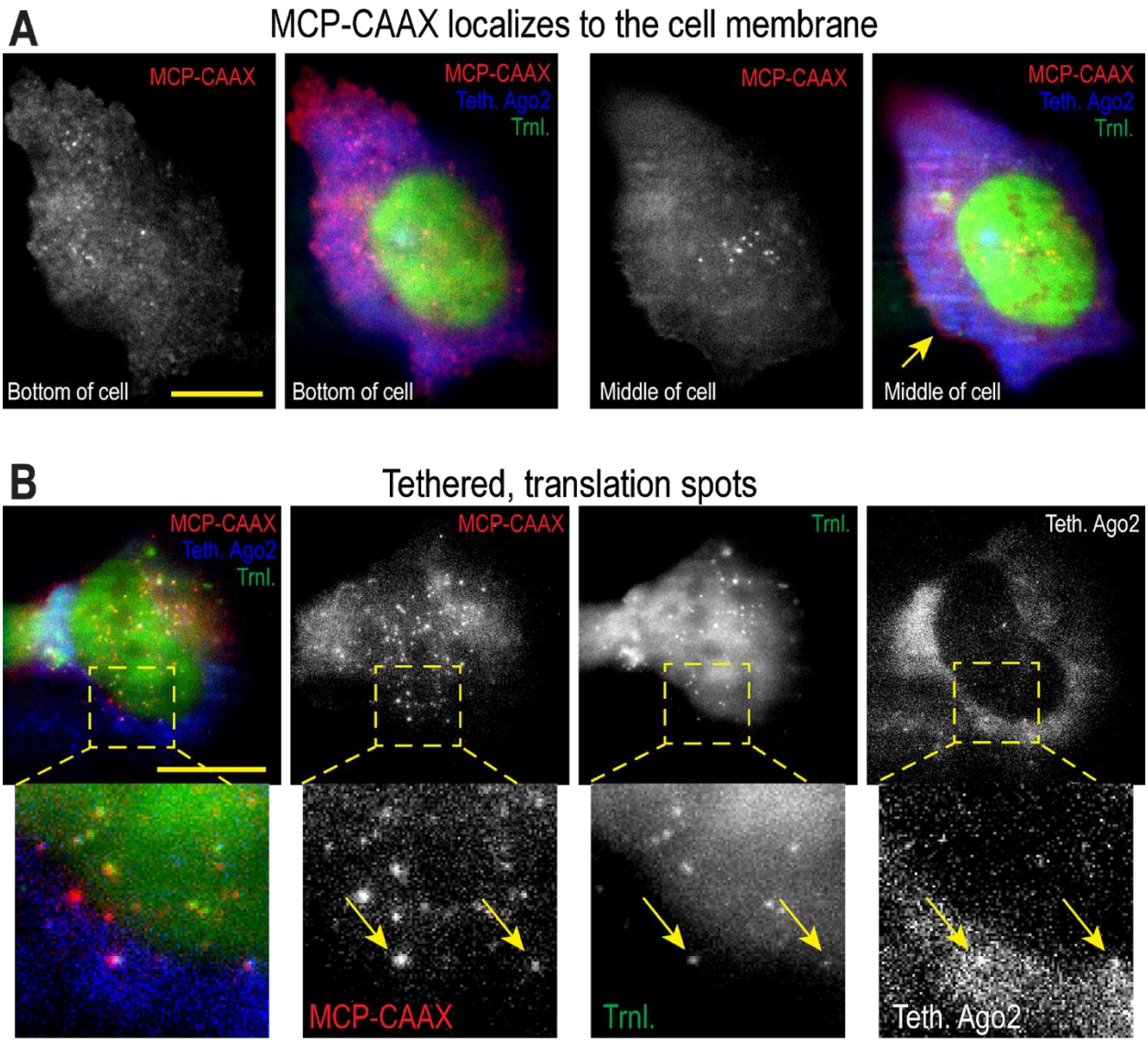

Figure A3.2. MCP-CAAX tethers TnT mRNA to the cell membrane
Representative cells expressing tetherable Ago2 and the TnT biosensor and components (smFLAG-KDM5B-15xBoxB-24xMS2 mRNA reporter, Cy3-FLAG-Fab, and JF646 HaloTag MCP) were imaged 6 h post loading. Exposure times were 100 ms. Scale bars, 10 μm.
A Single Z-slice image of a cell. Left: bottom of the cell. Right: middle of the cell (3 μm above the previous pair of images). Arrow marks midsection of cell membrane.
B Max-Z image of a cell. Arrows mark tethered, translation sites. Left: bottom of the cell. Right: middle of the cell (3 μm above the previous pair of images). Arrows mark tethered translation sites. Scale bar, 10 μm.

tethering (**Figure A3.2B**). Optimal expression of the MCP-CAAX plasmid was 6-10 hours post loading. Since the plasmid was continuously expressed, imaging after 10 hours resulted in too much MCP to see single mRNA foci above the high background. As expected, the CAAX-tethered mRNA resulted in less diffusive mRNA by eye. We did not quantify mean squared displacement of the spots but noticed that the mRNA foci were more or less immobilized at the plasma membrane. Freely-diffusing mRNA need a Δt between frames of <10 seconds for optimal tracking -- in **Chapter 3** tracking was achieved with 100 second intervals of green/blue images with 10 second intervals between red images to minimize green/blue photobleaching. Since the MCP-CAAX-immobilized TnT mRNA were so stationary, we anticipate that the Δt could be lengthened to 1-5 minutes without compromising mRNA tracking. Increasing the Δt would reduce photobleaching/phototoxicity and/or extend the time of the acquisition and thus produce longer tracks.

We also tested various microscope conditions. First, we tested exposure times that were standard (53.64 msec) or prolonged (100-200 msec). Unlike membrane-untethered mRNA, membrane-tethered mRNA were diffusing slowly enough to be captured using the prolonged 100 msec exposure time, and it resulted in increased signal-to-noise for mRNA foci. Increasing the exposure time from 53.64 ms (the imaging conditions used for live-cell imaging) to 100 ms improved visualization of mRNA puncta. However, a 200 ms exposure time resulted in blurry, poorly defined mRNA puncta. Also, since the majority of the mRNA were localized to the cell membrane, we turned the laser angle more acute until near-Total Internal Reflection Fluorescence (~TIRF) imaging was reached. Thus, only fluorophores directly the coverslip edge, i.e.

fluorophores tethered to the plasma membrane, were imaged and the background was greatly reduced. Imaging in ~TIRF greatly improved the imaging speed, since only ~1-3 Z-stack frames were needed to capture the entire plasma membrane. Additionally, it reduced phototoxicity since less Z-stack images were required at each timepoint and thus cells were exposed to the lasers for shorter periods of time.

We are very optimistic for the future of this strategy of immobilizing mRNA at the plasma membrane. The main downside that we anticipate is the progressive build-up of MCP-CAAX as the plasmid post-bead loading, which caused increased background at later timepoints. This issue could perhaps be circumvented by controlling the expression of MCP with a stable, low-expressing cell line or an inducible promoter. Instead of loading and expressing MCP-CAAX on a plasmid, recombinant MCP-CAAX protein could be loaded to achieve a more constant level of per cell over long periods of time.

The traditional, membrane-untethered NCT or TnT reporters provide valuable spatial and mobility information. It is therefore obvious that experiments that measure these parameters should not use MCP-CAAX. However, we anticipate projects could perform both membrane tethered and untethered translation assays to both measure native subcellular localization and mobility dynamics and achieve long-timeframe tracking data.